

Diss. ETH No. 14'351

**MASS TRANSFER CHARACTERISTICS OF A NOVEL
GAS-LIQUID CONTACTOR,
THE ADVANCED BUSS LOOP REACTOR**

A dissertation submitted to the
SWISS FEDERAL INSTITUTE OF TECHNOLOGY ZURICH
for the degree of
DOCTOR OF TECHNICAL SCIENCES

presented by
FRANK OLIVER BAIER

Dipl. Chem.-Ing. ETH
born on July 16th, 1972
citizen of Oberehrendingen AG, Switzerland

Accepted on the recommendation of
Prof. Dr. F. Widmer, examiner
Prof. Dr. M. Morbidelli, co-examiner

Zürich 2001

Acknowledgements

This work was carried out within the scope of a KTI project (Nr. 3736.1) at the Institute of Process Engineering at the Swiss Federal Institute of Technology in Zurich, Switzerland. I gratefully acknowledge the financial support of the Commission for Technology and Innovation (KTI), Bern, Switzerland, and Kvaerner Process Technology AG, Pratteln, Switzerland, who have financed this study in equal shares.

I wish to express my gratitude and thanks to my advisor, Prof. Dr. F. Widmer, for his scientific guidance and the freedom he granted me throughout the course of this work. I very much appreciated as well his skill to create an atmosphere of trust as his complete support even after his retirement.

I thank Prof. Dr. M. Morbidelli for accepting the task of co-examiner and for investing time in reading and discussing this thesis.

Many thanks belong also to Peter Cramers for his valuable advice and help. Over the past four years he has not only become someone I really enjoyed to work with but also a friend.

A very special thanks goes to Dr. W. Dörfler who helped me a lot with the design of the experimental setup.

I also wish to thank Bruno Kramer, Chris Rohrbach, Peter Hoffmann and René Plüss for the many hours of work they have put into the fabrication and construction of the experimental facility. Due to their experience and dedication my initial construction proposals were often massively improved. Furthermore, I am indebted to Urs Müller for his assistance with all matters regarding electronics.

I would also like to thank Martin Koller who carried out a significant part of the measurements with viscous solutions.

During my years at the Institute of Process Engineering I have met and befriended many people who I would like to mention specially: Beat Wellig, Christian Rähle, Andrea Grüniger and Michael Studer who shared the office with me, Emilio Trigo who was my "Kondi"-companion and Isabelle Vinage who joined me for many days in the Verfahrenshalle. Furthermore Flavio Bettoni, Detlef Roederer, Patrick Rüdiger, Elisabeth Harf-Bapin, Res Berger, Karl Ruloff, Gerhard Muhrer, Jörg Worlitschek, Karsten Wegner, Peter Stahl, Kai Lieball, Adrian Wegmann, Beat Borer, Cordin Arpagaus and Patricia Horn. To all a hearty thanks for making the life at the institute enjoyable and for the good time we have spent together! I also thank all other members of the institute for their support, help and companionship.

I also want to thank my brother for revising the orthography and the syntax in this thesis.

This section would not be complete without thanking my parents who have always supported me during my education.

Lastly I wish to thank Astrid for the years past, and those years to come. Thanks for your love, patience and understanding.

Summary

Ejector-type loop reactors with external circulation and heat exchanger stand out for dispersing the gas phase without the use of any stirrers, an efficient utilization of the applied power input, high mass transfer rates and an easily adjustable heat exchanger surface. These reactors utilize the kinetic energy of a liquid jet produced by a nozzle in order to disperse the gas phase. A very recent loop reactor development is the so-called *Advanced Buss Loop Reactor* (ABLR).

The objective of this work was the determination of the relevant mass transfer characteristics of the ABLR, i.e. the volumetric mass transfer coefficient $k_L a$, the gas holdup ϵ_G and the bubble size distribution, in dependence of as well different reaction mixer geometries as different operational conditions like the power input, the system pressure (up to 80 bar) and the properties of the gas and the liquid phase. For this purpose a pilot scale ABLR was designed and constructed which allowed the variation of the influencing parameters and the determination of the relevant mass transfer characteristics. The volumetric mass transfer coefficient $k_L a$ was determined at ambient pressure with the steady-state hydrazine feeding technique and at elevated pressures with a pressure step technique. At the same operating conditions both techniques produced the same values for $k_L a < 0.1 \text{ s}^{-1}$. The bubble size distributions were determined by two different photographic techniques, depending on the testing conditions. For measurements with fine bubble dispersions a special in-process video microscope for high speed applications was used. For dispersions with bubble diameters well above 1 mm a digital photcamera was applied. The evaluation of the obtained images was assisted by image analysis.

By the variation of as well the power input as the liquid batch volume it could be shown that $k_L a$ is a nearly linear function of the specific power input alone (at otherwise constant conditions). Furthermore, in contrast to common ejectors, it was found that the contribution of the reaction mixer volume to the overall mass transfer can be neglected.

The volumetric mass transfer coefficient $k_L a$ is also strongly influenced by the reaction mixer geometry. For the mixing tube an optimal length could be identified. An increased ratio of nozzle diameter to mixing tube diameter led to an increase of $k_L a$ due to an increase of the momentum of the dispersion jet charging from the mixing tube. A swirl flow induced on the liquid jet charging from the nozzle

resulted in increased gas entrainment rates but $k_L a$ decreased significantly. This could be explained by a reduced vertical momentum of the plunging dispersion jet which results in a decrease of the mixing intensity and, therefore, of the liquid sided mass transfer coefficient k_L . In contrast to $k_L a$ and the gas holdup the Sauter bubble diameter was not influenced by the reaction mixer geometry. On the basis of the dimensional analysis an empirical model was derived for the quantitative description of the made observations.

The liquid properties also had a strong influence on the mass transfer characteristics. With liquids at which the bubble coalescence was strongly hindered the Sauter bubble diameter was approximately ten times smaller than with pure water. This led to a massive increase of both $k_L a$ and the gas holdup.

Most industrial gas-liquid reactors are operated at elevated pressures and various gas types are applied, i.e. the physical properties of the gas phase vary within a rather broad range. Therefore, an eventual influence of the system pressure and the gas type has to be taken into account for the correct design of gas-liquid contactors. For this reason the mass transfer characteristics were measured with different gas types at elevated pressures. For pressures between 1-10 bar the Sauter bubble diameter was found to decrease with increasing gas densities. It was possible to derive the corresponding design correlation. Due to the reduced bubble size also the gas holdup and $k_L a$ increased. Additional measurements were carried out with a full scale pilot plant where pressures up to 80 bar were possible and the results obtained at lower pressures regarding the influence of the gas density on $k_L a$ could be confirmed.

Zusammenfassung

Ejektor-Schleifenreaktoren mit externer Zirkulation und externem Wärmetauscher zeichnen sich dadurch aus, dass sie die Gasphase ohne die Hilfe von Rührern dispergieren, die eingetragene Leistung effizient nutzen, hohe Stofftransportraten aufweisen und eine leicht anpassbare Wärmetauscheroberfläche besitzen. Für die Gasdispergierung verwenden diese Reaktortypen die kinetische Energie eines durch eine Düse erzeugten Flüssigkeitsstrahles. Eine der neuesten Entwicklungen auf dem Gebiet der Schleifenreaktoren ist der sogenannte *Advanced Buss Loop Reactor* (ABLR).

Das Ziel dieser Arbeit war die Bestimmung der relevanten Stoffübergangsmerkmale des ABLR, d.h. des spezifischen Stoffübergangskoeffizienten $k_L a$, des Gas holdups ε_G und der Blasengrößenverteilung, in Abhängigkeit sowohl der Geometrie des Reaktionsmischers als auch verschiedener Betriebsbedingungen wie dem Leistungseintrag, dem Betriebsdruck (bis zu 80 bar) und den Eigenschaften der Flüssig- bzw. der Gasphase.

Zu diesem Zweck wurde ein ABLR im Pilotmassstab entworfen und konstruiert, welcher es erlaubte, die einflussnehmenden Parameter zu variieren und die relevanten Stoffübergangsmerkmale zu bestimmen. Der spezifische Stoffübergangskoeffizient wurde bei Umgebungsdruck mittels der Hydrazin-Methode und bei erhöhten Drücken mit der Drucksprungmethode ermittelt. Für $k_L a < 0.1 \text{ s}^{-1}$ wurden mit beiden Methoden die gleichen Werte erhalten. Die Blasengrößenverteilungen wurden abhängig von den Testbedingungen mit zwei unterschiedlichen photographischen Methoden bestimmt. In feinen Blasendispersionen wurde eine spezielle Video-Mikroskopie-Sonde mit sehr kurzen Belichtungszeiten verwendet. Bei Dispersionen mit Blasendurchmessern über 1 mm kam eine digitale Photokamera zum Einsatz. Die Auswertung der erhaltenen Bilder wurde durch Bildanalyse unterstützt.

Durch Verändern sowohl des Leistungseintrages als auch des Befüllungsvolumens konnte gezeigt werden, dass der $k_L a$ -Wert eine annähernd lineare Funktion allein des spezifischen Leistungseintrages ist (bei ansonsten konstanten Bedingungen). Im Gegensatz zu herkömmlichen Ejektoren konnte weiter festgestellt werden, dass der Beitrag des Reaktionsmischervolumens zum gesamten Stoffübergang vernachlässigt werden kann.

Der $k_L a$ -Wert wird ebenfalls stark von der Geometrie des Reaktionsmischers beeinflusst. Bezüglich des Mischrohres konnte eine optimale Länge identifiziert werden. Eine Vergrößerung des Verhältnisses zwischen Düsen- und Mischrohrdurchmesser führte zu einer Erhöhung von $k_L a$. Diese konnte auf eine Zunahme des Impulses des Dispersionsstrahles, welcher aus dem Mischrohr austritt, zurückgeführt werden. Wenn dem aus der Düse austretenden Flüssigkeitsstrahl eine Drallströmung induziert wurde, resultierte zwar eine erhöhte Gasmitnahme aber auch eine signifikante Verringerung von $k_L a$. Dies liess sich anhand einer Verringerung des vertikalen Impulses des eintauchenden Dispersionsstrahles erklären, welche zu einer Verringerung der Mischintensität und somit des flüssigseitigen Stoffübergangskoeffizienten k_L führt. Im Gegensatz zu $k_L a$ und dem Gasholdup wurde der Sauter-Blasendurchmesser nicht von der Geometrie des Reaktionsmischers beeinflusst. Zur quantitativen Beschreibung der gemachten Beobachtungen wurde auf der Grundlage der Dimensionsanalyse ein empirisches Modell hergeleitet.

Die Eigenschaften der Flüssigphase hatten ebenfalls einen grossen Einfluss auf den Stoffübergang. In Flüssigkeiten, die eine starke Koaleszenzhemmung aufwiesen, war der Sauter-Blasendurchmesser ungefähr zehnmal geringer als in reinem Wasser. Dies führte zu einer starken Erhöhung des $k_L a$ -Wertes und des Gasholdups.

Die meisten industriellen Gas-Flüssig-Reaktoren werden bei erhöhten Drücken und mit verschiedenen Gastypen betrieben, d.h. die physikalischen Eigenschaften der Gasphase werden innerhalb eines grossen Bereichs variiert. Für die korrekte Auslegung von Gas-Flüssig-Reaktoren muss daher ein eventueller Einfluss des Systemdrucks oder des Gastyps berücksichtigt werden. Aus diesem Grunde wurden die Stoffübergangsmerkmale mit verschiedenen Gasen und bei erhöhten Drücken gemessen. Bei Drücken zwischen 1-10 bar wurde festgestellt, dass sich der Sauter-Blasendurchmesser mit zunehmender Gasdichte verringert. Eine entsprechende Korrelation konnte hergeleitet werden. Die verringerte Blasen-grösse führt ebenfalls zu einer Erhöhung des Gasholdups und von $k_L a$. Zusätzliche Messungen wurden mit einer technischen Pilotanlage durchgeführt, bei welcher Drücke bis 80 bar erreicht werden konnten. Die bei tieferen Drücken erhaltenen Resultate bezüglich des Einflusses der Gasdichte auf $k_L a$ konnten bestätigt werden.

Table of Contents

Acknowledgements.....	I
Summary	III
Zusammenfassung	V
Table of Contents	VII
Nomenclature	X
1 Introduction	1
1.1 Jet driven gas-liquid reactors	2
1.2 The Advanced Buss Loop Reactor (ABLR)	4
1.3 State of the current knowledge	7
1.3.1 Mass transfer characteristics of the ABLR	7
1.3.2 Mass transfer characteristics of ejector-type loop reactors	8
1.3.3 Influence of the liquid properties on the mass transfer characteristics in jet loop reactors	10
1.3.4 Influence of the system pressure and the gas type on the mass transfer characteristics in jet loop reactors	11
1.4 Motivation and goals	13
1.5 Structure of the thesis	14
2 Theory	15
2.1 Mass transfer	15
2.1.1 Physical absorption	15
2.1.2 Mass transfer with chemical reaction	17
2.1.3 Further definitions	19
2.2 Jet loop reactor specific theory	20
2.2.1 Calculation of the power input	20
2.2.2 Description of the jet swirl	21
2.3 Prediction of the mass transfer characteristics	22
3 Measuring techniques.....	25
3.1 Measurement of $k_L a$	25
3.1.1 Introduction	25
3.1.2 Review of existing techniques for the measurement of $k_L a$	26
3.1.3 Selection of the $k_L a$ measuring technique for experiments at ambient pressure	36
3.1.4 Testing of the hydrazine feeding technique	38

3.1.5 Selection and testing of the $k_L a$ measuring technique for experiments at elevated pressures	43
3.2 Bubble size measurement	46
3.2.1 Review of existing techniques	46
3.2.2 Selection of the measuring technique	48
3.3 Gas holdup measurement	49
3.3.1 Review of existing techniques	49
3.3.2 Selection of the gas holdup measuring technique	51
4 Experimental	52
4.1 Experiments at ambient pressure	52
4.1.1 Experimental Setup	52
4.1.2 Media	59
4.1.3 Experimental methods	61
4.2 Measurements at elevated pressures	63
4.2.1 Experimental setup	63
4.2.2 Media	66
4.2.3 Experimental methods	66
5 Results at ambient pressure with the air/water system.....	67
5.1 Influence of the specific power input	67
5.1.1 Experimental results	67
5.1.2 Discussion	68
5.2 Influence of the liquid batch volume on $k_L a$	69
5.2.1 Experimental results	69
5.2.2 Comparison with common ejector driven loop reactors	71
5.3 Influence of the reaction mixer geometry	74
5.3.1 Influence of the reaction mixer geometry on $k_L a$ and ϵ_{tot}	74
5.3.2 Influence of the reaction mixer geometry on the bubble size distribution	83
5.3.3 Combination of the present results	87
5.4 Derivation of an empirical model	91
5.4.1 Dimensional analysis	91
5.4.2 Regression analysis	96
5.5 Conclusions	99
6 Influence of the liquid properties (at ambient pressure).....	100
6.1 Influence of added electrolytes	100
6.1.1 Influence on $k_L a$ and ϵ_{tot}	101
6.1.2 Influence on the bubble size	104
6.1.3 Additional remarks	107
6.2 Influence of the liquid viscosity	108
6.3 Conclusions	109

7 Results at elevated pressures	110
7.1 Measurements between 1-10 bar	110
7.1.1 Influence of the system pressure and the gas type on the bubble size distribution	111
7.1.2 Influence of the system pressure and the gas type on the gas holdup and $k_L a$	117
7.1.3 Comparison between the pressure step technique and the hydrazine feeding method	118
7.1.4 Extension of the in Chapter 5.4 derived design correlation	120
7.2 Measurements between 10-80 bar	122
7.3 Conclusions	123
Appendices	
A 1 Analysis of the bubble pictures	124
Introduction	124
Description of the fully-automated image analysis procedure	126
Description of the procedure using manual bubble detection	135
A 2 Calculation of the bubble size distributions, d_{32} and the specific surface area	137
Bubble size distribution	137
The Sauter diameter d_{32}	138
Specific surface area	138
A 3 Mixing characteristics	141
Liquid phase RTD	142
Gas phase RTD	145
A 4 Experimental data	148
Air/water (ambient pressure)	148
Air/0.25 M Na_2SO_4 -solution	152
A 5 Bubble size distributions with different gas densities and reaction mixer geometries in water	155
References	159
Curriculum Vitae	170

Nomenclature

Latin letters

a	specific surface area	$[\text{m}^2/\text{m}^3]$
A	interfacial area	$[\text{m}^2]$
Al	Hinterland ratio	$[-]$
b_0, b_1	system coefficients (Eq. 3-8)	$[\text{mol m}^{-3}]$
c	concentration	$[\text{mol m}^{-3}]$
C_f	discharge coefficient	$[-]$
d	diameter	$[-]$
d_{32}	Sauter bubble diameter	$[\text{m}]$
D	diffusion coefficient in the liquid phase	$[\text{m}^2 \text{s}^{-1}]$
e_S	specific power input	$[\text{W m}^{-3}]$
e_S^*	specific power input, dimensionless	$[-]$
E	enhancement factor (chemical influence)	$[-]$
f_0, f_i	regression coefficients	$[-]$
g	acceleration due to gravity	$[\text{m s}^{-2}]$
h	lead of the swirl device helix	$[\text{m}]$
h_p	penetration depth of a plunging jet	$[\text{m}]$
h_R	aerated liquid surface level	$[\text{m}]$
h_S	static liquid surface level	$[\text{m}]$
H	Henry's law coefficient	$[\text{Pa m}^3 \text{mol}^{-1}]$
Ha	Hatta number	$[-]$
j_A	molar absorption flux	$[\text{mol m}^{-2} \text{s}^{-1}]$
k_G	gas sided mass transfer coefficient	$[\text{mol m}^{-2} \text{Pa}^{-1} \text{s}^{-1}]$
k_L	liquid sided mass transfer coefficient	$[\text{m s}^{-1}]$
$k_{m,n}$	chemical reaction rate constant	$[\text{mol}^{-(m+n)-1} \text{m}^{3(m+n)-1} \text{s}^{-1}]$
$k_L a$	volumetric mass transfer coefficient	$[\text{s}^{-1}]$
$k_L a^*$	dimensionless $k_L a$	$[-]$
l_M	mixing tube length	$[\text{m}]$
m	enhancement factor (coalescence influence)	$[-]$
Mo	Morton number	$[-]$
M_r	molecular weight	$[\text{kg mol}^{-1}]$
N	number of moles	$[\text{mol}]$

p	pressure	[Pa]
p_A	partial pressure of component A	[Pa]
P	power input	[W]
Q	volumetric flow rate	[m ³ s ⁻¹]
r	radius	[m]
r	chemical reaction rate	[mol m ⁻³ s ⁻¹]
R	gas constant	[J K ⁻¹ mol ⁻¹]
R	swirl device radius	[-]
Sc	Schmidt number	[-]
Sw	swirl number	[-]
Sw _b	swirl body number	[-]
t	time	[s]
T	temperature	[K]
u	velocity	[m s ⁻¹]
v	axial velocity	[m s ⁻¹]
V _L	liquid batch volume	[m ³]
V _{N₂H₄} [*]	hydrazine feeding rate	[m ³ s ⁻¹]
w	angular flow velocity	[m s ⁻¹]
x	room coordinate	[m]
X	influencing parameter, dimensionless	[-]
Y	target quantity, dimensionless	[-]

Greek letters

α	pitch of the swirl device helix (Fig. 2-2)	[°]
β	nozzle cone angle	[°]
χ	swirl device twist angle	[°]
γ	PVM insertion angle	[°]
δ	film thickness	[m]
Δ	difference	
ε	gas holdup	[-]
κ	exponent	[-]
λ	proportionality factor	[-]
σ	surface tension	[N m ⁻¹]
μ	dynamic viscosity	[Pa s]

ν	kinematic viscosity	$[\text{m}^2 \text{s}^{-1}]$
ν	stoichiometric coefficient	$[-]$
$\bar{\rho}$	homogeneous flow model density	$[\text{kg m}^{-3}]$
ρ	density	$[\text{kg m}^{-3}]$
τ	response time constant	$[\text{s}]$
Φ	absorption rate	$[\text{mol m}^{-3} \text{s}^{-1}]$
ω	ratio of two different nozzle diameters	$[-]$

Subscripts

0	fluid bulk
A	component A
B	component B
disp	Dispersion
G	gas phase
i	interface
in	inlet
J	jet
L	liquid phase
m, n	chemical reaction order
N	nozzle
M	mixing tube
out	outlet
probe	measuring probe
R	liquid recirculation pipe
tot	total

Abbreviations

ABLR	Advanced Buss Loop Reactor
BLR	Buss Loop Reactor
PVM	Process Video Microscopy probe

1 Introduction

Gas-liquid(-solids) reactions are common throughout many fields of today's industry. To mention are for example the petrochemical industry, the synthetic chemistry, biotechnological applications or waste water treatment applications.

The efficiency of gas-liquid(-solids) reactions is often influenced by the mass transfer characteristics of the applied reactor type, especially if gases of low solubility are used and the mass transfer between the different phases becomes the rate limiting step. Examples of mass transfer limited industrial applications include hydrogenation processes (e.g. hydrogenation of double and triple bonds), aminations, alkylations or oxidations. Low mass transfer characteristics result in as well lower conversion rates as longer reaction times and may also lead to lower selectivities and catalyst deactivation (see e.g. Nagel et al., 1978).

According to Lee and Tsui (1999) there exist three key factors for succeeding at gas-liquid reactions:

1. Fluid mechanics, that is, the geometric and physical aspects of the system that govern the distribution and flow of the fluids, the mixing intensity and the mass and heat transfer rates.
2. Integrity of the equipment regarding corrosion, service and safety aspects.
3. The kinetics in case of a chemical reaction, because it dictates the intrinsically attainable reaction rate.

From the above list it is evident that gas-liquid(-solids) reactors are one of the most difficult reacting systems to commercialize. Their development requires dealing with virtually all facets of chemical engineering sciences. This can be very well illustrated with the help of a diagram taken from a publication of

Kawase and Moo-Young (1990) which shows schematically the many interactions occurring with gas-liquid reactions (see Fig. 1-1).

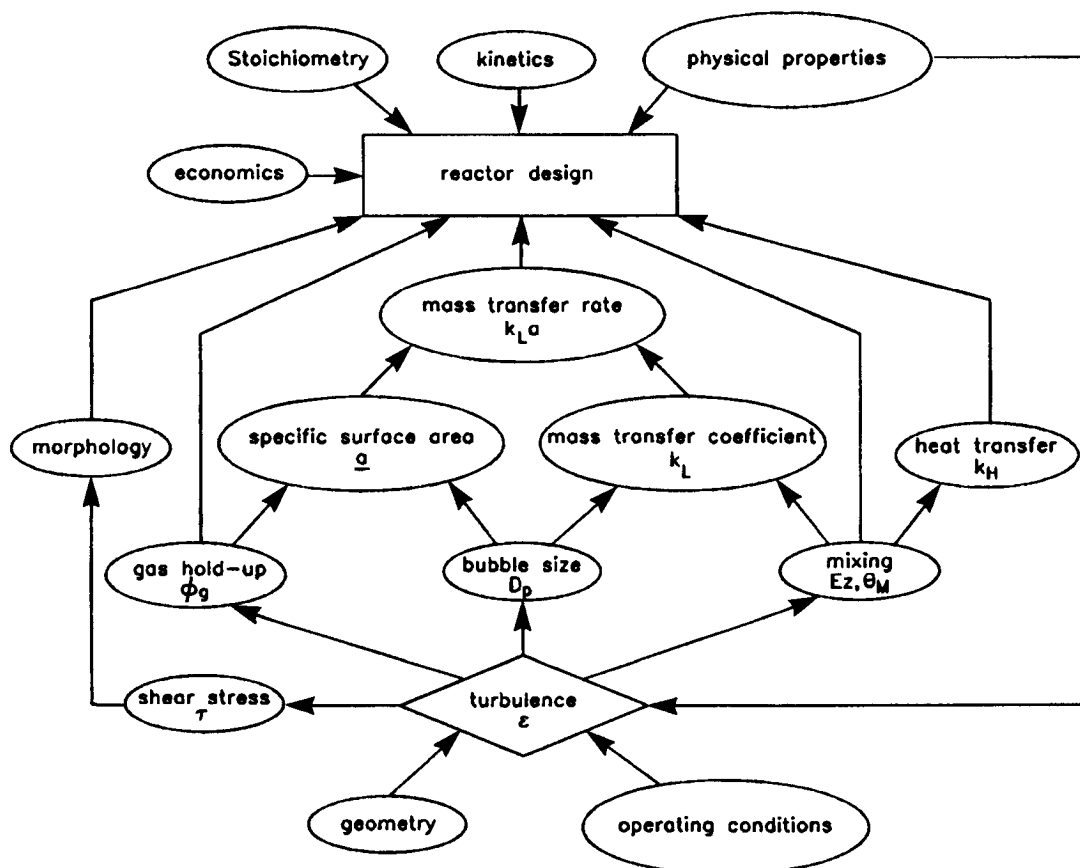


Fig. 1-1: Interactions in gas-liquid reactors (Kawase and Moo-Young, 1990)

With the above figure it becomes apparent that the mass transfer between two given phases can be increased by increasing the turbulence. This demands the dissipation of additional (e.g. mechanical) energy. However, the utilization of the dissipated energy can be very different according to the used reactor type.

1.1 Jet driven gas-liquid reactors

Today, a large selection of contact equipment for mass transfer processes in gas-liquid systems is available. However, all known reactors can be attributed to three

basic types (and combinations of these), which are distinguished by the means the two phases are mixed:

- Mixing due to buoyancy forces (e.g. gas sparged reactors)
- Mixing with stirrers (e.g. stirred tank)
- Mixing with liquid jets

Reactors of the last category stand out for dispersing the gas phase without the use of any stirrers and a more efficient utilization of the applied power input. These reactors utilize the kinetic energy of a liquid jet produced by a nozzle in order to disperse the gas phase.

It has been shown many times that at the same power input jet driven reactors have more favourable mass transfer characteristics than bubble columns or stirred tank reactors. See e.g. Nagel et al. (1970), Zlokarnik (1980), van Dierendonck et al. (1988), Warnecke and Hussmann (1989), Zaidi et al. (1991), Kastanek et al. (1993) or Evans et al. (2001).

Especially loop reactors with liquid jet driven dispersing units, operated in the downflow mode, have proven very favourable mass transfer characteristics. Ejectors are often used for the gas dispersion (e.g. Leuteritz, 1976; Dutta and Raghavan, 1987; Dirix and van der Wiele, 1990; Cramers et al., 1992a,b,1993) but it should be mentioned that also many other jet driven configurations are applied (e.g. Wachsmann et al., 1984; Langhans et al., 1977; Evans et al., 1992; Zaidi et al., 1991; Bin, 1993). With ejectors the liquid jet is utilized to suck in and disperse the gas phase, i.e. no injection of the gas phase is needed (see also Fig. 1-3).

The most widely known ejector loop reactor has been commercialized by Buss AG¹ in Switzerland and is commonly known as the *Buss Loop Reactor* (BLR). It is an ejector driven loop reactor with external circulation and heat exchanger and it stands out for its high mass transfer rates and its easily adjustable heat exchanger surface. A description of the BLR can be found in Ullmann's Encyclopedia of Industrial Chemistry (Elvers, 1992) for example.

The superiority of the BLR for industrial applications compared to stirred tank reactors or bubble columns has been reported e.g. by Leuteritz et al. (1976) for carbonylation and chlorination reactions or Greenwood (1986) and Concordia (1990) for slurry hydrogenations.

1. Today: Kvaerner Process Technology AG, Pratteln, Switzerland

A very recent development is the so-called *Advanced Buss Loop Reactor* (ABLR), which is a further development of the BLR.

1.2 The *Advanced Buss Loop Reactor* (ABLR)

Two major changes were made to the former design. The common 'for liquids only' circulating pump was replaced by the special two-phase pump and the very long ejector was exchanged for a much shorter one with no diffusor or draft tube. Due to the changes made to the dispersion unit it should no longer be called 'ejector'. Instead, the term 'reaction mixer' will be used in connection with the *Advanced Buss Loop Reactor*.

The basic configuration of the *Advanced Buss Loop Reactor* (ABLR) is shown in Fig. 1-2. The reactor is composed of 3 main parts: The reaction vessel [2], the reaction mixer [1] and the recirculation pipe containing the special multi-phase circulating pump [4] and the external heat exchanger [3].

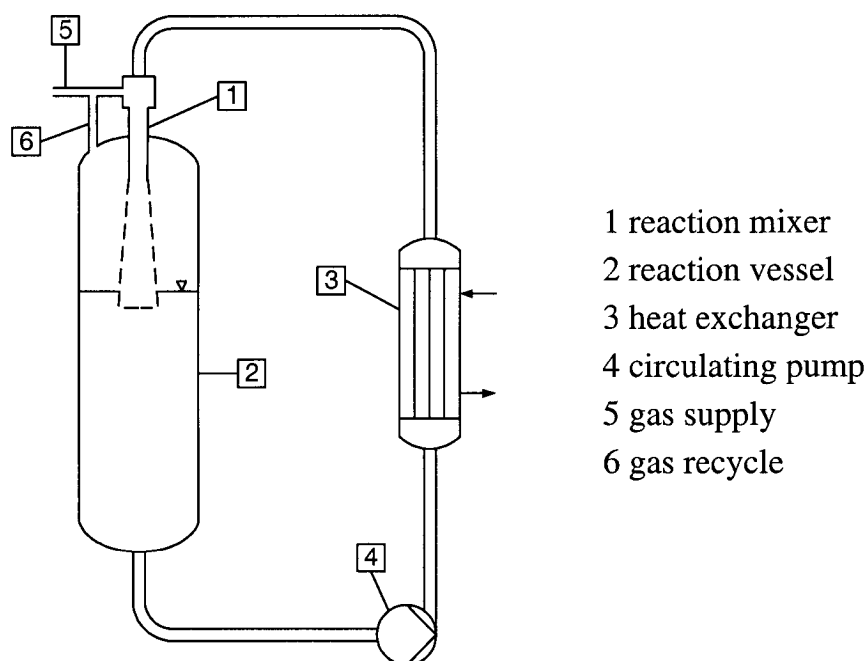


Fig. 1-2: Operating principle of the *Advanced Buss Loop Reactor*

The operating principle of the ABLR is as follows: The liquid phase is delivered by the circulating pump through the external heat exchanger and the reaction mixer back into the reaction vessel. The continuous circulation of the reaction solution causes the entrainment of the gas component and its intensive mixing with the liquid phase by the reaction mixer (see also Fig. 1-3). Gas which has not completely reacted disengages from the reaction solution and returns to the head space of the reaction vessel, where it is re-entrained by the reaction mixer.

Since the circulating pump is able to handle gas holdups up to 50%, the in loop reactors usually needed disengagement of the two phases at the bottom of the autoclave is not necessary. Thus, the effective contact volume is optimally enlarged to the complete reactor volume.

An illustration of the gas entrainment and dispersion mechanisms is shown in Fig. 1-3 in more detail.

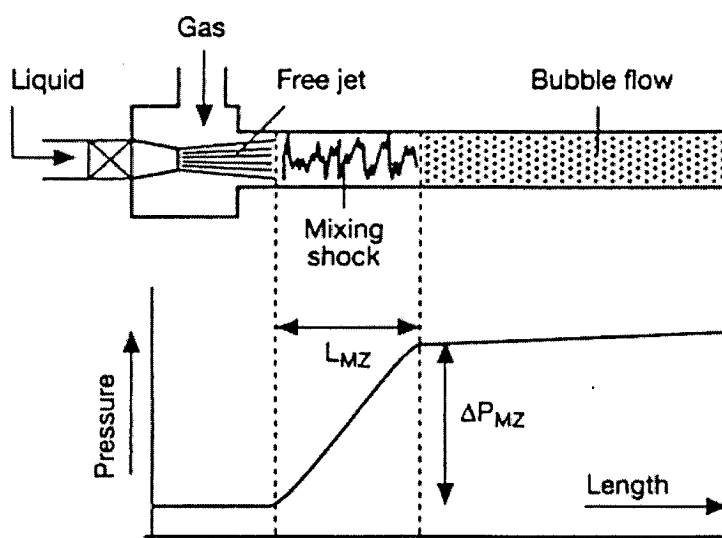


Fig. 1-3: Operating principle of the reaction mixer (Cramers et al., 1993)

The high velocity jet, discharging from the nozzle, entrains a considerable amount of gas into the mixing tube due to the jet envelope mechanism. The gas entrainment can be further enhanced by installing a swirl device upflow of the nozzle which accelerates the break-up of the liquid jet due to the tangential velocity component imposed on the liquid jet (Henzler, 1981; Cramers et al., 1993). Further down the mixing tube gas and liquid are intensively mixed in the mixing shock zone due to the local energy dissipation of the liquid jet. This process is accompanied by a sudden pressure build-up in the mixing tube (Witte, 1969). Since very high energy dis-

sipation rates are present in this section, very small bubbles are generated. From the mixing tube the gas-liquid dispersion charges into the reaction vessel where it additionally causes secondary gas dispersion and mixing with the reaction solution. This mode of dispersion formation provides high intensity interfacial contact and, for that reason, high mass transfer rates.

The design of the *Advanced Buss Loop Reactor* leads to the following advantages (some of these apply also for other jet driven gas-liquid reactors):

- Utilization of the entire reactor volume for the gas-liquid contacting due to the special circulating pump.
- Easy scale up of reaction mixer and heat exchanger surface (van Dierendonck et al., 1988, 1998).
- High mass transfer rates which lead to smaller operating volumes and lower reaction pressures for a defined mass transfer rate.
- The actual gas dispersion is achieved without any moving parts.
- Efficient primary dispersion of the gas phase. This is particularly advantageous for non coalescing systems in which fine primary bubbles are preserved throughout the whole reactor vessel (Kastanek et al., 1993).
- The only moving part in the reactor is the circulation pump. Deflections of the pump shaft are less than the deflections in an agitator shaft, and as shaft movements are damaging to the seals, the production time lost for seal changes are much lower than with stirred tank reactors (Greenwood, 1986).
- The high degree of macroscale turbulence in the reactor vessel provides favorable conditions for catalyst suspension with slurry reactions.
- Gas recirculation ensures complete gas utilization.
- Since the gas phase is sucked in and dispersed by the liquid jet, no extra compression device is required.

1.3 State of the current knowledge

1.3.1 Mass transfer characteristics of the ABLR

At the beginning of this work the only data available regarding the mass transfer characteristics of the ABLR were some results obtained with pilot tests. In these tests it was proven that the ABLR featured higher mass transfer rates than the BLR and, therefore, most other commonly used gas-liquid reactors (Baier, 1997).

Some examples of the pilot tests are given in Table 1-1 and Table 1-2. With the cobalt catalyzed sulfite oxidation the ABLR required only half the BLR's power input to attain the same oxygen transfer rate. With a slurry hydrogenation of an aldehyde compound the reaction rate could be increased by adding more catalyst, i.e. the reaction was kinetically controlled. This was not possible with the BLR which indicates complete rate limitation by the gas-liquid mass transfer.

	BLR	ABLR
Oxygen transfer rate (kg hr ⁻¹ m ⁻³)	10-12	10-12
Power input (kW m ⁻³)	5.0-6.0	2.5-3.0

Table 1-1: Cobalt catalyzed sulfite oxidation (at 1 atm and 30°C)

	Catalyst load (wt-%)	BLR	ABLR
Hydrogen transfer rate (Nm ³ hr ⁻¹ m ⁻³)	5	24.6	27.6
	7	25.2	32.4
	9	24.6	36.6
Power input (kW m ⁻³)		4.5-5.0	3.0-3.5

Table 1-2: Hydrogenation of an aldehyde compound (at 6 bar and 130°C)

With these results it is evident that the combination of the modified reaction mixer configuration and the special circulating pump resulted in mass transfer characteristics which are an improvement and apparently different compared to common downflow ejector loop reactors.

However, despite the observed differences regarding the mass transfer, still many processes taking place in the reaction mixer are comparable to the ones in common

ejectors. For the better understanding of these processes the knowledge regarding ejector-type loop reactors shall be reviewed. Also the influence of the gas and liquid properties on the mass transfer characteristics will be considered briefly.

1.3.2 Mass transfer characteristics of ejector-type loop reactors

Nagel et al. (1970a, 1973) were the first who proposed the application of liquid jet driven two-phase nozzles for the gas dispersion at the bottom of gas-liquid tower contactors. The primary dispersion took place in a draught tube directly installed above the two-phase nozzle. The measured interfacial area a was much higher than with a stand-alone two-phase nozzle. They related the measured values of a and $k_L a$ to the volumetric energy input and carried out comparisons regarding the performance of other reactor types.

Later more general studies were carried out devoted to the description of the mechanism of the dispersion formation in reactors with ejector distributors or the optimization of the ejector configurations. Jekat and Pilhofer (1975) investigated the gas entrainment rates in an upflow loop reactor with different ejector geometries. Zlokarnik (1979) introduced the so-called slot injector for the gas dispersion. On the basis of literature data, theoretical models and own experiments Henzler (1981) presented the 'concept of a favourable ejector'. However, it should be noted that this concept was derived on the basis of purely energetic criteria with the goal to maximize the gas entrainment rate. The resulting mass transfer characteristics were not investigated or considered for the optimization.

Dutta and Raghavan (1987) investigated the mass transfer characteristics of a loop reactor with downflow ejectors fitted with straight- and venturi-type throats. They reported that the average primary bubble size was smaller with a venturi-type throat but carried out no exact bubble size distribution measurements. With the air-water system the straight throat was found to be much better regarding the dispersion of the entrained gas in the entire reaction vessel (secondary dispersion). Also with the straight throat the bubble size in the vessel was much more uniform and the gas holdup was higher, i.e. the power input was utilized more effectively. However, with coalescence hindered solutions the venturi-type ejector had the higher $k_L a$ values, probably due to smaller primary bubbles.

Dirix and van der Wiele (1990) and later Cramers et al. (1992a,b, 1993) studied loop-venturi reactors with downflow liquid jet ejectors and found that the ejector and reaction vessel should be treated as two reactors in series. Dirix and van der

Wiele (1990) reported that with the water/air system, depending on the operating conditions, a good part of the mass transfer took place inside the ejector. They also recommend a pressure difference across the liquid jet nozzle of at least 2 bar for proper operation of the ejector.

Cramers et al. (1992b) carried out extensive investigations with a Henzler-type ejector. According to them the reaction vessel behaves like a bubble column where the ejector is used as a special gas distributor. For coalescence hindered systems they report specific surface areas between 40 000 to 70 000 m^{-1} in the ejector and 500 to 2500 m^{-1} in the entire reactor. The maximum values of $k_L a$ measured in the ejector were around 6 s^{-1} . These findings were later confirmed by Havelka (2000) who obtained with another ejector configuration $k_L a$ values of 7.5 s^{-1} inside the ejector. Cramers et al. (1993) even treated the mixing shock zone and the diffusor separately and found marked differences regarding their mass transfer characteristics. Most of the design correlations given by these authors are valid for the ejector zone only and not the entire reactor system.

A special variant of an ejector type reactor has been described by Evans et al. (1992), Evans and Jameson (1995) and Evans et al. (2001). Their so-called 'confined plunging liquid jet bubble column' is basically a downflow ejector reactor reduced to its jet nozzle and mixing tube. Like Cramers et al. (1993) they identified two different zones in the bubble column (aka mixing tube), the mixing zone (aka mixing shock zone) and the pipe flow zone (aka bubble flow zone). With a laboratory scale setup $k_L a$ reached 2.5 s^{-1} in the mixing zone and was an order of magnitude lower in the pipe flow zone. In tap water the bubbles in the mixing zone had a diameter of approximately 200 μm , the ones in the pipe flow zone ranged between 2-4 mm. However, the applicability of this reactor concept at larger industrial scale has still to be proven.

Different ejector configurations for upflow operation were extensively studied by Zahradnik et al. (1985), Kastanek et al. (1993), Havelka et al. (1997) and Zahradnik et al. (1997). One of their results was the definition of design recommendations for efficient operation of ejectors. Under efficiency the authors understood the optimization of the gas entrainment and the resulting gas holdup. Often they did not take any mass transfer rates into consideration for the optimization. Only very recently these authors (Havelka et al., 2000) carried out some mass transfer measurements with the proposed ejector configurations and found that the most 'efficient' ejector configuration was not the one that gave the highest $k_L a$ values, i.e. entrainment efficiency may not necessarily go hand in hand with mass transfer efficiency.

As already mentioned, swirl devices installed upflow of the jet nozzle can be used in order to enhance the jet breakup and the gas entrainment (Henzler, 1981). However, it is not entirely clear how the jet swirl affects the volumetric mass transfer coefficient $k_L a$ of the entire reactor system. According to Cramers et al. (1993) the local $k_L a$ value inside ejectors decreases when a swirl device is used, but it is not said how the overall $k_L a$ of the entire reactor is affected. Havelka et al. (1997) tested many different swirl devices with an upflow ejector. The measured gas entrainment rate and the resulting gas holdup were higher with a swirl device than without one. They also observed that, if the induced swirl was too small, no enhancement occurred and, if it was too high, the gas entrainment decreased again. Later the same authors (Havelka et al., 2000) measured the mass transfer rate in the same reactor and found a decrease of $k_L a$, if a swirl was installed. In their modelling however, they state that $k_L a$ is only a function of the gas holdup, which is contradictory to their previous paper.

The scale-up procedure is regarded as very simple with ejector loop reactors. The gas-liquid stream from the ejector into the reactor ensures according to Zahradnik et al. (1997) very good radial and axial distribution of the gas bubbles, i.e. homogeneous conditions. Therefore, the scale-up of these reactors is based on a constant value of the specific energy dissipation rate in the reaction solution (van Dierendonck et al., 1988 and 1998). Geometric quantities like the ratio of the nozzle and mixing tube diameters and the ratio of the mixing tube length and mixing tube diameter are kept constant during scale-up.

1.3.3 Influence of the liquid properties on the mass transfer characteristics in jet loop reactors

A general question in the whole field of gas-liquid reactors concerns the prediction of the effect of the liquid phase physical properties on the mass transfer characteristics. Most industrial processes are characterized by undefined components in the reaction solution which can strongly influence the hydrodynamic characteristics.

It is well known that the coalescence of small gas bubbles to larger bubbles can be decisively influenced in solutions of various inorganic salts or organic liquids such as lower fatty alcohols (e.g. Zahradnik et al., 1999). Bubble coalescence

takes place when the liquid film between two bubbles is drained. In pure water this process is very fast but in the presence of electrolytes it is slowed down significantly. The explanation of this effect can be formulated as follows: 'Ionic forces between the ionic species of the film (between the bubbles) and water molecules make the film more cohesive. This increases the strength of the film against bubble coalescence, decreases the bubble size and increases the gas holdup. The overall result of these effects is a higher specific surface area compared to pure water' (Zarraa, 1999).

For coalescence hindered salt solutions Zlokarnik (1979a,b) showed that the formation of small primary bubbles is decisive to enhance the mass transfer in these media. Since the primary bubble size depends on the applied gas dispersing device, the relative enhancement of the mass transfer rate due to coalescence hindrance compared to coalescing conditions can be very different for different reactor types, i.e. the definition of a general $k_L a$ enhancement factor due to coalescence hindrance is not possible.

The application of ejector driven loop reactors is particularly advantageous with coalescence hindered liquids since the fine primary gas dispersion is preserved throughout the entire reactor. Havelka (1997) reported $k_L a$ values up to 1.5 s^{-1} in the reaction vessel with a $0.3 \text{ M Na}_2\text{SO}_4$ -solution. This is in agreement with Nardin (1995) who reported values up to 1.2 s^{-1} for non-coalescing systems (compared to $0.05\text{-}0.25 \text{ s}^{-1}$ in bubble columns and $0.15\text{-}0.5 \text{ s}^{-1}$ in stirred tank reactors).

Regarding the influence of the liquid viscosity there exists a common consensus that an increase of the viscosity results in a decrease of the mass transfer performance. However, the exact effects have still to be determined through experiments.

1.3.4 Influence of the system pressure and the gas type on the mass transfer characteristics in jet loop reactors

Most industrial gas-liquid reactors are operated at elevated pressures (up to 100 bar). Also various gas types are applied industrially, i.e. the gas physical properties vary within a rather broad range. Therefore, an eventual influence of the system pressure and the gas type has to be taken into account for the correct design of gas-liquid contactors. Despite this fact, most of the available data in the literature

regarding the mass transfer characteristics of gas-liquid reactors is valid for ambient pressure only. A decade ago Oyevaar and Westerterp (1989) observed that only some twenty papers had been published which deal with or touch upon the influence of the operating pressure in gas-liquid systems!

The studies published so far all show significant pressure effects on the mass transfer characteristics and data obtained at ambient pressure only have to be regarded as insufficient for the design and scale-up for gas-liquid reactors operated at high pressures.

Most of these investigations have been carried out with bubble columns. Wilkinson (1991) and Wilkinson and Haringa (1994) report that the bubble breakup rate (especially of large bubbles) is enhanced by an increase of the gas density due to a promotion of Kelvin-Helmholtz instabilities on the bubble surface. This causes a decrease of the mean bubble diameter and a more narrow size distributions at elevated pressures. Their experiments show that both pressure and molecular weight of the gas phase contribute to the influence of the gas density. An increase of $k_L a$ and also the gas holdup with increasing gas density was found. The same observations were made later e.g. by Kojima (1994) and Letzel et al. (1998).

Luo et al. (1999) also observed a decrease of the bubble size in bubble columns at elevated pressures. They proposed an internal circulation model to quantify the observed pressure effects on the maximum bubble size.

The data regarding the influence of the gas properties with ejector loop reactors is very scarce. Henzler (1981) carried out experiments at atmospheric pressure using gases of different molecular weights (air, helium, air-helium mixtures) and concluded that the gas entrainment by the ejector increased with the gas density at constant liquid jet velocities. This was confirmed by Cramers et al. (1992a) who investigated an atmospheric reactor with a downflow liquid jet ejector. The studied densities ranged between 0.18 and 6.18 kg/m³. An increased gas density resulted in an increase of the gas entrainment rate. According to them the gas density influences the jet envelope development. They also observed a decrease of the mean bubble diameter in the reaction vessel with increasing gas densities which agrees with the findings of Wilkinson (1991). However, the influence of the system pressure on $k_L a$ was not investigated.

From this review it can be concluded that the gas properties will have an influence on the mass transfer characteristics of ejector loop reactors. However, no experimental data regarding $k_L a$ has been reported yet for jet driven loop reactors¹.

1.4 Motivation and goals

In pilot tests the *Advanced Buss Loop Reactor* has shown very favourable qualities. However, no systematic data regarding its mass transfer characteristics is available. Keeping the above review in mind, several questions arise: Is the current reactor configuration the optimum or can it be further improved? How is the mass transfer influenced by a swirl imposed on the liquid jet or by a change of the reaction mixer geometry? How do the liquid properties affect the performance of the reactor? What is the influence of the gas properties on the mass transfer characteristics?

The need to deepen the basic knowledge of the mass transfer characteristics of the ABLR is obvious and leads to the definition of the objectives of this work:

- Determination of the relevant mass transfer characteristics, i.e. the volumetric mass transfer coefficient $k_L a$, the gas holdup ϵ_G and the bubble size distribution, in dependence of as well different reaction mixer geometries as different operational conditions like the power input, the system pressure and the properties of the gas and the liquid phase.
- Identification of the influence of the varied parameters on the mass transfer characteristics and the proposition of the corresponding design correlations.
- For this purpose a pilot scale ABLR needs to be designed and constructed which allows as well the variation of the influencing parameters as the determination of relevant mass transfer characteristics. This also implies the evaluation and development of suited measuring techniques for the determination of the volumetric mass transfer coefficient $k_L a$, the gas holdup ϵ_G and the local bubble size distribution.

1. Near the end of this work Cramers and Beenackers (2001) reported that an increase of the gas density results in an increase of $k_L a$ inside a downflow ejector ($k_L a \sim \rho_G^{0.2}$).

1.5 Structure of the thesis

In Chapter 2 the theoretical basics of absorption processes will be shortly described. Also some design correlations for the calculation of the mass transfer characteristics in jet loop reactors will be introduced.

Chapter 3 deals with the description of the applied measuring techniques. Special emphasis is laid on the selection process of the proper techniques.

A detailed description of the experimental setup for measurements at as well ambient as elevated pressures will be given in Chapter 4. Here the properties of the used model media can also be found.

In Chapter 5 all the results can be found which were obtained with the air/water system at ambient pressure. First the experimental data regarding the influence of the power input and the liquid batch size will be discussed. In the second part the effect of the reaction mixer configuration on the mass transfer characteristics will be described. Also a design correlation for the quantitative description of the experimental data will be derived. The chapter will be finished by a summary of the made conclusions.

In Chapter 6 the influence of certain liquid properties on the mass transfer will be presented. First the effect of added electrolytes on the mass transfer characteristics will be discussed. As with the air/water system the performance of different reaction mixer geometries will be compared. Also a brief insight on the influence of the liquid viscosity will be given. In the last section a summary of all conclusions will be given.

Chapter 7 deals with the influence of the system pressure and the gas type. First the experimental data obtained with the in Chapter 4 described experimental setup will be presented and discussed. The second part describes additional measurements that were carried out with a large scale pilot plant¹ which could be operated at pressures up to 80 bar. Finally the made conclusions will be summarized.

1. The pilot plant was located at the testing facilities of Kvaerner Process Technology (SWITZERLAND) AG, Pratteln, Switzerland

2 Theory

2.1 Mass transfer

The general material balance for the mass transfer of a component A with chemical reaction is given by the following equation (valid for isothermal conditions, constant density and constant diffusion coefficient D_A):

$$\frac{\partial c_A}{\partial t} = \vec{u} \cdot \nabla c_A + D_A \nabla^2 c_A + r_A \quad (2-1)$$

There exist three basic models for the description of the processes taking place at the phase interface: the steady-state two-film theory, the penetration theory by Higbie and the surface renewal theory by Danckwerts (see e.g. Charpentier 1981). The later two are unsteady-state theories and are, from a physical point of view, more correct than the film theory. However, all these models lead to the same prediction concerning the effect of the driving force $c_{A,i} - c_A$ in the liquid phase on the average mass transfer rate. Therefore, due to simplicity, only the film theory will be used for illustration purposes.

2.1.1 Physical absorption

The process of the physical absorption of a gas phase component A into a liquid phase on the basis of the two-film theory is illustrated in Fig. 2-1. With the two-film theory it is assumed that on either side of the phase interface a stagnant film is formed where mass transfer takes place only by stationary diffusion. Right at the interface equilibrium exists between the two phases and Henry's law is valid ($p_{A,i} = H_A c_{A,i}$). Outside the films the phases are considered as well mixed.

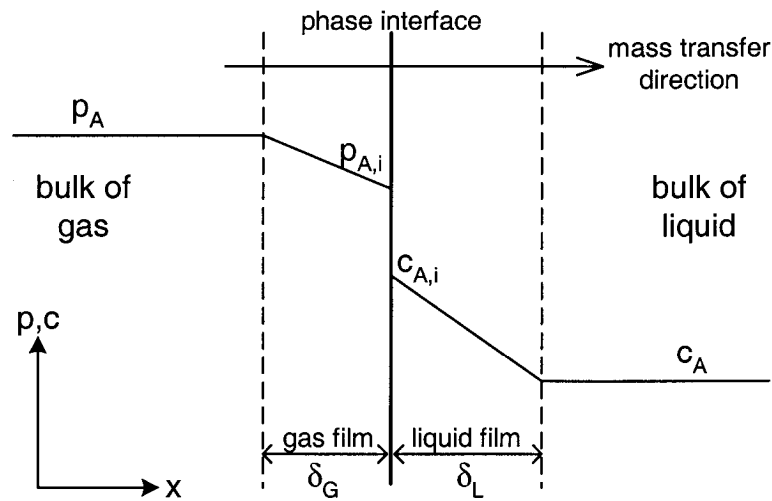


Fig. 2-1: Concentration profile for the absorption process (two-film theory)

With the application of the two-film theory Eq. 2-1 can be strongly simplified: The scalar product of the velocity vector \vec{u} and concentration gradient ∇c_A can be neglected near the phase interface since the vectors are perpendicular to each other. The absorption is a stationary problem and $(\partial c_A / \partial t) = 0$ is valid. If the extension and the radius of curvature of the interface are large compared to the thickness of the stagnant layer δ , a one-dimensional description is sufficient. The chemical reaction rate r_A can be set to zero.

For the stationary physical absorption through a stagnant film layer of the thickness δ Eq. 2-1 can be rewritten:

$$0 = D_A \frac{\partial^2 c_A}{\partial x^2} \quad 0 \leq x \leq \delta \quad (2-2)$$

The determination of the mass transfer rate is based upon the concept of the additivity of the gas phase resistance and the liquid phase resistance. With the help of Eq. 2-2 and Fick's law

$$j_A = -D_A \left(\frac{\partial c_A}{\partial x} \right)_i \quad (2-3)$$

the molar absorption flux of the component A by the liquid phase can be calculated.

$$j_A = -\frac{1}{A} \frac{dN_A}{dt} = \frac{1}{\left(\frac{1}{H_A k_{A,G}} + \frac{1}{k_{A,L}}\right)} \left(\frac{p_A}{H_A} - c_{A0}\right) \quad (2-4)$$

A is the interfacial area, $k_{A,G}$ and $k_{A,L}$ are the gas respectively the liquid sided mass transfer coefficients¹. For gases of low solubility the gas sided mass transfer resistance can usually be neglected, i.e. the partial pressure of component A at the gas-liquid interface is equal to the one in the gas bulk ($p_A = p_{A,i}$). With the introduction of the specific surface area a which is defined by

$$a \equiv \frac{A}{V_L} \quad (2-5)$$

Eq. 2-4 becomes

$$\Phi = j_A a = k_L a (c_{A,i} - c_{A0}) \quad (2-6)$$

The absorption rate Φ is characterized by the volumetric mass transfer coefficient, $k_L a$, and by the driving concentration difference.

It is seldom possible to separately measure the liquid sided mass transfer coefficient k_L and the specific surface area a. Therefore, the direct measurement of the product $k_L a$ is very established.

2.1.2 Mass transfer with chemical reaction

Now the absorbed gas component A undergoes a reaction with a reactant B dissolved in the liquid phase. The stoichiometry of the reaction is represented by



with the kinetic rate equation

$$r_A = -k_{m,n} c_A^m c_B^n \quad (2-8)$$

1. With the two-film theory: $k_{A,L} = \frac{D_{A,L}}{\delta_L}$ and $k_{A,G} = \frac{D_{A,G}}{RT\delta_G}$

If the reaction rate is fast compared to the mass transfer rate, an enhancement of the absorption rate occurs. This is caused by an increase of the concentration gradient dc_A/dx in the liquid film due to an extra decrease of A by reaction.

Generally, the mass transfer rate of a gas component A into a liquid followed by a homogeneous reaction can be described by extending Eq. 2-6.

$$\Phi_{\text{with reaction}} = Ek_L a (c_{A,i} - c_{A0}) \quad (2-9)$$

E is the so-called enhancement factor, representing the extent to which the rate of absorption is increased by the chemical reaction.

$$E \equiv \left(\frac{\Phi_{\text{with reaction}}}{\Phi_{\text{without reaction}}} \right) = f(\text{Ha}, Z, \text{Al}) \quad (2-10)$$

The enhancement factor is, depending on the reaction kinetics, a more or less complicated function of the *Hatta* number Ha, the ratio of the diffusion currents Z and the *Hinterland* ratio Al.

$$\text{Ha} \equiv \frac{\sqrt{\frac{2}{n+1} \cdot k_{m,n} \cdot c_A^{n-1} \cdot c_B^m \cdot D_{A,L}}}{k_{A,L}} \quad (2-11)$$

$$Z \equiv \frac{D_B c_{B0}}{v_B D_A c_{A,i}} \quad (2-12)$$

$$\text{Al} \equiv \frac{k_L}{aD_A} = \frac{V_L}{\delta_L A} = \frac{\text{liquid volume}}{\text{film volume}} \quad (2-13)$$

The description of the absorption of a gas component followed by a single first order irreversible reaction is straightforward. For all common mass transfer models (film, penetration and surface renewal) this process can be analytically solved. For other processes however, only for a limited number of special cases analytical solutions are possible and numerical techniques or approximations have to be applied.

The model system used in this work for the determination of $k_L a$ (see also Chapter 3) was an absorption process followed by a slow to moderate chemical reaction, i.e. $0 < c_{A0} < c_{A,i}$. Since the gas phase is dispersed in a liquid phase the *Hinterland* ratio is > 100 , i.e. most of the conversion takes place in the bulk of the liquid phase and the drop in concentration of A over the boundary region is

mainly due to a diffusional resistance. In that case the absorption is not chemically enhanced ($E=1$).

Due to this fact, the theory of absorption with chemical reaction will not be discussed in more detail. Additional information on this subject can be found elsewhere, e.g. in van Landeghem (1980), Charpentier (1981), Deckwer (1985) or van Swaaij and Versteeg (1992). Very recently an advanced model was also proposed by Schlüter and Schulzke (1999). Their *hybrid model* takes into consideration simultaneously as well physical as chemically enhanced absorption.

2.1.3 Further definitions

The bubble sizes in gas-liquid dispersions are never uniform but distributed. However, for practical calculations it is useful to define a single mean bubble diameter for the characterization of a bubble size distribution. For mass transfer processes the so-called *Sauter* diameter d_{32} is relevant. It represents the mean bubble size which has the specific surface area of the entire bubble population.

$$d_{32} \equiv \frac{\sum_{i=1}^k n_i d_i^3}{\sum_{i=1}^k n_i d_i^2} \quad (2-14)$$

d_i is the diameter of a single bubble and n_i is the number of bubbles of diameter d_i .

The volumetric fraction of the gas phase dispersed in a liquid phase is called the gas holdup and is defined as follows:

$$\varepsilon_G \equiv \frac{V_G}{V_G + V_L} \quad (2-15)$$

V_G and V_L are the volumes of the phases in the dispersion.

In Eq. 2-16 it is shown how the gas holdup ε_G , the specific surface area a and the *Sauter* mean bubble diameter d_{32} are connected:

$$a = \frac{6\varepsilon_G}{d_{32} \cdot (1 - \varepsilon_G)} \quad (2-16)$$

If as well a (or ϵ_G and d_{32}) as $k_L a$ are known, the usually not measurable liquid sided mass transfer coefficient k_L can be calculated.

$$k_L = \frac{k_L a}{a} = \frac{k_L a}{6\epsilon_G / (d_{32} \cdot (1 - \epsilon_G))} \quad (2-17)$$

2.2 Jet loop reactor specific theory

2.2.1 Calculation of the power input

For jet driven reactors the power input is calculated from the converted pressure energy in the jet nozzle. It has to be pointed out that with the ABLR there is also some gas dispersed in the recycle pipe. Therefore, the mean density of the dispersion instead of the pure liquid phase has to be used. With the homogeneous model approach¹ the mechanical energy balance of the two phase flow through the nozzle can be written as

$$\Delta p_N = C_f \cdot u_N^2 \cdot \bar{\rho} \quad (2-18)$$

Δp_N is the dynamic pressure difference across the jet nozzle, C_f the discharge coefficient, u_N the jet velocity at the nozzle outlet and $\bar{\rho}$ the density of the dispersion. The total flow rate through the nozzle Q_{tot} is given by

$$Q_{tot} = u_N \cdot \pi \cdot \frac{d_N^2}{4} \quad (2-19)$$

The power input P into the reaction vessel can be calculated by the combination of Eq. 2-18 and Eq. 2-19. At low pressures the mean dispersion density $\bar{\rho}$ in the recy-

1. Homogeneous model assumption for the ABLR

As well in the vertical as in the horizontal parts of the liquid recycle pipe the two phase flow could be assigned to the bubble flow regime (see the flow regime map in e.g. Ewing, 1999). This was confirmed by visual observations. Furthermore, the bubbles were re-dispersed by the circulating pump and remained small. Thus, the slip between the two phases was negligible. Therefore, the dispersion in the liquid recycle pipe was approximated by the homogeneous flow model with no slip.

cle pipe can usually be approximated by $(1-\varepsilon_R)\cdot\rho_L$ with ε_R being the gas holdup in the recirculation pipe.

$$P = Q_{\text{tot}}^* \cdot \Delta p_N = \frac{\pi}{4} d_N^2 \sqrt{\frac{2 \cdot \Delta p_N^3}{C_f \cdot (1 - \varepsilon_R) \cdot \rho_L}} = C_f \frac{\pi}{8} \rho_L d_N^2 u_N^3 (1 - \varepsilon_R) \quad (2-20)$$

In order to compare the performance of different reactor types or sizes not the absolute but the specific power input is used.

$$e_s \equiv \frac{P}{V_L} \quad (2-21)$$

It should be noted that some authors relate the power input to the dispersion volume and not to the liquid volume. However, this is not very practicable because now e_s would be also a function of the gas holdup and could not be varied independently.

2.2.2 Description of the jet swirl

A swirl body inserted into the jet nozzle transforms a part of the axial momentum of the liquid phase into an angular momentum. The extent of the liquid jet rotation can be generally characterized by a dimensionless swirl number, Sw , which is defined as the ratio of the angular and the axial momentum flows (see e.g. Duquenne et al., 1993).

$$Sw = \frac{2\pi \int_0^R \rho v(r) w(r) r^2 dr}{R \left[2\pi \int_0^R \rho v^2(r) r dr + 2\pi \int_0^R p(r) r dr \right]} \quad (2-22)$$

Where $v(r)$ and $w(r)$ denote the axial and angular component of the flow velocity, $p(r)$ the radial pressure profile in the jet and R the radius of the swirl device. The second term in the denominator is usually neglected due to the infeasibility of determining the radial pressure profiles. The exact velocity profiles can be determined e.g. by laser-Doppler velocimetry.

Recently Havelka et al. (1997) have proposed a simplified and much more practical method to calculate the swirl number of a swirl device. Their so-called swirl body

number, Sw_b , is solely a function of the swirl device geometry and describes the capability of a swirl device to induce a rotating motion on a liquid jet. For twisted sheet metals, as they were used in this work, the swirl body number can be obtained with the following formula:

$$Sw_b = \frac{1}{2 \tan \alpha} \quad (2-23)$$

The definition of α is shown in Fig. 2-2. The parameter h denotes the lead of the swirl device helix.

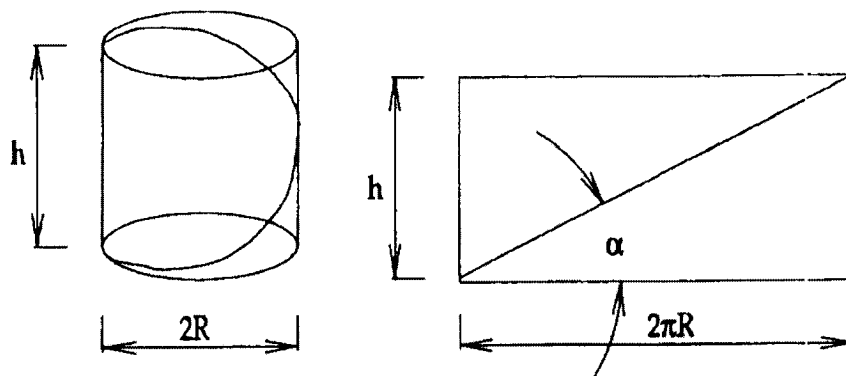


Fig. 2-2: Geometrical parameters of the swirl body

Since the swirl devices used in this work were conical (see also Chapter 3) the average swirl diameters were (arbitrarily) employed for the calculation of Sw_b . Havelka et al. (1997) tested their simplified approach by comparing the gas entrainment rates of different swirl device geometries. At equal swirl body numbers similar gas entrainment rates were measured. (Still, it should be pointed out that the predicted swirl number of a swirl device and the respective swirl number of a fluid evaluated from data measured in the fluid leaving the swirl device may differ significantly.)

2.3 Prediction of the mass transfer characteristics

Due to the very complex transport phenomena taking place in gas-liquid contactors and the large number of parameters influencing these processes it is generally not possible to calculate the mass transfer characteristics in advance. For a short time

now it has been possible to predict the hydrodynamics in gas-liquid-reactors of simple geometries (e.g. bubble columns) with the help of very extensive computer models (e.g. Pflieger et al., 1999). However, with most gas-liquid-reactors the volumetric mass transfer coefficient and its dependence on the system parameters have still to be determined experimentally. This is especially the case with new reactor designs since there is no or little data available in literature.

A selection of the most important parameters influencing the mass transfer in gas-liquid reactors is given in Table 2-1.

Physical and chemical properties	Operating parameters	Reactor design
<ul style="list-style-type: none"> • kinetics of the chemical reaction • viscosities of the two phases • densities of the two phases • surface tension • diffusion coefficients • coalescence behaviour • ... 	<ul style="list-style-type: none"> • mechanical energy input • liquid flow rate • gas flow rate • system pressure • ... 	<ul style="list-style-type: none"> • construction of the disperser • geometric dimensions • ...

Table 2-1: Parameters influencing the mass transfer characteristics of gas-liquid reactors

The influence of the listed parameters on the mass transfer characteristics can be quantified by many different modelling approaches, ranging from simple case-dependent ad hoc models to complete modelling of the flow pattern (computational fluid dynamics). In the literature empirical correlations prevail by far. Some exemplary collections of empirical models, valid for different reactor types, can for instance be found in van Landeghem (1980) or Lee and Tsui (1999).

Many model approaches are based on Kolmogoroff's theory of isotropic turbulence. A detailed description of this theory can for example be found in Kawase and Moo-Young (1990).

This theory leads to the conclusion that (at sufficiently high Reynolds numbers) the hydrodynamics in gas-liquid reactors can be accounted for by a single parameter, the average energy dissipation rate per unit mass or volume of fluid. The estimation of the energy dissipation rate is a prerequisite for the application of Kolmogoroff's theory. With jet driven reactors it can be readily evaluated from Eq. 2-20 and Eq. 2-21.

The theory implies that the diameter of the largest bubble stable against breakup is given by the following formula (Hinze, 1955):

$$d_{B,max} \propto \left(\frac{\sigma}{\rho_L} \right)^{0.6} \cdot e_S^{-0.4} \quad (2-24)$$

On the basis of the above equation Kawase and Moo-Young (1990) were able to derive an expression describing the influence of e_S on $k_L a$:

$$k_L a \propto e_S^\kappa \quad ; \quad \kappa \approx 1 \quad (2-25)$$

The theory of isotropic turbulence provides a useful guide for the understanding of the complex processes involved with gas-liquid reactors and for the comparison of the performance of different reactor types. However, it is (at present) not able to provide a complete description of the phenomena in these reactors. Therefore, the exact influence of the specific power input on the mass transfer can only be determined by regression analysis of the experimental data. Generally, it is also necessary to introduce additional influencing parameters next to e_S in order to obtain a useful model.

An extract of correlations describing the mass transfer characteristics of different ejector gas-liquid reactors is listed in Table 2-2.

Reference	Correlation	System
Dutta and Raghavan (1987)	$k_L a \propto (e_S)^\kappa \quad ; \quad 0.7 < \kappa < 0.8$	loop reactor with different ejectors; coalescence hindered
van Dierendonck et al. (1988)	$k_L a = 0.3 \cdot (e_S)^{0.9}$	downflow ejector + reaction vessel; coalescence hindered
Kastanek et al. (1993)	$k_L a = 0.04 \cdot (e_S)^{0.54}$	upflow ejector + reaction vessel; air/water
Cramers and Beenackers (2001)	$k_L a \propto (e_S)^{0.65} \epsilon_G \left(\frac{1 + 0.2\epsilon_G}{1 + \epsilon_G} \right)^{1.2}$	downflow ejector; air/water

Table 2-2: Mass transfer correlations of ejector loop reactors

3 Measuring techniques

3.1 Measurement of $k_L a$

3.1.1 Introduction

Generally all the existing measuring techniques for the volumetric mass transfer coefficient $k_L a$ can be divided either by their mode of operation into steady-state and dynamic (non-steady-state) techniques or by the chemical composition of the system into physical and chemical techniques.

To attain steady-state operation the absorbed gas component has to be constantly removed from the liquid phase. When doing this it is important to ensure that the gas removal is fast enough in order to maintain a significant concentration difference of the absorbing agent between the gas and the liquid phase. The removal of the absorbed gas component can be achieved by physical desorption or with the help of a chemical reaction.

The main advantages of the steady-state techniques are a higher accuracy and an easier interpretation of the measurements compared to the dynamic techniques. However, dynamic techniques generally demand less experimental equipment.

Physical techniques have the advantage that the properties of the liquid phase can be freely varied and are not subject to any limitations. This is generally not the case with chemical techniques where the properties of the liquid phase are set. Table 3-1 shows how the discussed techniques fit into the above described main categories.

	Steady-state	Dynamic
Physical	Steady-state physical absorption	Dynamic absorption technique Pressure gauge technique
Chemical	Hydrazine feeding technique Catalyzed sulfite oxidation Uncatalyzed sulfite oxidation	

Table 3-1: Measuring techniques for $k_L a$

In Section 3.1.2 the existing techniques for the measurement of $k_L a$ will be reviewed and discussed. In Section 3.1.3 it is explained how the most suited technique for measurements at ambient pressure was selected. A detailed description of the modifications that were needed in order to apply the selected technique successfully to the ABLR is given in Section 3.1.4. In Section 3.1.5 the selection and modification of the technique for the $k_L a$ measurements at elevated pressures is discussed.

3.1.2 Review of existing techniques for the measurement of $k_L a$

3.1.2.1 Dynamic physical absorption

The dissolved concentration of the gas component in the liquid phase is measured as a function of time after a step change (see e.g. Akita and Yoshida, 1973; García-Ochoa and Gomez, 1998).

Normally the systems air/water or oxygen/water are used since the dissolved oxygen concentration can be easily measured with polarographic oxygen probes. First the liquid is stripped of all oxygen by using nitrogen. Then the initially oxygen-free liquid is re-aerated in a batch experiment until oxygen saturation is achieved.

The absorption process is described using the following differential equation:

$$\frac{dc}{dt} = k_L a \cdot (\bar{c}_i - c_0(t)) \quad (3-1)$$

The equation is only valid if these assumptions are met:

- The liquid phase is well mixed (Lara Marquez, 1994a)

- Constant mean concentration of the absorbing component in the gas phase
- (Negligible gas sided mass transfer resistance)

This technique is by far the most used because it has several advantages:

- The expenses for technical equipment and installation into existing experimental setups are very low.
- The expenditure regarding the measuring time, the data analysis and the chemicals needed is relatively small.
- It is sufficient to monitor the relative changes of the dissolved oxygen concentrations, i.e. the absolute values do not have to be known. This is very convenient when there is no solubility data available for the used oxygen-liquid system.

But there also exist some major limitations resp. disadvantages:

- With dynamic concentration changes all polarographic oxygen probes show a certain lag time. Even the fastest have a response time constant τ_{probe} of approximately 2-3 seconds. As long as the condition $\tau_{\text{probe}} \ll 1/k_L a$ is valid the response characteristics of the oxygen probe do not affect the measurements and can be neglected. However, if the time constant of the mass transfer $1/k_L a$ has the same magnitude as τ_{probe} the measurements do not correspond to the actual dissolved oxygen concentration. This results in the calculation of too low $k_L a$ values (e.g. Merchuk et al., 1990).

If the exact value of τ_{probe} is known $k_L a$ can still be measured correctly. This is possible since the response of the oxygen probe after a concentration step change can be described with a first-order approximation (e.g. Merchuk et al., 1990). By applying a deconvolution algorithm on the measured data the actual dissolved oxygen concentration can be extracted from the measured one. The corresponding procedure can for example be found in Osorio and Onken (1988).

However, with fast absorption processes ($\tau_{\text{probe}} \geq 1/k_L a$) even this procedure gives incorrect results because now the measurements represent mainly the response characteristics of the oxygen probe. Thus the dynamic absorption technique is limited to the measurement of $k_L a$ values below $0.2\text{-}0.4 \text{ s}^{-1}$, even if fast response oxygen probes are used.

- Assumptions have to be made regarding the mean oxygen concentration in the gas phase in order to define \bar{c}_i . This may lead to considerable errors since the gas oxygen concentration is not constant during the measurement. Especially in the beginning the decrease of the oxygen concentration is more distinct due to the higher absorption rate and backmixing of the desorbing nitrogen (Menzel et al., 1998). Also the gas phase dilution by desorbing nitrogen is higher in the beginning. Depending on the model used for the calculation of \bar{c}_i different $k_L a$ values are measured. This effect gains importance particularly with high $k_L a$ values (Sick, 1985).

Osorio and Onken (1988) point out that the dynamic absorption technique is subject to higher systematical errors than steady-state techniques. They argue that the driving concentration difference is generally estimated to large which results in the calculation of too low $k_L a$ values.

To avoid problems regarding the gas phase mixing Linek et al. (1992) introduced pure oxygen as a step input to the completely degassed liquid batch. However, the gas holdup was being formed during the experiment, i.e. it was not in steady state. Therefore this method can only be applied correctly, if the gas holdup formation is much faster than the mass transfer rate.

- According to Weiland et al. (1986) the dynamic absorption technique becomes less reliable with increasing reactor volumes. He suggests that the mass transfer of industrial scale reactors should better be measured with chemical techniques.

3.1.2.2 Steady-state physical absorption

The gas and the measuring devices used for this technique are the same as with the dynamic physical absorption. Now a constant liquid stream with a low oxygen concentration is fed into the reactor. The same amount of liquid is continuously removed and fed into a desorber where the oxygen is stripped using nitrogen. The obtained liquid can again be used as feed for the first reactor.

From the oxygen mass balance $k_L a$ can be calculated (e.g. Gaddis, 1994). It is assumed that the liquid phase is well mixed.

$$k_L a = \frac{V_L^*}{V_L} \cdot \frac{c_{in} - c_{out}}{\bar{c}_i - c_{out}} \quad (3-2)$$

V_R : reactor volume, V_L^* : liquid feeding rate, c_{in} and c_{out} : oxygen concentrations in reactor inlet and outlet stream, $\bar{c}_i - c_{out}$ driving concentration difference.

Advantages:

- The measurements are not influenced by the response dynamics of the oxygen probe. According to Gaddis (1999) very high $k_L a$ values ($>2 \text{ s}^{-1}$) can be measured accurately with this technique.
- As with the dynamic physical absorption technique the absolute oxygen solubilities do not have to be known.

Disadvantages:

- The experimental setup is very costly since a desorber unit of at least the same mass transfer performance as the reactor is needed. Therefore this technique is seldom used with reactors of industrial scale.

In order to minimize the experimental error the two concentration differences $c_{in} - c_{out}$ and $\bar{c}_i - c_{out}$ should be of the same size and as large as possible (Sick, 1985). $c_{in} \approx 0$ and $c_{out} \approx 0.5\bar{c}_i$ would be ideal. However, this can only be achieved if the desorbing unit is dimensioned larger than the absorber to be examined. The costs would further increase.

3.1.2.3 Pressure gauge method

This technique was presented for the first time by Zlokarnik (1978). In fact this method corresponds to the dynamic method with the difference that a pressure step is used instead of a gas change.

The procedure is as follows (see Fig. 3-1): First the liquid phase is saturated with the pure gas at the starting pressure. Then the liquid mixing is stopped and the pressure is quickly increased (valve [1] open, valve [2] closed). Then valve [1] is closed and valve [2] is opened. When the reactor is started, parts of the gas are absorbed by the liquid phase according to the higher system pressure. To keep the pressure constant, gas losses are compensated from the gas cylinder using a regulating valve [3]. The pressure drop in the gas cylinder with time is a direct measure of the absorption rate and $k_L a$ can be calculated with Eq. 3-1.

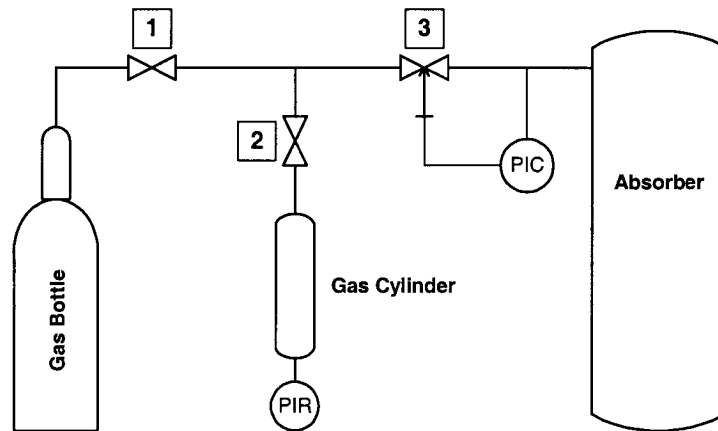


Fig. 3-1: Schematical representation of the pressure method according to Zlokarnik (1978)

Compared to the dynamic physical absorption technique the pressure gauge has the following advantages:

- $k_L a$ can also be measured at elevated pressures.
- Method is not limited to oxygen. Any pure gas can be used.
- The lag time of pressure transmitters can be neglected, i.e. higher mass transfer rates can be measured.
- Since pure gases are used, no assumptions regarding the gas phase mixing or the mean gas concentration have to be made.

Drawbacks of the technique are:

- The higher equipment costs since the entire setup has to be pressure proof.
- The gas holdup needs to be formed during the experiment, i.e. it is not in steady state at the beginning (e.g. Linek et al., 1992).

There also exists a modification of the pressure gauge method where the absorption rate of oxygen is monitored with an oxygen probe in the liquid phase (e.g. Linek et al., 1990). The benefit of this method is however questionable since concerning the probe lag time the same problems occur as discussed with the dynamic physical absorption technique. Linek et al. (1996) recommend that this technique should only be used with positive pressure changes. Negative pressure

steps would result in the formation of many small bubbles due to the oversaturation of the oxygen. This would result in an increase of $k_L a$.

3.1.2.4 Hydrazine feeding technique

With this technique hydrazine is fed at a defined rate into the absorber where it reacts with dissolved oxygen according to the following reaction equation:



At room temperature the reaction only takes place in the presence of a catalyst. It is assumed (Weiland, 1981) that only the molecular hydrazine takes part in the reaction. The oxidation is only quantitative in alkaline solutions. In acid media also ammonia, which is not further oxidized, is formed. A very comprehensive description of the reaction kinetics can be found in Sick (1985).

The hydrazine feeding rate depends on the intensity of the aeration. It is adjusted so that the steady-state oxygen concentration is > 0 (absorption with slow chemical reaction). The dissolved oxygen concentration is measured by a polarographic oxygen probe.

Under steady-state conditions the absorption rate equals the rate of the chemical reaction which also equals the hydrazine feeding rate. The system, although called a chemical technique, is equivalent to that of the steady-state physical absorption technique, i.e. $E=1$. The very low concentrated hydrazine only serves as an oxygen sink without chemically enhancing the absorption rate (Weiland et al., 1986) and $k_L a$ can be calculated from the steady-state oxygen mass balance:

$$\Phi_{\text{O}_2} = V_{\text{feed}}^* \cdot c_{\text{N}_2\text{H}_4, \text{feed}} = k_L a \cdot V_L \cdot (\bar{c}_{\text{O}_2, i} - c_{\text{O}_2, 0}) \quad (3-4)$$

Eq. 3-4 is only valid if the following conditions are fulfilled:

- The liquid phase is regarded as well mixed. Otherwise the interpretation of the measured oxygen concentration would be difficult¹.

- The steady-state concentration of the dissolved oxygen is > 0 , i.e. the absorption rate is not chemically enhanced.
- The hydrazine reacts completely with the oxygen and no accumulation takes place, i.e. $c_{\text{N}_2\text{H}_4} \approx 0$. Warnecke and Hussmann (1989) proved experimentally that this condition fulfilled.
- The hydrazine reacts only according to Eq. 3-3.
- (The gas sided mass transfer resistance can be neglected)
- The increase of the liquid volume V_L by the hydrazine feed can be neglected.

Advantages:

- The concentrations of all added chemicals are quite low and the liquid properties are not altered by the reaction products. Therefore the liquid phase still possesses approximately the properties of water. Since the hydrazine oxidation is not influenced by the addition of any salts (Lara Marques et al., 1994a), the mass transfer in as well coalescing as coalescence hindered liquids can be measured. This does not apply for any other chemical technique.
- The same reaction solution can be used several times because its chemical and physical properties do not change with time.
- It's a steady-state measurement, i.e. the oxygen probe response characteristics can be neglected.
- In comparison with most other techniques less assumptions regarding the model have to be made, i.e. the systematic error is smaller.
- Knowledge concerning the reaction kinetics is not needed since the absorption rate is not enhanced by the chemical reaction.
- There exists no limitation regarding the highest measurable $k_L a$ value.

Disadvantages:

- The absolute oxygen solubility in the liquid phase has to be known. This data may not be available for some solutions.
- Hydrazine is highly toxic.

1. Lara Marquez et al. (1994a) have developed a hydrazine feeding technique for liquids which are not well mixed. However, their method can only be applied under certain circumstances and the same problems arise as with the sulfite oxidation technique. Therefore, this technique won't be discussed any further.

- Reports on the correctness of this technique are ambiguous, see e.g. Gaddis (1999), Linek et al. (1996), Warnecke and Hussmann (1989), Judat (1982).

3.1.2.5 Oxidation of sulfite solutions by air or oxygen

Next to the dynamic physical absorption this is the most used technique for systematic $k_L a$ measurements in gas-liquid reactors. Usually in the presence of a cobalt or copper catalyst sulfite is oxidized by oxygen to sulfate. Without any catalyst the reaction is very slow.



At ambient conditions the reaction is second order with respect to the oxygen, zero order with respect to the sulfite and first order with respect to the cobalt catalyst. An in depth description of the reaction kinetics can be found e.g. in the review article of Linek and Vacek (1981).

The absorption rate can be measured by two different methods. Either by monitoring of the decrease of the sulfite concentration with time using a iodometric titration method or by the oxygen mass balance of the gas phase. The second method is much faster but also less accurate (Steiff and Weinspach, 1982).

There exist several variations of the technique (see also Linek and Vacek, 1981):

- Absorption with instantaneous reaction. In this case the specific surface area a is measured, e.g. Sedelies et al. (1987).
- Absorption where the reaction is slow in the mass transfer film but sufficiently fast in the liquid bulk that the dissolved oxygen concentration can be neglected. Here $k_L a$ is measured.
- Sometimes also the uncatalyzed sulfite oxidation is used (e.g. Wilkinson, 1991).
- (E.g. Imai et al. (1987) or Morão et al. (1999) used a sulfite feeding technique which is practically identical to the hydrazine feeding technique but no improvement. Very disadvantageous is the influence of the liquid properties by the reaction products with time.)

Advantages:

- The technique is independent of the liquid mixing characteristics since the oxygen concentration is zero in the bulk.
- The method is much used and quite propagated.

Disadvantages:

- The physical properties are heavily influenced by the high salt concentrations. Therefore, the method can only be applied to coalescence hindered solutions.
- Since the absorption is chemically enhanced an enhancement factor has to be defined. For its calculation the liquid sided mass transfer coefficient k_L , the diffusion coefficient D of the gas component and especially the chemical reaction rate k_R have to be known. Usually these can only be estimated. Therefore the error potential is very high.
- The maximally measurable $k_L a$ value is limited.
- The reaction kinetics are strongly influenced by impurities (Reith, 1968) and have to be newly measured for every batch. This can be very time consuming.
- The reaction enthalpy is rather high and it may be difficult to keep the reaction temperature constant.

3.1.2.6 Other chemical techniques

There exist several more chemical techniques but either their applicability or their reliability is often very limited. For the sake of completeness some examples will be shortly mentioned.

The reaction of amines or other alkaline solutions with carbon dioxide has been used for $k_L a$ measurements by e.g. Alvarez et al. (1980) or Oyevaar et al. (1990). The advantage of these reactions is that they are not catalytic and literature data of the reaction rates may therefore be used with some confidence. However, as well the gas as the liquid properties are prescribed by the method and the coalescence of the system is strongly hindered. Also the high solubility of CO_2 may cause significant problems (see e.g. Hofer and Mersmann, 1980).

Further techniques are e.g. the hydrogen peroxide feeding technique (Nienow, 1996), the reaction of isobutene with diluted sulfuric acid (Deckwer, 1977) or the oxydation of glucose catalyzed by glucoseoxidase (Lohse et al., 1980). A more detailed overview of these and many more model systems can be found for example in Sick (1985).

3.1.3 Selection of the $k_L a$ measuring technique for experiments at ambient pressure

The different measuring techniques were compared to the expected high mass transfer rates of the ABLR and the preferred experimental conditions. The summary of the evaluation is shown in Table 3-2. The hydrazine feeding technique was chosen because it corresponded to the desired qualities best. Especially decisive in the choice was that the maximally measurable $k_L a$ is not limited, the liquid properties are not influenced and the experimental error potential is minimized.

Measuring techniques →	Dynamic physical	St.-state physical	Sulfite	Hydrazine feeding	Pressure gauge	Experim. conditions
Maximally measurable $k_L a$ limited?	yes	no	depends	no	no	$k_L a > 0.1 s^{-1}$
Are the liquid properties influenced?	no	no	very much	approx. no	no	different media
Experimental error potential	increases with $k_L a$	small (st.-state)	medium-high	small (st.-state)	medium	as small as possible
Are any reaction kinetics needed?	no	no	yes	no	no	preferably no
Absolute gas solubility needed?	no	no	yes	yes	no	preferably no
Suited for ambient pressure?	yes	yes	yes	yes	no	1 bar
Is the method much propagated?	yes	no	yes	not yet	no	desirable
Experimental sacrifice of time	small	small-medium	large-very large	medium	small	as small as possible
Costs	low	very high	medium	medium	high	as high as necessary
Media toxicity	no	no	low	high	no	preferably no

Table 3-2: Comparison of the different $k_L a$ measuring techniques

As noted in Table 3-2 the hydrazine feeding technique is not very propagated yet. The reasons may be that it's rather new (compared to the other techniques) or that it was so far mainly applied by German researchers. Furthermore, there exists no agreement in literature regarding the accuracy of this technique.

As well Warnecke and Hussmann (1989) as Lara Marquez et al. (1994b) found no differences between measurements with the hydrazine and the dynamic physical absorption technique. By way of contrast Gaddis (1999) reported that the bubbles are a little smaller than with a pure physical technique. Also a decrease of the bubble size with time was observed.

Linek et al. (1996) reported that the hydrazine technique gives higher $k_L a$ values than the dynamic physical technique. They make oversaturation effects of the nitrogen and the spontaneous formation of very small gas bubbles responsible for this. However, this is very unlikely. Even if these small nitrogen bubbles are formed they wouldn't increase the specific surface area for the oxygen absorption since they contain only nitrogen. On the contrary, these nitrogen bubbles would rather withdraw oxygen from the solution and therefore decrease the dissolved oxygen concentration which would result in the calculation of a too low $k_L a$ value. Osorio and Onken (1988) observed the same difference between the two techniques. Unlike Linek et al. (1996) they think that the deviations are based on shortcomings of the model used with the dynamic technique. They substantiate their theory with the fact that the difference increases with increasing viscosity of the liquid phase.

Very surprising is the fact that these authors find no differences between the two methods for $k_L a > 0.05-0.1 \text{ s}^{-1}$. One would expect the exact contrary because the dynamic method is subject to considerable errors for $k_L a > 0.1 \text{ s}^{-1}$ (see Section 3.1.2).

According to Judat (1982) differences between the two methods may also occur if the applied catalyst concentration is too high.

On the basis of these inconsistent findings it was not possible to pass a final judgment on the accuracy of the method. Therefore, some preliminary experiments were carried out with the ABLR in order to check the applicability of the hydrazine feeding technique.

3.1.4 Testing of the hydrazine feeding technique

3.1.4.1 Catalyst system

Of great importance for the application of this technique is the selection of a suited catalyst system.

Zlokarnik (1978) applied this technique for the first time. As catalyst he used a heterogeneous CuSO_4 complex at a concentration of 0.01 mol/l. With NaOH he adjusted the pH to 11-12. Judat (1982) modified this technique slightly by using a CuSO_4 concentration of 1×10^{-3} mol/l.

Extensive studies on the CuSO_4 catalyst system were carried out by Weiland et al. (1981). They found that the reaction is actually catalyzed homogeneously by small amounts of dissolved Cu^{2+} -ions and that heterogeneous mechanisms can be neglected.

Apparently many problems occur with the CuSO_4 catalyst system. Weiland et al. (1981) observed that fresh suspensions lack the full catalytic activity which causes that not all of the hydrazine reacts according to Eq. 3-3. Also the authors observe that measured $k_L a$ values are not independent of the adjusted dissolved oxygen concentration, which stands in conflict to Eq. 3-4. This could be explained by the findings of Sick (1985). Equilibrium of the different copper compounds sets in very slowly. Therefore several hours of waiting time are needed after a change of the hydrazine feeding rate. Furthermore Weiland et al. (1986) found that with time parts of the copper precipitate from the solution which affects the catalytic activity and leads to incorrect measurements. Additionally the authors criticize the clinging of particles to the measuring probes as well the high turbidity which prevents the observation of bubbles and the flow pattern.

To avoid these problems Sick (1985) and Weiland et al. (1986) tried to find a better suited homogeneous catalyst. They carried out extensive experiments using different Co^{2+} - and Cu^{2+} -complexes. The best results were obtained with copper phthalocyanine with four sulphonic groups (CuTeSP) at a concentration of $0.1-5 \times 10^{-4}$ mol/l and a pH of 12-12.4. (To avoid the need of a pH control all CO_2 was removed from the air by leading it through a NaOH gas scrubber.) Later this catalyst was used by Osorio and Onken (1988) and Warnecke and Hussmann (1989), too. A disadvantage of the CuTeSP catalyst is its rather long activation time of 12-24 hours. Also, at $\text{pH} > 12$ the solution shows first signs of coalescence hindrance.

Lara Marquez et al. (1994b) also tried to use the CuTeSP system but they didn't observe any catalyst activity. As catalyst they proposed a 5×10^{-4} M CuCl_2 solution at a pH of 10.5. Instead of NaOH they use a 0.1 M $\text{NH}_4\text{OH}/\text{NH}_4\text{Cl}$ buffer which prevents the precipitation of any copper and keeps the pH constant. This system was applied successfully to three different gas-liquid-reactors. (It should be noted that Sick and Weiland et al. also considered this system but decided against it due to a possible ammonia desorption caused by its high vapour pressure. With time this would lead to a considerable pH drop.)

The test experiments were carried out in the ABLR¹ with the catalyst system as described by Lara Marquez et al. (1994b). It was chosen because it is homogeneous, does not need any activation and has the lowest pH of all the systems.

Solutions of as well pure water as tap water were tested. Both solutions proved to age very quickly during the measurements, at which the ageing of the tap water solution proved to be much faster. After 10-20 minutes the solutions which were clear at the beginning became turbid. Also a decrease of the bubble sizes with time was observed. These changes of the liquid properties resulted in a constant increase of $k_L a$ the longer the same solution was used.

It was presumed that the liquid property changes (especially the turbidity) were the caused by the precipitation of some copper complexes. According to Weiland et al. (1981) precipitation of copper may occur in the presence of ammonia below pH 10.5 which is equal to the applied system pH. To be on the safe side the pH was raised to 11 and the tests were repeated.

With the tap water solution the properties still changed with time. But with the ion-free water solution no ageing occurred. Therefore, for all later experiments the following system was used: Ion-free water, 5×10^{-4} M CuCl_2 , 0.1 M $\text{NH}_4\text{OH}/\text{NH}_4\text{Cl}$ buffer and pH 11. An excerpt from the described tests is given in Fig. 3-2.

The use of tap water is not to be recommended. The presumption seems likely that authors who observed changes of the liquid properties with time also used unfit catalyst systems (e.g. Gaddis, 1999).

1. Operating conditions: $V_L = 30\text{l}$, $\Delta p_N = 2.5$ bar, $d_N = 6.2$ mm, $l_M = 22\text{cm}$, 180° swirl device

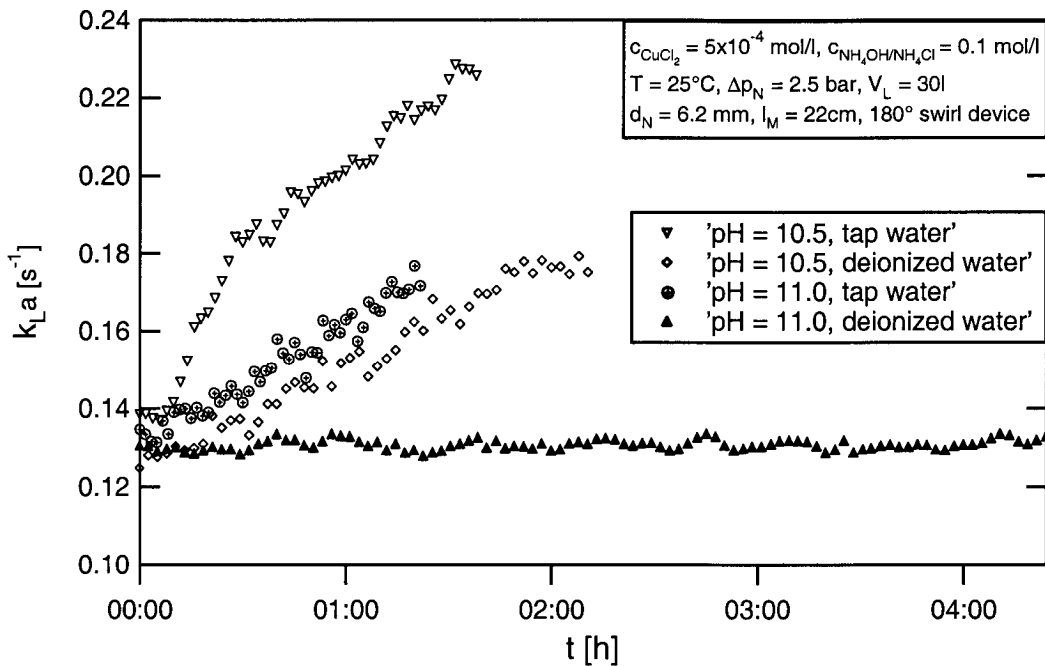


Fig. 3-2: $k_{L,a}$ in different catalyst systems versus time

The tests also proved that no CO_2 scrubber was needed and that the ammonia desorption could be neglected. Even after two days of operation no significant pH drop or changes of the liquid properties were observed.

At low mass transfer rates, i.e. if $(c_{\text{O}_2, \text{in}} - c_{\text{O}_2, \text{out}}) / (\bar{c}_{\text{O}_2, \text{i}} - c_{\text{O}_2, 0}) \ll 1$ is valid, the state of the gas phase mixing can be ignored (Gaddis, 1999). Here all mixing models give approximately the same results. However, the ABLR features relatively high mass transfer rates and the gas mixing characteristics have to be taken into consideration. For this purpose the residence time distribution of the gas phase was measured (see Appendix 3). It was found that the gas phase can be regarded as well mixed, i.e. the mean oxygen concentration of the gas phase inside the reactor equals the gas outlet concentration.

3.1.4.2 Confirmation of the applicability of the hydrazine feeding method

Residence time distribution measurements proved that the liquid phase can be described as well mixed (see Appendix 3).

The absorption rate is not chemically enhanced and not influenced by the reaction kinetics. This can be tested by the variation of the hydrazine feeding rate at constant mass transfer conditions. The measured $k_L a$ value has to be independent of the hydrazine feeding rate (as long $c_{O_2, \text{bulk}} > 0$). In other words, the plot of the oxygen concentration difference versus the hydrazine feeding rate has to result in a straight line. For different mass transfer rates this is proven in Fig. 3-3.

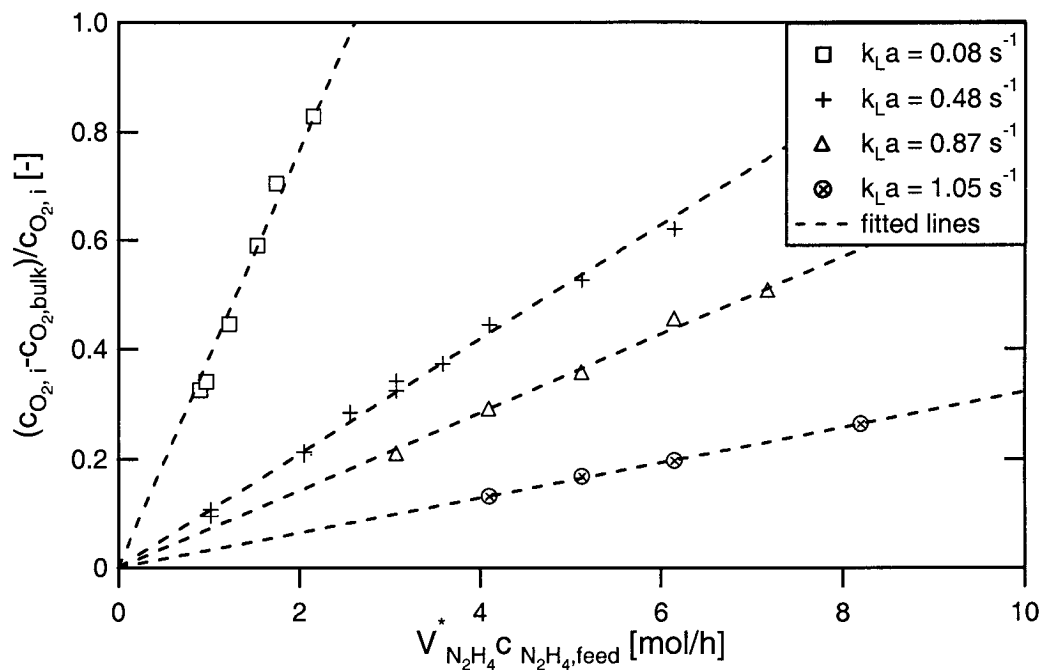


Fig. 3-3: Linear relation between the hydrazine feeding rate and the oxygen concentration difference

The hydrazine reacts only according to Eq. 3-3. The validity of its left side can easily be checked by comparing the oxygen consumption, calculated from the gas mass balance, with the hydrazine feeding rate. These have to be equal. The results of more than 100 measurements are summarized in Fig. 3-4. As can be seen the reaction rates of both components are approximately identical.

The right side of the equation must also be valid. If other products next to water and nitrogen would be formed the solution would change its properties with time. However, this is not the case (see Fig. 3-2).

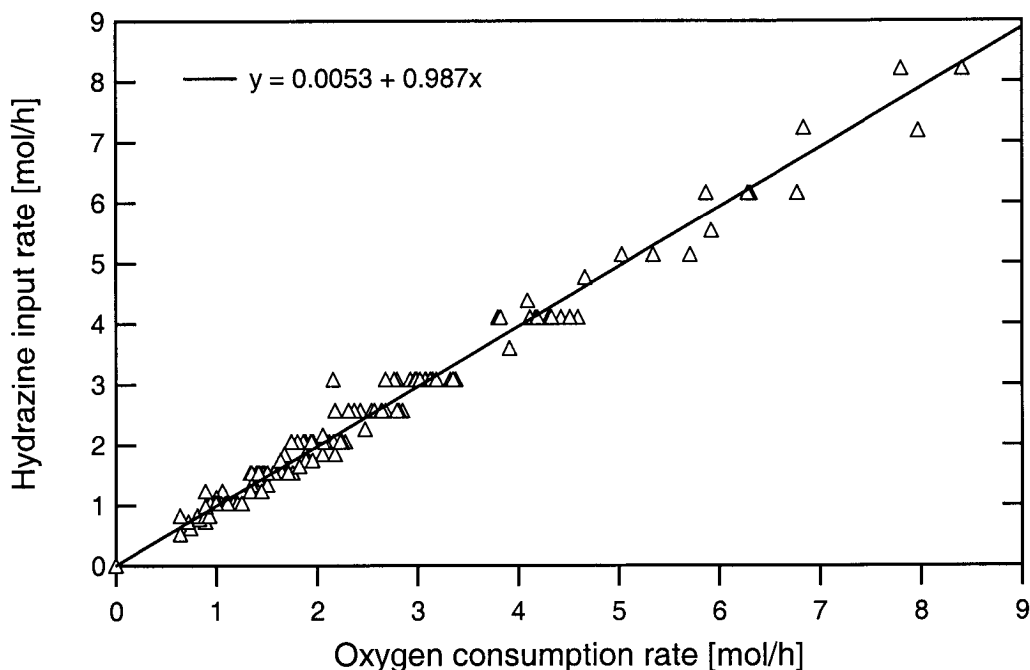


Fig. 3-4: Comparison of the oxygen consumption and the hydrazine feeding rate

3.1.4.3 Experimental error

The volumetric mass transfer coefficient could not be measured directly but was calculated from various quantities (see Eq. 3-4). Especially the measurement of the oxygen concentration in the liquid phase and in the gas outlet was subject to some errors. The resulting maximal error for the $k_L a$ measurements in water was found to be approx. 7%. The one for coalescence hindered solutions was higher and around 20%. This increase of the experimental error was the result of the much higher oxygen consumption which caused a strong decrease of the driving oxygen concentration difference compared to pure water. Errors regarding the oxygen concentration measurements were therefore of much greater weight.

3.1.5 Selection and testing of the $k_L a$ measuring technique for experiments at elevated pressures

3.1.5.1 Selection

Table 3-2 was expanded by two more criteria (see Table 3-3). The only measuring technique that fulfilled the planned experimental conditions was the pressure gauge method. Again, the technique was tested first before it was applied.

Measuring techniques →	Dynamic physical	St.-state physical	Sulfite	Hydrazine feeding	Pressure gauge	Experim. conditions
Different gases possible?	no	no	no	no	yes	different gases
Suited for elevated pressures?	no	yes	limited	no	yes	1-10 bar

Table 3-3: Extension of Table 3-2 for measurements at elevated pressures

3.1.5.2 Testing

The testing of this method showed that it could not be applied successfully in the way it was described in Section 3.1.2. While in theory the technique has no shortcomings the practical implementation proved difficult. Since the mass transfer rate in the ABLR is very high, equilibrium after a pressure step was reached very fast (10-20 sec.). No pressure control device was found that had the required sensitivity and fast reaction times. As a consequence mainly the dynamic characteristics of the control valve instead of the actual absorption rate were measured.

Therefore some changes were made to the original setup. The pressure control and the gas cylinder were removed. A schematic illustration of the new setup is shown in Fig. 3-5: After a rapid pressure step valve 1 is closed. Then the reactor is started and the pressure drop of the system (caused by absorption) is monitored. Since the extent of the pressure decrease due to absorption is rather small a differential pressure transmitter is used for better accuracy.

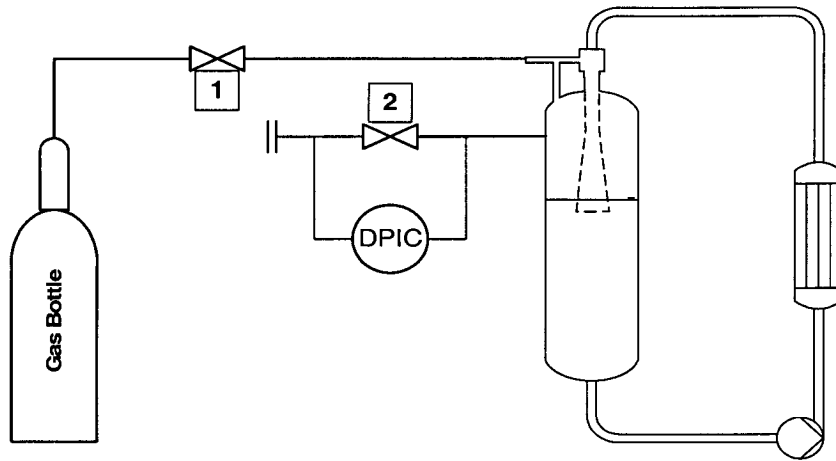


Fig. 3-5: Modified pressure gauge method

Eq. 3-1 can still be used for the calculation of $k_L a$ but now the gas concentration resp. the gas pressure is also a function of time. The mass balance for the gas phase can be formulated as follows:

$$-\frac{dN_G(t)}{dt} = V_L \cdot k_L a \cdot (c_i(t) - c_0(t)) \quad (3-6)$$

After closing the gas supply (valve 1) the total amount of the gas component in the reactor is constant:

$$N_{\text{tot}} = N_G(t=0) + N_L(t=0) = N_G(t) + N_L(t) = \text{const.} \quad (3-7)$$

With $N_L(t) = V_L \cdot c_L(t)$, the ideal gas law $N_G(t) = \frac{p(t) \cdot V_G}{R \cdot T}$

and Henry's law: $p(t) = H \cdot c_i(t)$

Eq. 3-6 becomes:

$$\frac{dp(t)}{dt} = k_L a \cdot \left(\underbrace{\frac{RTn_{\text{tot}}}{V_G}}_{b_0} - \underbrace{\left(\frac{RTV_L}{HV_G} + 1 \right)}_{b_1} \cdot p(t) \right) = k_L a \cdot (b_0 - b_1 \cdot p(t)) \quad (3-8)$$

In contrast to Zlokarnik's technique the measurements are now dependent on several system parameters. Especially the absolute value of the gas solubility has to be known now.

The tests also proved that the technique could not be applied to the ABLR, if coalescence hindered liquids were used. The problem is that the gas holdup is being formed during the beginning of the experiment, i.e. it is not in steady-state. Unlike with tap water the attainment of steady-state hydrodynamics with electrolyte solutions takes several seconds. Since the mass transfer is rather high in the ABLR the necessary start-up period is comparable with the duration of the dynamic experiment.

This is illustrated in Fig. 3-6 where as well the dynamic pressure difference across the nozzle Δp_N as the system pressure p_R are plotted versus time. Δp_N can be regarded as a measure of the gas holdup in the liquid recirculation pipe because it decreases with increasing gas holdup at a constant pump speed. It is evident that steady-state hydrodynamics are attained not before approximately 10 seconds have passed. However, nearly the entire absorption process has taken place during that time period. The measured volumetric mass transfer coefficients represent rather the behaviour of pure water than that of an electrolyte solution and, therefore, they are far too small (see also Linek et al., 1992).

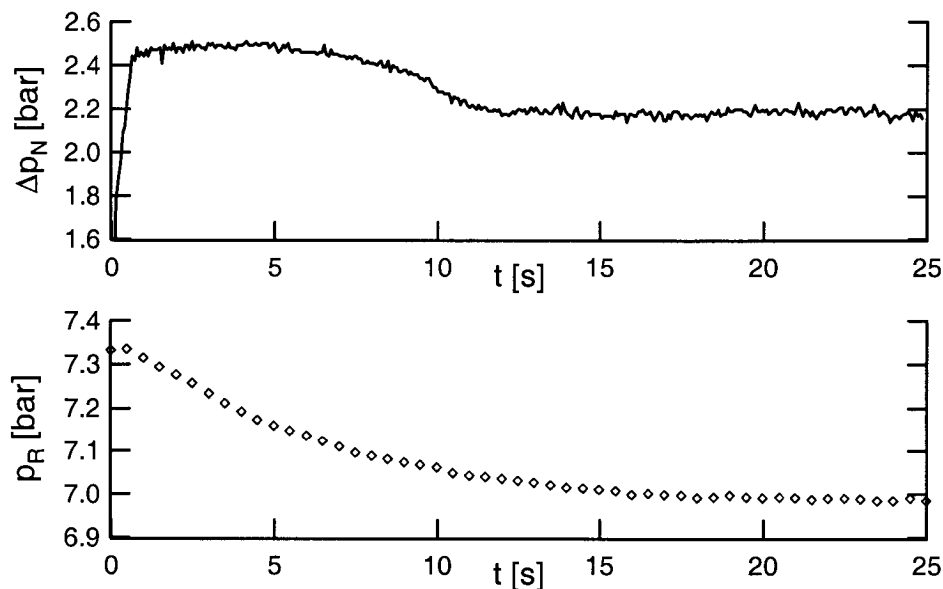


Fig. 3-6: Modified pressure gauge method with coalescence hindered solutions

3.2 Bubble size measurement

In the ABLR extreme conditions for bubble size measurements exist: High flow velocities, primary bubble sizes in the range of 30-1000 μm and high gas holdups. The combination of the high gas holdups and the small bubble sizes results also in a very poor range of vision. For the selection of a proper measuring technique all these limitations resp. requirements had to be taken into account.

3.2.1 Review of existing techniques

There exist many different techniques for the measurement of bubble size distributions:

Photographic methods are the most widely used techniques. E.g. Heim et al. (1997) or Bouaifi and Roustan (1998) used a common photo camera resp. a video camera which was positioned outside a reactor with transparent walls. A more advanced photographic technique was used by Chen and Fan (1992). They took pictures of the gas-liquid-dispersion by using a lasersheet for illumination (Particle Image Velocimetry, PIV). The advantage of taking pictures from the outside of a reactor is the absence of any flow disturbances induced by the measuring device. However, all these techniques can only be applied at low gas holdups where the range of vision permits optical access to the interior of the reactor.

Another approach is to use an endoscope together with a camera or a similar device which allows in-line photography (e.g. Ives, 1995). This way the measurements are not limited by the range of vision. However, the dispersion may be influenced by the endoscope.

The big disadvantage that all photographic techniques have in common is the very time consuming analysis of the taken images.

Contact probes rely on the conductive, dielectric or optical properties of the liquid media and can be used to measure bubble penetration or chord lengths (e.g. Buchholz et al., 1981; Kuncova and Zahradnik, 1995; Bentifraouine et al., 1999). To calculate bubble size distributions from the measured chord lengths both local flow velocities and statistical models are required (see Clark and Turton, 1988).

The smallest measurable bubble diameter is limited by the dimensions of the probe tip. The typical needle diameter of a conductive probe is about 0.1 mm. Additionally the wetting processes of the needle are not infinitely fast. This can especially become a problem with high flow velocities (Otake et al., 1981). A threshold has to be defined for the distinction between gas and liquid phase. If this is wrongly set, large errors can occur. Recently Fordham et al. (1999) were able to reduce the wetting problems by treating the probe surface, which prevented the formation of any persistent water films.

However, the fully automated and fast generation of bubble size distributions has to be regarded as very advantageous.

Barigou and Greaves (1992) and Genenger et. al (1992) measured the local bubble size distributions in a stirred tank reactor resp. in a loop reactor using an automated capillary suction probe. A small, constant stream is removed from the gas-liquid dispersion and enters a capillary of known diameter. The lengths of the bubble slugs formed in the capillary are measured using photoelectric detectors allowing the calculation of the bubble volumes.

A less sophisticated technique was used by Tung et al. (1998). They used photographs to analyze the number and size of the bubbles in the capillary.

Again, very advantageous is that an automatic generation of the bubble size distributions is possible. However, large errors can occur at high gas holdups because of bubble coalescence in the collection funnel or at high suction rates because of bubble breaking (Buchholz, 1981). Also the local hydrodynamics may be influenced by the suction probe. Recently an improved suction method was presented by Kamiwano et al. (1998) which allowed gas-holdups up to approx. 6%.

There also exist some measuring methods which use acoustic techniques as an analytical tool. Leighton et al. (1997) have recently reviewed and compared the different ultrasound techniques. Boyd and Varley (1998) describe a method that uses sound measurements. All these techniques have in common that the needed equipment is rather complex and that the system has to be calibrated each time the physical properties (e.g. viscosity) are changed. It is also not clear where the limits regarding the maximal gas-holdup are.

Some techniques measure mean bubble sizes only, e.g. the light extinction method (Hetsroni, 1982). But since it was the goal to measure bubble size distributions and not just the averages these methods will not be discussed here.

3.2.2 Selection of the measuring technique

After reviewing the existing techniques it is evident that only photographic methods can guarantee reliable bubble size measurements, especially at high gas hold-ups.

Regarding the bubble size two main cases were identified in the ABLR: Very small bubbles (<1 mm) in the plunging jet zone and everywhere in coalescence hindered solutions. Larger bubbles (1-8 mm) outside the plunging jet zone in coalescing solutions.

For the first case a special in-process video microscope for high speed applications called PVM™ (LASENTEC®) was used. (The PVM could only be used for bubbles <1 mm because its field of view is limited to 1.32 x 1.76 mm.) The PVM's very short exposure time (≈ 300 ns) and its high resolution guaranteed a sharp image of very small bubbles even at high flow velocities. Due to its in-line applicability every zone in the reactor could be accessed and limitations regarding the range of vision were avoided that way.

Since the PVM probe is inserted into the reactor a possible influence of the flow had to be taken into account. Of decisive importance is in this case the angle of the probe window to the flow direction. An example (measured in the plunging jet zone) is illustrated in Fig. 3-7. At angles < 20° to the flow direction the measured bubble size distributions are equal and independent of the insertion angle. Apparently the flow disturbances are minimal here. At angles > 20° the measured bubble sizes start to shift towards smaller values. This effect is intensified with increasing insertion angles. Therefore, to minimize the PVM's influence, bubble images were only taken at insertion angles < 20°.

For the second case (bubbles > 1mm) images were taken from the outside of the vessel by a digital photcamera.

The later evaluation of the images was assisted by image analysis. A detailed description of the used procedures can be found in Appendix 1.

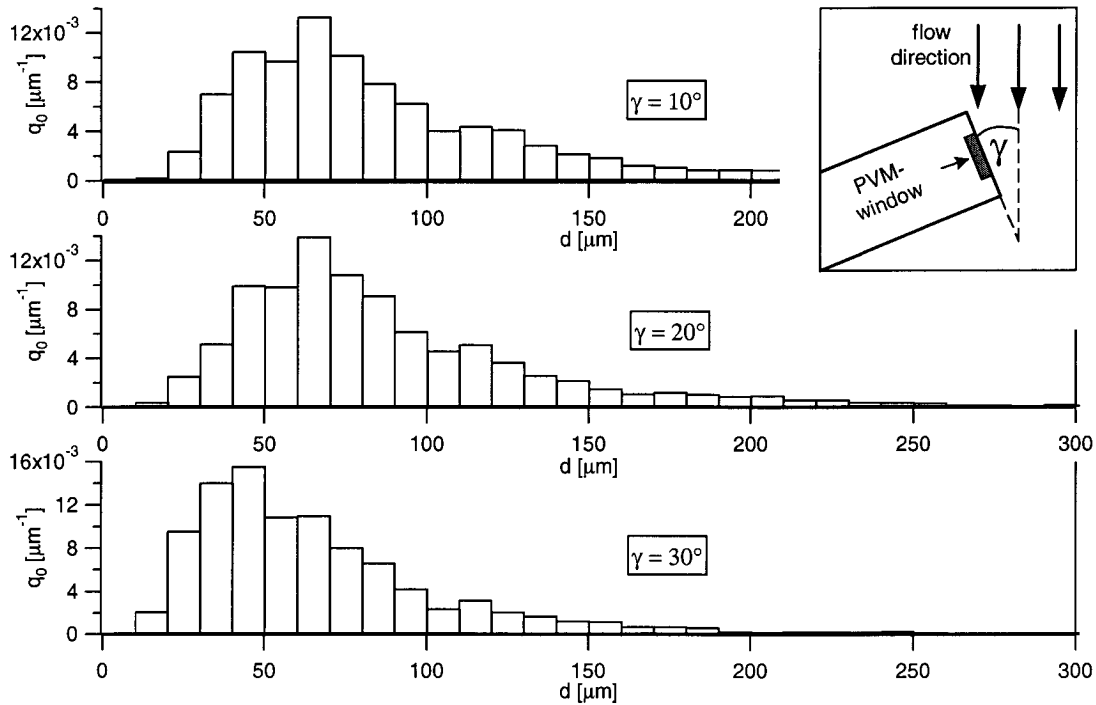


Fig. 3-7: Influence of the PVM insertion angle on the bubble size distribution

3.3 Gas holdup measurement

3.3.1 Review of existing techniques

This short review is structured in techniques for local and mean gas holdup measurements. A more detailed overview can be found for example in the review of Joshi et al. (1998).

Mean gas holdup

The volume expansion method is by far the most used technique for the measurement of the overall holdup. The holdup is calculated from the static liquid height h_S and that of the aerated liquid h_R (see Eq. 3-9).

The method is easy to apply and cheap. Problems may occur regarding the exact measurement of h_R , especially with heavily aerated liquids.

$$\varepsilon_G = \frac{h_R - h_S}{h_R} \quad (3-9)$$

Radiation absorption techniques are also often used. The intensity of a γ - or X-ray which passes through a two phase layer depends on the mean density of this layer exponentially. The needed experimental setup and safety precautions make these techniques rather expensive. Errors may occur because the measurements are influenced by the void orientation and because radiation sources are often not monoenergetic.

The quick closing valve technique is often used and produces reliable (volume averaged) results. The dispersion inside a reactor section is trapped by quickly and simultaneously closing all its inputs and outputs. The gas holdup is then calculated from the liquid volume in the section and the total section volume. Synchronization of the valves may be difficult but errors caused by this can be minimized by making the measuring volume large enough.

Capacitance measurements can also be used to determine the gas holdup in pipelines (Hersperger et al., 1995; Andreussi et al., 1988; Geraets and Borst, 1988). Two ring electrodes are mounted to the pipe wall, i.e. the method is non-intrusive. The capacitance between the two electrodes depends on their distance and the liquid holdup. The method is fully automated, but the signal processing and calibration are rather difficult. Furthermore the measurements are influenced by e.g. the temperature and inhomogeneities of the two phase flow.

Coriolis mass flow meters are another possibility, since they measure (next to the mass flow) the fluid's density. Lately there even exist flow meters made of one straight tube which causes no additional flow disturbances compared to a straight pipe (Drahm and Matt, 1998). However, gas-liquid dispersions are seldom perfectly homogeneous which may prevent correct measurements.

Local holdup

Barigou and Greaves (1992) and Genenger et. al (1992) measured the local gas holdup in a stirred tank reactor resp. in a loop reactor using an automated capillary

suction probe. A small, constant stream is removed from the gas-liquid dispersion and enters a capillary. The gas fraction is measured using photoelectric detectors. A suction technique using a simplified evaluation technique was recently presented by Sprehe et al. (1999). See Section 3.2.1 for a description of the pros and cons of this technique.

Contact probes that rely on the conductive, dielectric or optical properties of the liquid media are often used to measure local gas holdups (Buchholz et al., 1981; Linneweber and Blass, 1983; Barigou and Greaves, 1996; Bombac et al., 1997). The advantages and problems that may arise with this technique were already discussed in Section 3.2.1.

There exists a very wide variety of tomographic techniques, e.g. the γ -ray (Veera and Joshi, 1999) and X-ray transmission tomography, the positron emission tomography, the optical tomography or the ultrasonic tomography. Recently Chaouki et al. (1997) have published a very comprehensive review of all the known tomographic techniques suited for the monitoring of multi-phase flows. All these techniques are non-invasive, i.e. the flow is not disturbed, and they give complete informations regarding the holdup structure. However, they are also very expensive and difficult to install. Some of them are only suited for laboratory-scale equipment. Also the applicability of some of these techniques at high gas holdups is uncertain.

3.3.2 Selection of the gas holdup measuring technique

A high value was set on the reliability and the simplicity of measuring technique. Therefore the volume expansion method was used for the measurement of the holdup in the reaction vessel and the quick closing valve technique for the gas holdup measurement in the recycle pipe¹.

1. It should be noted that for the gas holdup measurements in the liquid recycle pipe a Coriolis mass flowmeter was taken into consideration first. But tests proved that this technique could not be applied correctly due to the suspected inhomogeneities in the gas-liquid dispersion.

4 Experimental

The experimental work was carried out in three stages. First a pilot scale reactor was designed and constructed for measurements at ambient pressure. With this setup all the experiments regarding the influence of the reaction mixer geometry, the power input and the liquid properties on the mass transfer characteristics were made.

In a second step the setup was modified for measurements at pressures up to 10 bar. Here particularly the influence of the gas properties on the mass transfer characteristics was investigated.

In a third step, in order to confirm the findings between 1-10 bar, some experiments were carried out in a pilot ABLR of the Kvaerner Process Technology AG, Pratteln, Switzerland. With this pilot plant system pressures up to 80 bar were possible.

4.1 Experiments at ambient pressure

4.1.1 Experimental Setup

During the design and construction of the first experimental facility special attention was paid to use as many components as possible for the later experiments at elevated pressures. Therefore many parts were made of stainless steel from the beginning. A flowsheet and two photographs of the setup are given in Fig. 4-1, Fig. 4-2 and Fig. 4-4.

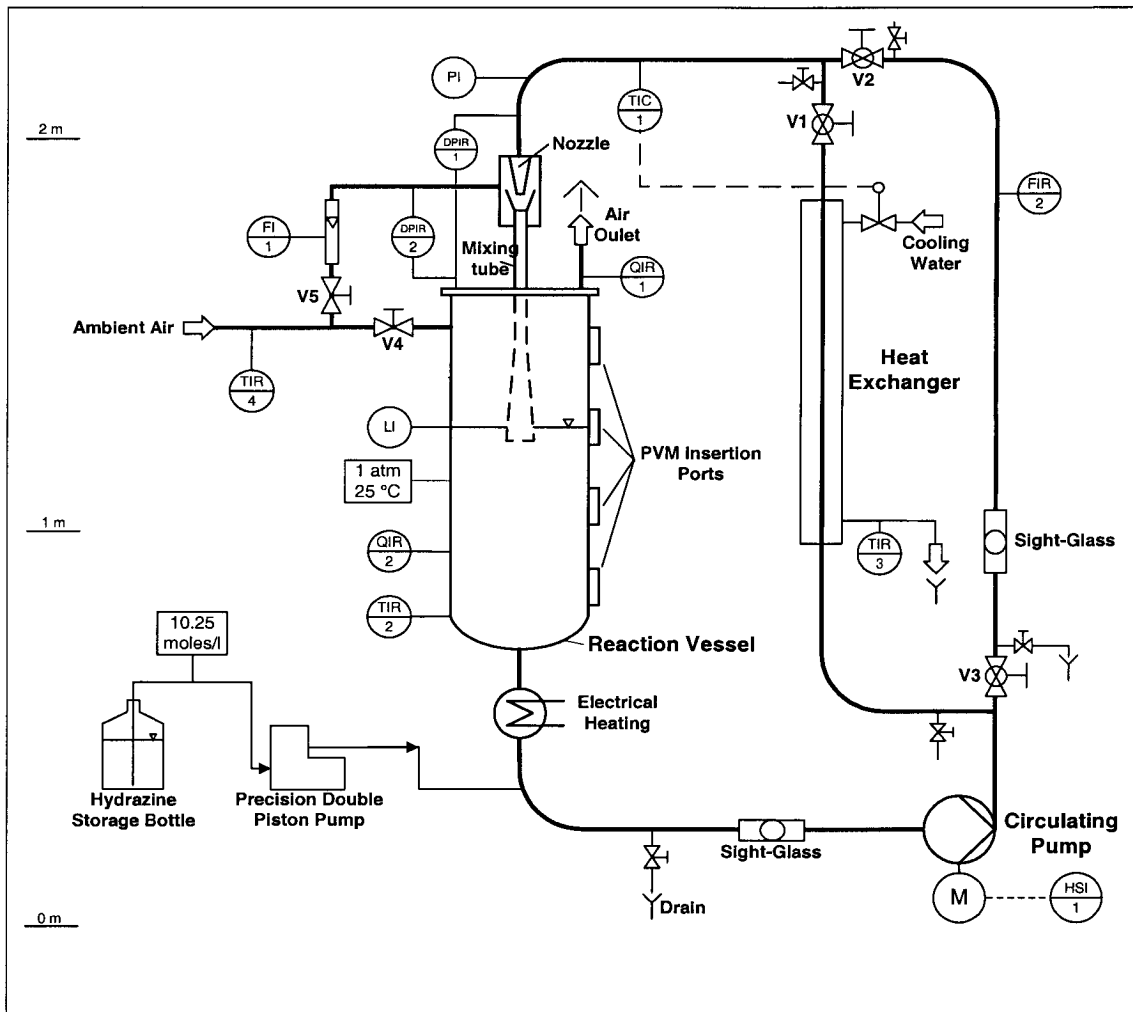


Fig. 4-1: Flowsheet of the experimental setup for measurements at ambient pressure with the main parts reaction vessel, reaction mixer (mixing tube, nozzle) and liquid recycle (electrical heating, circulating pump, heat exchanger)

Reaction vessel

The cylindrical part of the reaction vessel was made of transparent Plexiglas. It had an inner diameter of 30 cm and a height of 66 cm. A standard torispherical head (DIN 28011) of the same inner diameter served as the bottom of the vessel, a steel plate as its top cover. At one side of the vessel there were seven sealable openings which served to access the reaction vessel with the PVM probe. A ruler attached to the vessels wall was used to measure the level of the liquids free surface during operation.

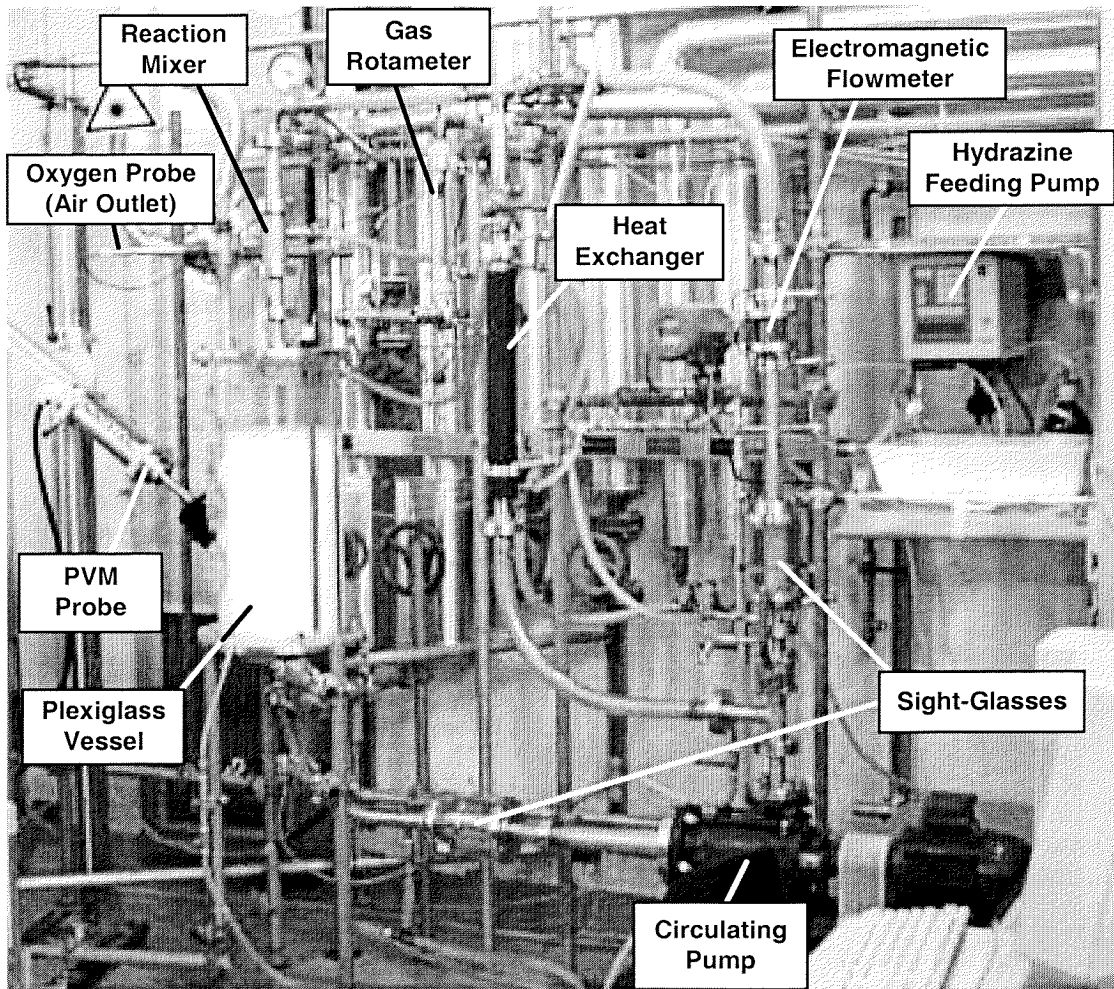


Fig. 4-2: Photograph of the experimental facility for measurements at ambient pressure

Reaction mixer and air supply

The reaction mixer was constructed in a modular way, allowing the testing of many different reaction mixer geometries. Table 4-1 gives an overview regarding the dimensions of the nozzles, mixing tubes and swirl devices which were used in this work. The swirl devices were fabricated of stainless sheet steel with a thickness of 0.8 mm and were wedged into the nozzle. With these components it was possible to assemble 24 different reaction mixer configurations¹.

The reaction mixer was mounted on the reactor in such a way that the end of the mixing tube, independent of its length, jutted out one centimeter into the reaction

1. Including the option "no swirl device"

vessel, ensuring that the dispersion jet entered the reaction vessel always at the same point.

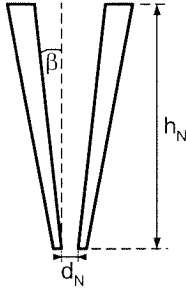
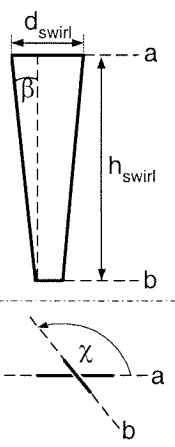
Nozzles			
	<u>Nozzle 1</u>	<u>Nozzle 2</u>	
	$d_N = 6.2 \text{ mm}$ $h_N = 90 \text{ mm}$ $\beta = 5.58^\circ$	$d_N = 8.0 \text{ mm}$ $h_N = 90 \text{ mm}$ $\beta = 5.58^\circ$	
Mixing tubes			
<u>Mixing tube 1</u>	<u>Mixing tube 2</u>	<u>Mixing tube 3</u>	
$d_M = 12 \text{ mm}$ $l_M = 120 \text{ mm}$	$d_M = 12 \text{ mm}$ $l_M = 220 \text{ mm}$	$d_M = 12 \text{ mm}$ $l_M = 370 \text{ mm}$	
Swirl devices			
	<u>Swirl 1</u>	<u>Swirl 2</u>	<u>Swirl 3</u>
	$d_{\text{swirl}} = 24 \text{ mm}$ $h_{\text{swirl}} = 75 \text{ mm}$ $\beta = 5.58^\circ$ $\chi = 90^\circ$	$d_{\text{swirl}} = 24 \text{ mm}$ $h_{\text{swirl}} = 75 \text{ mm}$ $\beta = 5.58^\circ$ $\chi = 180^\circ$	$d_{\text{swirl}} = 24 \text{ mm}$ $h_{\text{swirl}} = 75 \text{ mm}$ $\beta = 5.58^\circ$ $\chi = 270^\circ$

Table 4-1: Dimensions of the used reaction mixer components

The flow rate of the air entrained by the reaction mixer was measured by a rotameter (YOKOGAWA, model RAGH). The use of different floats made it possible to cover flow rates between 500-8000 NI/h. The ball valve V5 (see Fig. 4-1) could be used to reduce the flow rate of the entrained air. The dynamic pressure drop (Δp_S) in the gas suction chamber caused by this throttling was measured by a piezoresistive differential pressure transmitter (KELLER, series 23 PD) (DPIR 2 in Fig. 4-1).

Liquid recycle

For the liquid circulation a self priming combi-pump with extremely low NPSH values was used (SERO, series SRZS W). With this pump it was possible to convey dispersions with even very high gas holdups. A frequency converter (ABB, series ACS 300) was connected to the pumps motor in order to change its speed.

The pipeline between reaction vessel and circulating pump had an inner diameter of 40 mm. Built-in into it were a sight-glass of the same diameter, a ball valve for the emptying of the reactor and a connection port for the hydrazine feed. The pressure sided pipelines of the liquid recycle had an inner diameter of 32 mm. A piezoresistive differential pressure transmitters (KELLER, series 23 PD) (DPIR 1 in Fig. 4-1) was used to measure the dynamic pressure before the nozzle (Δp_N).

In order not to damage the circulation pump while applying the quick closing valves technique a branching of the pipeline for approx. 1.5 meters was necessary. This way it was avoided that the pump had to work against a closed pipeline.

Built-in into the first branch were two ball valves with full bore (V2 and V3 in Fig. 4-1), an electromagnetic flow meter (KROHNE, series IFM 1080 K + series IFC 090 F) and another sight-glass. The second branch contained a double pipe heat exchanger (length: 65 cm, surface: 650 cm²) and another ball valve with full bore (V1 in Fig. 4-1).

The handles of the valves V1 and V2 were connected by an aluminum bar in such a manner that their positions could be changed with one hand simultaneously, i.e. the opening of V2 resulted in the closing of V1.

Normally the branch with the heat exchanger was used. The other branch was only used for measurements of the gas-free liquid flow and the gas holdup in the recycle. It should be pointed out that measurements with the electromagnetic flowmeter were only accurate as long as the liquid phase contained gas holdups below 3 %. Therefore it was mainly used to determine the discharge coefficients C_f of the different nozzle configurations.

Temperature measurement and control

The reaction solution could be both cooled and heated. An electrical heating band was used to heat up the fresh solutions to the desired operating temperature which

was always 25 °C. Without any cooling the solution would have been slowly heated up by the circulation pump and the reaction enthalpy of hydrazine oxidation. Therefore a heat exchanger operated with cooling water was necessary to keep the temperature in the reactor constant. The combination of an electric temperature controller (EUROTHERM, series 2216) (TIC 1 in Fig. 4-1) and a magnetic control valve (BÜRKERT, series 6022) was used to control the flow rate of the cooling water.

The temperatures of the reaction solution, the ambient air and the cooling water were monitored with electric resistance thermometers of the type Pt 100. A fourth Pt 100, which was located in the recycle pipe, was used as sensor for the temperature control.

$k_L a$ -measurement

A precision double piston pump (DESAGA, type KP 2000) was employed for the time constant feeding of the hydrazine solution. The flow rate could be varied between 5-2000 ml/h. The inlet of the hydrazine into the reactor was located at the intake of the circulating pump (see Fig. 4-1). This way very good mixing with the liquid phase was guaranteed. To avoid any contact with the highly toxic hydrazine solutions and fumes (especially in the case of a hazard) the whole feeding device was located in a collecting basin under a hood with constant air removal.

Two Clark type oxygen probes (METTLER TOLEDO, series InPro 6000 + O₂ Transmitter 4100) were used. One (QIR 2 in Fig. 4-1) was inserted into the reaction vessel near its bottom for the measurement of the dissolved oxygen concentration in the liquid phase. The other (QIR 1) was used for the monitoring of the oxygen concentration in the air leaving the reactor.

Bubble size measurement

The PVM used in this work acquired images the size of 1320 x 1760 μm with a resolution of 480 x 640 pixels. The photographs were stored on a local computer where also the analysis of the images took place (see Appendix 1). The software package WIT (LOGICAL VISION) was used for the image analysis.

A special holding device for the PVM which allowed the access to all zones of the reaction vessel was constructed. Details of the construction are shown in Fig. 4-3. The PVM-probe was clamped to an aluminum profile. The profile itself was attached to an aluminum disk in such a way that shifting towards the reaction vessel was possible. The disk was mounted on a base-plate and could be turned in steps of five degrees. The base-plate was attached to a vertical steel pole and could be moved vertically. With this holding device it was possible not only to alter the height and penetration depth of the probe but also its angle to the flow direction. The reaction vessel could be entered by the PVM through seven openings in its wall. The flexible sealing between the PVM and the reaction vessel was achieved by using rubber bellows.

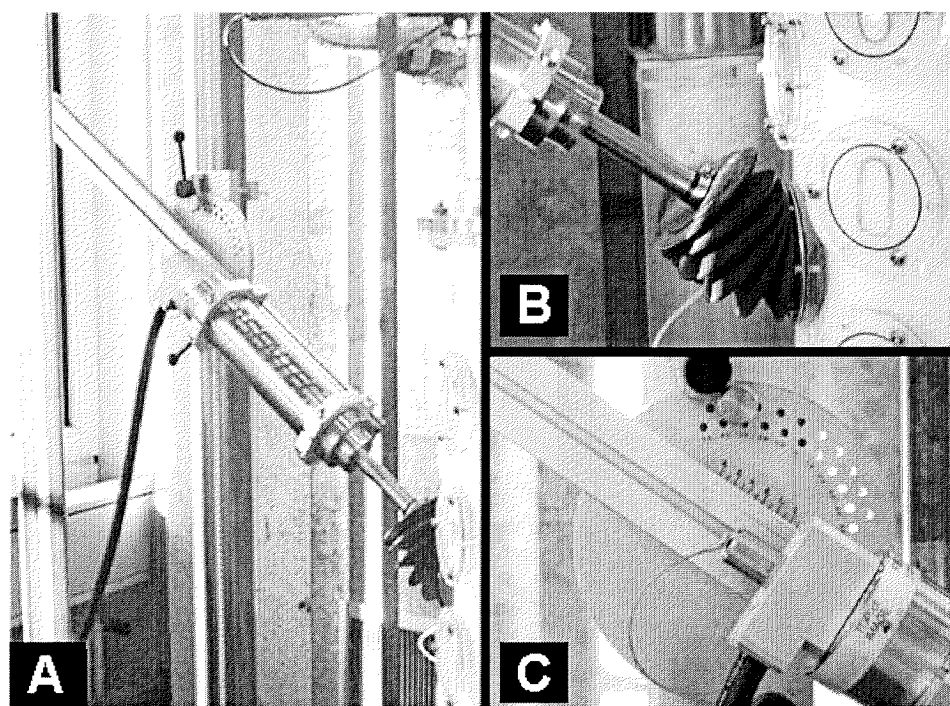


Fig. 4-3: Mounting device for the PVM. A: general view, B: sealing device and insertion holes, C: turntable

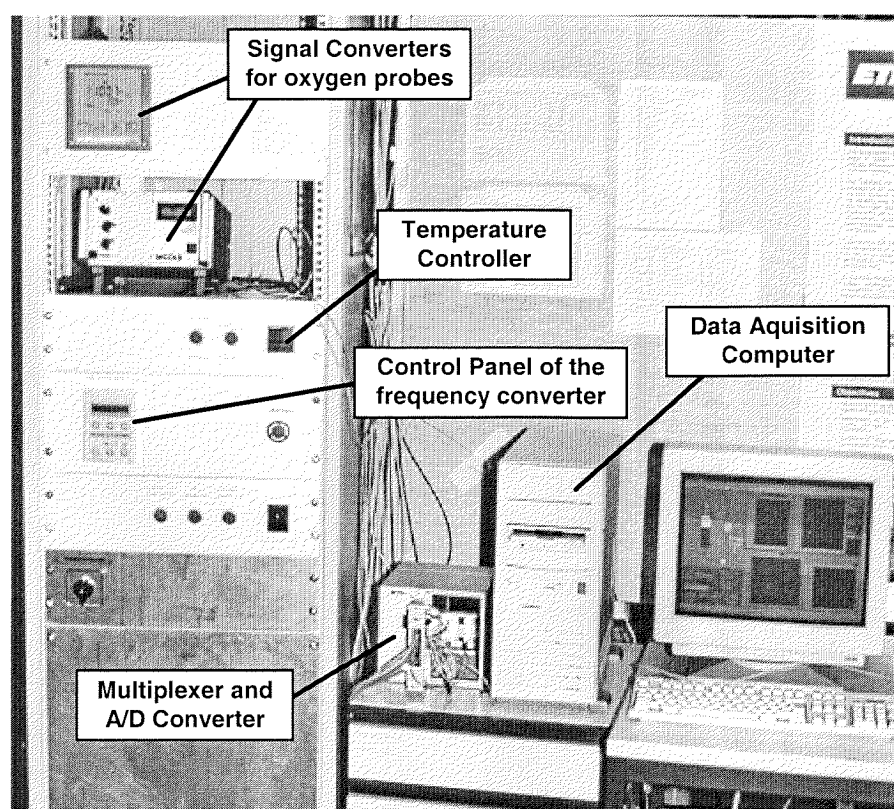


Fig. 4-4: Photograph of the peripheral electronic equipment

Data acquisition

All measured quantities were visualized and stored on a computer. As interface between the measuring devices and the computer served a multiplexer (NATIONAL INSTRUMENTS, SCXI 1000) and a data acquisition board (NATIONAL INSTRUMENTS, AT-MIO-16E-10). The software package used for the data acquisition was LabVIEW[®] (NATIONAL INSTRUMENTS).

4.1.2 Media

The only gas used with this first setup was ambient air. The model media for a coalescing liquid was ion-free water. For coalescence hindered systems a 0.25M Na₂SO₄-solution was chosen. The liquid properties of these systems are shown in Table 4-2. All measurements were carried out at a temperature of 25° C.

Na₂SO₄ concentration	Water	0.25 M
Dyn. viscosity η [mPa·s] ^a	0.95	1.17
Density ρ [kg/m ³]	997	1025
Surface tension σ [N/m] ^b	0.072	0.072
Oxygen solubility [mg/l] ^c	8.30	6.55

Table 4-2: Properties of different Na₂SO₄-solutions at 25 °C, 1 atm

a. CRC Handbook (1995) and Wilkinson (1991)

b. Lara Márquez (1994a)

c. Water: Tromans (1998), Na₂SO₄ solutions: Linek and Vacek (1981)

Some experiments were also carried out with viscous liquids. Different glucose solutions were used as a model system with Newtonian characteristics. The same system was used e.g. by Marquart (1981) in a jet loop reactor with internal circulation. According to Zlokarnik (1984) this system stands out for the possibility of varying the viscosity without altering the surface tension and the coalescence behaviour.

The properties of these solutions can be found in Table 4-3. The primary material for the preparation of these solutions was glucose syrup of a dry content of 78% (V-43, CERESTAR).

Glucose dry content	40%	45%	50%	55%	60%
Dyn. viscosity η [mPa·s] ^a	10	15	29	49	98
Density ρ [kg/m ³] ^a	1.20	1.22	1.25	1.27	1.30
Surface tension σ [N/m] ^a	0.074	0.074	0.074	0.074	0.074
Oxygen solubility [mg/l] ^b	4.9	4.4	4.2	3.9	3.6

Table 4-3: Properties of different glucose solutions at 25 °C, 1 atm

a. Measured

b. By fitting the experimental results in Sadler et al. (1988), Eya et al. (1994), van Stroe-Biezen et al. (1993) and Battino (1981)

4.1.3 Experimental methods

$k_L a$ measurements

The hydrazine feeding solution used for all the measurements was prepared by dilution of hydrazine monohydrate (FLUKA, puriss.) and had a concentration of 10.25 moles/liter.

For each new $k_L a$ measurement the hydrazine feeding rate was adjusted so that the steady-state dissolved oxygen concentration found its level at approx. 50 % of the saturation concentration. This way the experimental error was minimized and the hydrazine consumption was kept low. The oxygen concentrations measured during ten minutes of steady state operation were used for the calculation of $k_L a$.

In order to control that the solution did not change its properties with time (see chapter 3), it was proceeded as follows: The first $k_L a$ measurement with a fresh reaction solution was used as a reference point. In each case after approx. 10 further $k_L a$ measurements the operating conditions were set back to the ones of the first measurement and $k_L a$ was determined again. If there was no deviation from the reference the solution was used for another 10 $k_L a$ measurements. However, even with no observable aging a reaction solution was used for two days at the most.

To ensure that only fresh air was entrained into the reactor during the $k_L a$ -measurements the gas recycle was closed using valve V4 (see Fig. 4-1).

Gas holdup measurements

At the beginning of a gas holdup measurement in the liquid recycle the valves V2 and V3 (see Fig. 4-1) were open. Then they were quickly closed by hand simultaneously and the liquid trapped between them was drained, weighed and returned into the reactor. This procedure was repeated twice. The recycle holdup ϵ_R was calculated from the mean of these measurements.

Knowing ϵ_R and the total amount of liters filled into the reactor it was possible to determine the overall gas holdup ϵ_{tot} from the level of the dispersions free surface.

Bubble size measurements

In pure water coalescence occurred very quickly and resulted in bubble diameters in the range of 2-5 mm. Therefore, due to its small field of view (1.3 x 1.7 mm), the PVM could only be used in the uppermost part of the plunging jet zone. In this case pictures of the bulk bubbles were taken by a digital camera from the outside of the reaction vessel. With coalescence hindered solutions only the PVM was used.

A detailed description of the used image analysis procedures and the calculation of the bubble size distributions can be found in Appendix 1 and Appendix 2.

4.2 Measurements at elevated pressures

4.2.1 Experimental setup

The flow sheet of this new setup is shown in Fig. 4-5. A photograph of the modified reactor can be found in Fig. 4-6. The following changes and extensions were made to the first equipment:

Reaction vessel

The Plexiglas vessel was replaced by a stainless steel vessel with the same interior dimensions. Built-in into the vessels walls were three sight glasses allowing an insight along its entire length. As with the first setup rulers were attached next to the sight glasses to measure the level of the liquids free surface during operation. Another sight glass was installed at the vessels top. A cold light source was positioned in front of it to illuminate the vessels interior.

For the access of the PVM-probe two insertion ports in the lower half of the vessel were provided. The rubber bellows couldn't be used anymore for the sealing between the PVM-probe and the reaction vessel. They were replaced by two sealing devices at fixed insertion angles (10° and 30° to the horizontal).

The system pressure was monitored with a piezoresistive pressure transmitter (PIR 1) (KELLER, series 25). For the accurate measurement of the pressure history during the $k_L a$ experiments a piezoresistive differential pressure transmitters (DPIR 2) (KELLER, series 23 PD) was used. To prevent any exceeding of the permissible pressure a relief valve was installed in addition to a hand-operated ball valve (V9) for venting.

Since the pressure gauge technique is sensitive to small temperature changes during an experiment the whole plant had to be insulated.

Gas supply

A thermostat (JULABO, series F30) was employed to heat up the fresh gas coming from the gas bottles to the operating temperature of 25°C . A mechanical pres-

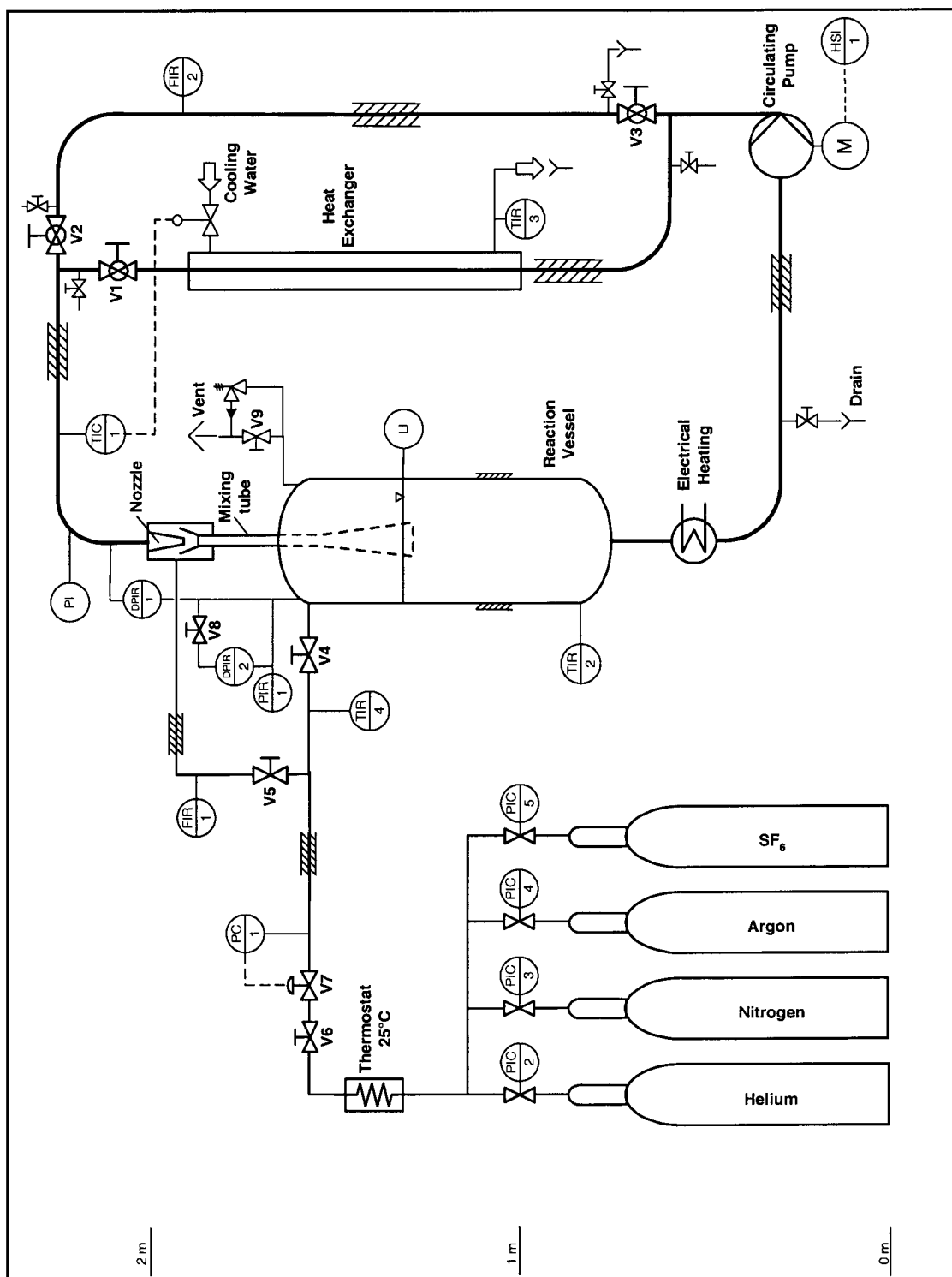


Fig. 4-5: Flowsheet of the experimental setup for measurements at elevated pressures

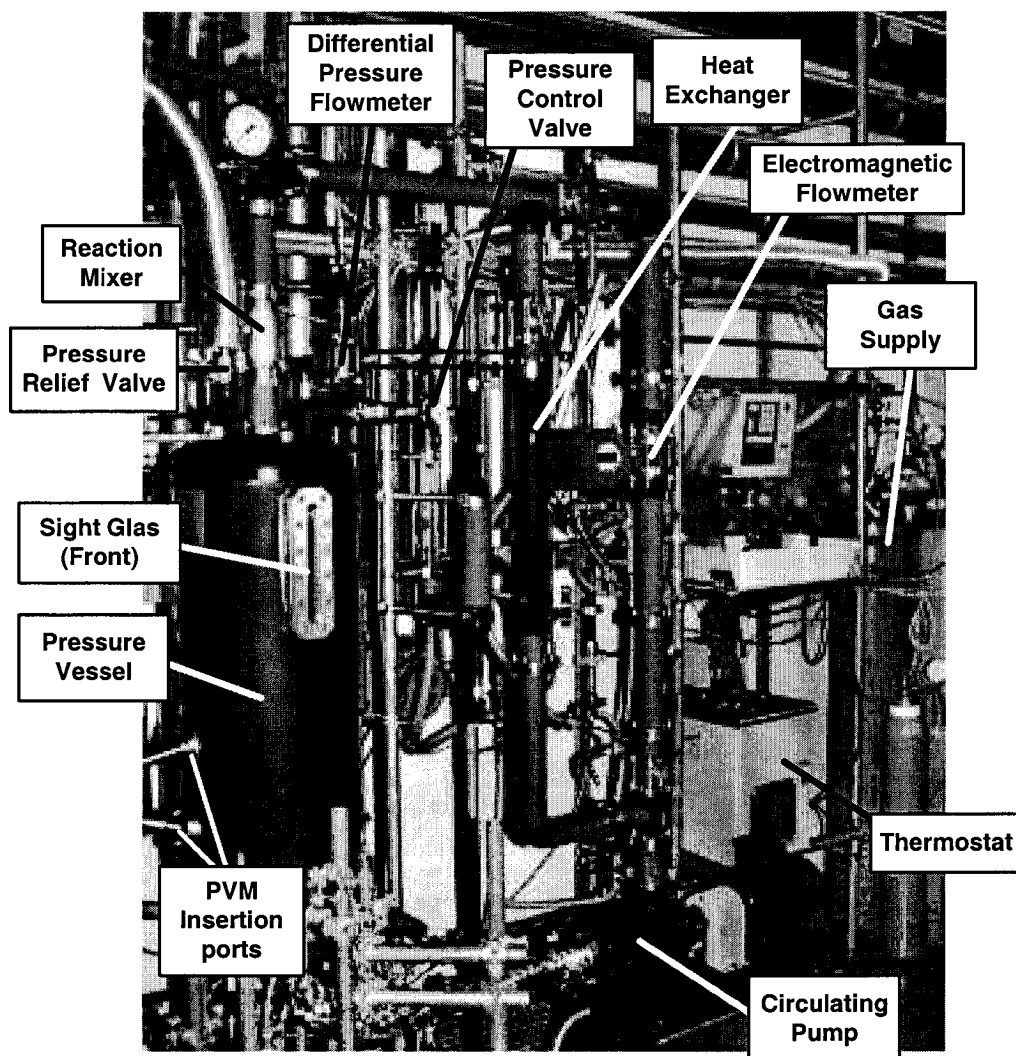


Fig. 4-6: Photograph of the experimental facility for measurements at elevated pressures

sure control valve (PC 1) (NORGREN) was used for setting the pressure in the reactor.

The flow rate of the entrained gas was measured by a differential pressure flowmeter (FIR 1) (McCROMETER, Waver-Cone Flowmeter). To cover the entrainment rates of all the used gases between up to 10 bar two differential pressure transmitters (not shown in Fig. 4-5) had to be used. One had a range of 0-50 mbar (smar[®], LD 301). The other a range of 0-2000 mbar (KELLER, series PD 23). Depending on the flow rate and the system pressure the connections between the two differential pressure transmitters and the V-Cone Flowmeter were switched from one to another.

4.2.2 Media

For the experiments at elevated pressures pure water was used. Four different gases were used: Helium, nitrogen, argon and sulfur hexafluoride (SF₆). Their properties are summarized in Table 4-4.

	He	N ₂	Ar	SF ₆
Mol. weight M_r [g/mol] ^a	4.003	28.013	39.948	146.056
Dyn. viscosity η [Pa·s] ^b	$1.94 \cdot 10^{-5}$	$1.75 \cdot 10^{-5}$	$2.10 \cdot 10^{-5}$	$1.51 \cdot 10^{-5}$
Density ρ [kg/m ³] ^b	0.16	1.13	1.61	5.87
Henry's law constant H [atm m ³ /kmol] ^c	2612	1544	731	4107
Diffusion coefficient in water [m ² /s] ^d	$2.5 \cdot 10^{-9}$	$1.9 \cdot 10^{-9}$	$2.1 \cdot 10^{-9}$	$1.1 \cdot 10^{-9}$

Table 4-4: Properties of the used gases at 25 °C and 1 bar

a. CRC Handbook of Chemistry and Physics (1995)

b. Wilkinson (1991)

c. Battino et al. (1984)

d. Wilke-Chang correlation (Deckwer, 1985)

4.2.3 Experimental methods

The gas holdup and the bubble size distributions were determined in the same manner as already described in Chapter 4.1.3.

The volumetric mass transfer coefficient $k_L a$ was measured with the pressure gauge method using the following procedure: After reaching equilibrium between the gas and liquid phase at starting conditions the circulating pump was stopped. Then the pressure was increased by 3-7 bar, depending on the solubility of the used gas type. First valve V6 then valve V8 (see Fig. 4-5) were closed. Now the pump was started and the pressure history was recorded by the computer. Later $k_L a$ was calculated by regression of the pressure history using Eq. 3-8.

5 Results at ambient pressure with the air/water system

In this chapter all the experimental results that were obtained at ambient pressure will be presented and discussed. The chapter is structured into five sections:

In the first two sections the influence of the power input and the liquid batch size on $k_L a$ will be described. The third and largest section of this chapter will deal with the influence of the reaction mixer configuration on the reactor's performance. In the fourth section a dimensionless model will be derived. In the last section all conclusions made in this chapter will be summarized.

5.1 Influence of the specific power input

5.1.1 Experimental results

For all tested reaction mixer geometries the volumetric mass transfer coefficient $k_L a$ was measured as a function of specific power input e_S . A plot of an exemplary extract¹ of these measurements is shown in Fig. 5-1. The presented measurements were obtained with the air/water system. To illustrate the experimental error the corresponding error bars were also included.

A strong correlation between $k_L a$ and e_S can be identified. The volumetric mass transfer coefficient increases with increasing specific power input.

1. It should be noted that $k_L a$ versus e_S was measured for all the 24 tested reaction mixer geometries. However, for a more comprehensive illustration of the obtained results only a part of the measurements is shown. The complete set of data can be found in Appendix 4.

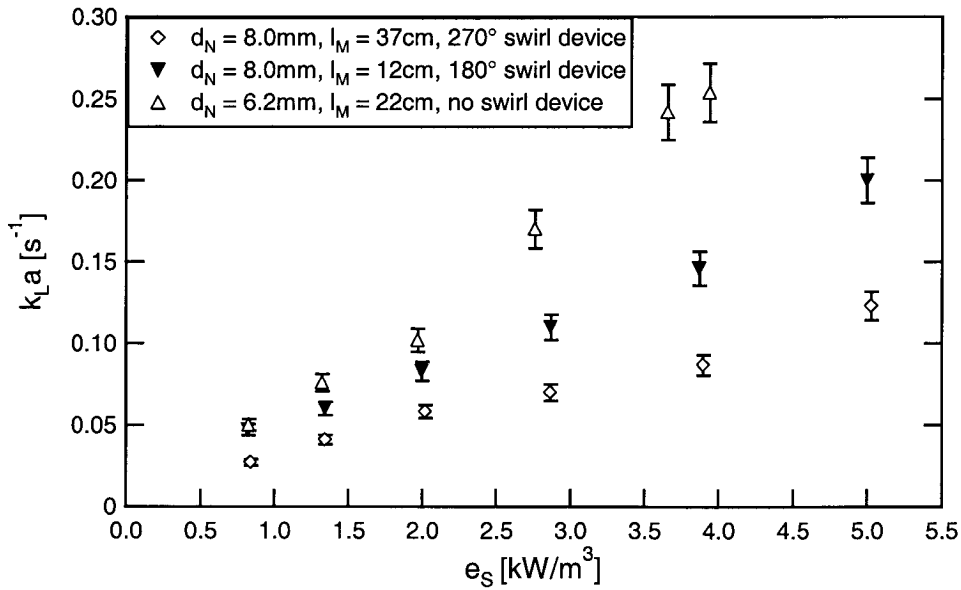


Fig. 5-1: Influence of the specific power input on $k_L a$ (air/water)

5.1.2 Discussion

In accordance to correlations presented in Chapter 2.2 the influence of e_s on $k_L a$ can be quantitatively described with the help of the following power law function

$$k_L a = C(\text{geometry, liquid properties}) \cdot (e_s)^x \quad (5-1)$$

where C represents the proportionality coefficient valid for a given reaction mixer configuration and set physical properties. Eq. 5-1 was fitted in each case to the experimental results obtained with one given reaction mixer configuration. The exponent x of all tested configurations was found to range between 0.8 and 1.1.

The observed influence of the specific power input on $k_L a$ is in good agreement with the findings for jet driven reactors reported by other authors. Dutta and Raghavan (1987) investigated differently shaped downflow ejectors and found x to range between 0.70 and 0.80. For a downflow ejector loop reactor van Dieren-donck et al. (1988) reports an x of 0.9. On the basis of the theory of isotropic turbulence Kawase and Moo-Young (1990) have estimated x to equal approximately 1.0. The applicability of this theory on the ABLR seems very likely. A further confirmation of this conclusion can be found in the next section.

5.2 Influence of the liquid batch volume on $k_L a$

The influence of the liquid batch volume V_L on the volumetric mass transfer coefficient $k_L a$ was investigated for two reasons:

1. The specific power input e_S could be varied without changing the absolute power input P . Results obtained this way could be used to confirm the findings made in Section 5.1 regarding the influence of the specific power input.
2. Similar experiments valid for reactors with common ejectors have been published by other authors. Therefore, results obtained this way are suited for comparing the ABLR with these reactors and identifying possible differences.

5.2.1 Experimental results

For one exemplary reaction mixer configuration a plot of $k_L a$ versus the specific power input e_S at different batch sizes V_L and power inputs P is shown in Fig. 5-2. The volumetric mass transfer coefficient is a direct function of e_S , i.e. the results of Section 5.1 can be confirmed. As long as e_S is constant, $k_L a$ is independent of the absolute values P and V_L . (Of course, this statement can only be regarded as granted inside the range of the varied batch volumes and power inputs.) As done in Section 5.1, the results can be approximated with a power law function ($x = 0.95$).

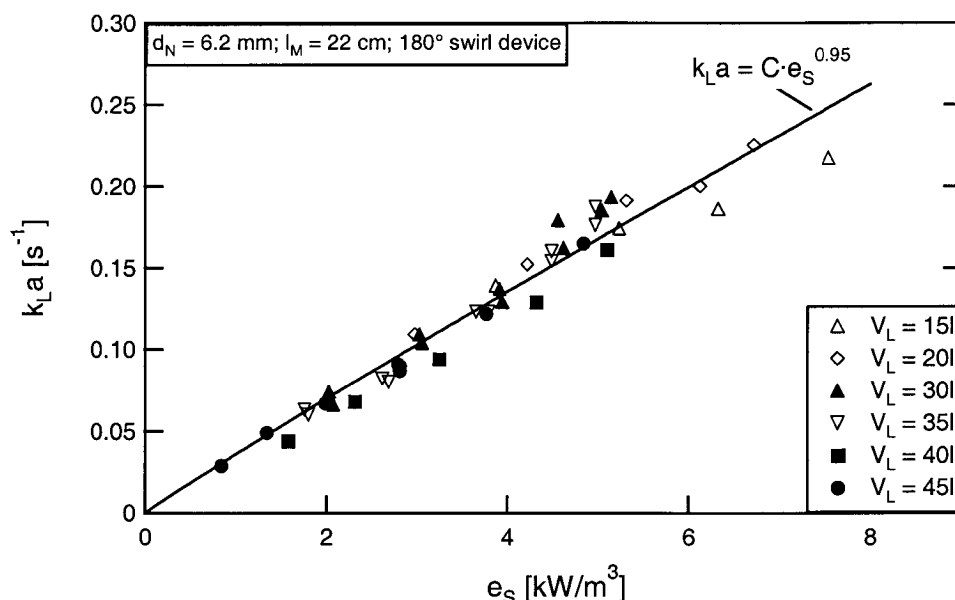


Fig. 5-2: $k_L a$ versus the volumetric power input at different batch sizes

These results could be confirmed with a different reaction mixer geometry and different liquid properties¹. This is shown in Fig. 5-3. Again, measurements obtained at different batch sizes but equal specific power inputs were comparable. Due to the much higher experimental error, the measured $k_L a$ values are more scattered with the sulfate solutions.

As before, the measured points were fitted with a power law function and again the values of the exponent agree well with the case of isotropic turbulence calculated by Kawase and Moo-Young (1990), i.e. $x \approx 1$. Therefore, the applicability of this theory on the mass transfer in the ABLR can be regarded as appropriate.

These findings were also of great importance for further experiments. Measurements of $k_L a$, that were obtained with one select batch size, were transferable to other batch sizes. Or in other words, it was sufficient to measure the influence of other operating conditions (reaction mixer geometry, liquid properties) on $k_L a$ at one batch size only. Thus, the number of needed experiments could be reduced and the meaningfulness of the measurements increased.

1. The influence of the reaction mixer configuration and the liquid properties on the mass transfer characteristics will be discussed in more detail in Section 5.3 and Section 6.

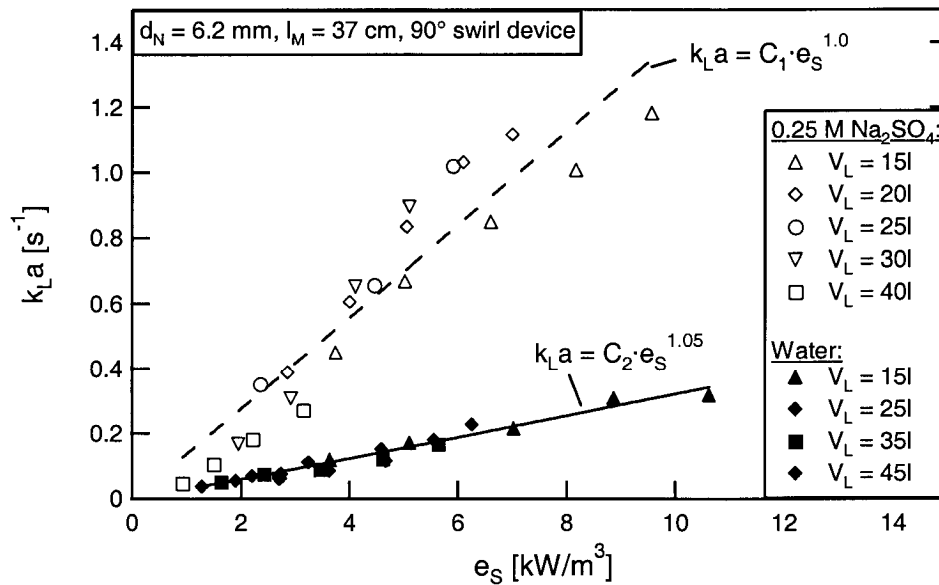


Fig. 5-3: $k_L a$ versus e_S at different batch sizes and liquid properties

5.2.2 Comparison with common ejector driven loop reactors

At the beginning of this chapter it has already been mentioned that similar experiments have been carried out by other authors with ejector driven reactors. Nagel et al. (1970) have measured the mass transfer in an upflow ejector loop reactor at different liquid heights h_1 above the ejectors outlet. At a constant liquid circulation flow rate (i.e. $P = \text{const.}$) they plotted the measured absolute phase interface area A versus the batch size. The area A was found to decrease with decreasing batch volume and by extrapolating to $h_1 = 0$ they obtained the approximate contribution of the ejector volume to A (see Fig. 5-4). It is evident that the mass transfer taking place in the ejector has a considerable effect on the overall mass transfer rate.

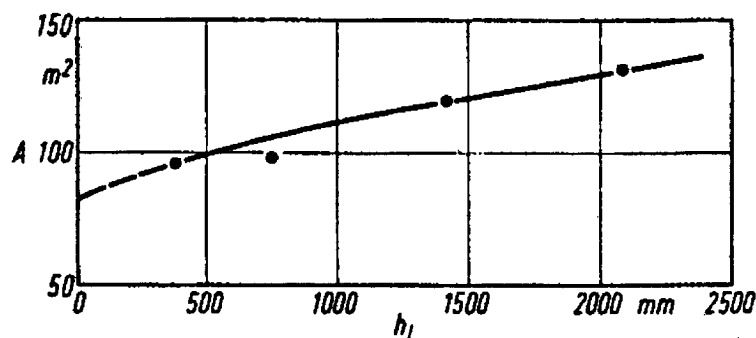


Fig. 5-4: Absolute interfacial area A vs. the liquid height h_l (Nagel et al., 1970)

These results point out one of the characteristics of the ejector loop reactors used e.g. by Nagel et al. (1970), Dirix and van der Wiele (1990) or Cramers et al. (1992, 1993). Nearly the entire energy input dissipates in the ejector. As long as P is constant also e_S in the ejector is constant and the interfacial area inside the ejector does not change with V_L . Once the dispersion leaves the ejector its behaviour is similar to that of a bubble column. The dispersion has lost nearly all of its momentum due to the much higher cross sectional area of the diffusor and the draft tube compared to the mixing tube. Therefore, after leaving the ejector, the gas-liquid mixing takes mainly place by buoyancy forces. The higher the liquid level above the ejector outlet is, the higher is the contribution of this 'bubble column section' to the mass transfer.

A plot similar to the one presented by Nagel et al. (1970) was generated for the ABLR (see Fig. 5-5). Instead of the absolute phase interface A , which was not measured in this work, the product $k_L a \cdot V_L$ was used. In a first approximation it can be assumed that the liquid sided mass transfer coefficient k_L is constant (see also Section 5.3).

No change of the interfacial area can be observed with the ABLR. Two explanations are possible for this behaviour.

One may assume that the entire mass transfer takes place in the mixing tube. However, this explanation is incompatible with other experimental observations. A very intensive gas-liquid mixture can be observed visually in the reaction vessel. Furthermore, an increase of the mixing tube length did not increase but decrease the mass transfer rate (see Section 5.3).

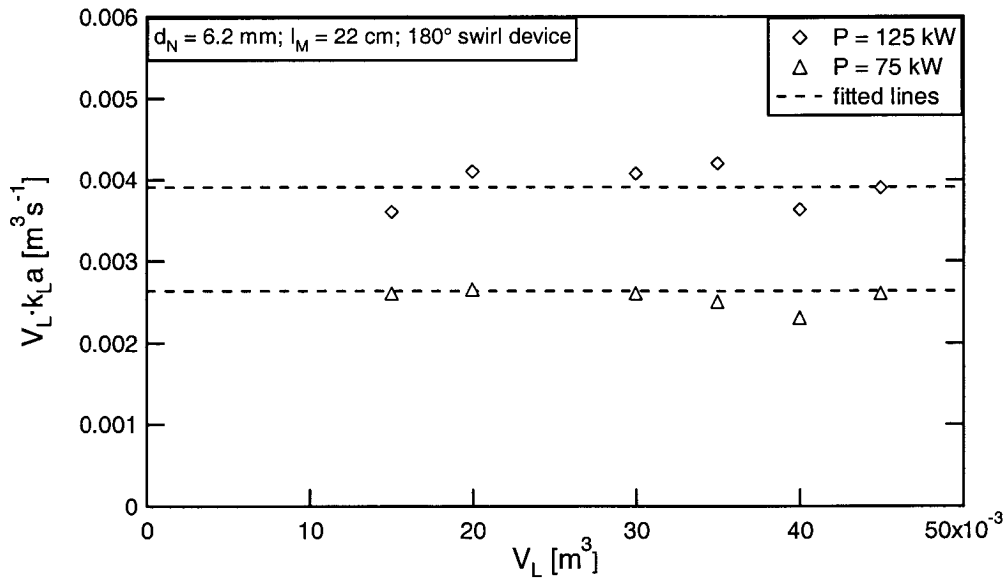


Fig. 5-5: $k_L a \cdot V_L$ vs. V_L with the absolute power input P as parameter

More obvious is the following explanation. The ABLR can be regarded a single unit where the energy dissipates in the entire liquid batch volume. This is also in good agreement with the findings regarding the influence of the specific power input on $k_L a$ and the applicability of the theory of isotropic turbulence. The halving of the liquid batch volume at a constant power input P leads to a doubling of e_S , and therefore $k_L a$, since it is directly proportional to e_S (because $x \approx 1$). However, as proven with Fig. 5-5, these changes do not affect the product $k_L a \cdot V_L$, which remains constant.

In the ABLR the reaction mixer serves primarily as a dispersion unit. Of course very high specific surface areas are present in the mixing tube but, due to its small volume compared to the liquid batch volume, its contribution to the overall mass transfer rate is negligible. This is a very different behaviour compared to common ejector loop reactors where the ejector itself contributes significantly to the mass transfer due to its much larger size and different geometry.

While with the ABLR's reaction mixer much of the liquid jet's momentum is preserved, nearly all the jet's energy dissipates inside common ejectors. Therefore, with measurements obtained with common ejector driven reactors the exponent x in Eq. 5-1 is well below 1.0.

5.3 Influence of the reaction mixer geometry

In the first part of this section the experimental data regarding the influence of the reaction mixer geometry on the volumetric mass transfer coefficient $k_L a$ and the gas holdup ϵ_{tot} will be presented and discussed. This is done simultaneously for these two quantities because they were often affected in a similar way. Later the same will be done for the influence of the reaction mixer geometry on the bubble size distribution. In the third part the results presented so far will be combined in order to deepen the knowledge regarding the effects caused by the different reaction mixer configurations. At the end of this section a design correlation based on dimensional analysis will be presented which allows the estimation of $k_L a$ at different reaction mixer geometries.

5.3.1 Influence of the reaction mixer geometry on $k_L a$ and ϵ_{tot}

5.3.1.1 Influence of the nozzle diameter

It should be noted that the volumetric mass transfer coefficients and the total gas holdups of all the 24 possible reaction mixer geometries were measured. However, for a more comprehensive illustration of the results only some extracts of the measured data will be used in this section. The complete set of data can be found in Appendix 4.

In Fig. 5-6 the influence of the nozzle diameter on $k_L a$ is illustrated for some exemplary reaction mixer configurations. If the same mixing tube and swirl device were used, the application of the 8 mm nozzle always resulted in higher mass transfer rates at the same power input.

The influence of the nozzle diameter on the total gas holdup ϵ_{tot} is shown in Fig. 5-7. As with the $k_L a$ measurements the nozzle with the larger diameter gave the higher total gas holdup ϵ_{tot} at otherwise constant operating conditions. Also the gas holdup was increased approx. linearly by an increased specific power input. This is in good agreement with the results of Zahradnik et al. (1997). They also observed a linear increase of the gas holdup between power inputs of 0-5 kW/m³.

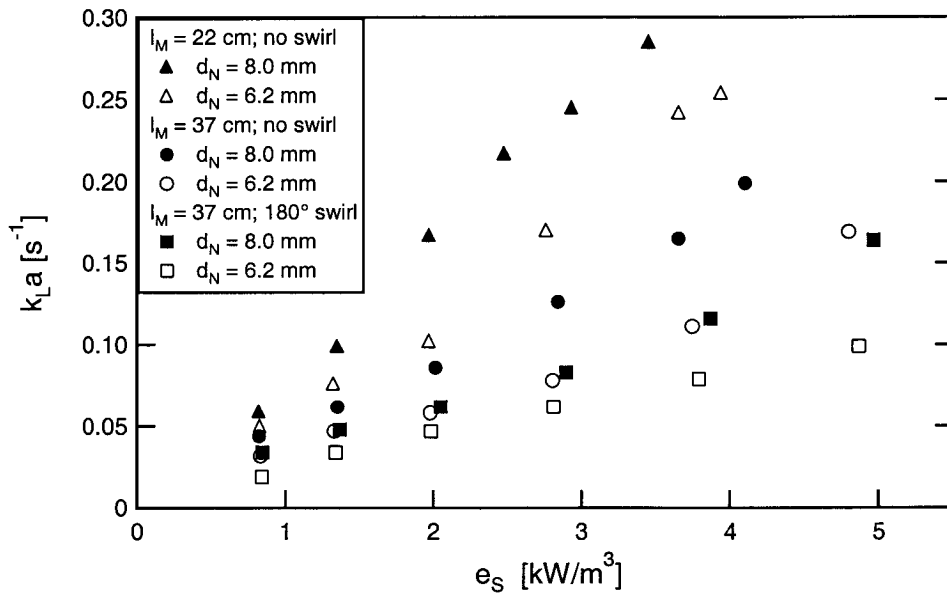


Fig. 5-6: Influence of the nozzle diameter on $k_L a$

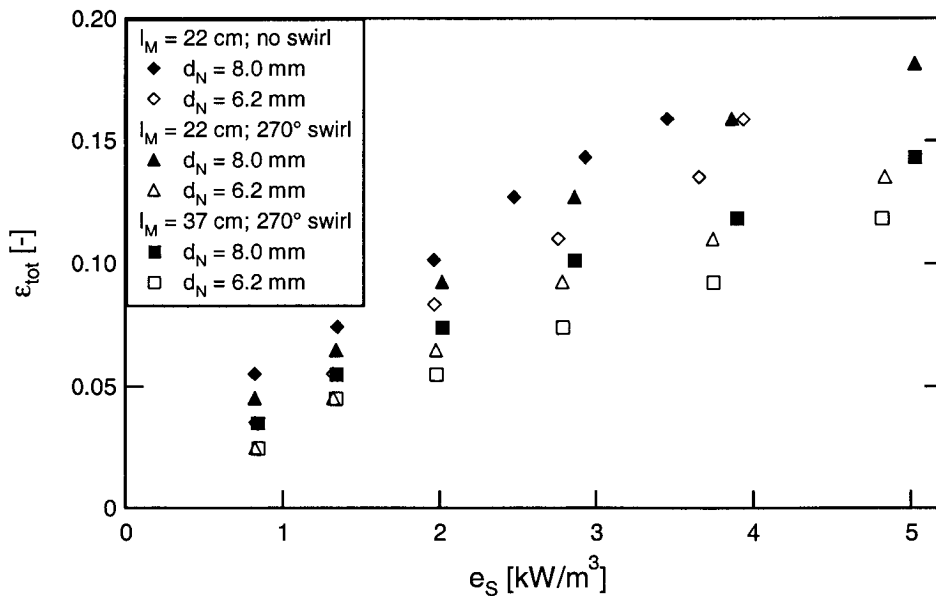


Fig. 5-7: Influence of the nozzle diameter on the total gas holdup

The influence of the nozzle diameter on $k_L a$ and ϵ_{tot} can be explained by taking a closer look at the gas entrainment rate and the momentum of the formed gas-liquid dispersion leaving the mixing tube.

Suppose there are two different nozzles with the diameters d_{N1} and d_{N2} . The ratio of these two diameters shall be defined by

$$\omega = \frac{d_{N2}}{d_{N1}} \quad (5-2)$$

At a constant power input the corresponding ratio of the flow rates through the nozzle can be calculated with the help of Eq. 2-20. In a first approximation the discharge coefficient C_f can be assumed as constant and the gas holdup in the recirculation pipe e_R can be neglected since it was seldom larger than 5 % with the air/water system under the applied operating conditions. Hence follows that, at a constant power input, the ratio of the resulting liquid flow rates Q_{L1} and Q_{L2} is given by

$$\frac{Q_{L2}}{Q_{L1}} = \omega^{4/3} \quad (5-3)$$

For rough turbulent jets emerging from nozzles the gas entrainment mainly takes place by the so-called jet envelope mechanism (e.g. Bin, 1993; Cramers et al. 1992a,b). Jet surface instabilities create an envelope surrounding the jet core. Gas trapped between these instabilities gets carried away by the liquid jet. This process can be promoted by an additional disturbance of the jet, e.g. by the application of swirl devices in the upflow region of the nozzle. The gas entrainment ratio Q_G/Q_L caused by this mechanism can be described by the following formula

$$\frac{Q_G}{Q_L} = \left[\left(\frac{d_J}{d_N} \right)^2 - 1 \right] \quad (5-4)$$

at which d_J denotes the diameter of the liquid jet at its plunging point into the mixing shock zone. Strictly speaking the above equation is only valid for liquid jets without any swirl induced on them. Also the diameter d_J was not measured in this work. However, on the basis of the measured liquid and entrained gas flow rates it was possible to modify Eq. 5-4 in order to get a quantitative approximation formula of the gas entrainment in the ABLR. The jet diameter d_J was substituted by the mixing tube diameter d_M and a proportionality factor was introduced. The following equation could be derived:

$$\frac{Q_G}{Q_L} = 0.8 \cdot \left[\left(\frac{d_M}{d_N} \right)^2 - 1 \right] \quad (5-5)$$

According to Eq. 5-5 the gas entrainment ratio Q_G/Q_L is only a function of the ratio of the mixing tube and nozzle diameter. Or in other words, the gas entrainment ratio

can be regarded as constant for the same nozzle diameter since d_M was not varied in this work. To illustrate this a plot of Q_G vs. Q_L , valid for the nozzle with a diameter of 8 mm, is shown in Fig. 5-8. It should be noted that the data points were obtained with all reaction mixer configurations possible with this nozzle.

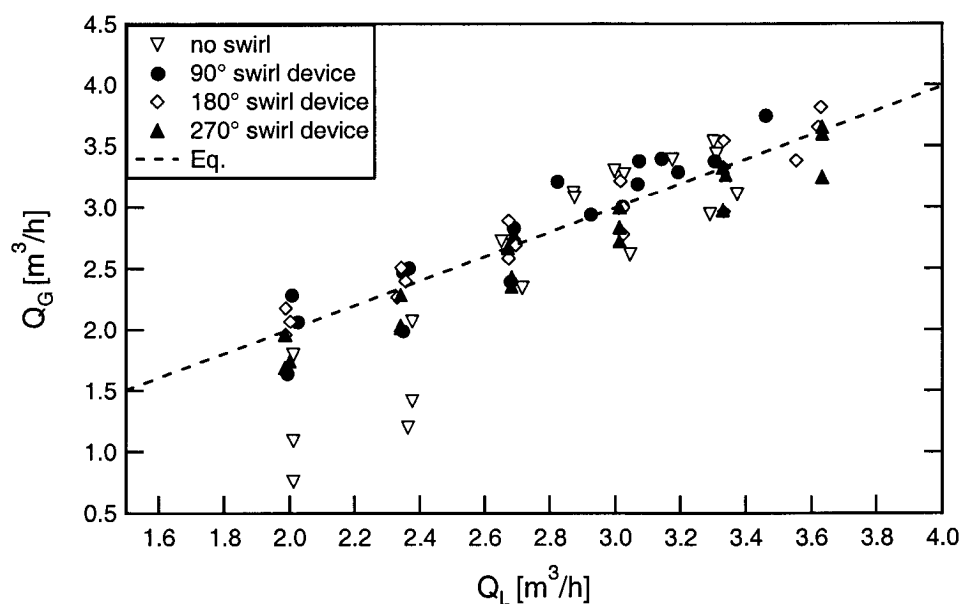


Fig. 5-8: Q_G vs. Q_L for all possible configurations with the 8 mm nozzle

It is assumed that the dispersion jet charging from the mixing tube can be described with the homogeneous flow model and that the slip between the two phases can be neglected due to the high degree of turbulence in the mixing tube. The corresponding flow rate Q_{disp} , the velocity of the dispersion jet u_{disp} and the homogeneous dispersion density ρ_{disp} can be calculated by the following formulas

$$Q_{disp} = Q_L + Q_G = Q_L \cdot \left(1 + \frac{Q_G}{Q_L} \right) \quad (5-6)$$

$$u_{disp} = \frac{4 \cdot Q_L \cdot \left(1 + \frac{Q_G}{Q_L} \right)}{\pi \cdot d_M^2} \quad (5-7)$$

$$\rho_{\text{disp}} = \rho_L \cdot \left(\frac{1}{1 + \frac{Q_G}{Q_L}} \right) \quad (5-8)$$

The momentum rate M^* of the dispersion jet plunging from the mixing tube into the reaction solution is given by

$$M^* = \rho_{\text{disp}} \cdot Q_{\text{disp}} \cdot u_{\text{disp}} = \frac{4}{\pi \cdot d_M^2} \cdot \rho_L \cdot Q_L^2 \cdot \left(1 + \frac{Q_G}{Q_L} \right) \quad (5-9)$$

And finally the ratio of the momentum rates obtained at constant power input with two nozzles of different diameters (with $d_{N1} < d_{N2}$) can be calculated by merging Eq. 5-2, Eq. 5-3, Eq. 5-5 and Eq. 5-9.

$$\frac{M_2^*}{M_1^*} = \frac{0.2 \cdot \omega^{8/3} + 0.8 \cdot \omega^{2/3} \cdot \frac{d_M^2}{d_{N1}^2}}{0.2 + 0.8 \cdot \frac{d_M^2}{d_{N1}^2}} > 1 \quad ; \quad \omega > 1 \quad (5-10)$$

It is evident that an increase of the nozzle diameter at a constant power input leads to an increase of the dispersion jet momentum if the same mixing tube is used. This strongly influences the gas-liquid mixing in the reaction vessel.

Bubbles entrained by a vertical plunging jet penetrate the pool liquid to some maximum depth h_p . This penetration depth is proportional to the jet momentum (see e.g. Bin, 1993). Although the increase of the ratio d_M/d_N results in an increase of the gas entrainment ratio, the formed dispersion jet does not carry the gas far beneath the batch surface. Thus the more loaded jet dissipates its energy in the biphasic region more diffusely and the volumetric mass transfer coefficient and the gas-holdup are less favourable than with a more coherent plunging jet.

At a first glance it might be a surprise that an increased gas entrainment leads to a decrease of $k_L a$. However, inside the range of the varied nozzle diameters the increased momentum can apparently more than compensate the decrease of the gas entrainment. It should also be noted that with the ABLR the gas entrainment takes place not only in the reaction mixer but also in the reaction vessel where the dispersion jet plunges into the reaction solution.

Regarding the concept of gas entrainment by the jet envelope mechanism it can be reasonably assumed that the amount of gas entrained by the liquid jet into the mixing tube decreases with $d_N \rightarrow d_M$ as the jet cross-section approaches that of the mixing tube, i.e. the momentum of the jet leaving the mixing tube would be steadily increased. However, with $d_N = d_M$ one would get a common plunging liquid jet, a system of rather limited mass transfer performance (Zlokarnik, 1999). Therefore, it has to be expected that a critical value regarding the ratio d_M/d_N exists, at which the gain in jet momentum does not compensate the decreased gas entrainment, i.e. from a certain point on $k_L a$ would start to decrease with $d_N \rightarrow d_M$. These considerations are in good agreement with the results by Cramers et al. (1993) who report that $k_L a$ inside a downflow ejector reaches its maximum at gas entrainment ratios around 1.

5.3.1.2 Influence of the mixing tube length

The mass transfer rate was also influenced significantly by the mixing tube length. In Fig. 5-9 $k_L a$ is plotted versus the mixing tube length l_M at otherwise constant test conditions. The mass transfer rate was highest, if the 22 cm long mixing tube was installed and decreased with the other two mixing tubes, i.e. there existed an optimum regarding the mixing tube length.

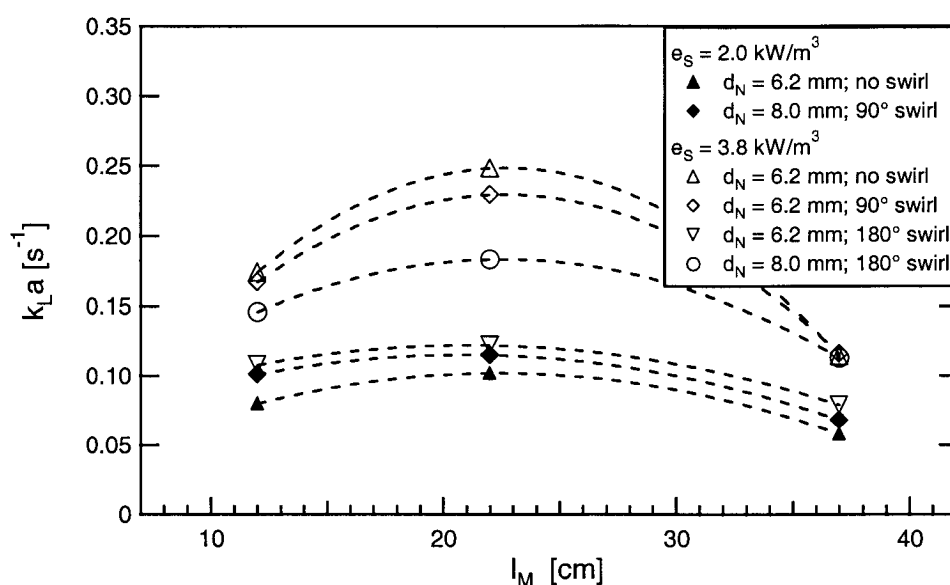


Fig. 5-9: Influence of the mixing tube length on $k_L a$

The influence of the mixing tube length on the total gas holdup ϵ_{tot} was similar to the one obtained with the $k_L a$ measurements. This is illustrated in Fig. 5-10. A significant decrease of ϵ_{tot} could be observed, if the 22cm long mixing tube was replaced by one with a length of 37 cm. However, the differences between the 12 cm and 22 cm mixing tube were not as clear. The 12 cm mixing tube yielded the highest total gas holdups if the 180° and 270° swirl devices were used. With the other swirl device configurations the 22 cm mixing tube lead to the highest gas holdups.

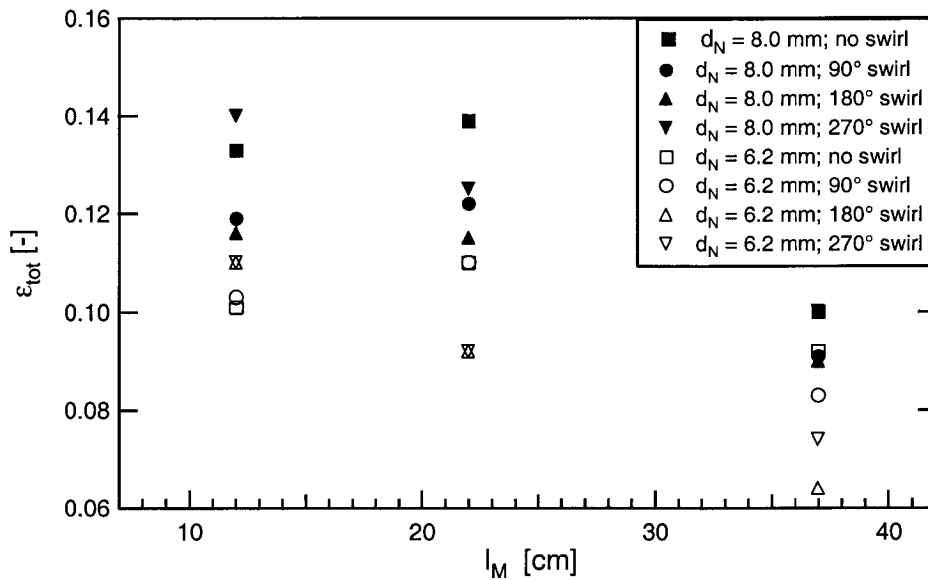


Fig. 5-10: Influence of the mixing tube length on the total gas holdup ϵ_{tot} ($e_S = 2.8 \text{ kW/m}^3$)

The influence of the mixing tube length on $k_L a$ and the gas holdup can be explained by taking a closer look at the dispersion process inside the mixing tube. According to e.g. Witte (1969) or Cramers et al. (1993) the dispersion of the gas phase takes place in a special region of the mixing tube, the so called mixing shock zone. This zone is distinguished by a steep and gradual increase of the pressure along its length. At the end of this zone the dispersion process is finished and the bubble flow regime is established.

If the mixing tube is too short, the momentum transport between the phases is incomplete, i.e. the gas dispersion cannot be finished properly before the mixing tube's end. The result is that not all the entrained gas is carried into the liquid phase of the reaction vessel by the two-phase jet. On the other hand, if the mixing tube is

too long the flow of the homogeneous gas-liquid mixture through the remaining part of the mixing tube results in considerable friction losses and therefore momentum losses of the two-phase jet (Havelka et al., 1997). Additionally the formed bubbles may coalesce again and partial phase separation takes place. Again not all the entrained gas is carried into the bulk liquid and the entrained bubbles are larger than with a properly dimensioned mixing tube length. Compared to the optimal mixing tube length the described phenomena always result in lower gas holdups and lower $k_L a$ values.

The starting point of the mixing shock zone depends on the used swirl device. The higher the swirl device torsion is the earlier the mixing shock region begins. That is the reason why swirl devices with a torsion of 180° or 270° show the maximal gas holdup already with the 12 cm long mixing tube.

5.3.1.3 Influence of the swirl device

The dependence of $k_L a$ on the installed swirl device is depicted in Fig. 5-11. At otherwise constant operating conditions the mass transfer rate decreased with increasing swirl device torsion. Also the effects of the nozzle diameter and the mixing tube length were strongly damped with an increasing swirl device torsion.

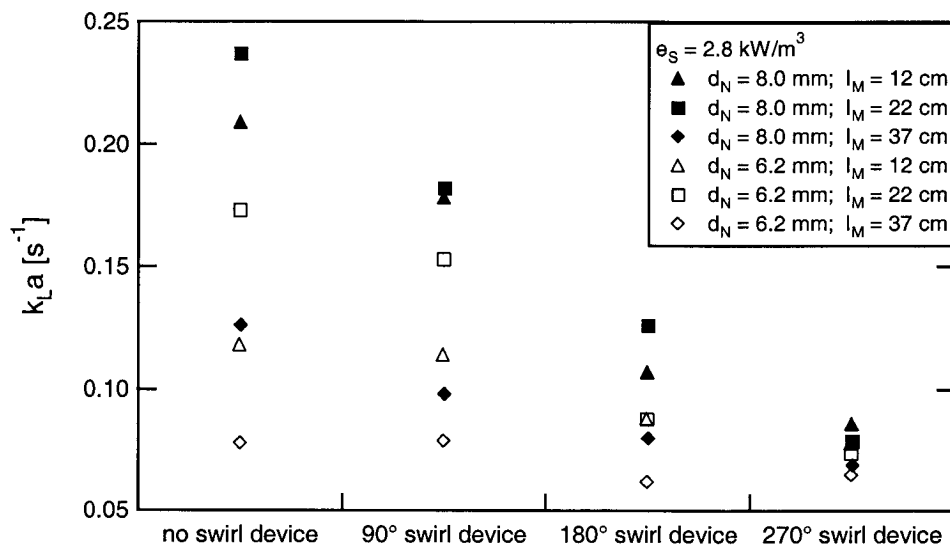


Fig. 5-11: Influence of the swirl device on $k_L a$

No clear trend regarding the influence of the swirl device on the gas holdup could be identified (see Fig. 5-12). Some reaction mixer configurations showed a decrease of the gas holdup with increasing swirl device torsion. However, the gas holdups of other configurations were not significantly influenced or even increased with increasing swirl device torsion. Additionally the damping of the differences with increasing swirl device torsion, which occurred with the $k_L a$ measurements, could not be observed.

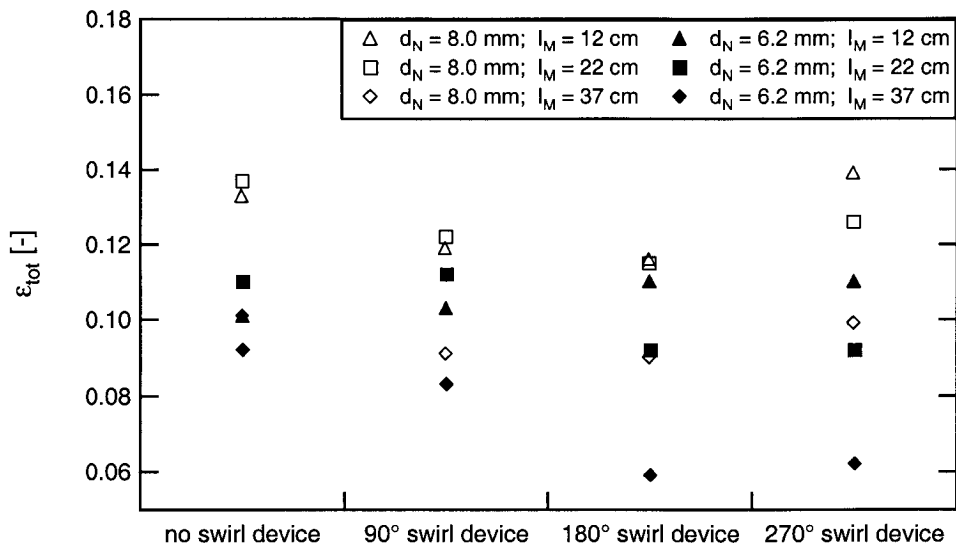


Fig. 5-12: Influence of the swirl device on the total gas holdup ϵ_{tot} ($e_S = 2.8 \text{ kW/m}^3$)

A detailed explanation regarding the influence of the swirl device on the mass transfer characteristics will be given in Section 5.3.3.

5.3.1.4 First conclusions

In a first conclusion it can be stated that as well the ratio of the nozzle and the mixing tube diameter as the mixing tube length as the geometry of the swirl device have a significant influence in the mass transfer characteristics. The highest volumetric mass transfer coefficient was obtained with a nozzle diameter of 8 mm, a mixing tube length of 22 cm and the absence of any swirl device.

In order to obtain a more detailed understanding regarding the influence of the different reaction mixer components on the mass transfer and the overall gas

holdup the corresponding bubble size distributions were measured in function of the reaction mixer configuration as well.

5.3.2 Influence of the reaction mixer geometry on the bubble size distribution

Detailed descriptions of the used procedures for the analysis of the bubble images, the generation of the bubble size distributions and the computation of the *Sauter* mean bubble diameter can be found in Appendix 1 and Appendix 2.

Since the determination of the bubble size distributions was extremely time consuming, these measurements were only done for three select reaction mixer configurations which showed very different mass transfer characteristics:

- $d_N = 8.0$ mm, $l_M = 22$ cm, no swirl device (high $k_L a$)
- $d_N = 6.2$ mm, $l_M = 22$ cm, no swirl device (medium $k_L a$)
- $d_N = 6.2$ mm, $l_M = 22$ cm, 180° swirl device (low $k_L a$)

Photographs taken at different heights from the outside of the reaction vessel showed no significant differences regarding the bubble sizes. Furthermore the small primary bubbles, which were formed in the mixing tube, coalesced nearly instantaneously to larger secondary bubbles once the two phase jet had entered the liquid in the reaction vessel. With the help of the PVM it was possible to observe that even in the plunging jet zone (~ 10 cm below the liquid surface) nearly no bubbles smaller than 1 mm existed. On the basis of the observations the assumption was made that the bubble size distribution could be regarded as uniform throughout nearly the entire reaction vessel and, therefore, could be described in good approximation by measurements made at one single height.

Exemplary bubble images taken from the outside of the reaction vessel at different power inputs (using the same reaction mixer configuration) are shown in Fig. 5-13. The visual impression that the differences are rather small can be confirmed by comparing the computed bubble size distributions and especially the *Sauter* bubble diameters, which are relevant for the mass transfer (see Eq. 2-16). This is illustrated in Fig. 5-14. The bubble size distributions differ only slightly from one another. The differences between the *Sauter* mean diameters can be regarded as not significant.

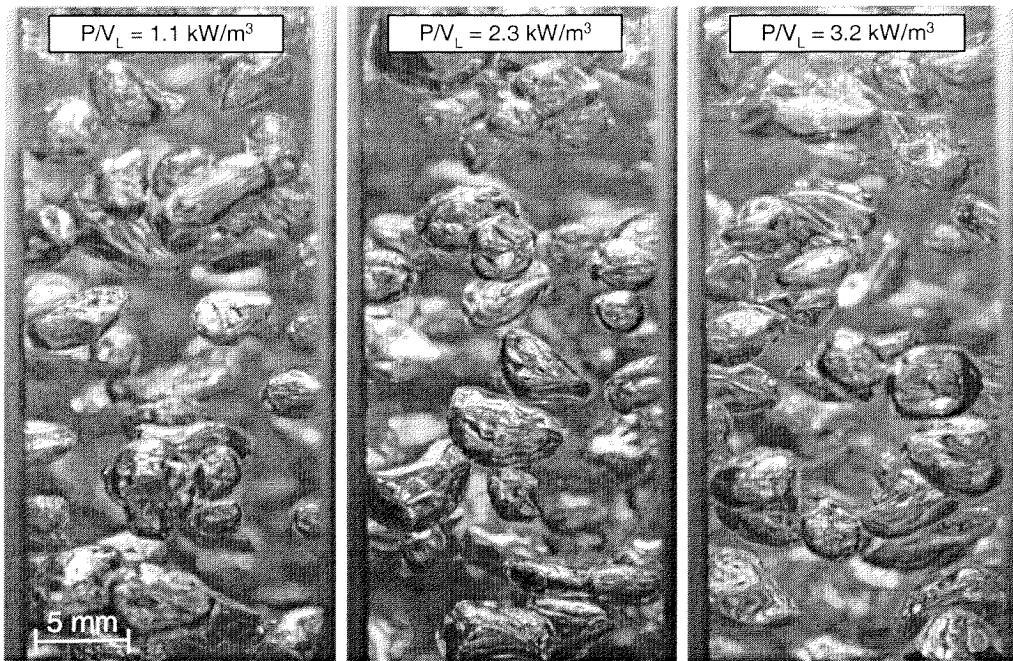


Fig. 5-13: Bubbles at different power inputs ($d_N = 8.0 \text{ mm}$, $l_M = 22 \text{ cm}$, no swirl device).

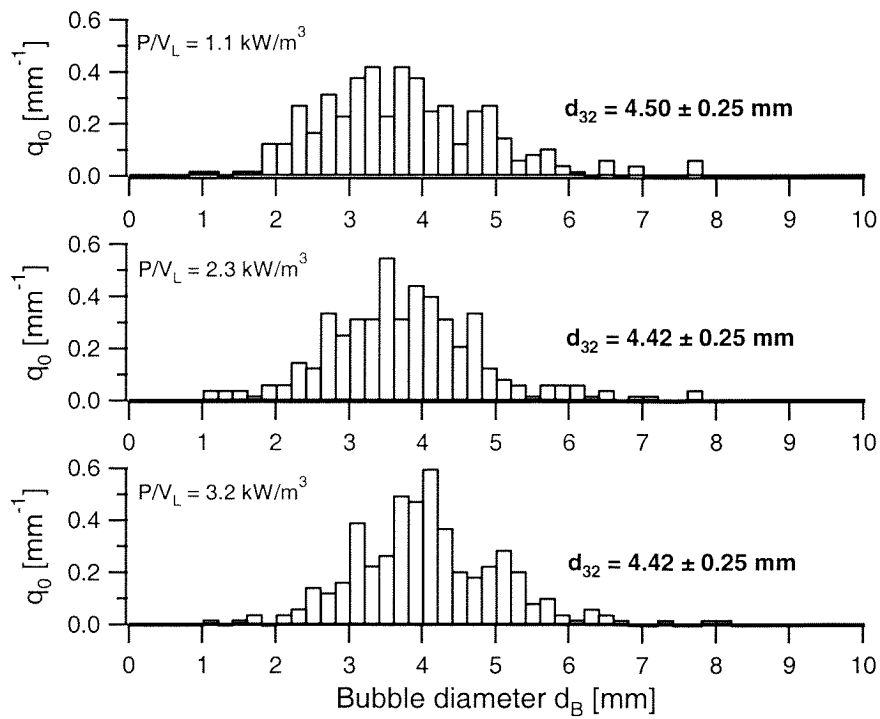


Fig. 5-14: Bubble size distributions at different power inputs; $d_N = 8.0 \text{ mm}$, $l_M = 22 \text{ cm}$, no swirl.

Similar observations were made, if different reaction mixer configurations were used. The corresponding bubble images and bubble size distributions can be found in Fig. 5-15 and Fig. 5-16. Again the bubble size distributions differed only slightly from one another and the corresponding *Sauter* mean bubble diameters were nearly identical.

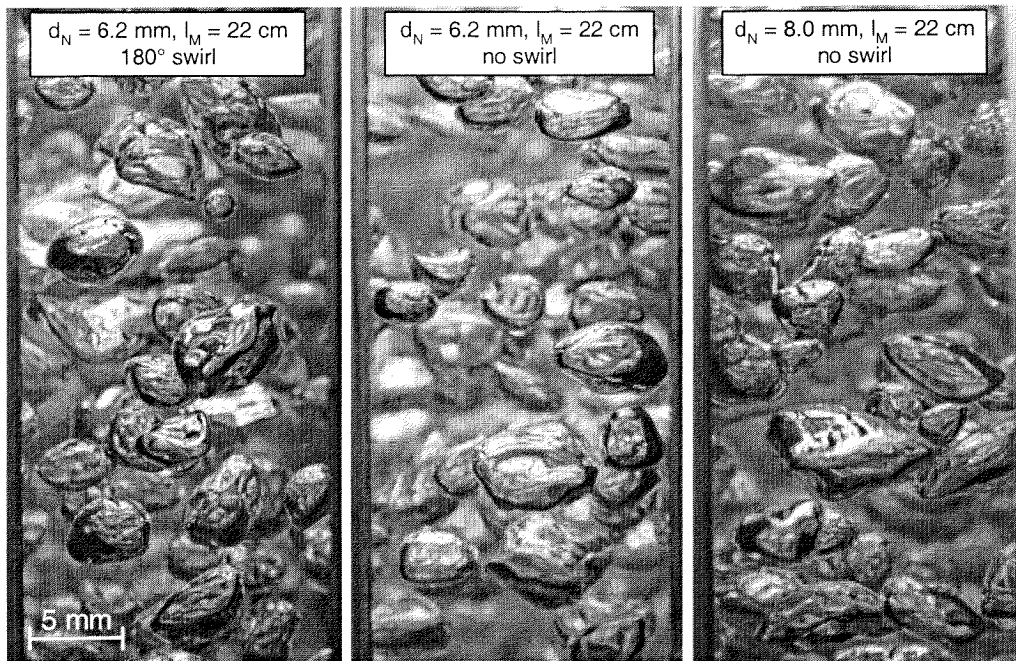


Fig. 5-15: Bubbles at different reaction mixer configurations ($e_S = 3.2 \text{ kW/m}^3$)

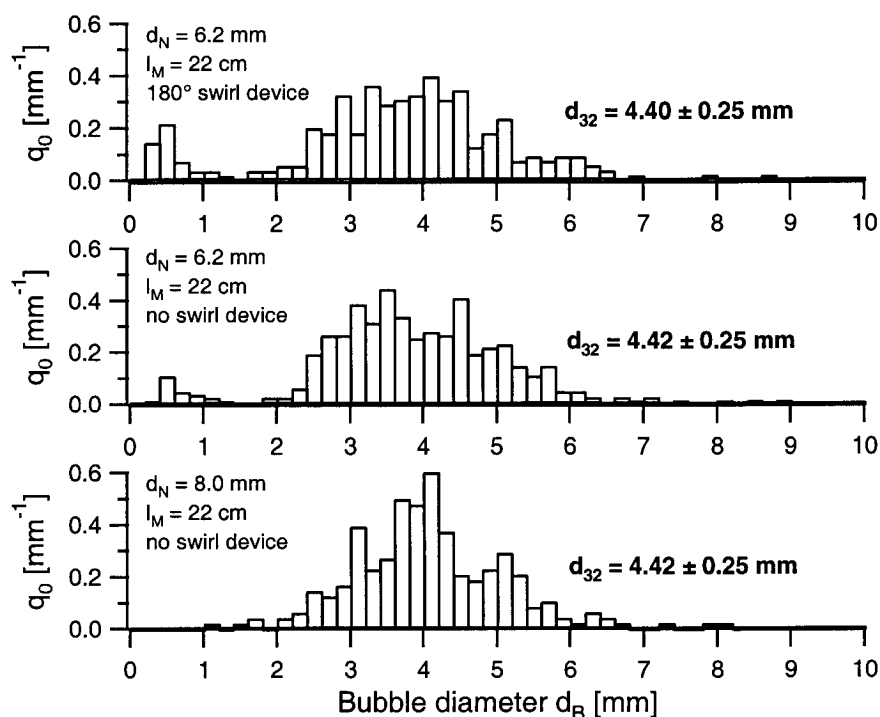


Fig. 5-16: Bubble size distributions at different reaction mixer configurations ($e_S = 3.2 \text{ kW/m}^3$).

A summary of the measured *Sauter* mean diameters is given in Table 5-1. In some cases the measured values of d_{32} even increased a little with increasing power inputs, which is very unlikely. Therefore, it was reckoned with an experimental error of at least approx. $\pm 0.25 \text{ mm}$ ($\approx 5\%$).

With these results it is apparent that in water and within the range of the varied parameters the mean bubble size can be regarded as approximately independent of the reaction mixer configuration and the power input.

$e_S \text{ [kW/m}^3\text{]}$	1.1	2.3	3.2
$d_N = 8.0 \text{ mm}, l_M = 22 \text{ cm}, \text{ no swirl}$	4.50 mm ($1 \pm 5\%$)	4.42 mm ($1 \pm 5\%$)	4.42 mm ($1 \pm 5\%$)
$d_N = 6.2 \text{ mm}, l_M = 22 \text{ cm}, \text{ no swirl}$	4.26 mm ($1 \pm 5\%$)	4.12 mm ($1 \pm 5\%$)	4.42 mm ($1 \pm 5\%$)
$d_N = 6.2 \text{ mm}, l_M = 22 \text{ cm}, 180^\circ \text{ swirl}$	4.46 mm ($1 \pm 5\%$)	4.68 mm ($1 \pm 5\%$)	4.40 mm ($1 \pm 5\%$)

Table 5-1: *Sauter* mean bubble diameters at different operating conditions

The fact that no significant differences regarding the mean bubble size were observed might be surprising, but one has to bear in mind that the power input was not varied within a very broad range and that the experimental error was estimated to be at least $\approx 5\%$.

Naturally a change of the mean bubble diameter would have been observed if the power input had been varied in a wider range as a consequence of the increase of shear rate and turbulence (see e.g. Bouaifi and Roustan, 1998). However, within the operating conditions used for this work the change of the bubble size was negligible and could not be made responsible for the significant differences regarding the mass transfer of the investigated reaction mixer configurations.

Furthermore, these findings are in good agreement with other published data. Pawelczyk and Pindur (1999) measured the local bubble size distributions in a jet reactor (air/water). They found that the local *Sauter* diameter was rather constant throughout the reactor and that the effect of the gas- and liquid-flow rate was not significant. Dutta and Raghavan (1987) observed nearly uniform bubble sizes in the reaction vessel of a downflow operated loop-reactor with a straight throat ejector very similar to the ABLR's reaction mixer. Also Havelka et al. (1997) reported axially and radially uniform bubble size distributions in an upflow ejector loop reactor. Bin (1993) has extensively reviewed a large number of studies carried out on plunging liquid jet systems. For the air/water system he found that the secondary bubbles were formed very quickly and had diameters of about 4 mm, practically independent of the jet velocity and the nozzle diameter.

Barigou and Greaves (1992) measured the local bubble size distributions in a stirred tank reactor with the air/water system. At gas holdups $> 5.0\%$ they found that the vast majority of the measured mean *Sauter* bubble diameters differed less than 10% from one another, independent of the applied stirring speeds and the location of the measurement.

5.3.3 Combination of the present results

In Section 5.3.1 it was shown that the reaction mixer geometry has a significant impact on the volumetric mass transfer coefficient $k_L a$ and the total gas holdup ϵ_{tot} . The knowledge regarding the reasons for the observed differences can be deepened

by combining these results with the findings made in Section 5.3.2 regarding the mean bubble size.

Since as well the total gas holdup as the *Sauter* mean bubble diameter are known, the specific surface area a in the reactor can be calculated with Eq. 2-16. Because d_{32} was found to be approximately constant, the specific surface area will be influenced by the reaction mixer geometry exactly the same way as the total gas holdup.

By plotting the measured $k_L a$ values versus the calculated specific surface area it can be determined whether only a is influenced by the reaction mixer configuration. The result is shown in Fig. 5-17. For a clearer illustration of the differences only the values of reaction mixer configurations with no swirl and the 270° swirl are depicted.

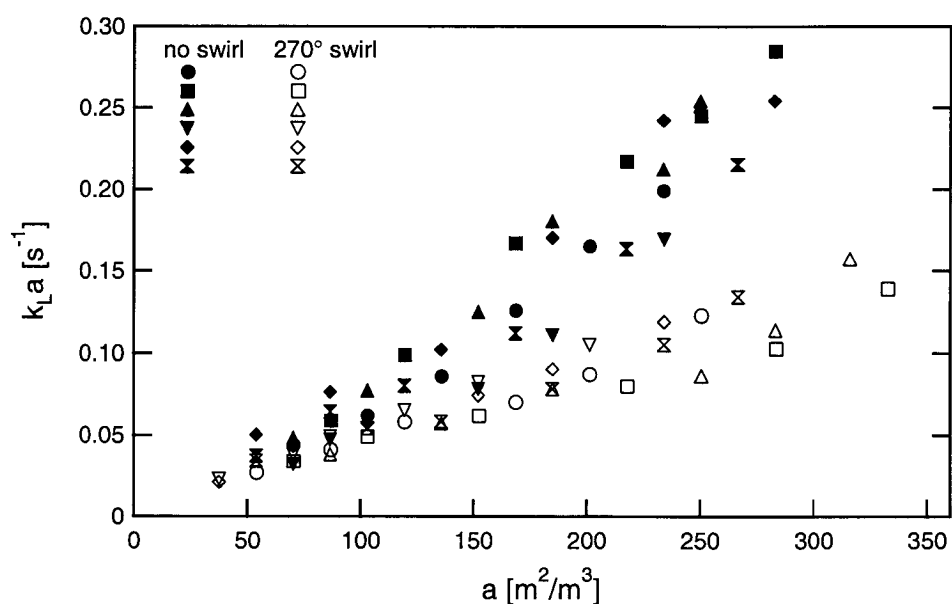


Fig. 5-17: $k_L a$ vs. a for all reaction mixer configurations without swirl and with the 270° swirl

The following conclusions can be drawn: Not only the specific surface area a but also the liquid sided mass transfer coefficient k_L is affected by the reaction mixer configuration. It is also evident that the nozzle diameter and the mixing tube length have an influence mainly on the specific surface area, while the swirl device has its main influence on k_L .

It should be noted that the points in Fig. 5-17 were obtained at different specific power inputs. To get an impression regarding its absolute value and its depen-

dence on the specific power input k_L is plotted versus the specific power input in Fig. 5-18. Again, due to illustration purposes, this was only done for the 'no swirl' and the '270° swirl' option. The values of the 90° and the 180° swirl device lay between these two extreme cases.

As before the higher k_L values are evident, if no swirl device is used. Also with no swirl device k_L appears to increase with increasing specific power input, while with the 270° swirl device it stays rather constant. Furthermore, the data of the 270° swirl device is much less scattered than that with no swirl device. Without any swirl device the nozzle diameter and the mixing tube length also seem to have some influence on k_L . However, no clear trends referring to this can be found. It should be pointed out that these findings should only be regarded as estimations because the calculation of k_L is subject to a rather large error of approximately 30%.

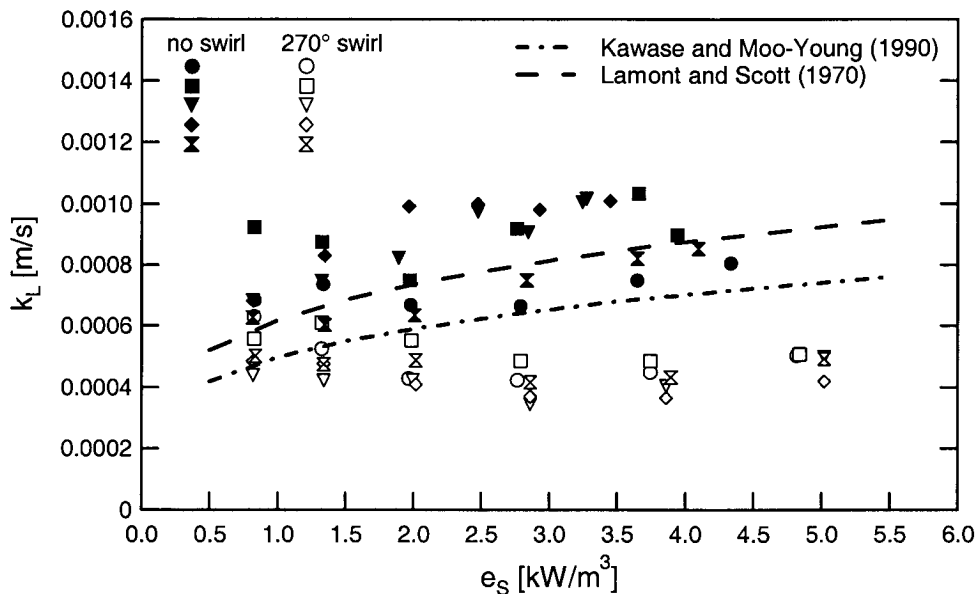


Fig. 5-18: k_L as a function of the specific power input and the swirl device torsion

In order to test the correctness of the order of magnitude of the obtained k_L values they were compared to established correlations based on Kolmogoroff's theory of isotropic turbulence.

Lamont and Scott (1970) proposed the following correlation:

$$k_L = 0.40 \cdot \left(e_s \frac{v}{\rho_L} \right)^{0.25} \cdot Sc^{-0.5} \quad (5-11)$$

A very similar correlation was published by Kawase and Moo-Young (1990):

$$k_L = 0.301 \cdot \left(e_s \frac{v}{\rho_L} \right)^{0.25} \cdot Sc^{-0.5} \quad (5-12)$$

Of the two introduced correlations the one by Lamont and Scott (1970) is in better agreement with the data obtained without any swirl device¹. The corresponding graphs are also illustrated in Fig. 5-18.

The differences regarding k_L can be explained the following way. If no swirl device is used, apparently a large part of the power put into the reactor at the jet nozzle dissipates in the liquid phase of the reaction vessel. If a swirl device is used, a certain part of this power input is lost due to a decrease of the vertical jet momentum, which results in a reduced mixing intensity in the liquid bulk and, therefore, in lower k_L values. Furthermore, due to the tangential velocity component, the dispersion jet spreads faster and the momentum of the jet is distributed over a greater cross sectional area.

1. Bouaifi and Roustan (1998) calculated k_L for a stirred tank reactor and also found the correlation of Lamont and Scott to fit their data better than the one of Kawase and Moo-Young (1990).

5.4 Derivation of an empirical model

The objective of this section is the derivation of a model which describes quantitatively the effect of the varied parameters on the volumetric mass transfer coefficient of the ABLR. Since the occurring processes are too complex to be described by a purely mechanistic model, an empirical model will be derived. This will be done on the basis of the dimensional analysis.

5.4.1 Dimensional analysis

The dimensional analysis is based on the theory of similarity which states that physical laws have to be independent of the used units and that they can be written in a dimensionless form. The Π -theorem forms the basis for the discussion of physical relationships in terms of the theory of similarity. It reads:

Every physical relationship between n physical quantities can be reduced to a relationship between $m = n-r$ mutually independent dimensionless groups, whereby r stands for the rank of the dimensional matrix, made up of the physical quantities in question and generally equal to the number of the basic quantities contained in them. (Zlokarnik, 1991)

One of the advantages of dimensional analysis is that the amount of the dimensionless numbers is smaller than the amount of the quantities contained in them. Nevertheless, the problem is still described equally comprehensively. Furthermore, the dimensional analysis also enables a reliable scale-up of a desired process condition and a deeper understanding of the physical processes occurring in a system.

5.4.1.1 Listing of all relevant variables

First, all parameters necessary to describe the problem have to be listed. This so-called 'relevance list' of the problem consists of the quantity in question (= target quantity) and of all parameters which have a relevant influence on it. The target quantity is the only dependent variable. All influencing parameters must be prima-

rily independent of one another. The target quantity of the sought model is the volumetric mass transfer coefficient $k_L a$. For the overall view the parameters influencing it will be subdivided into geometric, physical and process-related ones.

Geometric parameters: There is not point in overloading the relevance list by listing all geometric parameters. The relevance list is valid only for the specific geometrical configuration of the used experimental setup (form of the vessel, diameter of the liquid recirculation pipe etc.). Therefore only the relevant reaction mixer parameters d_N , d_M , l_M and the swirl body number Sw_b are listed.

Physical parameters: Into this category belong the gas density ρ_G , the liquid density ρ_L , the surface tension σ , the kinematic viscosity of the liquid phase ν_L , the diffusion coefficient D of the absorbing gas component in the liquid phase and an indefinite number of physical properties S_i which describe the coalescence behaviour of the material system. According to Zlokarnik (1991) the viscosity of the gas phase has no relevance with common gas-liquid contacting processes.

Process-related parameters: Due to the results obtained in Section 5.1 and Section 5.2 it is possible to replace the liquid recirculation rate Q_L , the dynamic pressure difference before the nozzle Δp_N and the liquid batch volume V_L by one single intermediate quantity, the specific power input e_S . The gravitational acceleration g is also decidedly relevant since large density differences occur¹.

It should be noted that the gas entrainment rate Q_G or the gas holdups ϵ_{tot} and ϵ_R must not be included into the above relevance list since they are directly influenced by the above parameters and cannot be adjusted independently.

The relevance list for the gas-liquid contacting described in this chapter contains 13 parameters.

$$\{k_L a; d_N, d_M, l_M, Sw_b; \rho_L, \rho_G, \nu_L, \sigma, D, S_i; e_S, g\} \quad (5-13)$$

1. Actually $g\Delta\rho$ with $\Delta\rho = \rho_L - \rho_G$ should be used here, but the corresponding dimensionless number would contain $g\Delta\rho/\rho_L \approx g\rho_L/\rho_L = g$.

5.4.1.2 Determination of the dimensionless numbers

The dimensionless numbers can be generated with the help of the dimensional matrix (Zlokarnik, 1991). All physical quantities are expressed by their basic units (here mass [kg], length [m] and time [s]) and their exponents are listed in the dimensional matrix. The rank of the dimensional matrix for the above relevance list is 3, i.e. the problem can be described by $13-3=10$ dimensionless numbers. The used dimensional matrix is shown in Table 5-2.

		ρ_L	v_L	g	$k_L a$	e_S	σ	d_N
mass	M	1	0	0	0	1	1	0
length	L	-3	2	1	0	0	-1	1
time	T	0	-1	-2	-1	-2	-3	0

core matrix
residual matrix

Table 5-2: Setting-up of the dimensional matrix

The dimensional matrix is composed of a core and a residual matrix. The residual matrix contains those elements of the relevance list which are later to occur individually in the numerators of the dimensionless numbers, where the core matrix is formed of quantities which are later permitted to occur in all the dimensionless numbers.

Parameters which are already dimensionless (Sw_b) or which result in obvious numbers such as ρ_G/ρ_L or v_L/D are not included in the dimensional matrix. S_i are physical properties of unknown dimension and number. However, this is no problem since, with the known relevant physical properties ρ_L , v_L , σ , one will always be able to transform S_i to the dimensionless numbers S_i^* (Zlokarnik, 1991). Since d_N , d_M and l_M all have the same dimension only one of these parameters has to be included in the matrix.

Now the core matrix is transformed into a unity matrix by the application of the Gaussian algorithm (zero-free main diagonal, only zeroes below) and further linear transformations. The result is shown in Table 5-3.

		ρ_L	v_L	g	$k_L a$	e_S	σ	d_N
mass	M	1	0	0	0	1	1	0
length	L	0	1	0	-1/3	1/3	4/3	2/3
time	T	0	0	1	2/3	4/3	1/3	-1/3

unity matrix
residual matrix

Table 5-3: Transformation of the core matrix into a unity matrix

The dimensionless numbers can now be derived according to the following rule: Each physical quantity in the residual matrix occurs in the numerator of a fraction whose denominator is formed from the physical quantities in the unit matrix. The residual matrix determines the exponents on the properties occurring in the denominator.

$$\Pi_1 = k_L a \cdot \left(\frac{v_L}{g}\right)^{1/3} \equiv k_L a^* \quad (5-14)$$

$$\Pi_2 = \frac{e_S}{\rho_L (v_L g^4)^{1/3}} \equiv e_S^* \quad (5-15)$$

$$\Pi_3 = \frac{\sigma}{\rho_L (v_L^4 g)^{1/3}} \equiv Mo^{1/3} \quad (5-16)$$

$$\Pi_4 = d_N \cdot \left(\frac{g}{v_L}\right)^{1/3} \quad (5-17)$$

$$\Pi_5 = d_M \cdot \left(\frac{g}{v_L}\right)^{1/3} \quad (5-18)$$

$$\Pi_6 = l_M \cdot \left(\frac{g}{v_L}\right)^{1/3} \quad (5-19)$$

$$\Pi_7 = \frac{v_L}{D} \equiv Sc \quad (5-20)$$

$$\Pi_8 = Sw_b \quad (5-21)$$

$$\Pi_9 = Si^* \quad (5-22)$$

$$\Pi_{10} = \frac{\rho_G}{\rho_L} \quad (5-23)$$

It can be seen that with the Morton number $Mo (= \Pi_3^3)$ and the Schmidt number $Sc (= \Pi_7)$ two classic dimensionless numbers for the characterization of the physical properties with gas-liquid systems were derived. The numbers Π_4 and Π_6 contain as well geometric as physical quantities. Therefore, in order to make these numbers

more meaningful, they are reshaped into forms which contain geometric parameters only.

$$\frac{\Pi_4}{\Pi_5} = \Pi'_4 = \frac{d_N}{d_M} \quad ; \quad \frac{\Pi_6}{\Pi_5} = \Pi'_6 = \frac{l_M}{d_M} \quad (5-24)$$

For the description of volumetric mass transfer coefficient $k_L a$ in the ABLR the compiled set of dimensionless numbers produces the relationship:

$$f\left(k_L a^*, e_S^*, Mo, Sc, \frac{\rho_G}{\rho_L}, Sw_b, \Pi_5, \frac{d_N}{d_M}, \frac{l_M}{d_M}, S_i^*\right) = 0 \quad (5-25)$$

However, all measurements discussed in this chapter were obtained with the air/water system, i.e. all physical properties were kept constant. Also the mixing tube diameter d_M was not varied. Therefore, the dimensionless numbers Mo , Sc , ρ_G/ρ_L , S_i^* and Π_5 can be excluded from Eq. 5-25 since they are all constant. The reduced set of the dimensionless numbers produces the relationship:

$$f\left(k_L a^*, e_S^*, Sw_b, \frac{d_N}{d_M}, \frac{l_M}{d_M}\right) = 0 \quad (5-26)$$

The relationship given in Eq. 5-26 is the maximum that can be derived with the dimensional analysis. The dimensional analysis cannot provide any information regarding the form of the function f . This information can only be derived from experimental results.

5.4.2 Regression analysis

The objective of this section is the derivation of a relationship which describes adequately the connection between the target quantity $k_L a^*$ and its influencing parameters, i.e. the function f in Eq. 5-26 has to be found.

5.4.2.1 Power law approach

For a first approach the regression will be carried out on the basis of a power law function of the following form:

$$Y = f_0 \prod_i X_i^{f_i} \quad (5-27)$$

Y stands for the dimensionless target quantity, X_i for the dimensionless influencing parameters. By means of the exponent f_i it can be easily recognized how strongly the corresponding influencing parameter X_i affects the target quantity. However, the above approach causes problems, if at least one X_i can take the value Zero without resulting also in $Y=0$. This is exactly the case with the swirl body number Sw_b . To avoid this problem not Sw_b but the term $\exp(Sw_b)$ was used with the above equation.

The actual calculation of the model parameters f_0 and f_i was carried out by taking the logarithm of Eq. 5-27. This way a robust linear regression could be applied.

$$\log Y = \log f_0 + \sum_i f_i \log X_i \quad (5-28)$$

The result of the regression ($R^2 = 0.90$) is shown in Eq. 5-29.

$$k_L a^* = 1.14 \times 10^{-4} \cdot (e_S^*)^{0.91} \cdot e^{-2.40 \cdot Sw_b} \cdot \left(\frac{d_N}{d_M}\right)^{0.89} \cdot \left(\frac{l_M}{d_M}\right)^{-0.29} \quad (5-29)$$

A comparison between the derived correlation and the experimental results is shown in Fig. 5-19. For $k_L a^* > 2.5 \times 10^{-4}$ rather large deviations can be observed. Especially the $k_L a$ values obtained with the 22 cm long mixing tube are generally underestimated by Eq. 5-29.

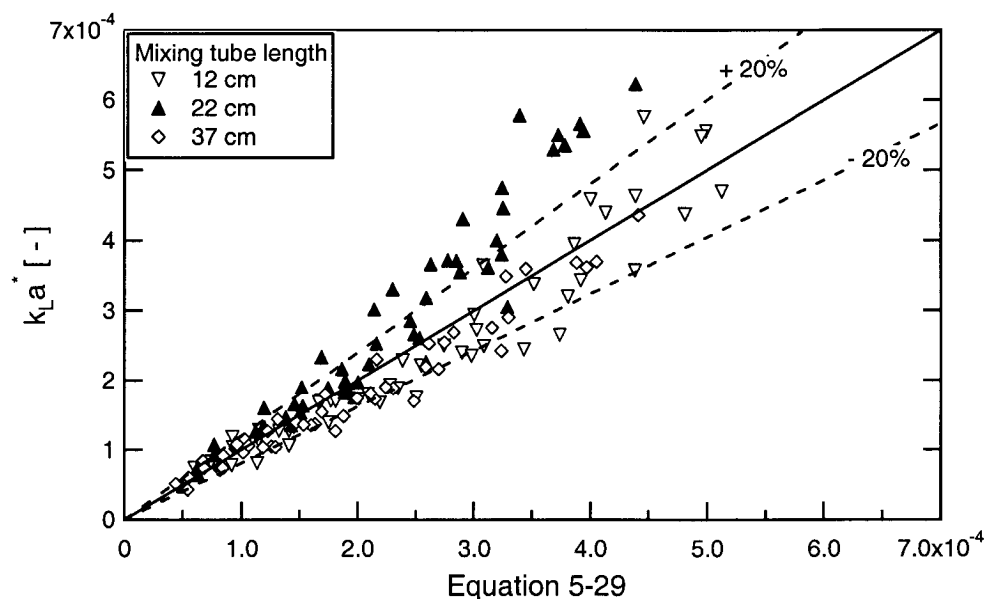


Fig. 5-19: Comparison between Eq. 5-29 and the experimental results

It is evident that the proposed model has to be further refined in order to improve its quality. This will be done in the next section.

5.4.2.2 Derivation of a refined model

The reason for the rather large deviations between the correlation and the measured data can be explained by comparing the influence of the mixing tube length in Eq. 5-29 with the experimental results shown in Fig. 5-9. It is apparent that a power law approach is not very suited to describe the influence of l_M . With Eq. 5-29 an increase of the mixing tube length always results in a decrease of $k_L a$ which is not true for the measured values.

Based on the experimental results in Fig. 5-9 it was decided that a polynomic approach would describe the influence of the mixing tube (at otherwise constant conditions) more precisely:

$$k_L a^* \Big|_{\text{const.}} = g\left(\frac{l_M}{d_M}\right) = g_0 + g_1\left(\frac{l_M}{d_M}\right) + g_2\left(\frac{l_M}{d_M}\right)^2 \quad (5-30)$$

Instead of the ratio l_M/d_M the function g was used with Eq. 5-28 and the regression was carried out again. The following model equation was obtained ($R^2 = 0.94$):

$$k_L a^* = 5.7 \times 10^{-5} \cdot (e_S^*)^{0.93} \cdot e^{-2.57 \cdot S_{w_b}} \cdot \left(\frac{d_N}{d_M}\right)^{1.01} \cdot \left(g\left(\frac{l_M}{d_M}\right)\right)^{0.82} \quad (5-31)$$

$$\text{with } g\left(\frac{l_M}{d_M}\right) = 0.58 + 0.064\left(\frac{l_M}{d_M}\right) - 0.002\left(\frac{l_M}{d_M}\right)^2$$

A comparison between the derived model equation and the experimental values is shown in Fig. 5-20. The correlation describes the measurements sufficiently well. The systematic deviations regarding the influence of the mixing tube length could be eliminated.

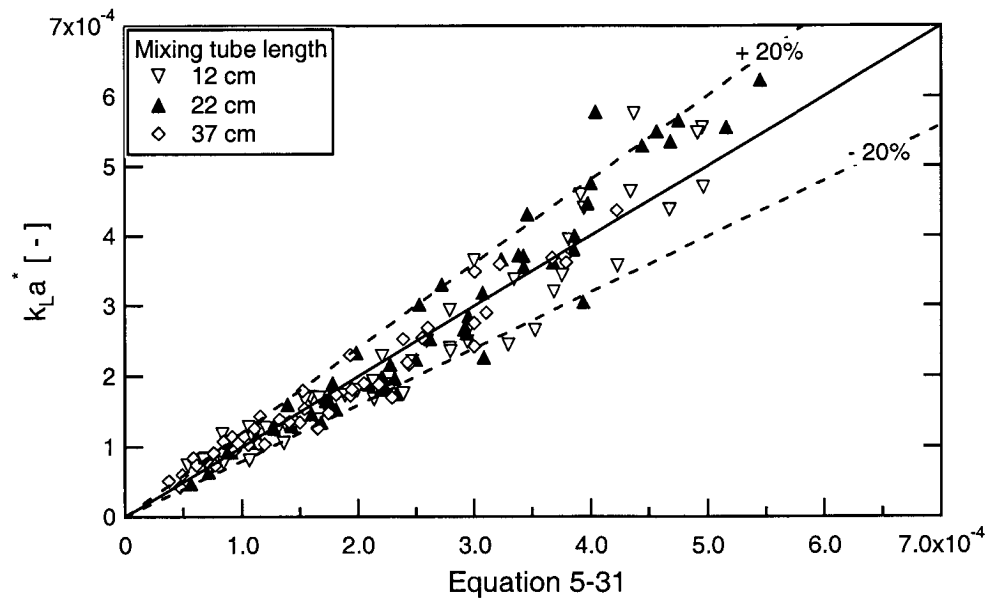


Fig. 5-20: Comparison between Eq. 5-31 and the experimental results

It should be noted that the proposed model is valid only inside the experimentally varied parameter range. This applies particularly for the ratio between the nozzle and the mixing tube diameter. With $d_N/d_M \rightarrow 1$ a decrease of $k_L a$ has to be expected (see Section 5.3.1.1) and Eq. 5-31 would no longer describe the system properly.

5.5 Conclusions

In this chapter the influence of different process parameters on the mass transfer characteristics of the ABLR has been discussed for the air/water system.

By the variation of as well the power input as the liquid batch volume it was possible to prove that the volumetric mass transfer coefficient $k_L a$ is an approx. linear function of the specific power input (at otherwise constant conditions) and that the gas-liquid mixing can be described with the theory of isotropic turbulence. Furthermore, it was found that the contribution of the reaction mixer volume to the overall mass transfer rate can be neglected which is a significant difference compared to common ejector loop reactors.

It was also shown that the reaction mixer geometry has a significant influence on the mass transfer characteristics. An increase of the nozzle diameter d_N (or better the ratio d_N/d_M) leads to an increase of $k_L a$ due to an increase of the momentum of the dispersion jet charging from the mixing tube. Regarding the mixing tube length an optimum could be identified. If the mixing tube is too short, the mixing shock cannot be finished properly. If it is too long, increased friction forces and phase separation result in a decrease of $k_L a$. An increase of swirl device torsion leads to the decrease of $k_L a$ which can be mainly put down to a decrease of the liquid sided mass transfer coefficient k_L .

The optimum of the varied reaction mixer geometries was found to have the following dimensions: Nozzle diameter = 8.0 mm ($d_M/d_N = 1.5$), mixing tube length = 22 cm, no swirl device.

On the basis of the dimensional analysis an empirical model was derived for the quantitative description of the made observations.

6 Influence of the liquid properties (at ambient pressure)

This chapter will deal mainly with the influence of added electrolytes on the mass transfer characteristics of the ABLR. The performance of different reaction mixer geometries with a strongly coalescence hindered model system will be discussed and compared to the results obtained with the air/water system. At the end of this chapter the influence of the liquid viscosity on $k_L a$ will be illustrated briefly and a summary of the made conclusions will be given.

6.1 Influence of added electrolytes

In Section 1.3.3 it has already been mentioned that the addition of electrolytes to pure water leads to a strong hindrance of the bubble coalescence. This will generally lead to a significant decrease of the mean bubble size and, therefore, to an increase of the gas holdup and the volumetric mass transfer coefficient. The model electrolyte system used for this work was a 0.25 M Na_2SO_4 -solution. As with the air/water system the mass transfer characteristics of all 24 reaction mixer geometries were also measured with this system.

Again it should be noted that the volumetric mass transfer coefficients and the total gas holdups of all the 24 possible reaction mixer geometries were measured and that only some extracts of the measured data will be used for a more comprehensive illustration of the results. The complete set of data can be found in Appendix 4.

6.1.1 Influence on $k_L a$ and ε_{tot}

In Fig. 6-1 measurements of $k_L a$, valid for an exemplary reaction mixer configuration, are plotted versus the specific power input e_S . Also included are the corresponding values obtained with pure water and the experimental errors of both systems. Three conclusions can be immediately drawn from this figure:

- $k_L a$ is increased significantly by the addition of electrolytes (in this case by a factor of approx. 5-6).
- As with the air/water system $k_L a$ increases rather linearly with an increasing specific power input e_S .
- Due to the much larger experimental error (see Section 3.1.4.3) the data obtained with the electrolyte solution are much more scattered.

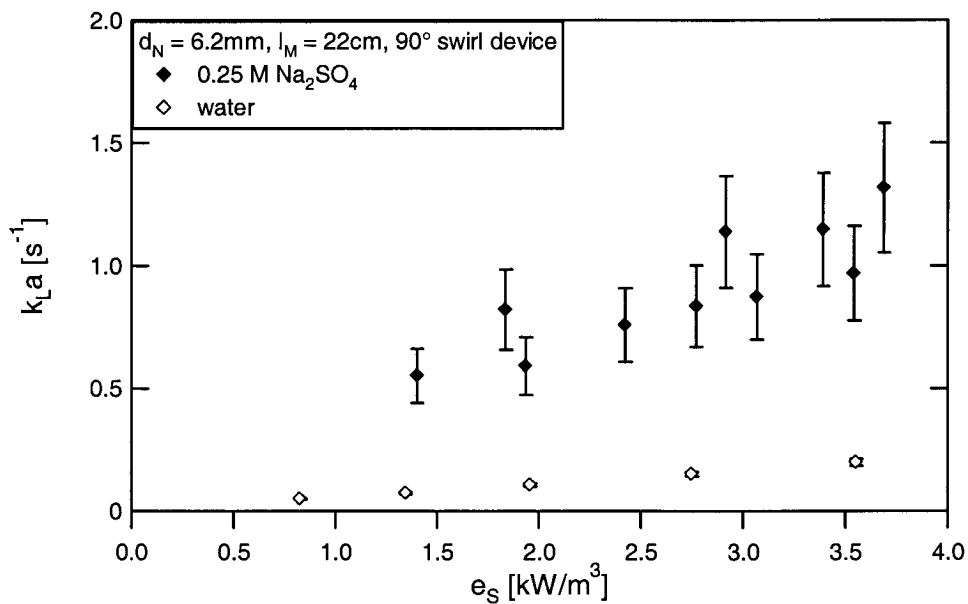


Fig. 6-1: $k_L a$ in a 0.25 M Na_2SO_4 -solution and water for a select reaction mixer geometry

The enhancement of $k_L a$ caused by the addition of the sodium sulfate compared to pure water can be described by the help of the so-called m-factor (Zlokarnik, 1979a). It is defined as follows

$$m \equiv \frac{(k_L a)_{\text{solution}}}{(k_L a)_{\text{pure water}}} \quad (6-1)$$

The enhancement factor m is a function of the reactor geometry, the type of electrolyte and its concentration. However, since the last two quantities were kept constant in this work, m is only a function of the reactor geometry.

The fact that m can have quite different values with different reactor geometries is illustrated in Fig. 6-2. Here the $k_L a$ values of three select reaction mixer configurations which performed very differently with the air/water system are compared. It is evident that m is not constant. With 'Conf. a' m ranges between 4-5, while with 'Conf. c' m is approx. twice as large.

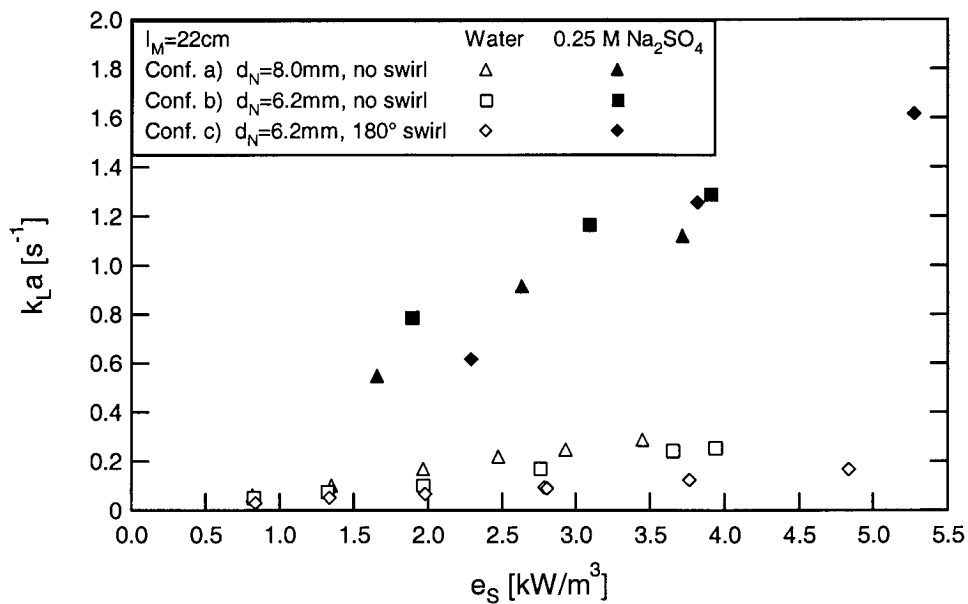


Fig. 6-2: $k_L a$ in water and in a 0.25 M Na_2SO_4 -solution with different reaction mixers

From the above plot a further conclusion can be drawn. With the 0.25 M Na_2SO_4 -solution the performance of the different reaction mixer configurations is quite similar. Eventual differences regarding $k_L a$ are well inside the experimental error range and, therefore, not significant. With coalescence hindered solutions $k_L a$ is apparently much less influenced by the reaction mixer configuration than it is the case with pure water.

This reduction of the influence of the reaction mixer geometry and the simultaneous increase of the experimental error result in the problem that many of the measured differences regarding $k_L a$ cannot be regarded as significant. Therefore, a detailed discussion regarding the influence of the separate reaction mixer compo-

nents, as it was done with the air/water system, is not possible. At best some trends can be identified.

In Fig. 6-3 the measured $k_L a$ values of all tested reaction mixer geometries are summarized. It can be seen that the relative difference between the best and the worst performing reaction mixer geometry is much smaller than it was the case with the air/water system. There are some exceptions but the trends that were identified with the air/water system apply also with the coalescence hindered solution. Reaction mixer configurations with the larger nozzle diameter, a mixing tube of medium length and without any swirl device tend to show the higher mass transfer rates. However, again it has be stressed that most differences are not significant due to the large experimental error.

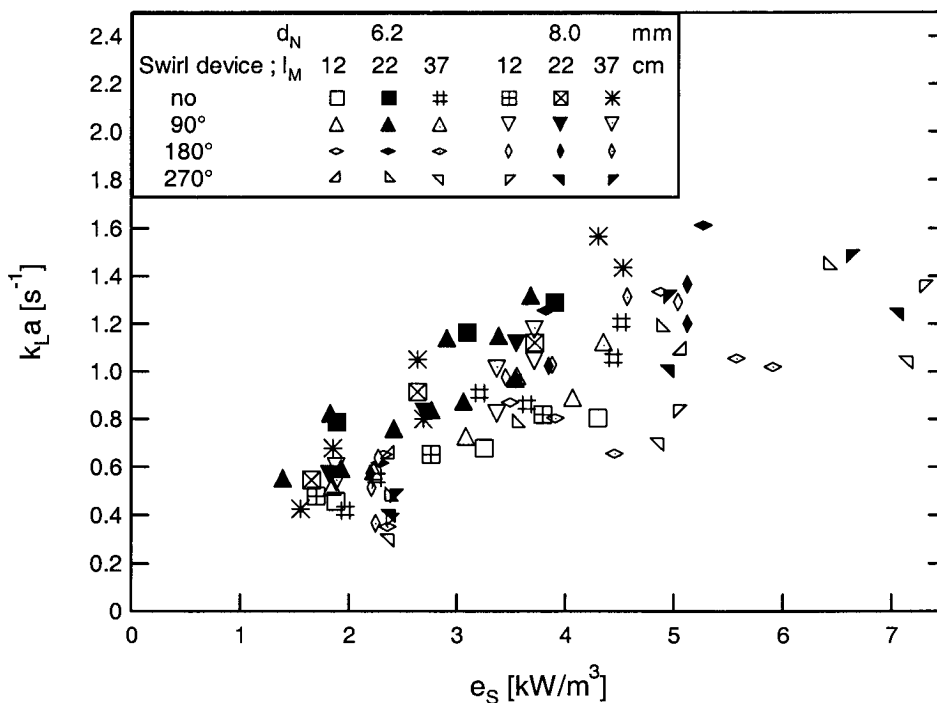


Fig. 6-3: Influence of the reaction mixer geometry on $k_L a$ (in a 0.25 M Na_2SO_4 -solution)

The measurement of the gas holdup ϵ_{tot} was also subject to an increased experimental error. The addition of the sodium sulfate caused the formation of a foam layer above the actual level of the aerated solution. It was often very difficult to determine the exact boundary between the foam and the actual dispersion. Therefore, it has to be reckoned with a much larger experimental error compared to the measurements with pure water.

Compared to pure water the gas holdup is nearly doubled by the electrolyte addition. This is shown for some select reaction mixer geometries in Fig. 6-4. As with k_L the relative differences regarding ϵ_{tot} are smaller than with pure water.

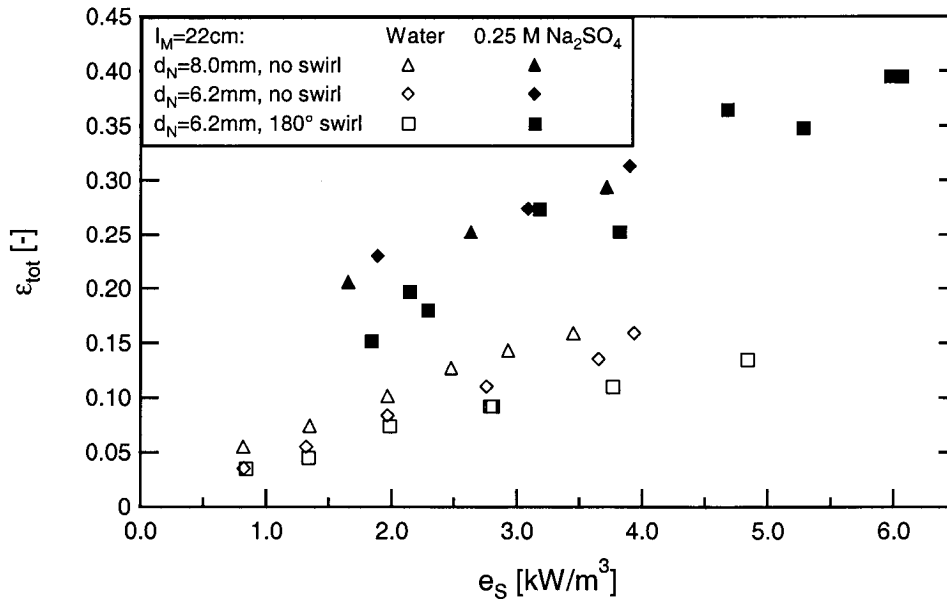


Fig. 6-4: ϵ_{tot} in water and in a 0.25 M Na_2SO_4 -solution with different reaction mixers

Regarding the influence of the reaction mixer configuration on ϵ_{tot} the same trends that were observed with k_L seem to apply. Again the reaction mixer configurations with the larger nozzle diameter, a mixing tube of medium length and without any swirl device tend to result in the higher values. But also here the quality of the data does not allow any clear conclusion.

6.1.2 Influence on the bubble size

The bubble sizes are much smaller with the coalescence hindered solution than with the air/water system. An example is shown in Fig. 6-5. On the left side the bubble size distribution valid for the air/water system is shown. On the right side the corresponding bubble size distribution with the sodium sulfate solution is depicted. It can be seen that the bubble size is reduced by a factor of approx. 10. In order to illustrate these observations two images of the above example are shown in Fig. 6-6.

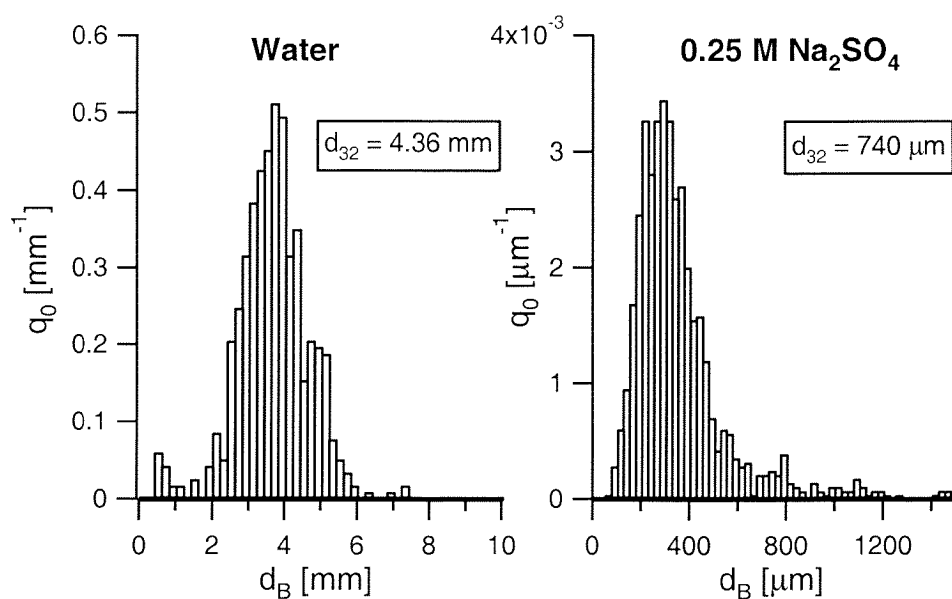


Fig. 6-5: Characteristic bubble size distributions in water and in the 0.25 M Na₂SO₄-solution ($d_N = 6.2$ mm, $l_M = 22$ cm, no swirl device; $e_S = 2.3$ kW/m³)

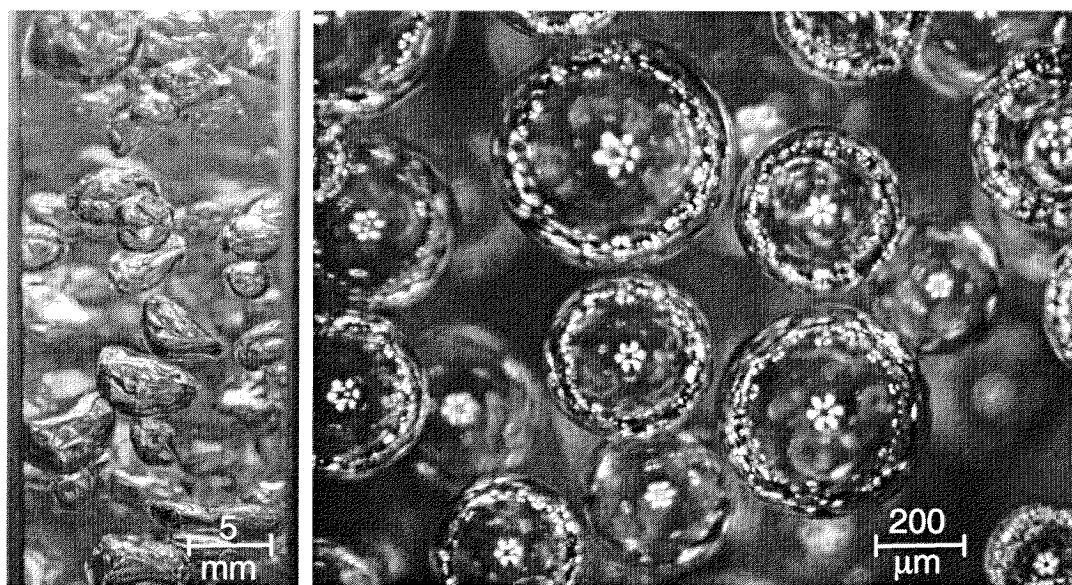


Fig. 6-6: Exemplary bubble images: left: water (image size: 32 x 16 mm)
right: 0.25 M Na₂SO₄ (image size: 1.76 x 1.32 mm)

In contrast to the air/water system, where the bubbles coalesced very quickly, it was possible with the electrolyte solution to distinguish zones of different bubble size distributions. This is illustrated in Fig. 6-8 for a select reaction mixer geometry. Two examples of the corresponding PVM-images are shown in Fig. 6-9.

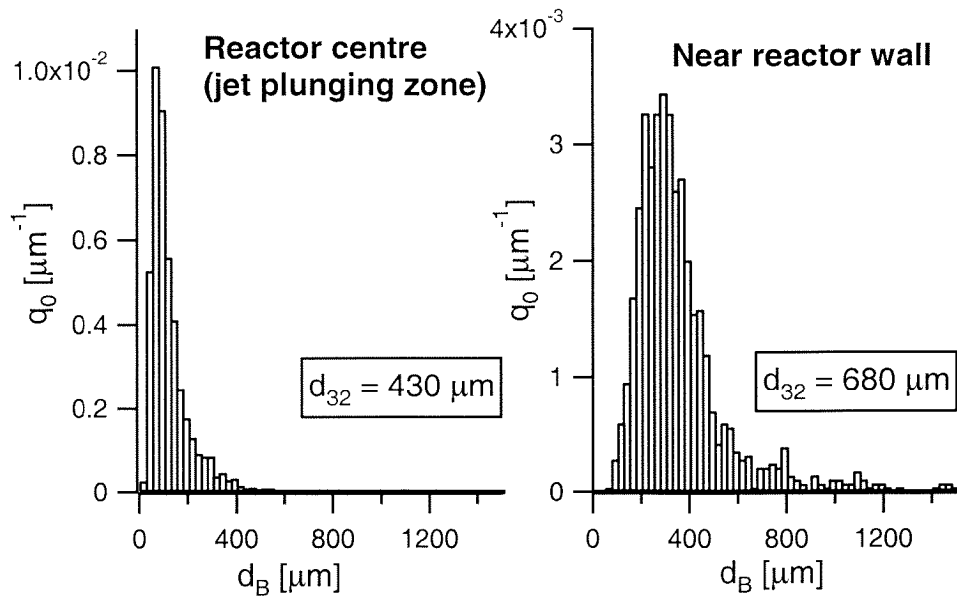


Fig. 6-8: Bubble size distributions in two different zones of the reaction vessel ($d_N = 8.0 \text{ mm}$, $l_M = 22 \text{ cm}$, no swirl device; $e_S = 3.6 \text{ kW/m}^3$)

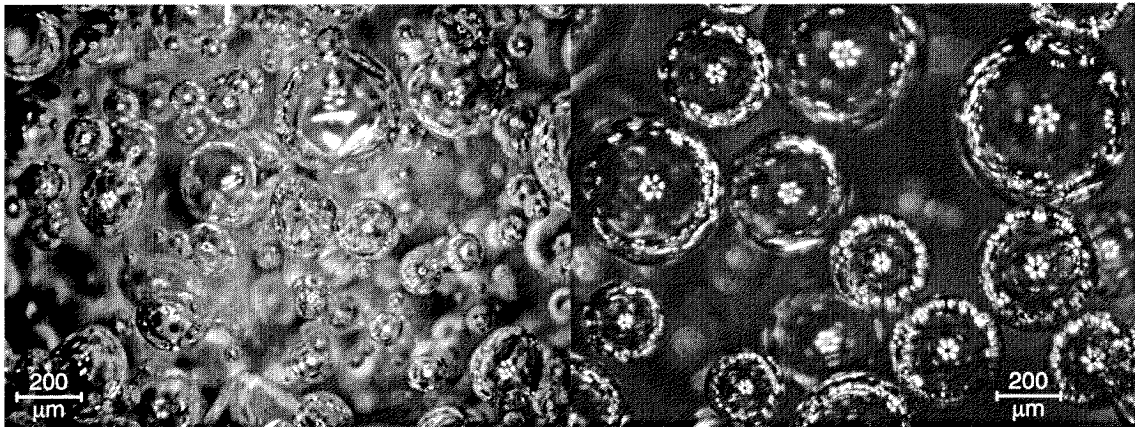


Fig. 6-9: Bubble swarms in the plunging zone (left) and near the reactor wall (right)

The bubble size distribution on the left side was obtained in the centre of the vessel approx. 15 cm below the plunging point of the dispersion jet. The majority of the bubbles has diameters well below 400 μm . These bubbles represent the primary bubbles which are formed in the mixing tube. The bubble size distribution on the right side was measured near the reactor wall where the turbulence is lower than in the centre. Here the average bubble diameter is approximately twice as high compared to the centre region. However, it should be pointed out that the volume of the

plunging jet zone is estimated to be much smaller (~ factor 10-20) than the remaining 'annular' volume, i.e. the main contribution to the mass transfer still comes from 'near-wall'-type bubbles. Therefore, distributions measured near the reactor wall were used to determine the overall Sauter bubble diameter. This way it is also guaranteed that later estimations of the specific surface area were conservative.

As with the air/water system no significant differences regarding the reaction mixer geometry were observed. This applies as well for the plunging jet zone as for the 'near-wall' zone.

On the basis of these observations it can be concluded that the tested reaction mixer geometries produce primary bubbles of rather equal size. The performance of gas-liquid reactors with coalescence hindered solutions is, according to Zlokarnik (1979a,b), determined by the size of these formed primary bubbles. Therefore, it is not very surprising that it was difficult to identify any significant differences regarding the performance of the tested reaction mixer geometries.

6.1.3 Additional remarks

A separate calculation of the specific surface area a and the liquid sided mass transfer coefficient k_L was renounced in this chapter due to the large experimental errors occurring with the coalescence hindered solution. Instead, an estimation of the order of magnitude of these quantities will be given. With an average *Sauter* bubble diameter of $\sim 700 \mu\text{m}$ and a gas holdup between 0.15-0.40 a specific surface area in the range of $\sim 1500\text{-}6000 \text{ m}^{-1}$ results. By comparing this estimation with the values given in Fig. 5-17 it can be concluded that the specific surface area is increased by a factor of ~ 20 compared to the air/water system. Since $k_L a$ is only increased by a factor of 5-10 it can be assumed that the liquid sided mass transfer coefficient is 2-4 times smaller than in pure water.

With the available data it was not possible to derive a sufficiently accurate design correlation for the description of $k_L a$ with the sodium sulfate solution. A model approach, similar to the one presented in the previous chapter, that took into consideration as well the influence of e_S^* as of all the three geometric parameters was not able to increase the accuracy compared to a model considering e_S^* only. This can be regarded as another indication of the rather large experimental error and the decrease of the relative differences due to equally sized primary bubbles.

6.2 Influence of the liquid viscosity

With one select reaction mixer geometry ($d_N = 6.2$ mm, $l_M = 22$ cm, 90° swirl device) the influence of the liquid viscosity on $k_L a$ was investigated. Glucose solutions of different concentrations were used as a model system with Newtonian behaviour (see also Section 4.1.2). The obtained results are illustrated in Fig. 6-10. As expected the volumetric mass transfer coefficient decreases with an increasing liquid viscosity. The increased viscosity also leads to a lessening of the relative differences regarding the influence of the specific power input. However, it is not clear whether this can be attributed to a physical phenomenon or to an increased experimental error, since the liquid phase cannot be regarded as perfectly mixed anymore.

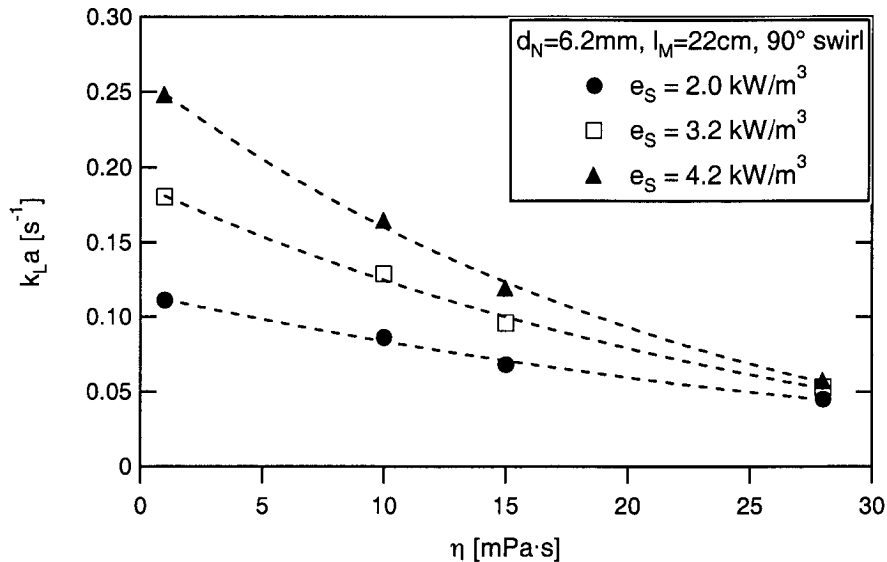


Fig. 6-10: Influence of the liquid viscosity on $k_L a$

The obtained results regarding the effect of the liquid viscosity on the mass transfer are in good agreement with the work of other authors. Terasaka and Hideki (1991) measured the mass transfer characteristics in a bubble column at different viscosities (1-109 mPas) using glycerol/water solutions. At 109 mPas they observed a decrease of $k_L a$ by a factor of approx. 10 compared to measurements valid with pure water. Sedelies et al. (1987) investigated the influence of the viscosity on the volumetric surface area a of several reactor types by using different non-Newtonian CMC-solutions. With a bubble column they observed a decrease by a factor of approx. 10 at 100 mPas. Stein and Schäfer (1984) report also a decrease by a factor of 10 in CMC solutions at 95 mPas.

6.3 Conclusions

In this chapter the influence of the liquid properties was discussed. The focus was set particularly on the influence of electrolytes added to the liquid phase which cause a hindrance of the bubble coalescence.

In these electrolyte solutions the average bubble size was by a factor of ~ 10 smaller than with pure water. This led to a strong increase of both $k_L a$ and the gas holdup. It was found that the relative differences regarding the performance of the tested reaction mixer geometries were much smaller than with water. Due to this fact and the higher experimental error it was not possible to identify any distinct trends regarding the reaction mixer influence or to derive a proper design correlation.

Measurements of the local bubble size distributions have shown that the size of the primary bubbles was not strongly influenced by the reaction mixer geometry, which explains the rather small relative differences regarding the $k_L a$ measurements. With all reaction mixer configurations the *Sauter* bubble diameter equaled $\sim 700 \mu\text{m}$ and the specific surface area a was estimated to range between 1500 and 6000 m^{-1} .

The influence of the liquid viscosity on $k_L a$ was also discussed briefly. As expected the mass transfer rate decreased with an increasing liquid viscosity. The measurements are in good agreement with the literature.

7 Results at elevated pressures

This chapter deals with the influence of the system pressure and the gas type on the mass transfer characteristics of the ABLR. These two quantities have an effect only on the physical properties of the gas phase, especially on the gas density. The liquid properties can be regarded as constant for the pressures and the gas types that were used in this work.

In the first part of this chapter the results that were obtained with the in Chapter 4 described experimental setup will be discussed. With these experiments the system pressure was varied between 1-10 bar. The second part describes additional measurements that were carried out with a full scale pilot plant at pressures between 10-80 bar. Finally the made conclusions will be summarized.

7.1 Measurements between 1-10 bar

First, the influence of the pressure and the gas type on the bubble size distribution will be described. Following, the same will be done for the volumetric mass transfer coefficient and the gas holdup. A comparison between the pressure step technique and the hydrazine feeding method will also be presented. At the end of this section it will be discussed how the in Chapter 5 proposed design correlation should be extended in order to incorporate effects of the gas properties.

The measurements were carried out with the same three reaction mixer configurations which have already been employed for the bubble size measurements at ambient pressure (see Chapter 5). Tap water was used for all the experiments.

7.1.1 Influence of the system pressure and the gas type on the bubble size distribution

The bubble size distributions were measured for the gases helium, nitrogen, argon and sulfurhexafluoride at select pressures between 1-10 bar.

It was found that neither the reaction mixer geometry nor e_S had any significant influence of the *Sauter* bubble diameter, if the pressure was kept constant and the same gas type was used. This confirms the observations which were made in Section 5.3.2.

The above findings are illustrated by means of two examples: Fig. 7-1 shows bubble size distributions valid for a select reaction mixer configuration with argon at 7 bar ($\rho_G = 11.2 \text{ kg/m}^3$) as a function of the specific power input e_S . Fig. 7-2 shows the bubble size distributions obtained with helium at 1 bar ($\rho_G = 0.16 \text{ kg/m}^3$) with the tested reaction mixer configurations.

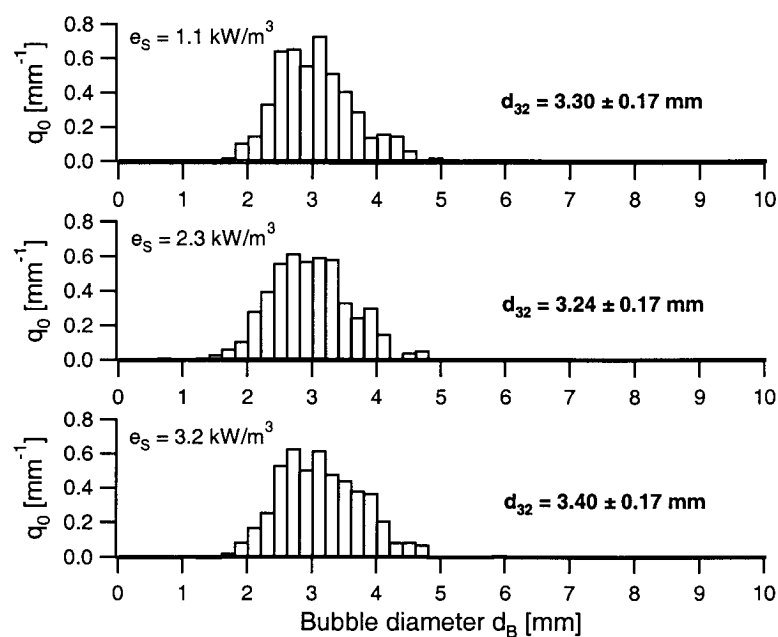


Fig. 7-1: Bubble size distributions at different specific power inputs (Argon, 7 bar, $\rho_G = 11.2 \text{ kg/m}^3$; $d_N=8.0\text{mm}$, $l_M=22 \text{ cm}$, no swirl)

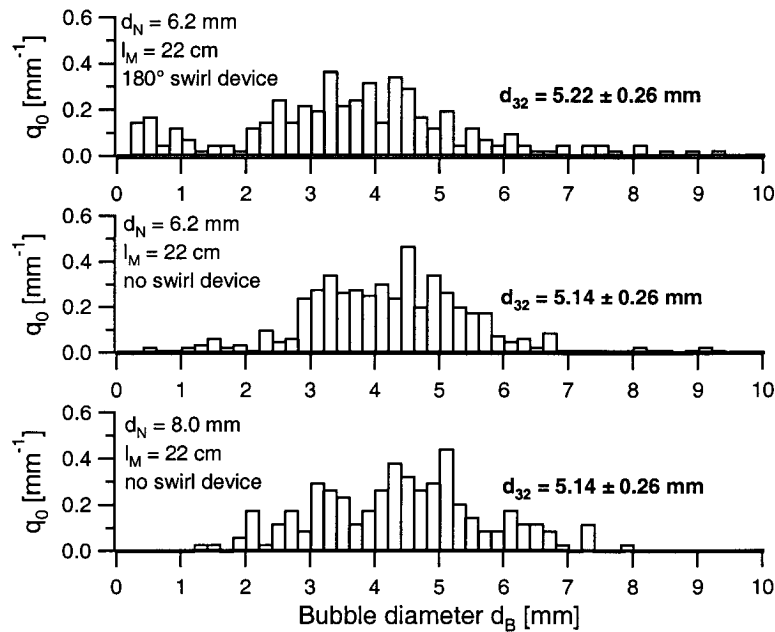


Fig. 7-2: Bubble size distributions at different reaction mixer configurations
(Helium, 1 bar, $\rho_G = 0.16 \text{ kg/m}^3$; $e_S = 2.3 \text{ kW/m}^3$)

On the other hand it was found that as well the system pressure as the gas type have a significant influence on the bubble size. With increasing pressure and molecular weight of the gas component the *Sauter* bubble diameter decreases and the bubble size distribution becomes more narrow. It will be shown later (see Fig. 7-5) that the observed differences can be attributed fully to the influence of the gas density. One example regarding the influence of the system pressure is shown in Fig. 7-3, another one regarding the influence of the gas type in Fig. 7-4.

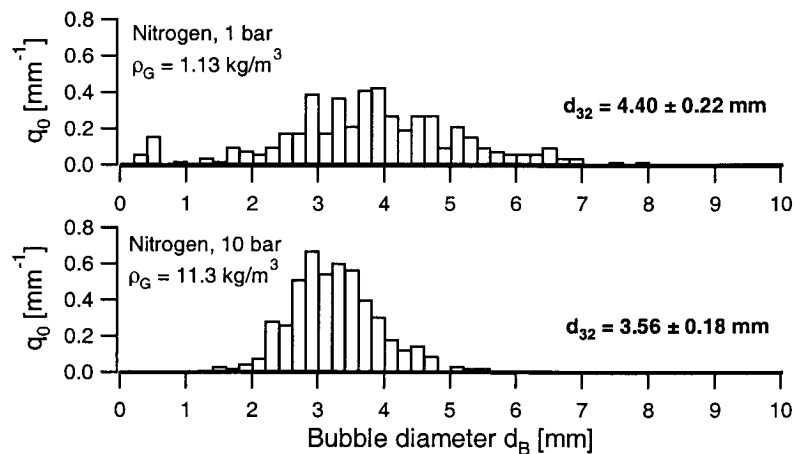


Fig. 7-3: Bubble size distributions with nitrogen at different pressures

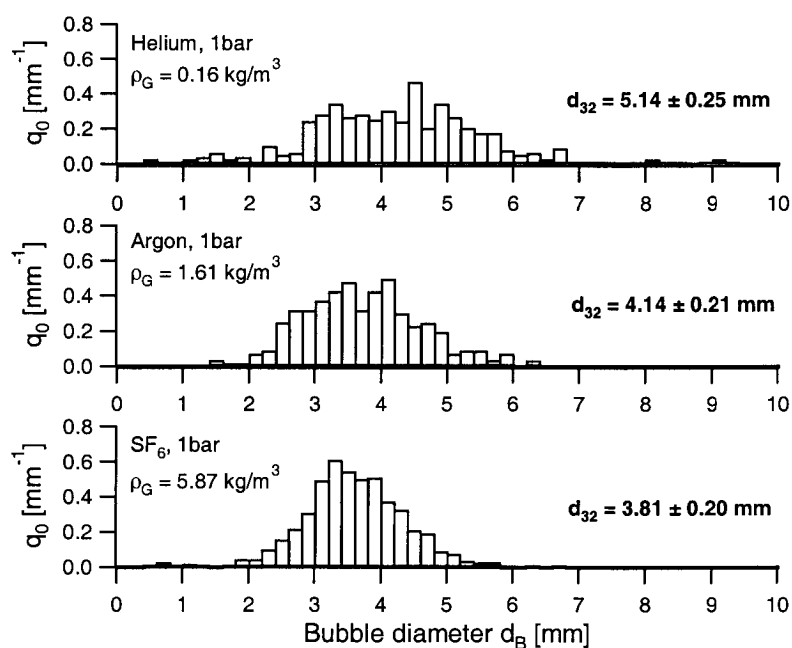


Fig. 7-4: Bubble size distributions with different gas types at 1 bar

A summary of the measured *Sauter* bubble diameters is given in Table 7-1. As with the measurements at ambient pressure it had to be reckoned with an experimental error of approximately 5%.

gas type	p [bar]	ρ_G [kg/m ³]	$d_{32} (1 \pm 5\%)$ [mm]		
			$d_N = 8.0$ mm, $l_M = 22$ cm, no swirl	$d_N = 6.2$ mm, $l_M = 22$ cm, no swirl	$d_N = 6.2$ mm, $l_M = 22$ cm, 180° swirl
He	1.0	0.16	5.14	5.14	5.22
He	7.0	1.12	4.81	4.54	4.77
N ₂	1.0	1.13	4.42	4.42	4.40
Ar	1.0	1.61	4.14	4.07	4.03
Ar	7.0	11.27	3.40	3.23	3.47
SF ₆	1.9	11.25	3.72	3.66	3.52

Table 7-1: d_{32} at different pressures, gas types and reaction mixer configurations ($e_S=2.3$ kW/m³)

In Fig. 7-5 the values of Table 7-1 are plotted versus the gas density. A strong correlation between the gas density and the *Sauter* bubble diameter can be identified. The *Sauter* bubble diameter decreases with increasing gas density, i.e. the influence of the system pressure and the gas type can be fully attributed to changes of the gas density. In other words: If different gas types of the same density are used, comparable bubble size distributions and *Sauter* diameters are obtained.

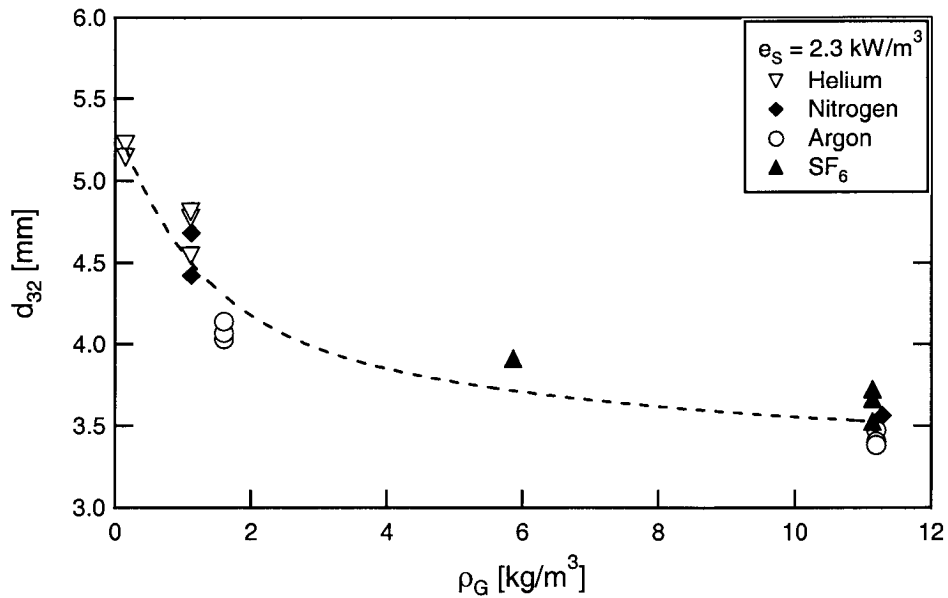


Fig. 7-5: d_{32} versus the gas density

The above findings will be illustrated by some exemplary bubble images. Fig. 7-6 shows some bubble images which were obtained with gases of different type and density. Significant differences regarding the bubble size can be easily recognized. Bubble images valid for gases of different type but equal density are shown in Fig. 7-7. Here the bubbles look alike.

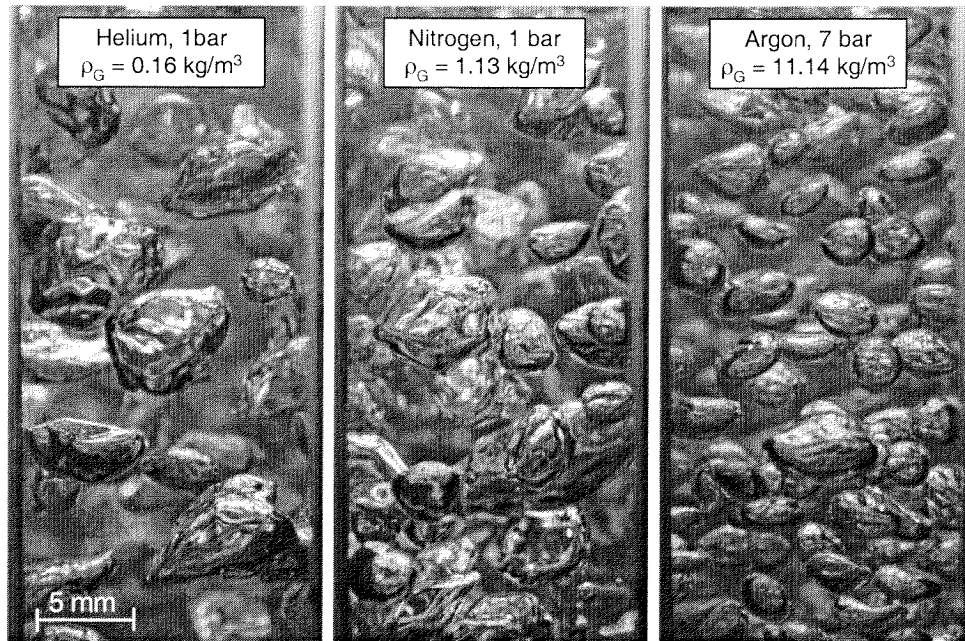


Fig. 7-6: Bubble images at gas different densities

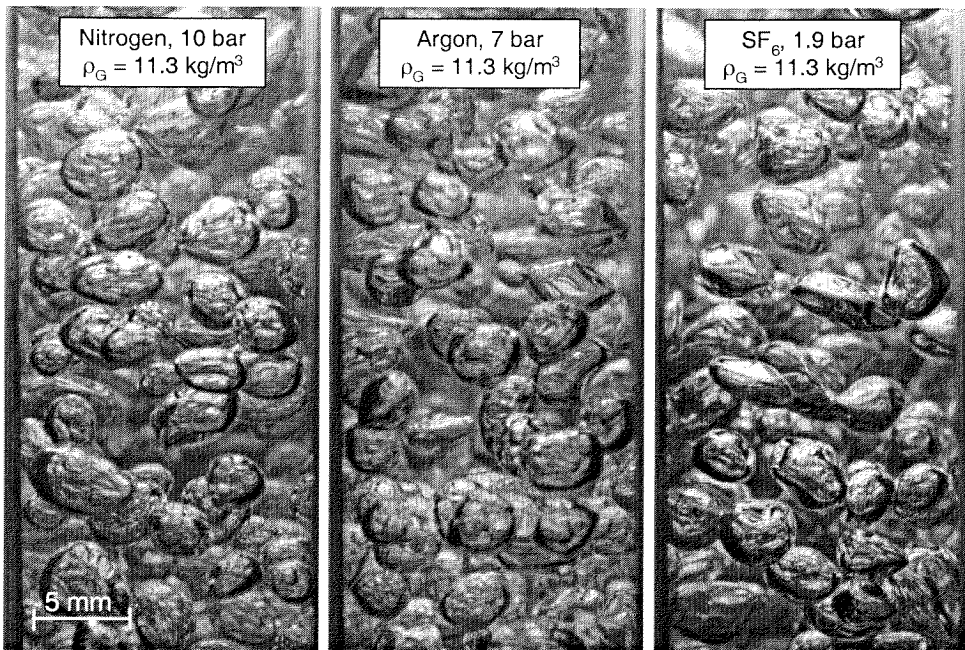


Fig. 7-7: Bubble images with different gas types but the same gas density

Based on the data in Table 7-1 an empirical correlation can be derived for the description of the gas density influence on the *Sauter* bubble diameter. This will again be done in a dimensionless form and the content of section 5.4.1 will serve as basis for the following steps.

The target quantity is d_{32} . The measurements have shown that the bubble diameter was not influenced significantly by the reaction mixer geometry or the specific power input (within the varied parameter range). Therefore, no parameters describing the reaction mixer geometry are included in the relevance list. It can also be assumed that the diffusion coefficient D has no relevance for the bubble formation. The resulting relevance list is given by

$$\{d_{32}, \rho_L, \rho_G, v_L, \sigma, S_i, g\} \quad (7-1)$$

and the corresponding dimensionless numbers can be determined with the dimensional matrix. Since the liquid properties can be regarded as constant for pressures between 1-10 bar the following relationship applies:

$$d_{32} \cdot \left(\frac{g}{v_L^2} \right)^{1/3} = f \left(\frac{\rho_G}{\rho_L} \right) \quad (7-2)$$

For the regression analysis a power law approach is used (see Eq.5-27). The following formula is obtained ($R^2 = 0.91$):

$$d_{32} \cdot \left(\frac{g}{v_L^2} \right)^{1/3} = 50.5 \cdot \left(\frac{\rho_G}{\rho_L} \right)^{-0.1} \quad (7-3)$$

In order to accentuate the influence of the pressure on d_{32} the above correlation can be rewritten by applying the ideal gas law¹:

$$d_{32} \cdot \left(\frac{g}{v_L^2} \right)^{1/3} = 50.5 \cdot \left(\frac{M_r}{RT\rho_L} \cdot p \right)^{-0.1} \quad (7-4)$$

Once more it should be pointed out that the derived model is valid only with tap water and inside the varied parameter range. Especially if the specific power input would be varied inside a broader range than done in this work, the correlation would have to be extended by an energy term.

1. Of course this should only be done, if the used gas phase can be described by this law.

7.1.2 Influence of the system pressure and the gas type on the gas holdup and $k_L a$

In the previous section it was found that the mean bubble size decreases with increasing gas density. It can be expected that this will also have an effect on the gas holdup and the volumetric mass transfer coefficient.

In Fig. 7-8 and Fig. 7-9 the mass transfer performances of two select reaction mixer configurations are shown in dependence of the gas density and the specific power input. It is evident that $k_L a$ is increased slightly with increasing gas densities.

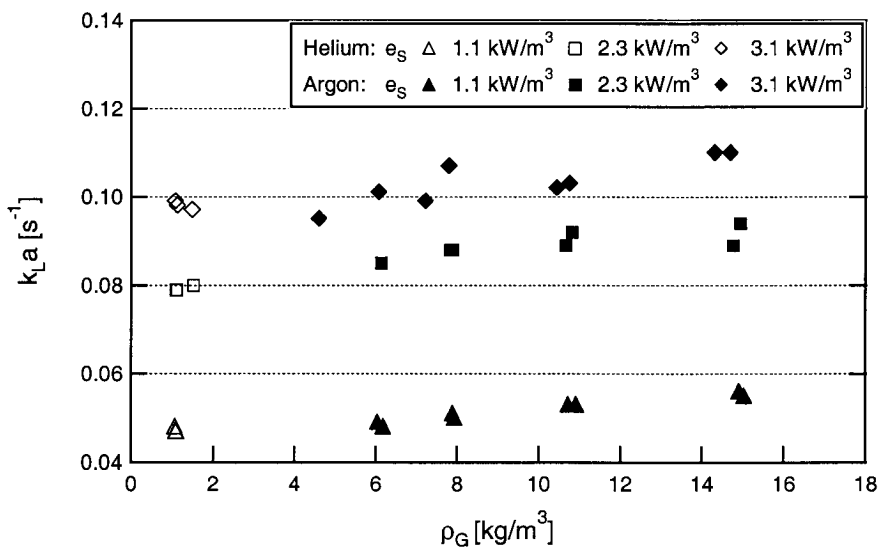


Fig. 7-8: Influence of ρ_G on $k_L a$ ($d_N=6.2\text{mm}$, $l_M=22\text{cm}$, 180° swirl device)

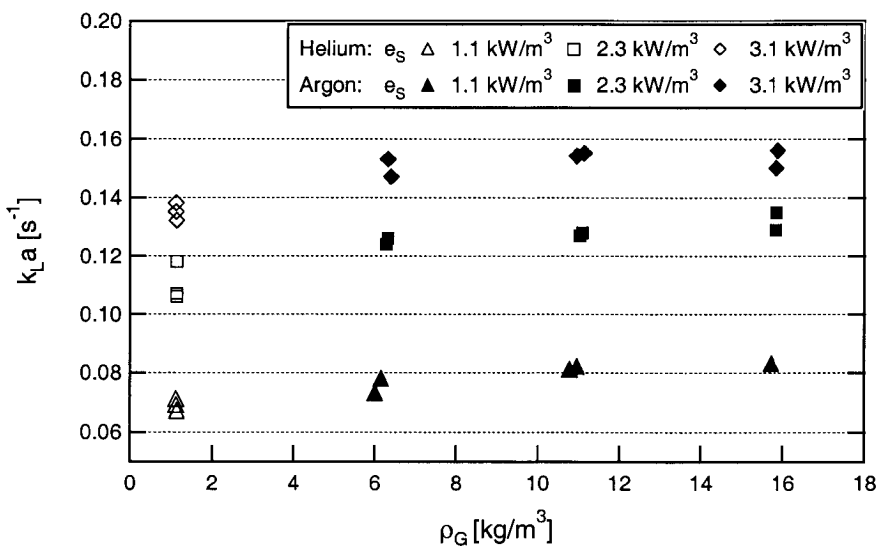


Fig. 7-9: Influence of ρ_G on $k_L a$ ($d_N=6.2\text{mm}$, $l_M=22\text{cm}$, no swirl device)

An example regarding the effect of the gas density on the gas holdup is illustrated Fig. 7-10. Here also an increase of ϵ_{tot} could be observed with an increasing gas density. The increase is rather steep at low gas densities and flattens at higher gas densities.

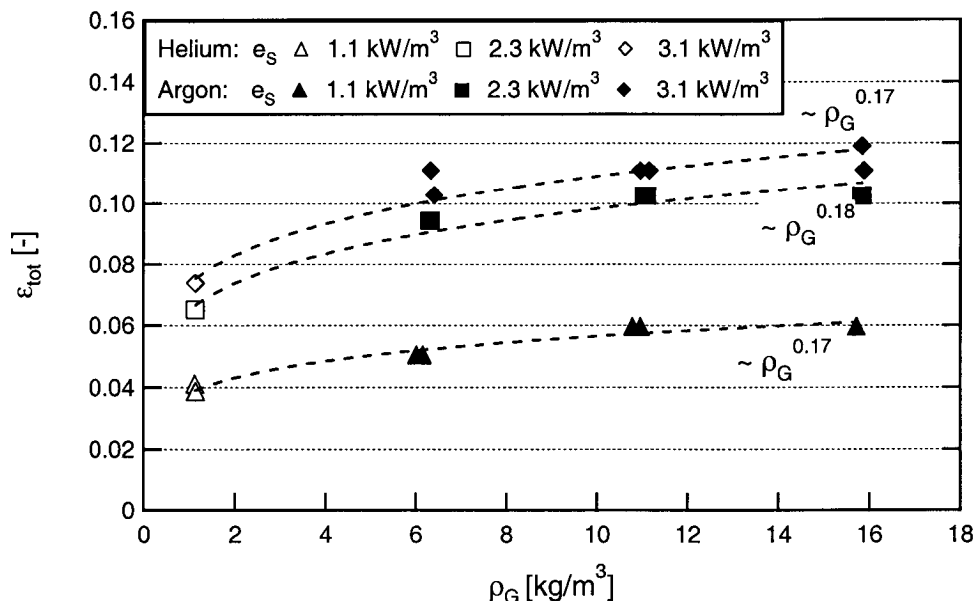


Fig. 7-10: Influence of ρ_G on ϵ_{tot} ($d_N=6.2\text{mm}$, $l_M=22\text{cm}$, no swirl device)

Wilkinson (1991) has reviewed the influence of the gas density on the gas holdup in bubble columns and found:

$$\epsilon_G \propto \rho_G^{0.15 - 0.19} \quad (7-5)$$

The measured data in Fig. 7-10 show a similar dependency. Obviously, the above relationship applies not only to bubble columns but also to the ABLR.

7.1.3 Comparison between the pressure step technique and the hydrazine feeding method

Since two different techniques for the $k_L a$ measurement were applied during this work, it is obvious to compare the obtained data with each other. This was done for helium at 7.2 bar which has the same density as air at ambient pressure. Due to the findings in the previous chapter these two systems are equivalent in terms of the gas density and should lead to identical $k_L a$ values.

The comparison valid for the three tested reaction mixer configurations is shown in Fig. 7-11. If $k_L a$ is low ($< 0.1 \text{ s}^{-1}$) the two measuring techniques are in good agreement. However, at higher mass transfer rates ($k_L a > 0.1 \text{ s}^{-1}$) the pressure step data is always significantly lower than the hydrazine feeding data¹. Also, the deviations between the two techniques increase with increasing $k_L a$ values.

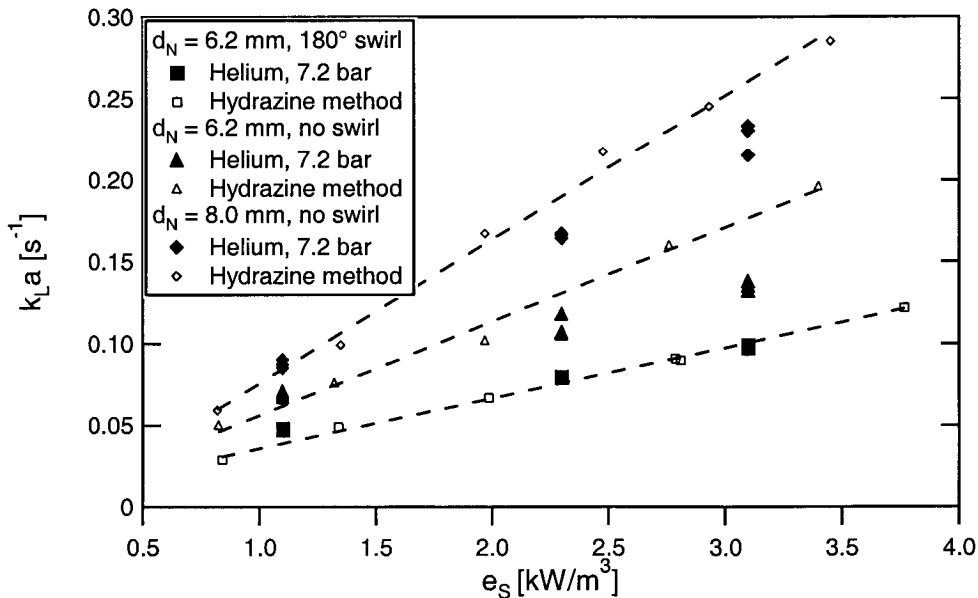


Fig. 7-11: Pressure step technique in comparison to the hydrazine feeding method

The reasons for these deviations lie most probably with the pressure step technique. Apparently, as with coalescence hindered solutions (see Chapter 3.1.5), the start-up period at the beginning of a measurement cannot be neglected even in water. If $k_L a$ is $> 0.1 \text{ s}^{-1}$ a large part of the gas has already been absorbed before steady-state hydrodynamic conditions are reached. Since the gas holdup is lower during the start-up period than at steady-state conditions the measured volumetric mass transfer coefficients are too small.

As a consequence it can be concluded that the pressure step method provides values that are too low if $k_L a$ is $> 0.1 \text{ s}^{-1}$. Correct absolute measurements cannot be obtained with this technique for the ABLR. However, the technique seems to preserve relative differences, i.e. the measured $k_L a$ values still increase with increas-

1. Theoretically the opposite should apply, i.e. it had to be expected that the measurements with the helium would give the somewhat higher $k_L a$ values since its diffusion coefficient is higher than the one of oxygen.

ing power inputs (although not linearly) and the ranking of different reaction mixer geometries regarding their mass transfer performance is preserved. This implies that at least some trends and relative differences can still be identified with the pressure step technique.

However, for future works a more reliable technique should be applied to measure $k_L a$ with the ABLR at elevated pressures.

7.1.4 Extension of the in Chapter 5.4 derived design correlation

In the previous section it has been shown that the pressure step technique does not provide correct absolute values if $k_L a > 0.1 \text{ s}^{-1}$. As a consequence a large part of the experimental data at issue is subject to significant systematic errors (see Fig. 7-11). Evidently, under these circumstances it will not be possible to derive a design correlation that gives a correct description of the mass transfer in the ABLR. Therefore, in this section only a description will be given on how Eq. 5-31 should be extended in order to include the influence of the gas properties.

Since $k_L a$ is the target quantity the same relevance list and, therefore, the same dimensionless numbers can be used that were determined already in Section 5.4.1. The liquid phase properties are generally not influenced by the gas phase and the dimensionless numbers Mo , Π_5 and S_i^* can be excluded from Eq. 5-25. The reduced set of dimensionless numbers produces the relationship

$$f\left(k_L a^*, e_S^*, Sc, \frac{\rho_G}{\rho_L}, Sw_b, \frac{d_N}{d_M}, \frac{l_M}{d_M}\right) = 0 \quad (7-6)$$

It is seen that the consideration of the gas phase properties leads to the addition of two more dimensionless numbers compared to the model for ambient pressure (Eq. 5-26), the Schmidt number Sc and density ratio of the two phases ρ_G/ρ_L . The influence of the specific power input and the reaction mixer geometry can be regarded as given from the experiments at ambient pressure. If a power law approach is used for the two new numbers the following formula is obtained

$${}_L a^* = b_0 \cdot h\left\{e_S^*, Sw_b, \frac{d_N}{d_M}, \frac{l_M}{d_M}\right\} \cdot \left(\frac{\rho_G}{\rho_L}\right)^{b_1} \cdot Sc^{b_2} \quad (7-7)$$

with the function $h\{..\} = \text{Eq. 5-31}$.

With Eq. 7-7 the basis for a following regression analysis is given.

If only the gas properties are changed Eq. 7-7 can be simplified to:

$$k_L a^* \propto \left(\frac{\rho_G}{\rho_L}\right)^{b_1} \cdot Sc^{b_2} \quad (7-8)$$

A rough estimation regarding the two exponents b_1 and b_2 can be obtained by combining some of the previous results. In a first approximation it can be assumed that k_L is primarily affected by the diffusion coefficient, i.e. Sc , and that the gas density influences mainly the specific surface area a . Hence it follows:

$$k_L \propto Sc^{b_2} \quad (7-9)$$

$$a = \frac{6\varepsilon_G}{d_{32} \cdot (1 - \varepsilon_G)} \propto \left(\frac{\rho_G}{\rho_L}\right)^{b_1} \quad (7-10)$$

According to the correlations of Lamont and Scott (1970) and Kawase and Moo-Young (1990) given in Section 5.3.3 it follows that $b_2 = -0.5$. Regarding the influence of the gas density on the bubble size it was found that $d_{32} \propto \rho_G^{-0.1}$ (see Eq. 7-4). And with the help of Fig. 7-10 it follows that $\varepsilon_G \propto \rho_G^{0.17}$. By inserting these findings in Eq. 7-10 it follows that $b_1 \approx 0.25$. Thus, the influence of the gas density can be estimated by the following formula:

$$k_L a^* \propto \left(\frac{\rho_G}{\rho_L}\right)^{0.25} \cdot Sc^{-0.5} \quad (7-11)$$

7.2 Measurements between 10-80 bar

With the experimental facility constructed for this work the maximum pressure was limited to 10 bar. Thus, the observable changes of $k_L a$ were rather small and not always significant. To be on the safe side and to confirm the results obtained between 1-10 bar it would be desirable to carry out measurements inside a broader pressure range. Therefore, further experiments were conducted with another pilot scale reactor which allowed pressures up to 80 bar. This pilot plant was located at the testing facilities of Kvaerner Process Technology (SWITZERLAND) AG in Pratteln, Switzerland.

The system nitrogen/water and a liquid batch size of 50 liters were used for these measurements. The obtained results are shown in Fig. 7-12. In spite of the rather large errors (see section 7.1.3) a significant increase on $k_L a$ with increasing pressure (i.e. gas density) can be observed. At 80 bar the mass transfer performance is by a factor of 2-3 higher than at ambient pressure. Again it should be pointed that the absolute $k_L a$ values in Fig. 7-12 are probably not correct since they were obtained with the pressure step technique.

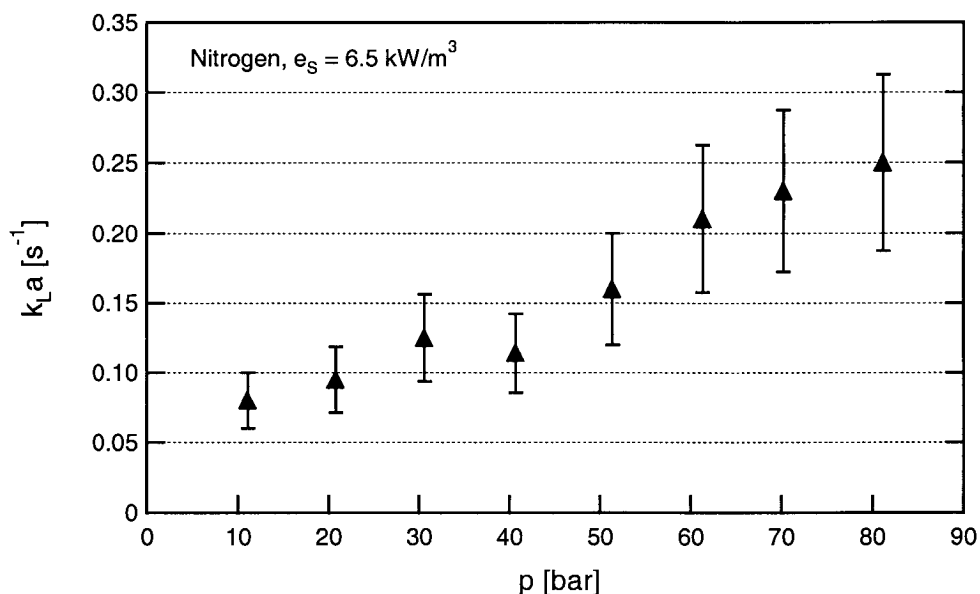


Fig. 7-12: Influence of the pressure on $k_L a$ between 10-80 bar

Unfortunately, it was not possible to determine the gas holdup or the bubble size distributions with the high pressure pilot plant due to technical restrictions.

Although Eq. 7-3 was derived at different conditions and with another reactor it still can be used to give a rough estimation of the *Sauter* bubble diameter. At 80 bar the nitrogen bubbles can be expected to have *Sauter* diameters of ~3 mm.

7.3 Conclusions

Measurements regarding the influence of the system pressure and the gas type were carried out in two differently scaled reactors featuring different pressure ranges.

First, experiments were carried out at pressures between 1-10 bar. It was found that the *Sauter* bubble diameter decreases with increasing gas densities. On the basis of the experimental data it was possible to derive a design correlation which describes the influence of the gas density on the *Sauter* bubble diameter in the ABLR. Further experiments have proven that, due to the reduced bubble size, also $k_L a$ and the gas holdup increase with increasing gas densities.

A comparison with the hydrazine feeding method has shown that $k_L a$ values measured with the pressure step technique are too low without exception if $k_L a$ is $> 0.1 \text{ s}^{-1}$. Due to the poor quality of the $k_L a$ measurements it was not possible to derive a correct design correlation. For future works a more reliable technique has to be applied to measure $k_L a$ with the ABLR at elevated pressures.

Further experiments were carried out with a pilot plant at pressures between 10-80 bar. Again it was found $k_L a$ is increased by increasing pressures, i.e. the results obtained at lower pressures could be confirmed for a much broader pressure range.

Appendix 1

Analysis of the bubble pictures

A1.1 Introduction

For the measurement of meaningful bubble size distributions lots of pictures have to be analyzed. This is often done manually but the task can be very tedious and time consuming. Therefore, the goal was to develop an image analysis approach which would allow the automatic determination of the bubble size distribution.

In this chapter many expressions coming from image analysis sciences will be used. Although the effort was made to keep matters as simple as possible one may have to consult other literature for more detailed explanations. At this place the excellent handbook by Russ (1995) which covers almost all aspects of image analysis (especially the basics) is recommended.

Three different types of images had to be analyzed in this study: PVM pictures of the plunging jet zone, PVM pictures of the bulk bubbles in coalescence hindered liquids and photographs of the bulk bubbles in coalescing liquids (taken from the outside of the reaction vessel). The characteristics of these images are described in Fig. A1-1.

It is apparent that the development of one single, fully-automated image analysis procedure for all these picture types was not possible. In image analysis sciences a rule of thumb says, that a successful object detection with image analysis is only possible if the human eye can identify the objects easily. In addition the objects should possess distinctive features which distinguish them from the rest of the picture (e.g. spherical shape). As seen in Fig. A1-1 this is only the case to some extent with the PVM pictures of bulk bubbles in coalescence hindered liquids (type b).

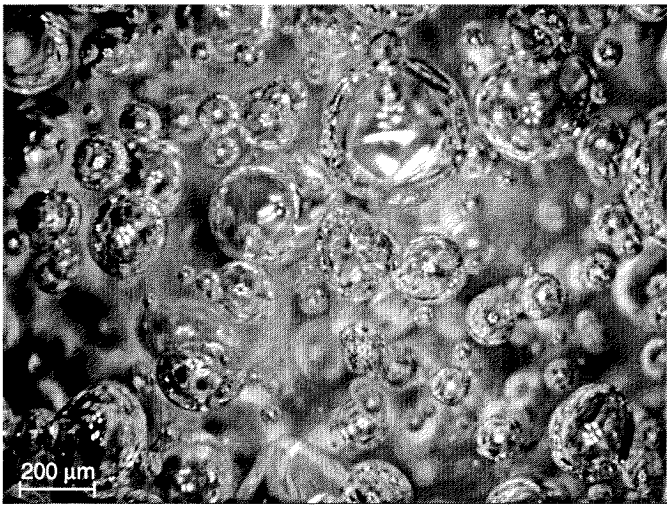
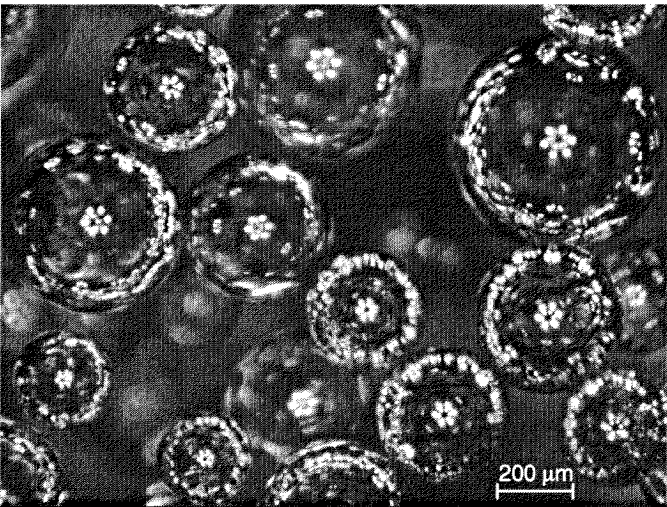
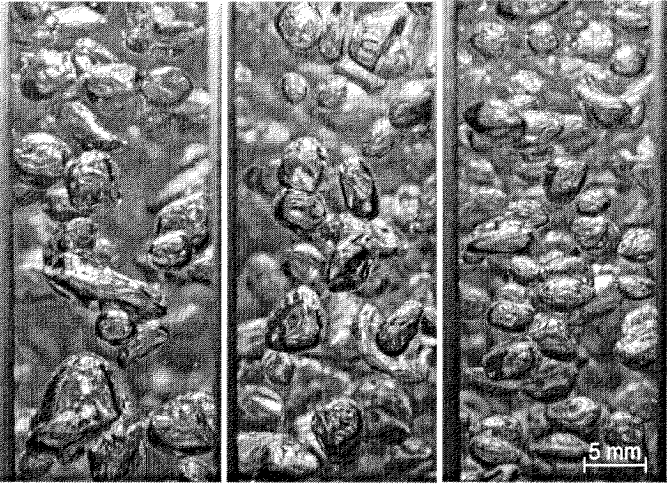
	<p>a) Plunging jet zone</p> <p>Source: PVM</p> <p>In this region the bubbles are very small. Due to the very high gas holdups in this region much bubble overlapping takes place. It can also be seen that several bubbles are (despite their small size) deformed because of the high shear rates in this region. The distinction of single bubbles by eye is sometimes difficult.</p>
	<p>b) Bulk bubbles in coalescence hindered liquids</p> <p>Source: PVM</p> <p>Most bubble diameters are within in the range of 100-600 μm. Since the shear rates in this region are moderate all bubbles have the shape of rigid spheres. The degree of bubble overlapping is rather low. The distinction of single bubbles by eye is very easy.</p>
	<p>c) Bulk bubbles in coalescing liquids</p> <p>Source: Digital camera</p> <p>The bubbles are much larger than in the two other cases. Most of the bubbles are of ellipsoidal shape, some are even more deformed. Massive bubble overlapping takes place. The distinction of single bubbles is even by eye in many cases rather difficult.</p>

Fig. A1-1: Description of the three different image types

Therefore, the following approach was chosen: For pictures of the type b) a fully-automated image analysis procedure was developed (see Appendix A1.2). For the types a) and c) the bubble detection had to be carried out by hand¹. The corresponding procedure is described in Appendix A1.3.

A1.2 Description of the fully-automated image analysis procedure

The first thing to do when trying to apply image analysis is to look for distinctive features in the pictures which could help in the recognition of specific objects or patterns by the computer. One always has to bear in mind that for a computer an 8 bit greyscale picture is just a matrix containing elements with values between 0 (= black) and 255 (= white). Therefore, the basic difficulties regarding the application of image analysis will be discussed in more detail.

Picture A in Fig. A1-2 was taken using a microscope, a camera and rear lightening and shows small air bubbles in a salt solution. Picture B was taken in the ABLR (near the wall of the reaction vessel) using the PVM and shows air bubbles in a 0.25 M Na₂SO₄-solution.

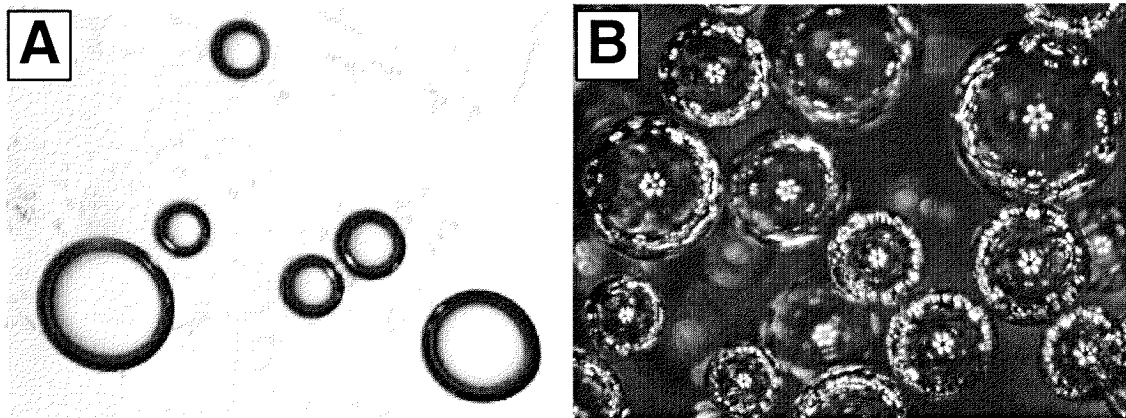


Fig. A1-2: Bubble pictures of different quality

1. Ritter and Kraume (1999) for instance had to proceed likewise because in their case heavy drop overlapping prevented an automated image analysis.

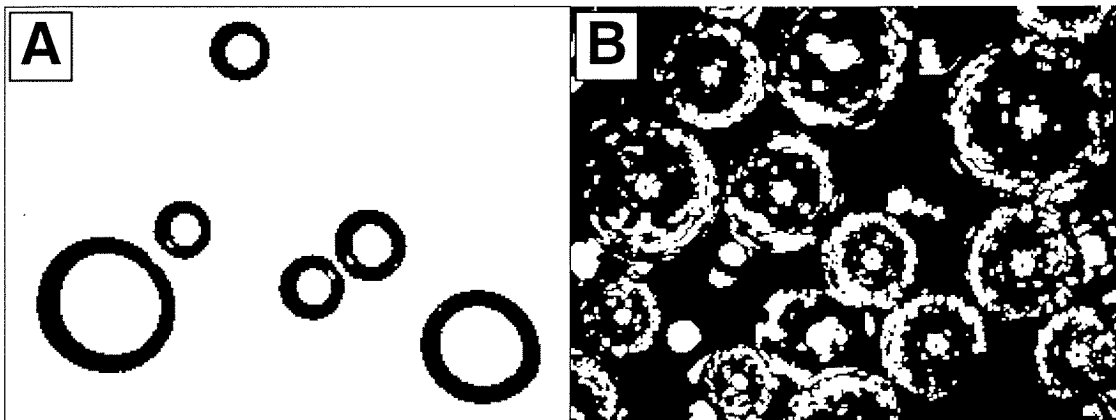


Fig. A1-3: Binary pictures created by the thresholding function

While the human eye has no problem to discern the bubbles in both pictures several difficulties arise when using image analysis with picture B.

In picture B the bubble features do not correspond to a specific brightness level. High greylevels can be found as well in the centre or the rim of the bubbles as in the background. The same can be said for the low greylevels. By way of contrast the bubble rims in picture A contain exclusively pixels of low greylevels which makes feature detection very easy.

This is illustrated in Fig. A1-3. A simple thresholding function was applied to both pictures of Fig. A1-2. The results are binary pictures containing only black and white pixels. In picture A objects (= connected black pixels) which correspond to the bubble rims are obtained. However no usable results could be generated in picture B this way, i.e. direct extraction of the bubble diameters is not possible.

Another difficulty to cope with is the increasing number of overlapping bubbles at high gas-holdups. Next to the sharp bubbles nearest to the probe window there are also many other, though blurred bubbles in the background. At high gas-holdups the number of bubbles is so large that the blurred bubbles will fill almost the entire background (see Fig. A1-2, picture B). Therefore, the image analysis approach had also to be able to make a distinction between the sharp bubbles and their background.

The image analysis procedure that was developed for this work is structured in three steps which will be described in more detail on the following pages:

1. Binarization of the PVM picture
2. Circle detection
3. Blob detection and bubble diameter measurement

Binarization of the PVM picture

The approach takes advantage of the many reflections on the bubble rims and the very bright spots in the bubble centres caused by the laser flashes. The sharp bubbles in the foreground show many and very steep greylevel changes on their surface whereas the bubbles in the background show only rather smooth changes in their greyscale values.

This fact can be used for the distinction between the bubbles to be detected and the background. A function for edge detection which calculates the maximum of eight directional derivatives finds areas of high slope. The result is a grayscale image in which the brightness of the pixels represents the gradient magnitude.

To select only the pixels with the highest slopes a thresholding function is applied to this image. Pixels with greylevels higher than a specified value are converted into white pixels, all others into black pixels. The result is a binary image in which the white pixels represent parts of the bubble rims or the bubble centres. To increase the number of white pixels a hole filling operation is used. The summary of the image conditioning step is depicted in Fig. A1-4.

Circle detection

In the second step the binary image is scanned for circular structures. This is done by using a circular Hough transform. The forward transform generates a vector of images where each image in the vector corresponds to circles of one radius. A pixel value in an output image represents the fraction of white pixels in the input image on a circle centred at the corresponding pixel with a radius equal to the radius value associated with the image. The pixel values are normalized to a value

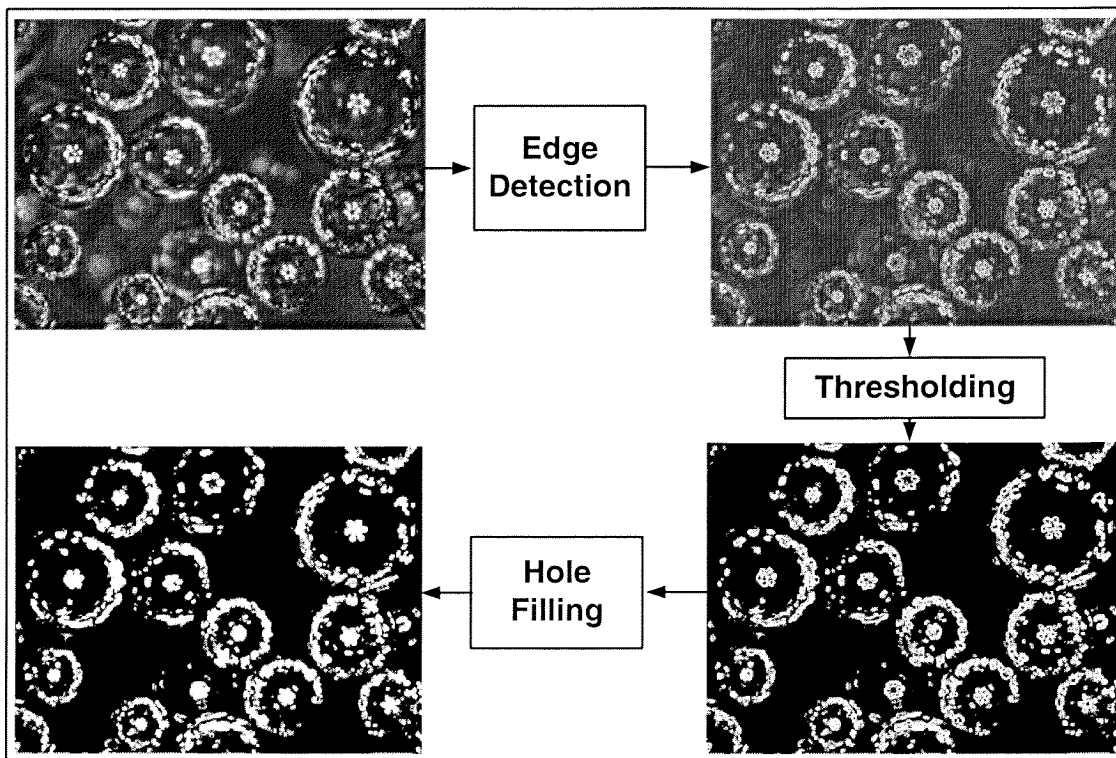


Fig. A1-4: Binarisation of the original picture

of 255 for a complete circle. In other words the circular Hough transform of a binary image is a three dimensional function of x,y and r (radius) giving the fraction of pixels on a circle of radius r centred at (x,y) that are white.

The binary picture is scanned for radii between 15 and 240 pixels. Only circles with a fraction of white pixels larger than 65% (i.e. greyscale value = 165) are accepted. This is achieved by applying a thresholding function to the transformed images. Additionally only circles which are centred on the brightest spots of the original image are used for further processing. This way wrongly detected circles are deleted since the brightest pixels in the original image mainly correspond to the blossom like reflections in the bubble centres. The selection is done by using an AND-operator.

The reverse Hough transform converts the obtained images for each radius r to images containing circles of radius r . In the end all images are summed up. The result is a greyscale image where the pixel brightness is a measure how often a pixel was found to be part of a circle. The summary of the procedures for the circle detection is illustrated in Fig. A1-5.

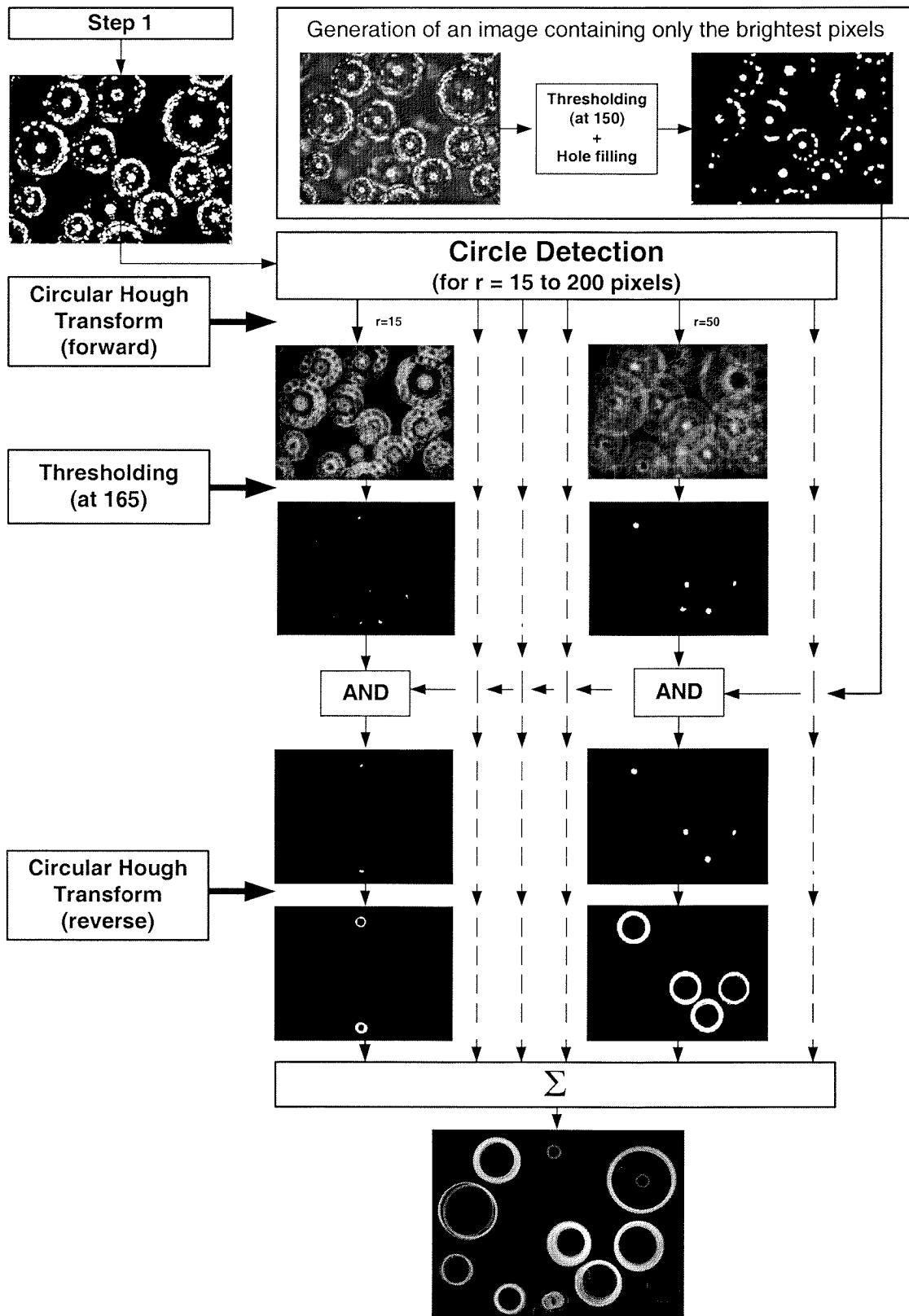


Fig. A1-5: Procedure for the circle detection

Blob detection and bubble diameter measurement

In the third and last step the actual image analysis, i.e. the measurement of the bubble diameters takes place. An illustration of the occurring operations is given in Fig. A1-6.

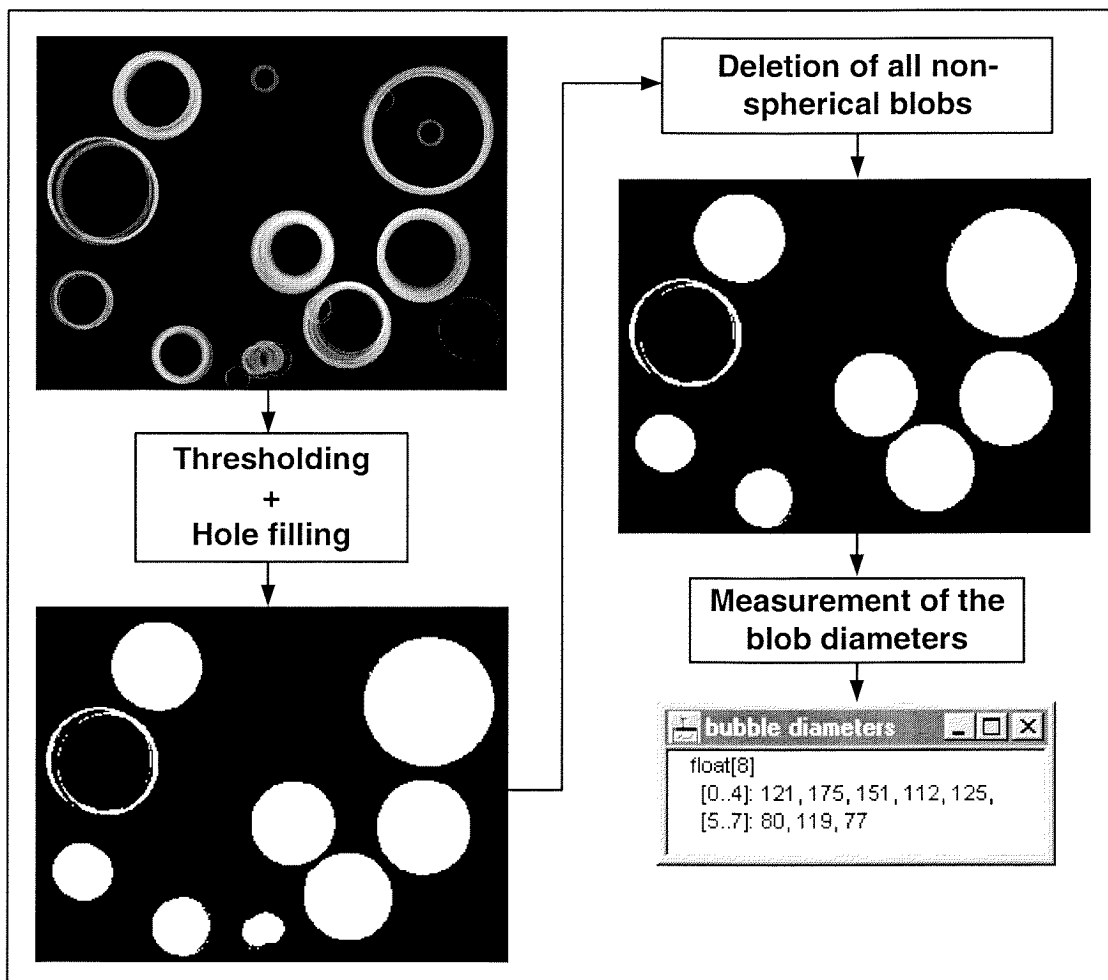


Fig. A1-6: Blob generation and diameter measurement

As already mentioned the greyscale values in the summed up picture from step 2 are a measure for how often a pixel was found to be part of a circle, i.e. the greyscale values can be regarded as the probability that a pixel really belongs to a bubble rim. Therefore every pixel below a specified greyscale value should be deleted since the probability that it belongs to a bubble rim is very low. This is done by a thresholding function which returns a binary image. Holes are filled using a hole filling operator.

Once the binary image is generated the bubbles can be extracted in the form of blobs¹. There may still be some blobs which do not represent entire bubbles but bubble fragments or several overlapping bubbles.

Small fragments are removed by accepting only blobs which contain more than 100 pixels. Larger fragments and overlapping bubbles are filtered out by accepting only blobs which fulfill the following condition:

$$\frac{\text{Best fit ellipse minor axis}}{\text{Best fit ellipse major axis}} \geq 0.8 \quad (\text{A1-1})$$

This step also leads to the deletion of bubbles which cross the border of the image because their blobs are not of circular shape. The diameters of the remaining blobs are calculated from the difference of the maximum and minimum x-coordinate of each blob. This allows the correct diameter measurement even for circular blobs that are not filled.

Finally all diameters are saved for the later calculation of the bubble size distribution. Then the next picture is opened and the image analysis procedure starts again.

Discussion

The results of the image analysis procedure were compared with measurements carried out by hand (with image analysis support, see Appendix A1.3) in order to get an indication of the procedures quality. It has to be pointed out that with the manual measurements overlapping bubbles and bubbles crossing the image borders were also recorded. The manual analysis of 100 pictures took approx. 3-5 hours whereas the fully automated computation needed around 7 hours, i.e. the image analysis procedure could not be used for on-line measurements².

The comparison showed that about 30-50% of all the manually identified bubbles were also detected by the image analysis procedure. The low detection ratios are the result of the very strict acceptance criteria for blobs in the procedure. During the development of the image analysis procedure a high value was set on avoiding

-
1. Blobs are connected regions of equally valued pixels
 2. The fact that the automated analysis takes more time than the manual one might be a surprise. The reason for this is the circular Hough transform which is responsible for > 90% of the computation time.

any false detection of bubbles. Therefore, a questionable blob is rather rejected than accepted.

An example of both bubble size distributions is illustrated in Fig. A1-7. It can be seen that the modes of both distributions compare rather well. The number density of the computed distribution is between 150 and 350 μm higher and at all other diameters lower than the manual one. Apparently the image analysis procedure works best for mid-sized bubbles, i.e. the probability for successful bubble detection is highest between 150 and 350 μm .

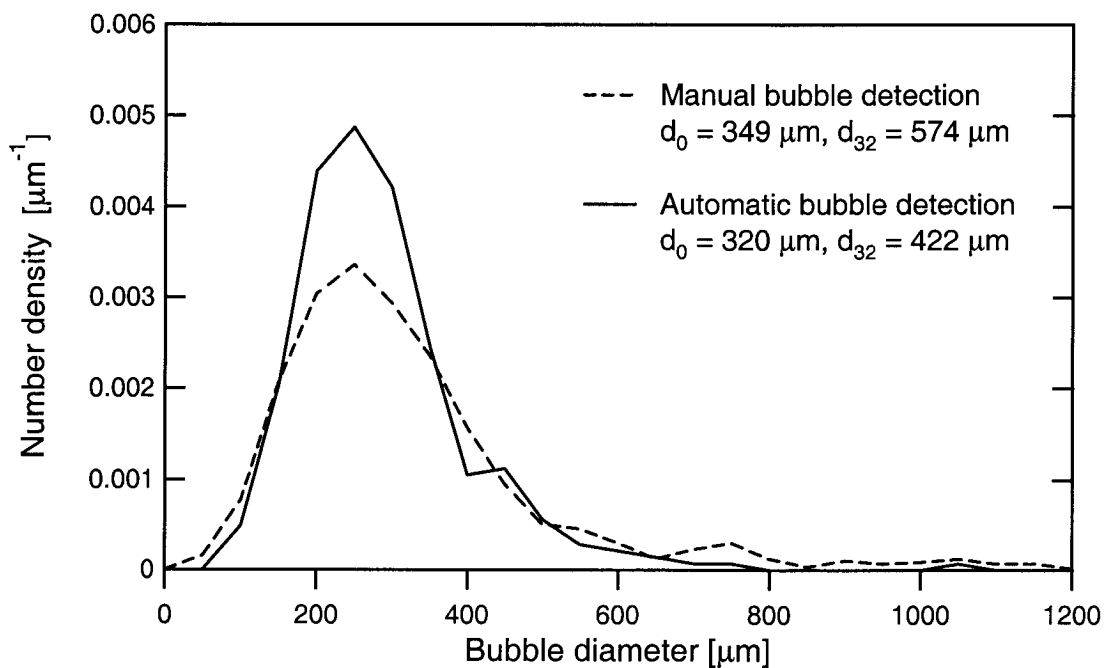


Fig. A1-7: Computed bubble size distribution in comparison with the actual distribution

Bubbles that exceed the image borders are either not detected by the circle detection step or later deleted because their blobs are not of circular shape. Therefore the probability that a bubble is detected decreases with its size because the larger a bubble is, the larger is the chance that it crosses the image borders. This is the reason for the rather few detected bubbles with diameters over 700 μm .

The image analysis procedure also shows some errors regarding the identification of very small bubbles. This has two reasons. First the scanning for circles starts at a radius of 15 pixels (= diameter of 82.5 μm) and therefore smaller bubbles are not

detected. (The lower radius boundary could be reduced but that would result in even higher errors. Every centre reflection and many fragments of the bubble rims would then be wrongly detected as small bubbles). Secondly very small bubbles do not show the characteristic rim reflections which are required for the bubble detection.

The effect of the described detection errors on the number mean bubble diameter d_0 and the *Sauter* bubble diameter d_{32} is also exemplarily shown in Fig. A1-7. While the deviations have little impact on the number mean diameter (<10%), their influence on the *Sauter* bubble diameter is rather large (approx. 30%).

Conclusions

The efforts to develop a fully automated image analysis procedure lead to a very limited success. The image analysis procedure showed considerable errors even with images containing only spherical bubbles. Therefore the image sequences had to be checked by eye first, making sure that the image analysis procedure was only applied if the vast majority of the bubble diameters was between 100 and 500 μm . Image sequences not meeting this criteria had to be analyzed by hand. Thus, the applicability of the image analysis procedure was very limited.

A1.3 Description of the procedure using manual bubble detection

Although the bubbles were detected manually the actual bubble size measurement was still carried out by the computer. Fig. A1-8 illustrates the used procedure schematically.

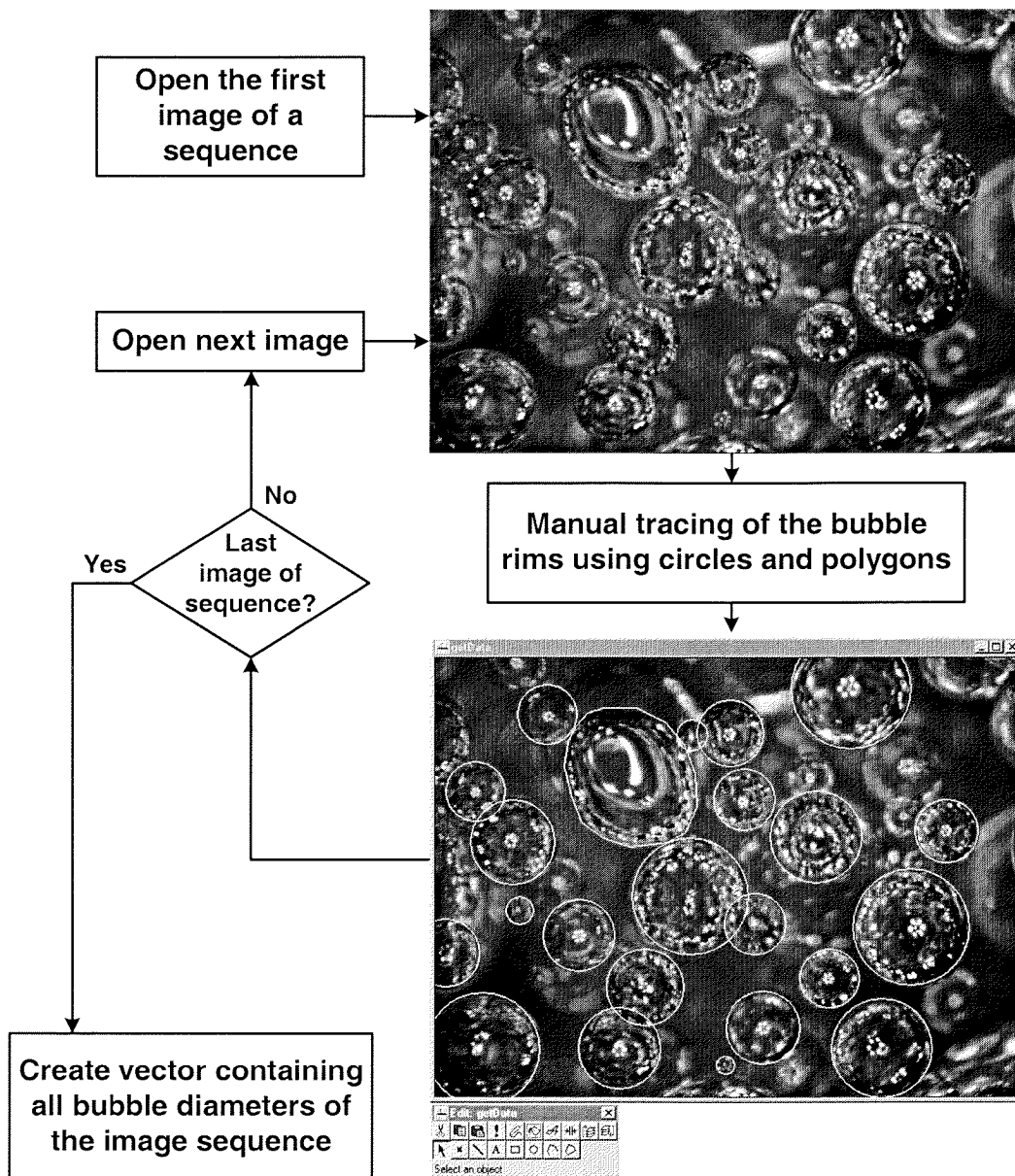


Fig. A1-8: Image analysis procedure using manual bubble detection

The images of one sequence were opened in turn automatically. For every image manual input was needed to point out the bubbles to the computer. Two possibilities were available for this task. Approximative spherical bubbles could be described with circles. The rims of deformed bubbles could be traced using polylines with connected ends. After all bubbles of an image were marked the diameters of the bubbles were computed by the software¹ and stored in a buffer. Then the next image was opened.

When all images were treated this way the computer returned a vector containing the bubble diameters of the entire image sequence.

1. The equivalent circle diameter (see Rhodes, 1990) was used to describe the size of the deformed bubbles.

Appendix 2

Calculation of the bubble size distributions, d_{32} and the specific surface area

A2.1 Bubble size distribution

The image analysis procedure returns a vector containing all measured bubble diameters of one image sequence (see Appendix A1). The bubble size distribution that can be calculated directly from this vector is the number distribution because every element corresponds to one single bubble. The corresponding definition of the cumulative distribution function for bubbles of the diameter d is given in Eq. A2-1:

$$Q_0(d_i) = \frac{\text{Number of bubbles with } d \leq d_i}{\text{Total number of bubbles}} \quad (\text{A2-1})$$

If the proportion of bubbles with a diameter between d_i and d_{i-1} is related to the width of this interval, one gets the number density:

$$q_{0,i} = \frac{Q_0(d_i) - Q_0(d_{i-1})}{d_i - d_{i-1}} = \frac{\Delta Q_{0,i}}{\Delta d_i} \quad (\text{A2-2})$$

For both the density and the cumulative distribution the scaling condition of Eq. A2-3 applies. It should be noted that in this chapter sums are rather used than integrals since the on hand data was discrete.

$$\sum_{d_{\min}}^{d_{\max}} q_{0,i} \cdot \Delta d_i = \sum_{d_{\min}}^{d_{\max}} \Delta Q_{0,i} = 1 \quad (\text{A2-3})$$

The arithmetic mean bubble diameter \bar{d}_0 can be calculated using the following equation:

$$\bar{d}_0 = \sum_{i=1}^n \bar{d}_i \cdot q_{0,i} \cdot \Delta d_i = \sum_{i=1}^n \bar{d}_i \cdot \Delta Q_{0,i} \quad (\text{A2-4})$$

In order to calculate the bubble size distribution in relation to the dispersed volume instead to the number of bubbles, the following equation is used:

$$q_{3,i} = \frac{\bar{d}_i^3 \cdot q_{0,i}}{\sum_{i=1}^n \bar{d}_i^3 \cdot q_{0,i} \cdot \Delta d_i} \quad (\text{A2-5})$$

A2.2 The *Sauter* diameter d_{32}

However, for absorption processes the arithmetic mean bubble diameter of the number distribution is of little relevance or use. For these processes another mean diameter is used, the surface mean diameter d_{32} also called the *Sauter* diameter. It represents the mean bubble size that has the specific surface area of the entire bubble population. The *Sauter* diameter can be calculated directly from the number distribution:

$$d_{32} = \frac{\sum_{i=1}^n \bar{d}_i^3 \cdot \Delta Q_{0,i}}{\sum_{i=1}^n \bar{d}_i^2 \cdot \Delta Q_{0,i}} = \frac{\sum_{i=1}^n \bar{d}_i^3 \cdot q_{0,i} \cdot \Delta d_i}{\sum_{i=1}^n \bar{d}_i^2 \cdot q_{0,i} \cdot \Delta d_i} = \frac{\bar{d}^3}{\bar{d}^2} \quad (\text{A2-6})$$

A2.3 Specific surface area

With d_{32} and the gas-holdup ϵ the specific surface area a can be calculated. Attention should be paid that Eq. 2-16 has strict validity only for spheres. However, one has to bear in mind that the diameter of deformed bubbles was defined as the equivalent circle diameter (see Rhodes, 1990). The bubble surface calculated from this

diameter is therefore smaller than the actual one. This has to be taken into account when calculating the specific surface area.

The bubble deformation can be taken into consideration using the shape factor ψ , also called sphericity. Its definition is shown in the following equation:

$$\psi = \frac{\text{surface of the volume-same sphere}}{\text{actual surface}} = \left(\frac{d_v}{d_s}\right)^2 \quad (\text{A2-7})$$

Especially in coalescing solutions most of the bubbles were deformed. In nearly all cases the bubbles were of elliptical shape. Therefore, ellipses were used to describe the bubble deformations. The procedure was as follows: The blobs of the deformed bubbles were fitted with ellipses of the same area. Then the best fit major axis b and the best fit minor axis a were extracted. The bubble shapes could now be described with a single parameter by forming the axis ratio a/b .

Over 1000 bubbles were analyzed this way and the result is shown in Fig. A2-1. It can be seen that the large majority of the bubbles has an axis ratio larger than 0.6. The mean axis ratio is 0.75.

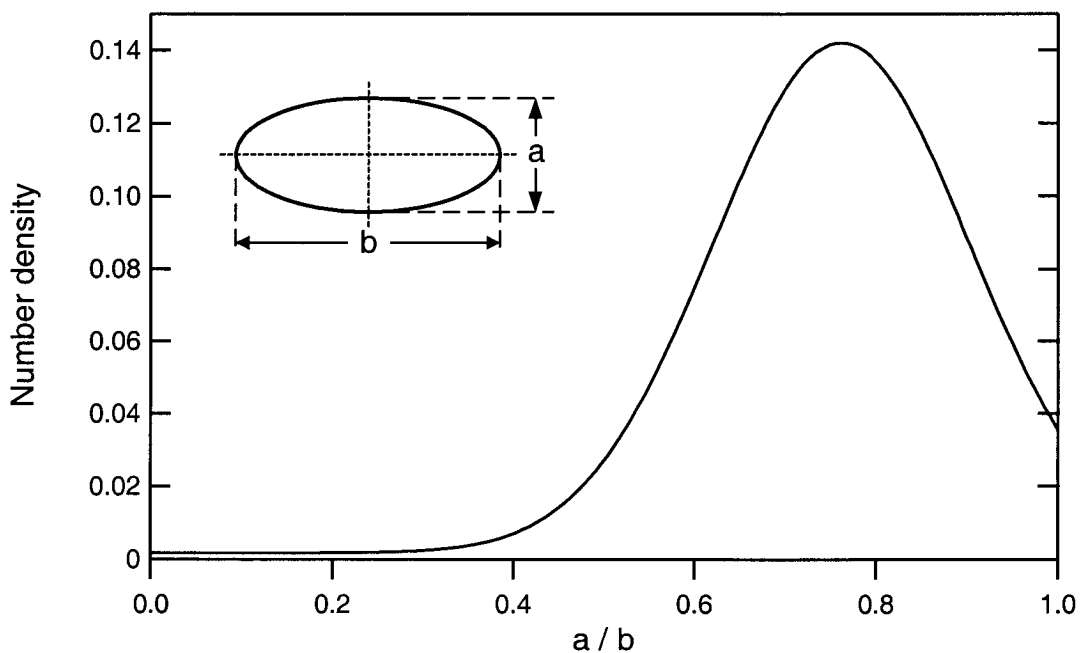


Fig. A2-1: Distribution of ellipse axis ratios with deformed bubbles

With the assumption that the bubbles feature rotary symmetry the corresponding sphericity can be determined from Fig. A2-2. For the major part of the bubbles the

sphericity can be approximated with $\psi \approx 1$. Therefore, the deformation of the bubbles can be neglected and the specific surface area a can be calculated with Eq. 2-16.

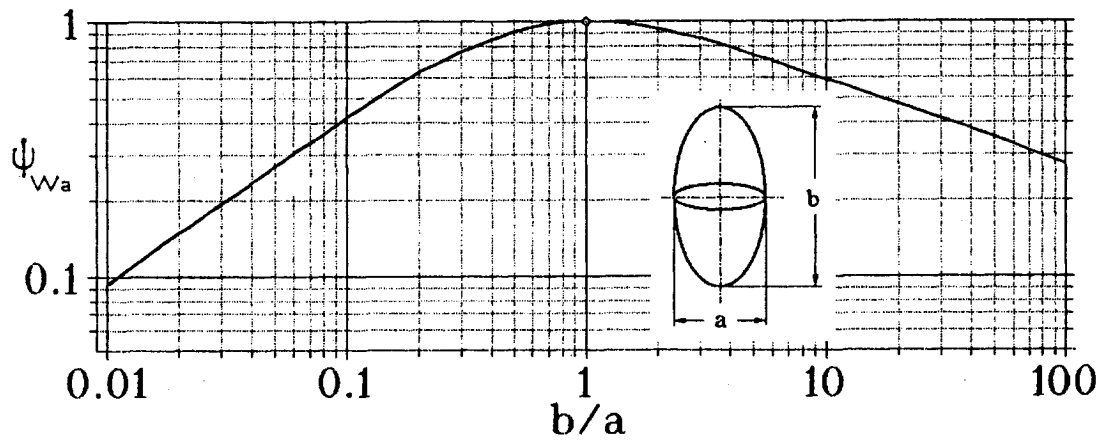


Fig. A2-2: Sphericity ψ of an ellipsoidal shaped particle (taken from Stieß, 1992)

Appendix 3

Mixing characteristics

To determine the mixing characteristics of the two phases inside the reactor their residence time distributions (RTD) were measured. This was done by applying a stimulus-response technique. With no tracer initially present in the reactor a pulse tracer input signal was imposed on the fluid stream entering the reactor. Then the concentration-time curve at the reactor outlet was measured. Thereof the E-function of the liquid phase was calculated according to Eq. A3-1.

$$E(t) = \frac{c_{\text{tracer}}(t)}{\int_0^{\infty} c_{\text{tracer}}(t) \cdot dt} \quad (\text{A3-1})$$

Or using the dimensionless form with $\theta = t/\tau_{\text{reactor}}$, where τ_{reactor} is the mean residence time of the fluid in the reactor:

$$E(\theta) = \frac{c_{\text{tracer}}(\theta)}{\int_0^{\infty} c_{\text{tracer}}(\theta) \cdot d\theta} = \tau_{\text{reactor}} \cdot E(t) \quad (\text{A3-2})$$

Attention should be paid that the concentration-time curve can only be used directly if the response time of the measuring probe is negligible, i.e. if $\tau_{\text{probe}} \ll \tau_{\text{reactor}}$ is fulfilled. If this is not the case the measured signal has to be corrected first. This is done by modelling the probe lag with a suited function and applying a deconvolution algorithm to the experimental data. This procedure is described in Appendix A3.2 in more detail.

All measurements were carried out with the air/water system using the following reaction mixer geometry: Nozzle diameter 6.2 mm, mixing tube length 22.0 cm, swirl device 180°.

A3.1 Liquid phase RTD

To determine the overall mixing characteristics of the liquid phase the reactor was operated in continuous mode. A constant water stream (1000 l/h) was fed into the vessel and at a different point water was let out at the same flow rate. A concentrated KCl-solution served as tracer. It was injected into the feeding stream by using a syringe. The tracer concentration was measured in the outlet stream by a conductivity probe. The applied setup is illustrated in part a) of Fig. A3-1. By changing the pumping speed it was possible to vary the recirculation number R , which is defined as the ratio of the recirculation and the exit flow rate.

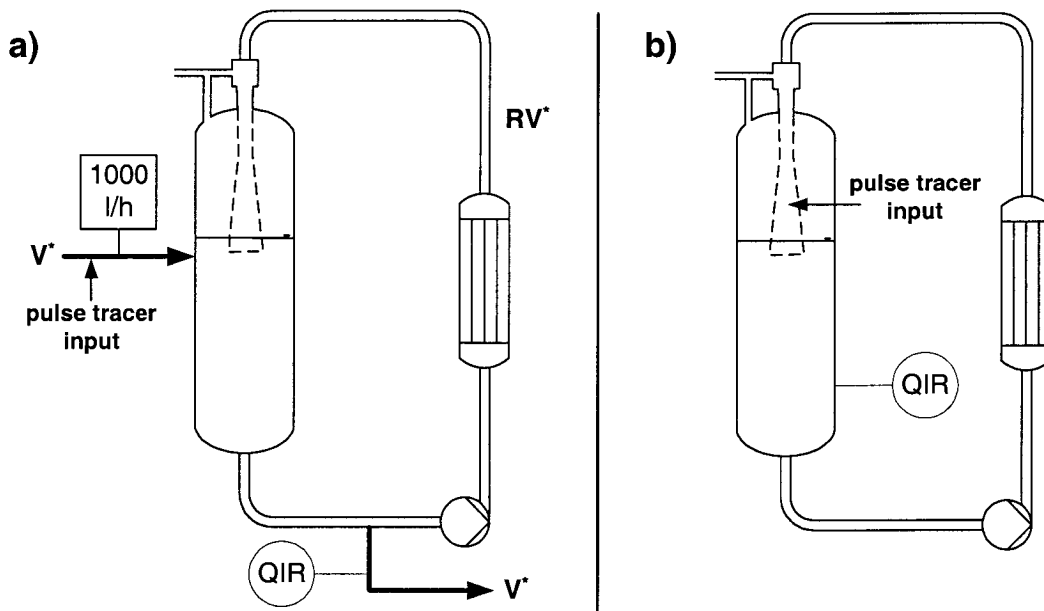


Fig. A3-1: Measurement of the liquid mixing characteristics: a) Setup for continuous operation, b) Setup for batch operation

Since the conductivity measurements are very fast regarding the response time of the probe no correction of the experimental data was needed.

The results are shown in Fig. A3-2. The measured data coincides very well with the ideal case of a constant flow stirred tank reactor (CFSTR). Even at the lowest recirculation rate ($R = 1.5$) the liquid phase can be described as ideally mixed. This is of great importance regarding the applicability of the hydrazine feeding technique since it gives only correct results if the liquid phase is well mixed (see Section 3.1.2.4).

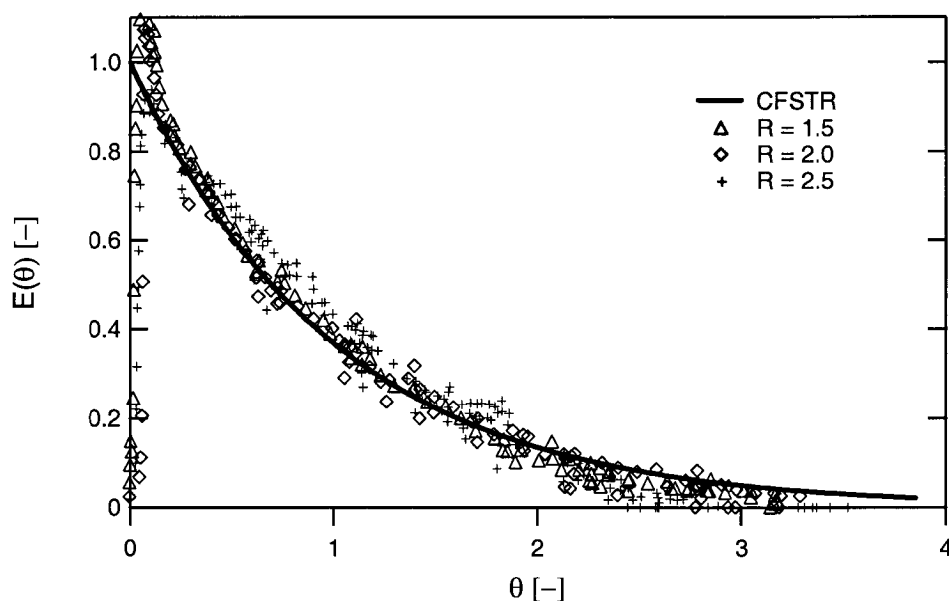


Fig. A3-2: Dimensionless RTD of the liquid phase during continuous operation

In addition the reactor was also operated in batch mode in order to get more information regarding the mixing processes inside the vessel and the liquid recycle pipe. The relevant setup is shown in part b) of Fig. A3-1.

The tracer was injected into the plunging jet and its concentration was monitored with a conductivity probe located in the lower part of the vessel, near its wall. By changing the pump speed the liquid circulation flow Q_L was varied.

It should be pointed out that only 20 liters of water were filled into the reactor. With a larger batch the contribution of the liquid recycle ($V_{\text{recycle}} = 5.2$ liter) to the total liquid volume would have become too small for any distinctive measurements.

The dimensionless representation of two concentration-time curves measured during batch operation is shown in Fig. A3-3. $c(t=\infty)$ is the homogeneous tracer concentration at the end of a measurement and τ_{recycle} is the mean liquid residence time in the recycle pipe. The measurements are compared to a model consisting of a CFSTR for the reaction vessel and a plug flow reactor (PFR) for the recycle pipe. As can be seen the curves agree very well. Hence, the liquid phase mixing inside the ABLR can be modelled with a loop which is built of one CFSTR and one PFR. If the amount of liquid filled into the reactor (V_{liq}) is much larger than the volume of the recycle pipe (V_{recycle}), the influence of V_{recycle} can be neglected and the mixing can be described with a single CFSTR.

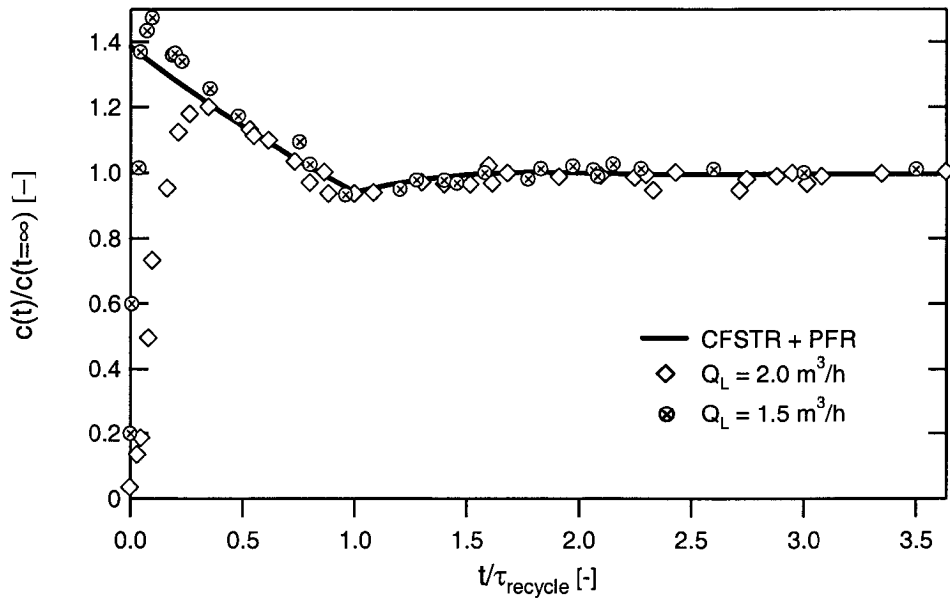


Fig. A3-3: Tracer concentration in the vessel after a pulse input during batch operation

A3.2 Gas phase RTD

The residence time distribution of the gas phase was measured using Dichlorodifluoromethane (CCl_2F_2) as tracer. The tracer was injected into the entrained gas stream and its concentration was measured by a leak detector (BALZERS) at the gas outlet. A schematic illustration of the applied setup can be found in Fig. A3-4.

The gas residence time distribution was measured under different operating conditions. The liquid recirculation rate Q_L and the gas entrainment ratio Q_G/Q_L were varied within the same range as it was used later with the $k_L a$ measurements. Some examples of the measured concentration-time curves are shown in Fig. A3-5. Despite the different operating conditions the shapes of the curves are very similar. Therefore, it can be concluded that the mixing characteristics of the gas phase are virtually identical within the examined range and can be described with the same residence time distribution.

However, the measured E curves do not represent the actual mixing characteristics of the gas phase. Unlike the measurements with the conductivity probe the response lag of the gas leak detector cannot be neglected. A description of the procedure that was applied to determine the actual E curves follows next.

It was found that the measured E curves could be approximated very well with the following equation:

$$E(\theta)_{\text{meas}} = b_0 \cdot \theta \cdot e^{-b_1 \theta} \quad (\text{A3-3})$$

On the other hand the response lag of the leak detector was quantified by measuring its response to a step tracer signal. It was found that its response curve could be

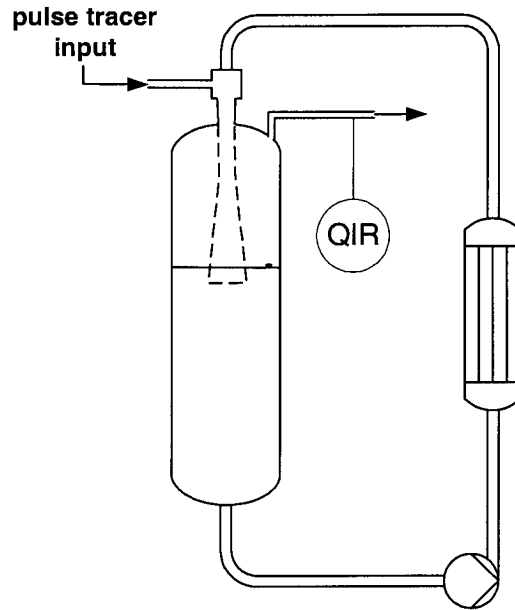


Fig. A3-4: Setup for the gas RTD measurement

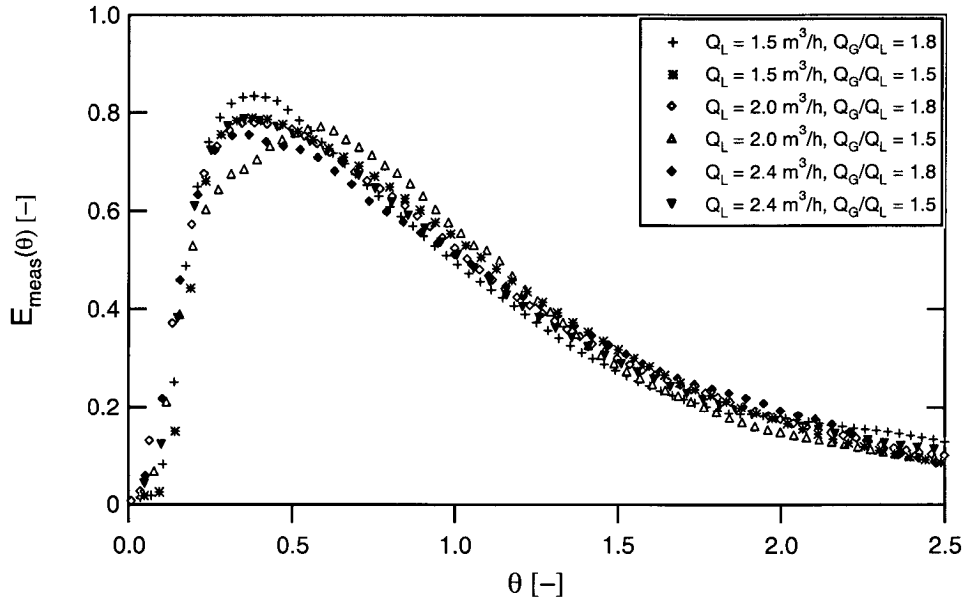


Fig. A3-5: Measured E-curves of the gas phase at different operating conditions

described as a first-order lag with a time constant T of 3.2 seconds. Thus it was possible to formulate a relation between the measured and the effective E curve:

$$E(\theta)_{\text{eff}} = T^* \cdot \frac{dE(\theta)_{\text{meas}}}{d\theta} + E(\theta)_{\text{meas}} \quad (\text{A3-4})$$

T^* is defined as the ratio of the time constant T and the mean residence time of the gas phase in the reactor τ .

To calculate $E(\theta)_{\text{eff}}$ the Laplace transformation was applied to Eq. A3-4. Hence follows:

$$E(s)_{\text{eff}} = \mathcal{L}\{E(\theta)_{\text{eff}}\} = sT^* \cdot E(s)_{\text{meas}} + E(s)_{\text{meas}} \quad (\text{A3-5})$$

And by inserting the Laplace transformation of the measured E curve $E(\theta)_{\text{meas}}$

$$E(s)_{\text{meas}} = \mathcal{L}\{E(\theta)_{\text{meas}}\} = \frac{b_0}{(b_1 + s)^2} \quad (\text{A3-6})$$

Eq. A3-5 becomes

$$E(s)_{\text{eff}} = \mathcal{L}\{E(\theta)_{\text{eff}}\} = (1 + sT^*) \cdot \frac{b_0}{(b_1 + s)^2} \quad (\text{A3-7})$$

The effective E curve $E(\theta)_{\text{eff}}$ can now be calculated using the Laplace back-transformation:

$$E(\theta)_{\text{eff}} = \mathcal{L}^{-1}\{E(s)_{\text{eff}}\} = b_0 \cdot \theta \cdot e^{-b_1\theta} + b_0 \cdot T^* \cdot (1 - b_1\theta) \cdot e^{-b_1\theta} \quad (\text{A3-8})$$

An example of the entire deconvolution procedure is illustrated in Fig. A3-6.

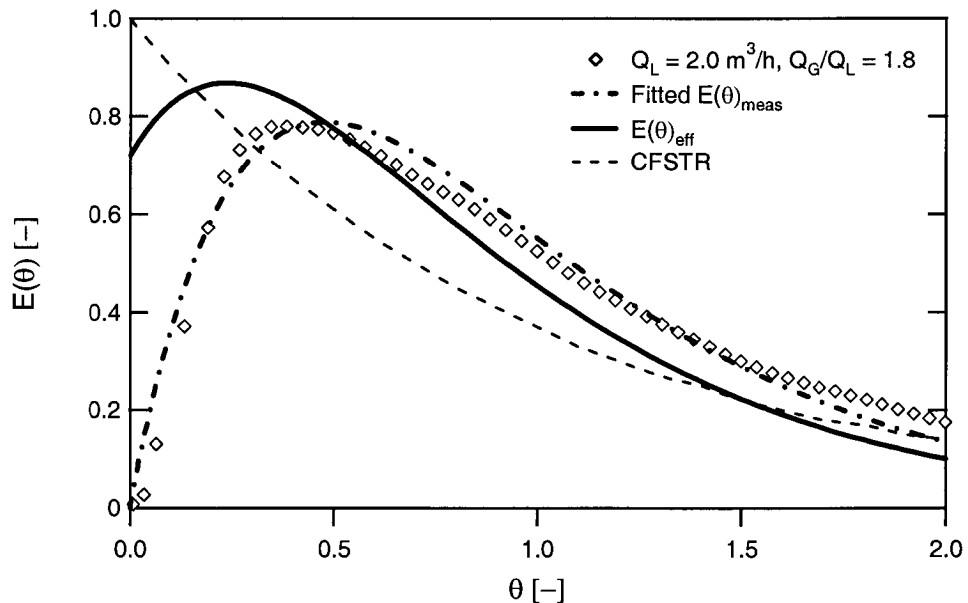


Fig. A3-6: Measured and effective E curves

The shape of the effective E curve was compared to the extreme cases of CFSTR and plug flow behaviour. As can be seen the effective E curve is approximated rather good by the CFSTR curve. Therefore, the gas phase can be considered as approximately well mixed. For the measurement of k_L this means, that the oxygen concentration at the gas outlet equals the mean oxygen concentration in the gas bubbles.

Appendix 4

Experimental data

A4.1 Air/water (ambient pressure)

Temperature: 25°C

Mixing tube diameter: 12.0 mm

Liquid batch size: 45 l

d_N	l_M	χ_{swirl}	e_S	Q_G	Q_G/Q_L	e_{tot}	k_{La}
[mm]	[mm]	°	[kW/m ³]	[m ³ /h]	[-]	[-]	[s ⁻¹]
6.2	220	180	0.84	2.88	1.97	0.03	0.03
6.2	220	180	1.34	3.35	1.96	0.04	0.05
6.2	220	180	1.98	3.78	1.94	0.07	0.07
6.2	220	180	2.81	4.15	1.90	0.09	0.09
6.2	220	180	2.79	4.15	1.90	0.09	0.08
6.2	220	180	2.79	4.15	1.90	0.09	0.09
6.2	220	180	2.81	4.15	1.90	0.09	0.08
6.2	220	180	2.79	4.26	1.95	0.09	0.08
6.2	220	180	2.81	4.26	1.95	0.09	0.08
6.2	220	180	2.81	4.26	1.95	0.09	0.09
6.2	220	180	3.77	4.58	1.90	0.11	0.12
6.2	220	180	4.84	4.91	1.87	0.14	0.17
6.2	220	0	0.83	0.71	0.49	0.03	0.05
6.2	220	0	1.32	0.94	0.55	0.05	0.08
6.2	220	0	1.97	1.31	0.68	0.08	0.10
6.2	220	0	2.76	2.24	1.04	0.11	0.17
6.2	220	0	3.66	4.15	1.75	0.13	0.24
6.2	220	0	3.94	4.75	1.98	0.16	0.25
6.2	220	270	0.83	2.95	2.03	0.02	0.02
6.2	220	270	1.32	3.49	2.05	0.04	0.04
6.2	220	270	1.98	3.93	2.02	0.06	0.06
6.2	220	270	2.79	4.42	2.03	0.09	0.07
6.2	220	270	3.75	4.86	2.02	0.11	0.09
6.2	220	270	4.84	5.29	2.02	0.14	0.12
6.2	220	90	0.83	1.42	0.97	0.03	0.05
6.2	220	90	1.34	1.75	1.02	0.05	0.07
6.2	220	90	1.96	2.22	1.14	0.07	0.11
6.2	220	90	2.75	3.27	1.52	0.11	0.15
6.2	220	90	3.55	4.26	1.81	0.13	0.20

d_N	l_M	χ_{swirl}	e_S	Q_G	Q_G/Q_L	e_{tot}	$k_L a$
[mm]	[mm]	°	[kW/m ³]	[m ³ /h]	[-]	[-]	[s ⁻¹]
6.2	220	90	4.21	5.02	2.03	0.14	0.26
6.2	220	90	1.75	1.69	0.98	0.06	0.09
6.2	220	90	2.54	2.95	1.52	0.09	0.14
6.2	220	90	3.13	3.98	1.95	0.12	0.15
6.2	220	90	3.52	4.42	2.12	0.14	0.16
6.2	220	90	4.00	4.69	2.17	0.16	0.17
8.0	220	90	0.82	1.54	0.77	0.05	0.05
8.0	220	90	1.35	1.89	0.80	0.06	0.07
8.0	220	90	2.00	2.29	0.86	0.08	0.12
8.0	220	90	2.63	2.84	0.97	0.11	0.17
8.0	220	90	3.13	3.09	1.01	0.14	0.20
8.0	220	90	3.64	3.19	1.00	0.15	0.25
8.0	220	180	0.82	1.86	0.93	0.03	0.04
8.0	220	180	1.32	2.16	0.93	0.06	0.06
8.0	220	180	2.00	2.48	0.93	0.09	0.09
8.0	220	180	2.90	2.67	0.88	0.12	0.13
8.0	220	180	3.87	2.86	0.86	0.14	0.18
8.0	220	180	4.83	3.27	0.92	0.16	0.26
8.0	220	270	0.82	1.58	0.80	0.04	0.03
8.0	220	270	1.34	1.91	0.82	0.06	0.05
8.0	220	270	2.02	2.25	0.84	0.09	0.06
8.0	220	270	2.87	2.62	0.87	0.13	0.08
8.0	220	270	3.87	2.87	0.86	0.16	0.10
8.0	220	270	5.03	3.14	0.86	0.18	0.14
8.0	220	0	0.82	0.98	0.49	0.05	0.06
8.0	220	0	1.35	1.31	0.55	0.07	0.10
8.0	220	0	1.97	2.62	0.98	0.10	0.17
8.0	220	0	2.48	3.01	1.05	0.13	0.22
8.0	220	0	2.93	3.17	1.05	0.14	0.24
8.0	220	0	3.45	3.29	1.03	0.16	0.29
8.0	120	0	0.82	0.65	0.33	0.04	0.05
8.0	120	0	1.33	1.09	0.46	0.06	0.08
8.0	120	0	1.89	2.62	0.99	0.09	0.12
8.0	120	0	2.48	2.95	1.02	0.11	0.18
8.0	120	0	2.85	3.17	1.06	0.13	0.21
8.0	120	0	3.28	3.27	1.05	0.14	0.25
8.0	120	0	3.25	3.27	1.06	0.14	0.25
8.0	120	90	0.82	1.96	0.97	0.04	0.05
8.0	120	90	1.33	2.40	1.01	0.06	0.08
8.0	120	90	1.98	2.73	1.01	0.08	0.10
8.0	120	90	2.44	3.11	1.10	0.11	0.17
8.0	120	90	3.24	3.27	1.07	0.13	0.21
8.0	120	90	3.65	3.49	1.11	0.13	0.26
8.0	120	180	0.82	2.07	1.04	0.05	0.05
8.0	120	180	1.35	2.40	1.02	0.07	0.06
8.0	120	180	2.00	2.78	1.04	0.09	0.08

d_N	l_M	χ_{swirl}	e_S	Q_G	Q_G/Q_L	e_{tot}	$k_L a$
[mm]	[mm]	°	[kW/m ³]	[m ³ /h]	[-]	[-]	[s ⁻¹]
8.0	120	180	2.87	3.11	1.03	0.12	0.11
8.0	120	180	3.87	3.44	1.03	0.14	0.15
8.0	120	180	5.00	3.71	1.02	0.16	0.20
8.0	120	270	0.82	1.86	0.93	0.05	0.04
8.0	120	270	1.34	2.18	0.93	0.08	0.06
8.0	120	270	2.00	2.57	0.96	0.11	0.08
8.0	120	270	2.87	2.89	0.96	0.14	0.09
8.0	120	270	3.87	3.22	0.97	0.16	0.11
8.0	120	270	5.03	3.49	0.96	0.17	0.16
6.2	120	0	0.83	0.65	0.45	0.03	0.04
6.2	120	0	1.33	0.82	0.48	0.05	0.06
6.2	120	0	1.98	1.09	0.56	0.07	0.08
6.2	120	0	2.79	2.18	1.00	0.10	0.11
6.2	120	0	3.65	3.38	1.42	0.13	0.16
6.2	120	0	4.34	4.58	1.83	0.15	0.21
6.2	120	90	0.83	0.94	0.64	0.03	0.04
6.2	120	90	1.33	1.16	0.68	0.05	0.06
6.2	120	90	1.95	1.47	0.76	0.07	0.08
6.2	120	90	2.75	2.73	1.26	0.10	0.11
6.2	120	90	3.61	3.88	1.65	0.13	0.15
6.2	120	90	4.31	5.02	2.02	0.14	0.20
6.2	120	180	0.83	3.27	2.23	0.04	0.04
6.2	120	180	1.34	3.79	2.22	0.06	0.06
6.2	120	180	2.00	4.27	2.18	0.08	0.08
6.2	120	180	2.83	4.78	2.18	0.11	0.09
6.2	120	180	3.79	5.28	2.19	0.14	0.11
6.2	120	180	4.87	5.68	2.16	0.16	0.12
6.2	120	270	0.83	3.20	2.20	0.03	0.03
6.2	120	270	1.32	3.77	2.21	0.06	0.05
6.2	120	270	1.97	4.28	2.20	0.08	0.06
6.2	120	270	2.77	4.80	2.21	0.11	0.08
6.2	120	270	3.75	5.29	2.20	0.14	0.10
6.2	120	270	4.82	5.74	2.19	0.15	0.13
6.2	370	0	0.83	1.75	1.19	0.04	0.03
6.2	370	0	1.33	2.27	1.33	0.05	0.05
6.2	370	0	1.98	2.73	1.40	0.06	0.06
6.2	370	0	2.81	3.20	1.46	0.09	0.08
6.2	370	0	3.75	3.67	1.52	0.11	0.11
6.2	370	0	4.80	4.09	1.56	0.14	0.17
6.2	370	90	0.84	1.69	1.15	0.03	0.04
6.2	370	90	1.34	2.18	1.27	0.05	0.05
6.2	370	90	1.99	2.67	1.37	0.06	0.06
6.2	370	90	2.78	3.06	1.40	0.08	0.08
6.2	370	90	3.73	3.44	1.43	0.11	0.12
6.2	370	90	4.78	3.82	1.46	0.14	0.16
6.2	370	180	0.84	2.51	1.72	0.03	0.02

d_N	l_M	χ_{swirl}	e_S	Q_G	Q_G/Q_L	e_{tot}	$k_L a$
[mm]	[mm]	°	[kW/m ³]	[m ³ /h]	[-]	[-]	[s ⁻¹]
6.2	370	180	1.34	2.89	1.69	0.04	0.03
6.2	370	180	1.98	3.22	1.65	0.06	0.05
6.2	370	180	2.81	3.55	1.62	0.06	0.06
6.2	370	180	3.79	3.88	1.60	0.08	0.08
6.2	370	180	4.87	4.20	1.60	0.10	0.10
6.2	370	270	0.84	2.51	1.72	0.02	0.02
6.2	370	270	1.34	3.00	1.76	0.04	0.04
6.2	370	270	1.98	3.38	1.74	0.05	0.05
6.2	370	270	2.79	3.77	1.73	0.07	0.07
6.2	370	270	3.75	4.09	1.70	0.09	0.08
6.2	370	270	4.82	4.42	1.69	0.12	0.11
8.0	370	0	0.82	1.69	0.84	0.04	0.04
8.0	370	0	1.35	1.96	0.83	0.06	0.06
8.0	370	0	2.01	2.24	0.82	0.08	0.09
8.0	370	0	2.84	2.51	0.82	0.10	0.13
8.0	370	0	3.65	2.84	0.86	0.12	0.17
8.0	370	0	4.10	3.00	0.89	0.13	0.20
8.0	370	90	0.84	2.18	1.09	0.03	0.03
8.0	370	90	1.35	2.37	1.01	0.05	0.05
8.0	370	90	2.03	2.62	0.97	0.07	0.07
8.0	370	90	2.87	2.90	0.96	0.09	0.10
8.0	370	90	3.75	3.27	0.99	0.11	0.13
8.0	370	90	4.49	3.65	1.05	0.13	0.17
8.0	370	180	0.84	1.96	0.98	0.04	0.03
8.0	370	180	1.37	2.29	0.97	0.05	0.05
8.0	370	180	2.05	2.59	0.96	0.07	0.06
8.0	370	180	2.90	2.89	0.96	0.09	0.08
8.0	370	180	3.87	3.22	0.97	0.12	0.12
8.0	370	180	4.96	3.55	0.98	0.14	0.16
8.0	370	270	0.84	1.64	0.82	0.03	0.03
8.0	370	270	1.34	1.93	0.82	0.05	0.04
8.0	370	270	2.02	2.33	0.87	0.07	0.06
8.0	370	270	2.87	2.73	0.91	0.10	0.07
8.0	370	270	3.90	3.17	0.95	0.12	0.09
8.0	370	270	5.03	3.55	0.98	0.14	0.12

A4.2 Air/0.25 M Na₂SO₄-solution

Temperature: 25°C

Mixing tube diameter: 12.0 mm

Liquid batch size: 25 l

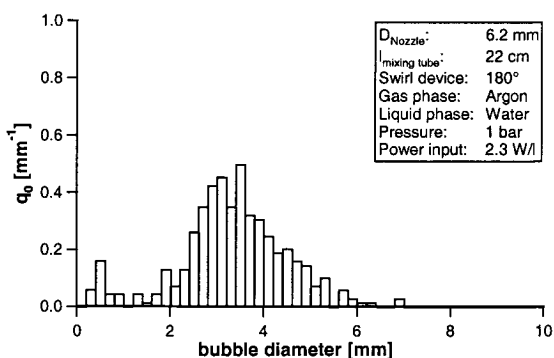
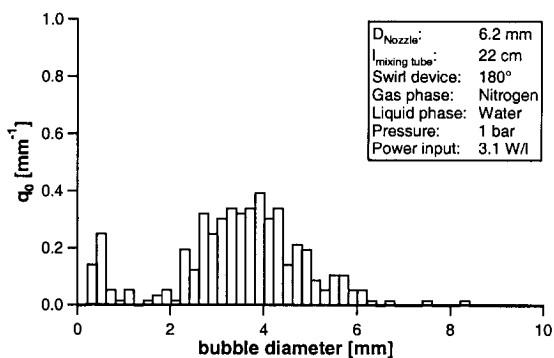
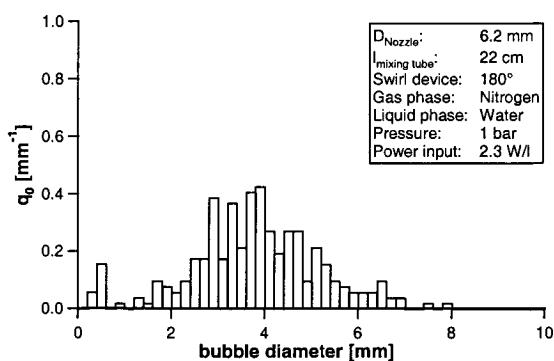
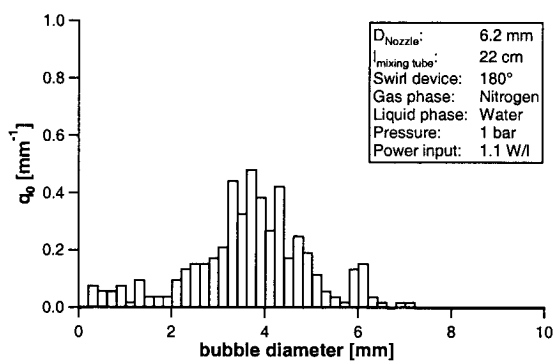
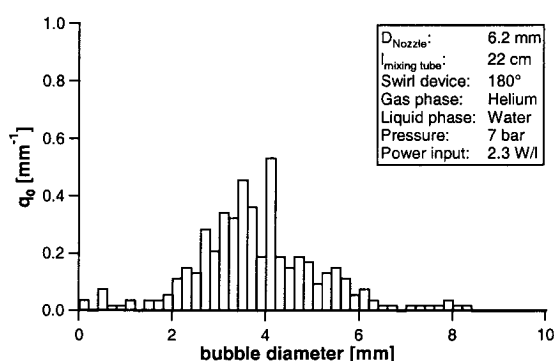
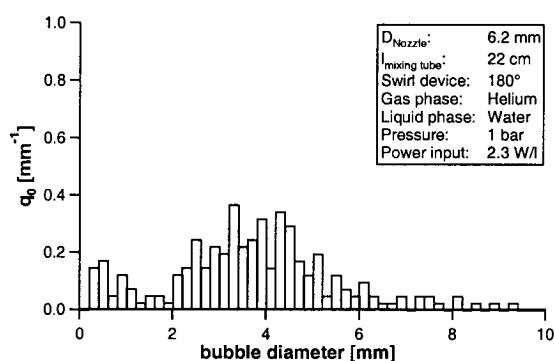
d_N	l_M	χ_{swirl}	e_S	Q_G	Q_G/Q_L	e_{tot}	k_{La}
[mm]	[mm]	°	[kW/m ³]	[m ³ /h]	[-]	[-]	[s ⁻¹]
8.0	370	0	1.86	1.86	0.90	0.15	0.68
8.0	370	0	2.64	2.07	0.93	0.23	1.15
8.0	370	0	3.31	2.24	0.96	0.27	1.57
8.0	370	0	1.56	1.64	0.81	0.12	0.43
8.0	370	0	3.09	2.02	0.81	0.16	0.80
8.0	370	0	4.53	2.24	0.80	0.21	1.44
8.0	370	90	1.89	1.53	0.74	0.09	0.54
8.0	370	90	3.37	1.75	0.72	0.18	1.01
8.0	370	90	3.72	1.86	0.76	0.23	1.17
8.0	370	180	2.21	1.20	0.54	0.12	0.51
8.0	370	180	3.88	1.36	0.52	0.18	1.03
8.0	370	180	4.58	1.36	0.51	0.23	1.31
8.0	370	180	2.25	1.20	0.53	0.12	0.37
8.0	370	180	4.10	1.42	0.53	0.18	0.53
8.0	370	270	2.43	1.15	0.49	0.09	0.49
8.0	370	270	4.95	1.42	0.48	0.23	1.32
8.0	370	270	6.63	1.36	0.44	0.29	1.49
6.2	370	270	2.38	2.62	1.55	0.09	0.30
6.2	370	270	4.87	3.17	1.49	0.23	0.70
6.2	370	270	7.16	3.49	1.46	0.27	1.04
6.2	370	180	2.36	2.84	1.69	0.09	0.35
6.2	370	180	4.46	3.33	1.64	0.18	0.66
6.2	370	180	5.91	3.71	1.70	0.23	1.02
6.2	370	180	3.92	3.27	1.62	0.19	0.80
6.2	370	180	5.58	3.60	1.61	0.22	1.05
6.2	370	90	2.23	2.13	1.30	0.15	0.58
6.2	370	90	3.56	2.95	1.60	0.21	0.98
6.2	370	90	4.36	3.27	1.69	0.23	1.12
6.2	370	0	2.26	2.13	1.28	0.15	0.55
6.2	370	0	3.64	2.95	1.59	0.23	0.86
6.2	370	0	4.45	3.38	1.73	0.27	1.06
6.2	370	0	1.97	1.80	1.09	0.12	0.42
6.2	370	0	3.21	2.46	1.32	0.19	0.91
6.2	370	0	4.52	2.95	1.44	0.21	1.21
6.2	220	0	1.89	2.29	1.50	0.23	0.79
6.2	220	0	3.09	2.78	1.60	0.27	1.16
6.2	220	0	3.91	3.17	1.70	0.31	1.29
6.2	220	180	2.30	3.22	1.93	0.18	0.61

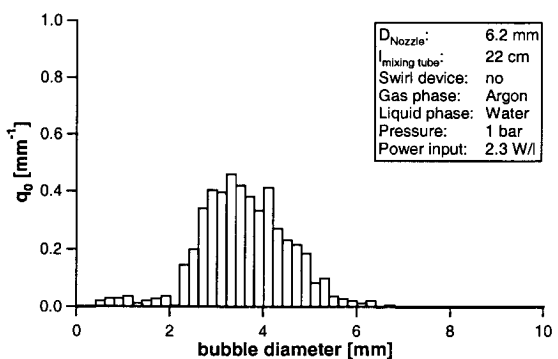
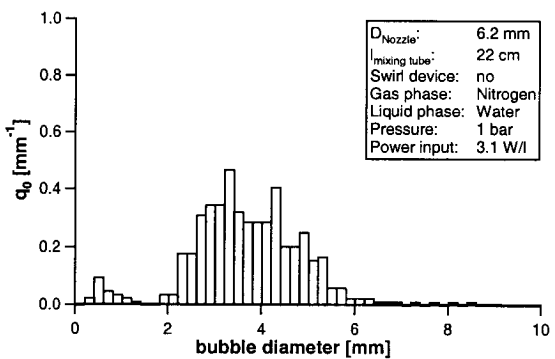
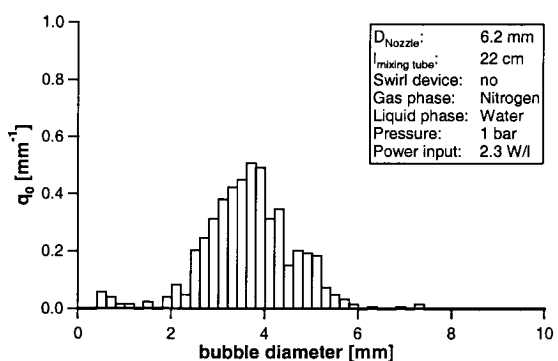
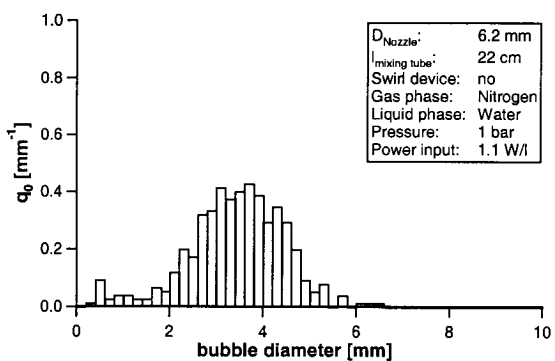
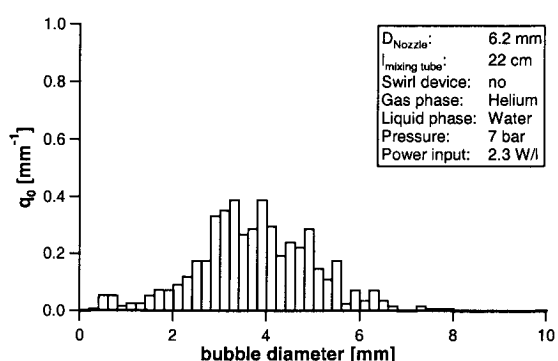
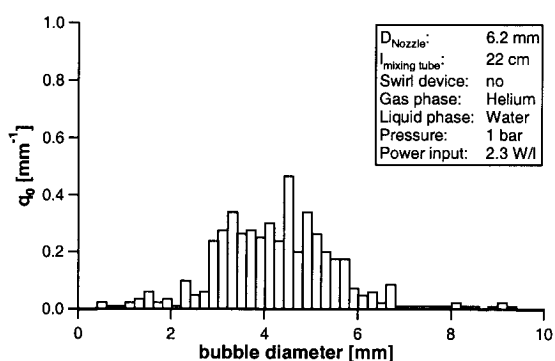
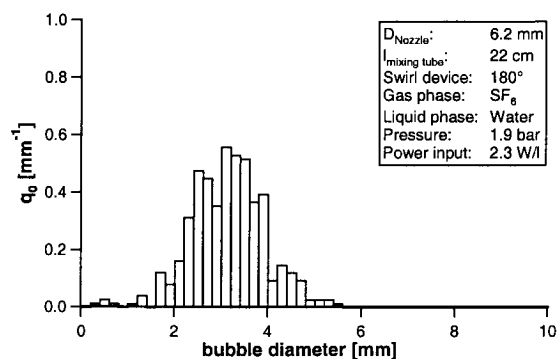
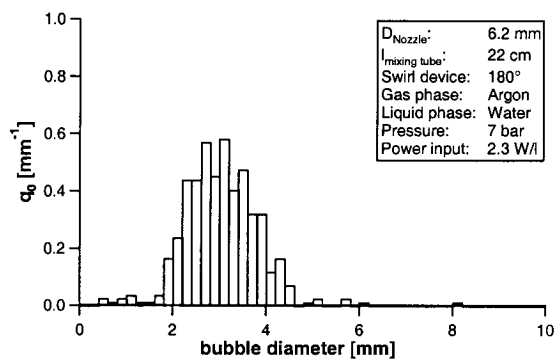
d_N	l_M	χ_{swirl}	e_s	Q_G	Q_G/Q_L	e_{tot}	$k_L a$
[mm]	[mm]	°	[kW/m ³]	[m ³ /h]	[-]	[-]	[s ⁻¹]
6.2	220	180	3.82	4.04	2.10	0.25	1.25
6.2	220	180	5.28	4.48	2.13	0.35	1.61
6.2	220	180	1.84	3.44	1.99	0.15	0.18
6.2	220	180	2.15	3.49	2.02	0.20	0.36
6.2	220	180	3.18	3.98	2.02	0.27	0.53
6.2	220	180	4.68	4.37	2.10	0.36	0.89
6.2	220	180	5.98	4.64	2.07	0.39	0.99
6.2	220	180	6.07	4.69	2.11	0.39	0.97
6.2	220	90	1.94	1.75	1.14	0.19	0.64
6.2	220	90	2.42	2.02	1.25	0.23	0.76
6.2	220	90	2.77	2.18	1.31	0.25	0.78
6.2	220	90	3.07	2.35	1.37	0.25	0.82
6.2	220	90	3.54	2.57	1.44	0.27	0.87
6.2	220	270	2.38	3.47	2.06	0.17	0.48
6.2	220	270	3.55	3.95	2.05	0.23	0.78
6.2	220	270	4.89	4.37	2.04	0.29	1.19
6.2	220	270	6.42	4.80	2.08	0.35	1.44
8.0	220	180	2.20	1.86	0.83	0.21	0.57
8.0	220	180	3.85	2.18	0.83	0.27	1.02
8.0	220	180	5.13	2.29	0.82	0.33	1.20
8.0	220	180	5.13	2.29	0.82	0.33	1.36
8.0	220	0	1.66	1.64	0.84	0.21	0.55
8.0	220	0	2.64	2.02	0.91	0.25	0.71
8.0	220	0	3.72	2.35	0.96	0.29	0.92
8.0	220	270	2.39	1.80	0.78	0.18	0.40
8.0	220	270	4.96	2.40	0.82	0.25	1.01
8.0	220	270	7.07	2.73	0.87	0.31	1.25
8.0	220	90	1.83	1.86	0.92	0.21	0.57
8.0	220	90	2.70	2.18	0.98	0.25	0.83
8.0	220	90	3.55	2.40	1.01	0.29	1.12
8.0	120	90	1.70	1.86	0.95	0.21	0.60
8.0	120	90	2.60	2.18	1.00	0.25	0.82
8.0	120	90	3.53	2.46	1.04	0.27	1.04
8.0	120	0	1.70	1.42	0.72	0.18	0.48
8.0	120	0	2.76	1.69	0.75	0.24	0.65
8.0	120	0	3.79	2.02	0.82	0.27	0.82
8.0	120	270	2.39	2.13	0.92	0.15	0.39
8.0	120	270	5.04	2.84	0.96	0.31	0.84
8.0	120	270	7.30	3.17	0.97	0.36	1.36
8.0	120	180	2.28	2.29	1.01	0.21	0.64
8.0	120	180	3.46	2.51	0.98	0.31	0.97
8.0	120	180	5.04	2.84	1.01	0.36	1.29
6.2	120	0	1.88	2.13	1.41	0.18	0.46
6.2	120	0	3.25	2.51	1.42	0.23	0.68
6.2	120	0	4.30	2.84	1.48	0.27	0.80
6.2	120	90	1.85	2.13	1.43	0.18	0.52

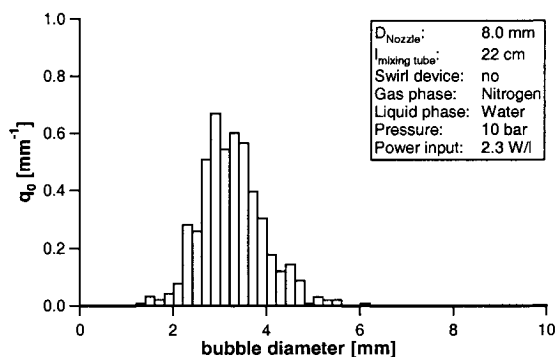
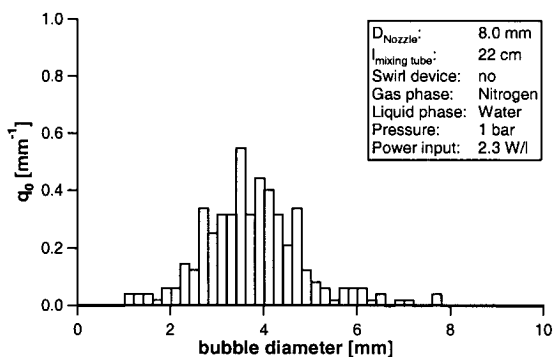
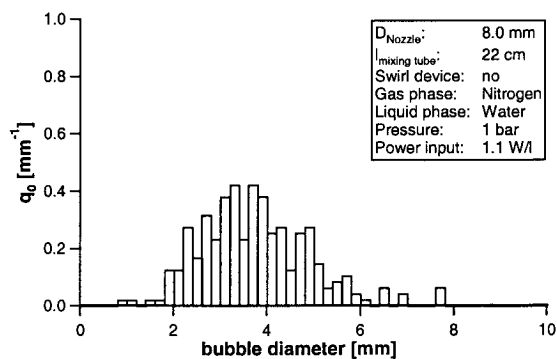
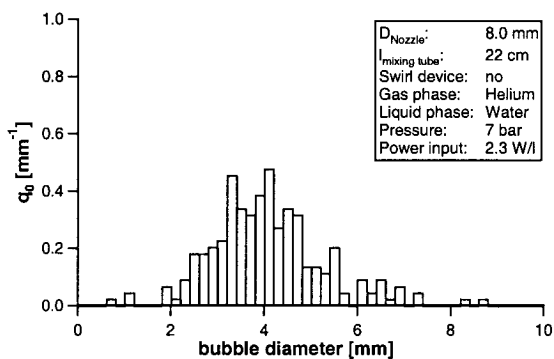
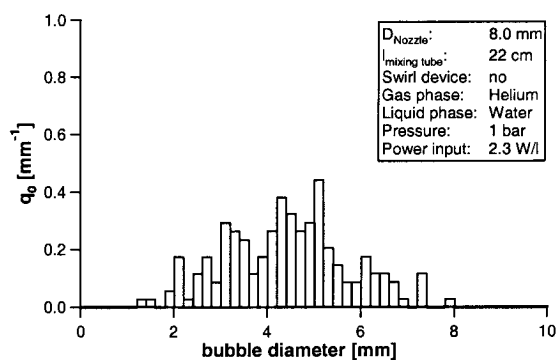
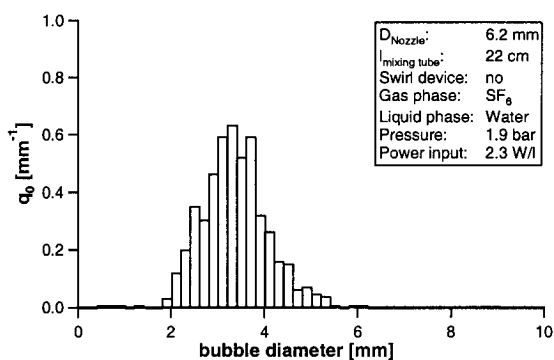
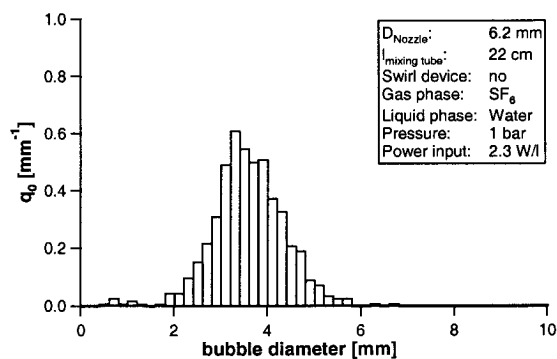
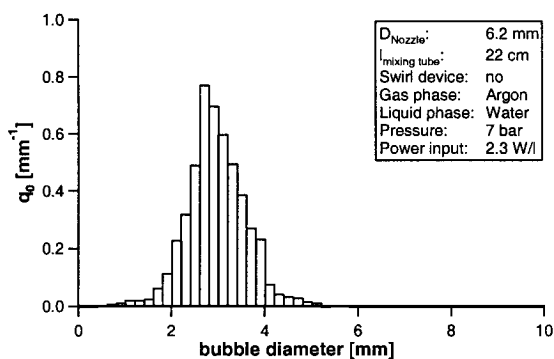
d_N	l_M	χ_{swirl}	e_S	Q_G	Q_G/Q_L	e_{tot}	$k_L a$
[mm]	[mm]	°	[kW/m ³]	[m ³ /h]	[-]	[-]	[s ⁻¹]
6.2	120	90	3.09	2.73	1.58	0.23	0.73
6.2	120	90	4.07	3.06	1.63	0.29	0.89
6.2	120	270	2.38	3.71	2.20	0.21	0.65
6.2	120	270	5.08	4.75	2.24	0.36	1.09
6.2	120	270	3.55	4.26	2.21	0.31	0.95
6.2	120	180	2.32	3.77	2.25	0.18	0.65
6.2	120	180	3.49	4.26	2.25	0.29	0.87
6.2	120	180	4.88	4.69	2.26	0.38	1.33

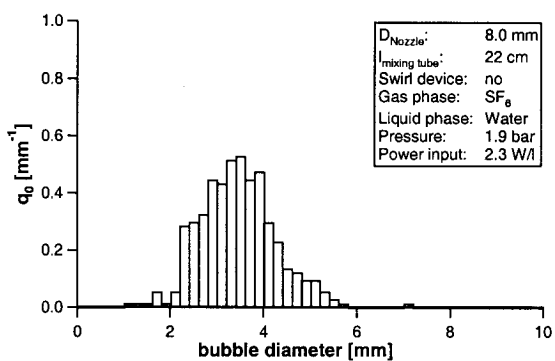
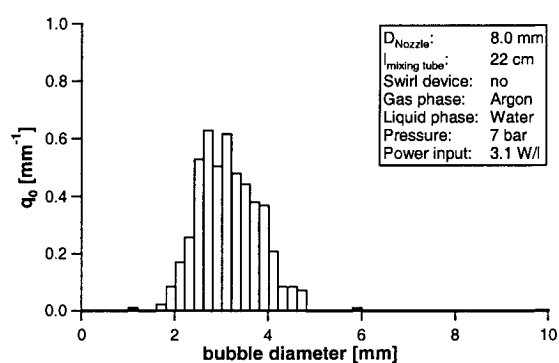
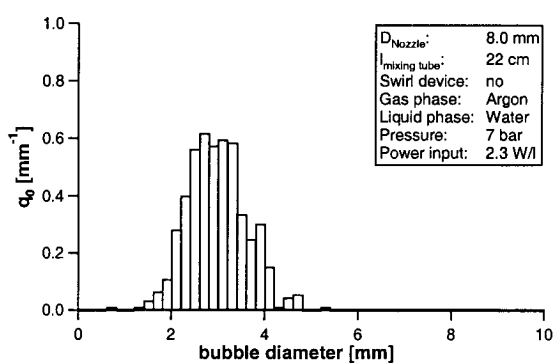
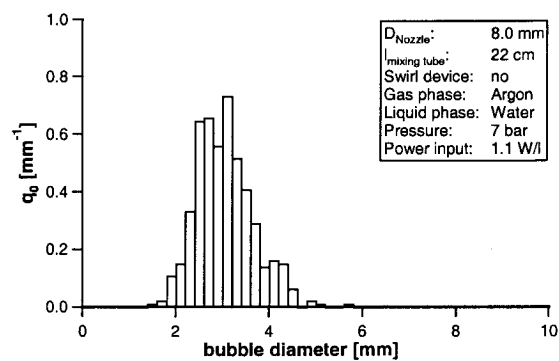
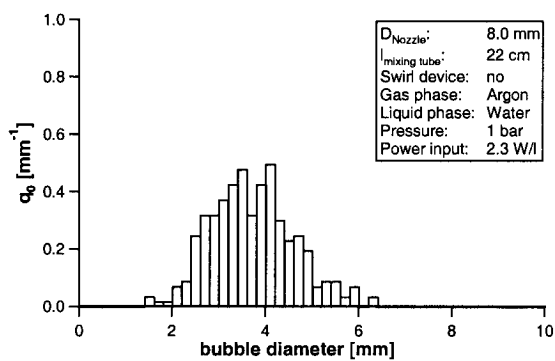
Appendix 5

Exemplary bubble size distributions with different gas densities and reaction mixer geometries in water









References

- Alvarez Fuster, C., Midoux, N., Laurent, A., Charpentier, J.C. (1980). "Chemical kinetics of the reaction of carbon dioxide with amines in pseudo nth order conditions in aqueous and organic solutions." Chemical Engineering Science **35**: 1717-1723.
- Andreussi, P., Di Donfrancesco, A., Messia, M. (1988). "An Impedance Method for the Measurement of Liquid Hold-up in Two-Phase Flow." Int. J. Multiphase Flow **14**(6): 777-785.
- Baier, F. (1997). "Vergleich des Buss-Loop-Reaktors und der Buss-Intensivbegasung bezüglich ihrer Funktionsweise und Stofftransporteigenschaften." Diploma Thesis, Zürich, Swiss Federal Institute of Technology
- Barigou, M., Greaves, M. (1992). "Bubble-Size Distributions in a Mechanically Agitated Gas-Liquid Contactor." Chemical Engineering Science **47**(8): 2009-2025.
- Barigou, M., Greaves, M. (1996). "Gas Holdup and interfacial area distributions in a Mechanically Agitated Gas-Liquid Contactor." Trans IChemE **74**(Part A): 397-405.
- Battino, R., Ed. (1981). Oxygen and Ozone. Solubility Data Series. Oxford, Pergamon Press.
- Battino, R. (1982). Nitrogen and Air. Oxford, Pergamon Press.
- Battino, R., Rettich, T.R., Tominaga, T. (1984). "The Solubility of Nitrogen and Air in Liquids." J. Phys. Chem. Ref. Data **13**(2): 563-600.
- Bentifraouine, C., Xuereb, C., Riba, J.P. (1999). "Local Gas Hydrodynamics in an External-Loop Airlift Reactor: Newtonian and non-Newtonian Fluids." Bioprocess Engineering **20**: 303-307.
- Bin, A.K. (1993). "Gas entrainment by plunging liquid jets." Chemical Engineering Science **48**(21): 3585-3630.
- Bombac, A., Zun, I., Filipic, B. (1997). "Gas-Filled Cavity Structures and Local Void Fraction Distribution in an Aerated Stirred Vessel." AIChE Journal **43**(11): 2921-2931.
- Bonfig, K.W. (1987). Technische Durchflussmessung: Unter besonderer Berücksichtigung neuartiger Durchflussmessverfahren. Essen, Vulkan-Verlag.

- Bonfig, K.W. (1990). Technische Füllstandsmessung und Grenzstandskontrolle. Ehnningen bei Böblingen, Expert Verlag.
- Bonfig, K.W. (1990). Durchflussmessung von Flüssigkeiten und Gasen. Ehnningen bei Böblingen, Expert Verlag.
- Bouaifi, M., Roustan, M. (1998). "Bubble Size and Mass Transfer Coefficients in Dual-Impeller Agitated Reactors." The Canadian Journal of Chemical Engineering **76**(june): 390-397.
- Boyd, J.W.R., Varley, J. (1998). "Sound Measurement as a Means of Gas-Bubble Sizing in Aerated Agitated Tanks." AIChE Journal **44**(8): 1731-1739.
- Buchholz, R., Zakrzewski, w., Schügerl, K. (1981). "Techniques for Determining the Properties of Bubbles in Bubble Columns." International Chemical Engineering **21**(2): 180-187.
- Chaouki, J., Larachi, F., Dudukovic, M. (1997). "Noninvasive Tomographic and Velocimetric Monitoring of Multiphase Flows." Ind. Eng. Chem. Res. **36**(11): 4476-4503.
- Charpentier, J.-C. (1981). "Mass-Transfer Rates in Gas-Liquid Absorbers and Reactors." Advances in Chemical Engineering **11**: 2-133.
- Chen, R.C., Fan, L.-S. (1992). "Particle Image Velocimetry for Characterizing the Flow Structure in Three-Dimensional Gas-Liquid-Solid Fluidized Beds." Chemical Engineering Science **47**(13/14): 3615-3622.
- Clark, N.N., Turton, R. (1988). "Chord Length Distributions Related to Bubble Size Distributions in Multiphase Flows." Int. J. Multiphase Flow **14**(4): 413-424.
- Concordia, J.J. (1990). "Batch Catalytic Gas/Liquid Reactors: Types and Performance Characteristics." Chemical Engineering Progress **86**(3): 50-54.
- Cramers, P.H.M.R., van Dierendonck, L.L., Beenackers, A.A.C.M. (1992). "Influence of the gas density on the gas entrainment rate and gas holdup in loop-venturi reactors." Chemical Engineering Science **47**(9-11): 2251-2256.
- Cramers, P.H.M.R., Beenackers, A.A.C.M., van Dierendonck, L.L. (1992). "Hydrodynamics and mass transfer characteristics of a loop-venturi reactor with a downflow liquid jet ejector." Chemical Engineering Science **47**(13/14): 3557-3564.
- Cramers, P.H.M.R., Smit, L., Leuteritz, G.M., van Dierendonck, L.L., Beenackers, A.A.C.M. (1993). "Hydrodynamics and local mass transfer characteristics of gas-liquid ejectors." The Chemical Engineering Journal **53**(1): 67-73.

- Cramers, P.H.M.R., Beenackers, A.A.C.M. (2001). "Influence of the ejector configuration, scale and the gas density on the mass transfer characteristics of gas-liquid ejectors." Chemical Engineering Journal **82**: 131-141.
- Danckwerts, P.V. (1970). Gas-Liquid Reactions. New York, McGraw-Hill.
- Deckwer, W.-D. (1985). Reaktionstechnik in Blasensäulen. Aarau, Verlag Sauerländer.
- Dirix, C.A.M.C., van der Wiele, K. (1990). "Mass Transfer in Jet Loop Reactors." Chemical Engineering Science **45**(8): 2333-2340.
- Drahm, W., Matt, Ch. (1998). "Colioli-Massendurchflussmessung - Gerades Einrohrsystem mit neuer Schwingungskompensation." Automatisierungstechnische Praxis **40**(9): 24-29.
- Duquenne, A.M., Guiraud, P., Bertrand, J. (1993). "Swirl-induced improvement of turbulent mixing: Laser study in a jet-stirred tubular reactor." Chemical Engineering Science **48**(22): 3805-3812.
- Dutta, N.N., Raghavan, K.V. (1987). "Mass transfer and Hydrodynamic Characteristics of Loop Reactors with Downflow Liquid Jet Ejectors." The Chemical Engineering Journal **36**: 111-121.
- Elvers, B., Hawkins, S., Schulz, G., Ed. (1992). Ullmann's Encyclopedia of Industrial Chemistry: Principles of chemical reaction engineering and plant design. Weinheim, VCH Verlagsgesellschaft.
- Evans, G.M., Jameson, G.J., Atkinson, B.W. (1992). "Prediction of the bubble size generated by a plunging liquid jet bubble column." Chemical Engineering Science **47**(13/14): 3265-3272.
- Evans, G.M., Jameson, G.J. (1995). "Hydrodynamics of a plunging liquid jet bubble column." Trans IChemE, Part A **73**(August): 679-684.
- Evans, G.M., Bin, A.K., Machniewski, P.M. (2001). "Performance of confined plunging liquid jet bubble column as a gas-liquid reactor." Chemical Engineering Science **56**: 1151-1157.
- Ewing, M.E., Weinandy, J.J., Christensen, R.N. (1999). "Observations of Two-Phase Flow Patterns in a Horizontal Circular Channel." Heat Transfer Engineering **20**(1): 9-14.
- Eya, H., Mishima, K., Nagatani, M., Iwai, Y., Arai, Y. (1994). "Measurement and Correlation of Solubilities of Oxygen in Aqueous Solutions Containing Glucose, Sucrose and Maltose." Fluid Phase Equilibria **97**: 201-209.

- Fordham, E.J., Simonian, S., Ramos, R.T., Holmes, A., Huang, S.-M. (1999). "Multi-Phase-Fluid Discrimination with local fibre-optical probes: II. Gas/Liquid Flows." Meas. Sci. Technol. **10**: 1338-1346.
- Gaddis, E.S. (1994). "Hydrodynamics and Mass Transfer in an Impinging-Stream Loop Reactor Aerated from the Top." Chemical Engineering and Processing **33**: 285-289.
- Gaddis, E.S. (1999). "Mass Transfer in Gas-Liquid Contactors." Chemical Engineering and Processing **38**: 503-510.
- Gagnon, H., Lounès, M., Thibault, J. (1998). "Power Consumption and Mass Transfer in Agitated Gas-Liquid Columns: A Comparative Study." The Canadian Journal of Chemical Engineering **76**(June): 379-389.
- García-Ochoa, F., Gómez, E. (1998). "Mass Transfer in Stirred Tank Reactors for Xanthan Gum Solutions." Biochemical Engineering Journal **1**: 1-10.
- Genenger, B., Lohrengel, B. (1992). "Measuring Device for Gas-Liquid-Flow." Chemical Engineering and Processing **31**: 87-96.
- Geraets, J.J.M., Borst, J.C. (1988). "A Capacitance sensor for the Two-Phase Void Fraction Measurement and Flow Pattern Identification." Int. J. Multiphase Flow **14**(3): 305-320.
- Gesellschaft Deutscher Chemiker, B.f.u.A.B. (1997). Hydrazin, Hydrazinhydrat und Hydrazinsulfate, BUA-Stoffbericht 205, S. Hirzel, Wissenschaftliche Verlagsgesellschaft.
- Greenwood, T.S. (1986). "Loop reactors for catalytic hydrogenation." Chemistry and Industry **3**(February).
- Havelka, P., Linek, V., Sinulke, J., Zahradnik, J., Fialova, M. (1997). "Effect of the ejector configuration on the gas suction rate and gas holdup in ejector loop reactors." Chemical Engineering Science **52**(11): 1701-1713.
- Havelka, P., Linek, V., Sinulke, J., Zahradnik, J., Fialova, M. (2000). "Hydrodynamic and mass transfer characteristics of ejector loop reactors." Chemical Engineering Science **55**: 535-549.
- Heim, A., Rzycki, E., Stelmach, J. (1997). "Diameters of Air Bubbles Generated by Self-Aspiring Mixer." Chem. Biochem. Eng. Q. **11**(3): 143-146.
- Henzler, H.-J. (1981). "Das Sogverhalten von Strahlsaugern für das Stoffsystem: flüssig-gasförmig." vt Verfahrenstechnik **15**(10): 738-749.

- Hersperger, T.U., Rudolf von Rohr, Ph., Neukomm, P.A. (1995). "A Non-Intrusive, High-Speed System for Measuring Void Fraction Fluctuations in Annular Flow." Two-Phase Flow Modelling and Experimentation: 689-693.
- Hetsroni, G. (1982). Handbook of Multiphase Systems. New York a.o., Hemisphere publishing Corporation.
- Hinze, J.O. (1955). "Fundamentals of the Hydrodynamic Mechanisms of Splitting in Dispersion Processes." AIChE Journal 1(3): 289-295.
- Hitchman, M.L. (1978). Measurement of dissolved Oxygen. New York a.o., John Wiley & Sons, Inc. and Orbisphere Corp.
- Thermodynamische Betrachtung der Sauerstofflöslichkeit in Abhängigkeit von Temperatur, Druck und Salzgehalt. Enthält viele Löslichkeitstabellen
- Hofer, H., Mersmann, A. (1980). "Physical and chemical determination of the interfacial areas in gas-liquid contact equipment." Germ. Chem. Eng. 3: 347-352.
- Horvath, A.L. (1982). Halogenated Hydrocarbons: Solubility-Miscibility with Water. New York, Marcel Dekker, Inc.
- Imai, Y., Takei, H., Matsumura, M. (1987). "A Simple Na₂SO₃ Feeding Method for $k_L a$ Measurement in Large-Scale Fermentors." Biotechnology and Bioengineering 29(June): 982-993.
- Jekat, H., Pilhofer, Th. (1975). "Selbstansaugende Ejectoren für die Begasung von Flüssigkeiten." vt Verfahrenstechnik 9: 572-577.
- Joshi, J.B., Veera, U.P., Prasad, Ch.V., Phanikumar, D.V., Deshpande, N.S., Thakre, S.S., Thorat, B.N. (1998). "Gas Holdup Structure in Bubble Column Reactors." PINSA 64, A(4): 441-567.
- Judat, H. (1982). "Gas/Liquid Mass Transfer in Stirred Vessels - A Critical Review." German Chemical Engineering 5: 357-363.
- Kamiwano, e.a. (1998). "A Method for Measuring Bubble Diameter Distribution in Gas-Liquid Agitated Vessel under High Gas Holdup Using Real-Time High-Speed Image Processing System." Journal of Chemical Engineering of Japan 31(3): 366-373.
- Kastanek, F., Zahradnik, J., Kratochvil, J., Cermak, J. (1993). Chemical Reactors for Gas-Liquid-Systems. Chichester, Ellis Horwood.
- Kawase, Y., Moo-Young, M. (1990). "Mathematical Models for the Design of Bioreactors: Applications of Kolmogoroff's Theory of Isotropic Turbulence." The Chemical Engineering Journal 43(1): B19-B41.

- Kojima, H., Sawai, J., Suzuki, H. (1997). "Effect of pressure on the volumetric mass transfer coefficient and gas holdup in bubble column." Chemical Engineering Science **52**(21/22): 4111-4116.
- Kuncova, G., Zahradnik, J. (1995). "Gas Holdup and Bubble Frequency in a Bubble Column Reactor Containing Viscous Saccharose Solutions." Chemical Engineering and Processing **34**: 25-34.
- Lamont, J.C., Scott, D.S. (1970). "An Eddy Cell Model of Mass Transfer into the Surface of a Turbulent Liquid." AIChE Journal **16**(4): 513-519.
- Langhans, G., Liepe, F., Richter, K., Schlaf, G. (1977). "Untersuchungen zum Stoffver-einigen in flüssiger Phase." Chem. Tech. **29**(12): 662-665.
- Lara Márquez, A., Wild, G., Midoux, N. (1994). "A review of recent chemical techniques for the determination of the volumetric mass-transfer coefficient $k_L a$ in gas-liquid reactors." Chemical Engineering and Processing **33**: 247-260.
- Lara Márquez, A., Nguyen, C., Poncin, S., Wild, G., Midoux, N. (1994). "A Novel Hydrazine Oxidation Rechnique for the Determination of $k_L a$ in Gas-Liquid and Gas-Liquid-Solid Reactors." Chemical Engineering Science **49**(24B): 5667-5679.
- Lee, S.-Y., Tsui, Y.P. (1999). "Succeed at Gas/Liquid Contacting." Chemical Engineering Progress(July): 23-49.
- Leighton, T.G., Ramble, D.G., Phelps, A.D. (1997). "The detection of tethered and rising bubbles using multiple acoustic techniques." The Journal of the Acoustical Society of America **101**(5): 2626-2634.
- Letzel, M.H., Schouten, J.C., van den Bleek, C.M., Krishna, R. (1998). "Effect of Gas Density on Large-Bubble Holdup in Bubble Column Reactors." AIChE Journal **44**(10): 2333-2336.
- Leuteritz, M., Reimann, P., Vergéres, P. (1976). "Loop reactors: Better gas/liquid contact." Hydrocarbon Processing(June): 99-100.
- Lide, D.R., Ed. (1995). CRC Handbook of Chemistry and Physics. Boca Raton, CRC Press, Inc.
- Linek, V., Vacek, V. (1981). "Chemical Engineering Use of Catalyzed Sulfite Oxidation Kinetics for the Determination of Mass Transfer Characteristics of Gas-Liquid Con-tactors." Chemical Engineering Science **36**(11): 1747-1768.

- Linek, V., Benes, P., Sinkule, J. (1990). "Critical Assessment of the Steady-State Na_2SO_3 Feeding Method for $k_L a$ Measurement in Fermentors." Biotechnology and Bioengineering **35**(April): 766-770.
- Linek, V., Sinkule, J., Benes, P. (1992). "Critical Assessment of the Dynamic Double-Response Method for Measuring $k_L a$: Experimental Elimination of Dispersion Effects." Chemical Engineering Science **47**(15/16): 3885-3894.
- Linek, V., Havelka, P., Sinkule, J. (1996). "Supersaturation Effect in Steady-State and Dynamic Methods for Measuring $k_L a$ in Gas-Liquid Dispersions." Chemical Engineering Science **51**(23): 5223-5226.
- Linneweber, K.-W., Blass, E. (1983). "Measurement of Local Gas And Solids Holdups in Three-phase Bubble Columns." Ger. Chem. Eng. **6**: 28-33.
- Luo, X., Lee, D.J., Lau, R., Yang, G., Fan, L.-S. (1999). "Maximum Stable Bubble Size and Gas Holdup in High-Pressure Slurry Bubble Columns." AIChE Journal **45**(4): 665-680.
- Marquart, R. (1981). "Circulation of High Viscosity Newtonian and non-Newtonian Liquids in Jet Loop Reactors." International Chemical Engineering **21**(3): 399-407.
- Menzel, K.-D., Biermann, A., Driesch, D. (1998). "Untersuchungen zur $k_L a$ -Bestimmung mit der Ausgasungsmethode." BIOforum(12): 777-782.
- Merchuk, J.C., Yona, S., Siegel, M.H., Ben Zvi, A. (1990). "On the First-Order Approximation to the Response of Dissolved Oxygen Electrodes for Dynamic $k_L a$ Estimation." Biotechnology and Bioengineering **35**: 1161-1163.
- Morão, A., Maia, C.I., Fonseca, M.M.R., Vasconcelos, J.M.T, Alves, S.S. (1999). "Effect of Antifoam Addition on Gas-Liquid Mass Transfer in Stirred Fermenters." Bioprocess Engineering **20**: 165-172.
- Nagel, O., Kürten, H., Sinn, R. (1970). "Strahldüsenreaktoren - Teil I: Die Anwendung des Ejektorprinzips zur Verbesserung der Gasabsorption in Blasensäulen." Chemie Ingenieur Technik **42**(7): 474-479.
- Nagel, O., Kürten, H., Hegner, B. (1973). "Die Stoffaustauschfläche in Gas/Flüssigkeits-Kontaktapparaten - Auswahlkriterien und Unterlagen zur Vergrößerung." Chemie Ingenieur Technik **45**(14): 913-920.
- Nagel, O., Hegner, B., Kürten, H. (1981). "Criteria for the selection and design of gas/liquid reactors." International Chemical Engineering **21**(2): 161-172.

- Nardin, D. (1995). "Trends and opportunities with modern Buss loop reactor technology." Chemspec Europe 95 BACS Symposium.
- Nienow, A.W. (1996). "Gas-Liquid Mixing Studies: A Comparison of Rushton Turbines with Some Modern Impellers." Trans IChemE, Part A **74**: 417-423.
- Osorio, C., Onken, U. (1988). "Influence of Liquid Properties on the Determination of the Volumetric Mass Transfer Coefficient with the Hydrazine Method." Chem. Eng. Comm. **68**: 43-56.
- Otake, T., Tone, S., Kuboi, R., Takahashi, Y., Nakao, K. (1981). "Dispersion of a gas by a liquid-jet ejector." International Chemical Engineering **21**(1): 72-80.
- Oyevaar, M.H., Westerterp, K.R. (1989). "Mass Transfer Phenomena and Hydrodynamics in Agitated Gas-Liquid Reactors and Bubble Columns at Elevated Pressures: State of the Art." Chem. Eng. Process. **25**: 85-98.
- Oyevaar, M.H., Morssinkhof, W.J., Westerterp, K.R. (1990). "The kinetics of the reaction between CO₂ and diethanolamine in aqueous ethylene glycol at 298 K: a viscous gas-liquid reaction system for the determination of interfacial areas in gas-liquid contactors." Chemical Engineering Science **45**: 3283-3298.
- Palmer, H.J., Hughes, Ch.M.C., Lessen, M., Greenleaf, J., Buehler, K.L., Villalobos, C. (1999). "Novel Mixing Tank for Improved Gas-Liquid Mass Transfer and Solids Suspension." AIChE Journal **45**(10): 2117-2127.
- Pawelczyk, R., Pindur, K. (1999). "A dynamic method for dispersing gases in liquids." Chemical Engineering and Processing **38**: 95-107.
- Pfleger, D., Gomes, S., Gilbert, N., Wagner, H.-G. (1999). "Hydrodynamic simulations of laboratory scale bubble columns; fundamental studies of the Eulerian-Eulerian modelling approach." Chemical Engineering Science **54**: 5091-5099.
- Rauen, D., Aufderheide, E., Vogelpohl, A. (1984). "Automatischer Abgleich der Absaugsonde zur Tropfengrößenmessung." Technisches Messen **51. Jahrgang**(11): 408-412.
- Rhodes, M.J., Ed. (1990). Principles of powder technology. Chichester, John Wiley & Sons.
- Ritter, J., Kraume, M. (1999). "Inline-Messtechnik zur Tropfengrößenbestimmung in flüssigen Zweiphasensystemen bei hohen Dispersanteilen." Chemie Ingenieur Technik **71**(7): 717-720.
- Russ, J.C. (1995). The Image Processing Handbook. London, CRC Press cop.

- Sadler, G.D., Roberts, J., Cornell, J. (1988). "Determination of Oxygen Solubility in Liquid Foods Using a Dissolved Oxygen Electrode." Journal of Food Science **53**(5): 1493-1496.
- Sauer, T., Hempel, D.-Ch. (1987). "Fluid Dynamics and Mass Transfer in a Bubble Column with Suspended Particles." Chem. Eng. Technol. **10**: 180-189.
- Schlüter, S., Schulzke, T. (1999). "Modellierung des Stoffübergangs mit schneller chemischer Reaktion in Gas/Flüssigkeitsreaktoren." Chemie Ingenieur Technik **71**(4): 364-368.
- Schmidt, E., Grigull, U. (1989). Properties of Water and Steam in SI-Units, 0-800°C, 0-1000 bar. Berlin, Heidelberg, New York, Springer-Verlag.
- Sedelies, R.S., A., Weinspach, P.-M. (1987). "Mass Transfer Area in Different Gas-Liquid Reactors as a Function of Liquid Properties." Chem. Eng. Technol. **10**: 1-15.
- Sick, R. (1985). Die homogen katalysierte Hydrazin-Oxidation: Eine Methode zur Bestimmung volumenbezogener Stoffübergangskoeffizienten. Abteilung Chemietechnik. Dortmund, Universität Dortmund: 108
- Sprehe, M., Mudimu, A.O., Gaddis, E.S., Kim, S.-M. (1999). "Einfache Messmethode zur Bestimmung des lokalen Gasgehaltes in turbulenten Zweiphasenströmungen." Chemie Ingenieur Technik **71**(5): 477-480.
- Steff, A., Weinspach, P.-M. (1982). "Fluid Dynamics, Heat and Mass Transfer in Agitated Aerated Slurry Reactors." German Chemical Engineering **5**: 342-350.
- Stein, W.A., Schäfer, H. (1984). "Aeration of Viscous Liquids with a Downward Directed Two-fluid Nozzle." Ger. Chem. Eng. **7**: 115-125.
- Stiess, M. (1992). Mechanische Verfahrenstechnik 1. Berlin, Springer-Verlag.
- Terasaka, K., Tsuge, H. (1991). "Mass Transfer in Highly Viscous Liquids in a Bubble Column with Constant-Flow Nozzles." Journal of Chemical Engineering of Japan **24**(4): 424-429.
- Tromans, D. (1998). "Temperature and Pressure Dependent Solubility of Oxygen in Water: A Thermodynamic analysis." Hydrometallurgy **48**: 327-342.
- Tung, H.-L., Tu, C.-C., Chang, Y.-Y., Wu, W.-T. (1998). "Bubble Characteristics and Mass Transfer in an Airlift Reactor with Multiple Net Draft Tubes." Bioprocess Engineering **18**: 323-328.

- van Dierendonck, L.L., Meindersma, G.W., Leuteritz, G.M. (1988). Scale-up of G-L Reactions Made Simple with Loop Reactors. 6th European Conference on Mixing, Pavia, Italy.
- van Dierendonck, L.L., Zahradnik, J., Linek, V. (1998). "Loop Venturi Reactor - A Feasible Alternative to Stirred Tank Reactors?" Ind. Eng. Chem. Res. **37**(3): 734-738.
- van Landeghem, H. (1980). "Multiphase Reactors: Mass Transfer and Modelling." Chemical Engineering Science **35**: 1912-1949.
- van Stroe-Biezen, S.A.M., Janssen, A.P.M., Janssen, L.J.J. (1993). "Solubility of Oxygen in Glucose Solutions." Analytica Chimica Acta **280**: 217-222.
- van Swaaij, W.P.M., Versteeg, G.F. (1992). "Mass Transfer Accompanied with Complex Reversible Chemical Reactions in Gas-Liquid Systems: An Overview." Chemical Engineering Science **47**(13/14): 3181-3195.
- Veera, U.P., Joshi, J.B. (1999). "Measurement of Gas Holdup Profiles by Gamma Ray Tomography: Effect of Sparger Design and Height of Dispersion in Bubble Columns." Trans IChemE, Part A **77**(June): 303-317.
- Wachsmann, U., Rübiger, N., Vogelpohl, A. (1984). "The Compact Reactor - A Newly Developed Loop Reactor with a High Mass Transfer Performance." Ger. Chem. Eng. **7**: 39-44.
- Warnecke, H.-J., Hussmann, P. (1989). "Volumetric Mass Transfer Coefficients of Gas Liquid Jet Loop Reactors by Oxidation of Hydrazine." Chem. Eng. Comm. **78**: 131-138.
- Weiland, P., Sick, R., Onken, U. (1981). "Determination of the Volumetric Mass Transfer Coefficients in Gas/Liquid Dispersions by the Oxidation of Hydrazine." German Chemical Engineering **4**: 379-386.
- Weiland, P., Sick, R., Osorio, C., Onken, U. (1986). "Oxidation of Hydrazine - A Reliable Method for the Determination of Volumetric Mass transfer Coefficients in Gas/Liquid Systems." German Chemical Engineering **9**: 143-148.
- Wilkinson, P.M. (1991). Physical Aspects and Scale-up of High Pressure Bubble Columns. Groningen, Groningen: 235
- Wilkinson, P.M., Haringa, H., van Dierendonck, L. (1994). "Mass transfer and bubble size in a bubble column under pressure." Chemical Engineering Science **49**(9): 1417-1427.
- Witte, J.H. (1969). "Mixing shocks in two-phase flow." J. Fluid Mech. **36**(4): 639-655.

- Zaara, M.A. (1999). "Effect of Electrolytes on the Hydrodynamic Behaviour in a Batch Packed Bubble Column." Chem. Biochem. Eng. Q. **13**(2): 47-52.
- Zahradnik, J., Kratochvil, J., Rylek, M. (1985). "Gas holdup and interfacial mass transfer in gas-liquid tower contactors with ejector-type gas distribution." Collect. Czech. Chem. Comm. **50**: 2535-2544.
- Zahradnik, J., Fialova, M., Linek, V., Sinulke, J., Reznickova, J., Kastanek, F. (1997). "Dispersion efficiency of ejector-type gas distributors in different operating modes." Chemical Engineering Science **52**(24): 4499-4510.
- Zahradnik, J., Kuncova, G., Fialova, M. (1999). "The effect of surface active additives on the bubble coalescence and gas holdup in viscous aerated batches." Chemical Engineering Science **54**: 2401-2408.
- Zaidi, A., Ghosh, P., Schumpe, A., Deckwer, W.-D. (1991). "Xanthan production in a plunging jet reactor." Applied Microbiology and Biotechnology **35**: 330-333.
- Zlokarnik, M. (1978). "Sorption Characteristics for Gas-Liquid Contacting in Mixing Vessels." Advances in Biochemical Engineering, Springer, Berlin **8**: 133-151.
- Zlokarnik, M. (1979). "Die Leistungsfähigkeit optimierter Injektoren für den Sauerstoffeintrag in biologischen Abwasserreinigungsanlagen." vt Verfahrenstechnik **13**(7/8): 601-604.
- Zlokarnik, M. (1979). "Sorption Characteristics of Slot Injectors and Their Dependency on the Coalescence Behaviour of the System." Chemical Engineering Science **34**: 1265-1271.
- Zlokarnik, M. (1980). "Eignung und Leistungsfähigkeit von Volumenbelüftern für biologische Abwasserreinigungsanlagen." Korrespondenz Abwasser **27**(3): 194-209.
- Zlokarnik, M. (1984). "Scale-up in Process Engineering." Ger. Chem. Eng. **7**: 150-159.
- Zlokarnik, M. (1991). Dimensional Analysis and Scale-up in Chemical Engineering. Berlin, Springer-Verlag.
- Zlokarnik, M. (1999). Rührtechnik: Theorie und Praxis. Berlin, Springer.

Curriculum Vitae

Name: Frank Oliver Baier
Date of birth: July 16, 1972
Place of birth: Baden (AG), Switzerland
Nationality: Swiss, citizen of Oberehrendingen (AG)

04/1979 - 03/1984 Primary school, Oberehrendingen (AG)
04/1984 - 03/1988 Intermediate school, Baden (AG)
04/1988 - 01/1992 Secondary school, Type C, Baden (AG)
02/1992 - 05/1992 Military service
10/1992 - 01/1997 Study of Chemical Engineering at the Swiss Federal
Institute of Technology (ETH), Department of Chemistry,
Zurich
Graduation as Chemical Engineer ETH
03/1997 - 02/1998 Assistant at the Institute of Process Engineering,
Swiss Federal Institute of Technology, Zurich
03/1998 - 06/2001 Doctoral Thesis under the supervision of Prof. Dr. F. Widmer
at the Institute of Process Engineering,
Swiss Federal Institute of Technology, Zurich
10/1998 - 09/2001 Postgraduate study of Industrial Engineering and Manage-
ment, ETH Zurich